Development and Assessment of Renewable Ammonia and Methanol Production Systems

by

Ahmed M. Hasan

A Thesis Submitted in Partial Fulfillment of
the Requirements for the Degree of Doctor of Philosophy
in
Mechanical Engineering

Faculty of Engineering and Applied Science
Mechanical Engineering Program
University of Ontario Institute of Technology (Ontario Tech University)
Oshawa, Ontario, Canada
April 2020

Thesis Examination Information

Submitted by: Dr.Ahmed Hasan

Doctor of Philosophy in Mechanical Engineering

Thesis title:
Development and Assessment of Renewable Ammonia and Methanol Production Systems

An oral defense of this thesis took place on April 1, 2020 front of the following examining committee:

Examining Committee:

Chair of Examining Committee	Dr. Martin Agelin-Chaab
Research Supervisor	Dr. Ibrahim Dincer
Examining Committee Member	Dr. Kamiel Gabriel
University Examiner	Dr. Franko Gaspari
External Examiner	Dr. Wael H. Ahmed

The above committee determined that the thesis is acceptable in form and content and that a satisfactory knowledge of the field covered by the thesis was demonstrated by the candidate during an oral examination. A signed copy of the Certificate of Approval is available from the School of Graduate and Postdoctoral Studies.

Abstract

In this thesis, four renewable energy-based integrated systems for sustainable communities are developed. System 1 consists of a single-stage OTEC plant integrated with an ammonia production and district cooling system. Two different operation cases of the analyzed system are considered, where for the first case 50% of the power produced is used to produce ammonia as an energy storage medium. The second case considers the power production system integrated with district cooling system. The highest energy and exergy efficiencies are found to be 1.37% and 56.17% for case 1, respectively. As for the case 2 the maximum energy and exergy efficiency of the OTEC plant is found to be 1.83% and 78.02% respectively. System 2 consists of wind turbines and solar PV units for power production. The plant integrates a power production system with a district cooling and ammonia synthesis system. The system provides 40% of the system produced to the ammonia synthesis system. Ammonia is used as an energy storage medium. The maximum energy and exergy efficiencies of the system are found to be 21.2% and 21.3%. System 3 is a trigeneration system, that consists of a two-stage Rankine cycle that integrated with an electrolytic cation exchange membrane (ECEM) reactor for carbon dioxide and hydrogen production to feed the methanol production system. The system performance is analysed under three different cases: case 1: ECEM reactor operates at its current efficiency with fuel production and district cooling being the only products, case 2: ECEM reactor operates at proton exchange membrane (PEM) efficiency, and case 3: Only power is produced with no fuel. The maximum overall energy efficiencies of the cycle are found to be 8.0, 8.6, and 7.3% for cases 1, 2, and 3, respectively. Finally, system 4 takes into consideration a novel integration of a thermal management system integrated within a bifacial PV module. The bifacial modules are assessed for offshore use. The modules are able to boil ammonia at a pressure of 8.97 bar under a temperature of -5^{o}C and a peak solar irradiance of 620 W/m^{2}.

Keywords: Ammonia; methanol; thermal management; renewable energy; cooling

Author's Declaration

I hereby declare that this thesis consists of original work of which I have authored. This is a true copy of the thesis, including any required final revisions, as accepted by my examiners.

I authorize the University of Ontario Institute of Technology (Ontario Tech University) to lend this thesis to other institutions or individuals for the purpose of scholarly research. I further authorize University of Ontario Institute of Technology (Ontario Tech University) to reproduce this thesis by photocopying or by other means, in total or in part, at the request of other institutions or individuals for the purpose of scholarly research. I understand that my thesis will be made electronically available to the public.

_____ Ahmed Hasan

Acknowledgments

I would like to express my gratitude to my supervisor Professor Ibrahim Dincer, for his guidance, patience, knowledge and experience. He gave me the courage and the support to work, research and publish.

I would like to thank my father Moayad Hasan and mother Ayda Tahoun for their support and encouragement. They have always believed in me and guided me to success, I couldn't have done it without them. I would also like to thank my brother Mahmoud and sisters Lina and Lara for their support and encouragement.

Finally, I would like to thank my friends Maan and Mohammed and everyone in Lab ACE 3030B in Ontario Tech University for their support.

Statement of Contributions

Part of the work described in Chapters 4 and 5 has been published as:

[1] Hasan, A., and Dincer, I., 2020, "A New Integrated Ocean Thermal Energy Conversion-Based Trigeneration System for Sustainable Communities," J. Energy Resour. Technol., 142(6).

[2] Hasan, A., and Dincer, I., 2019, "Development of an Integrated Wind and PV System for Ammonia and Power Production for a Sustainable Community," J. Clean. Prod., 231, pp. 1515–1525.

[3] Hasan, A., and Dincer, I., 2020, "An Ocean Thermal Energy Conversion Based System for District Cooling, Ammonia and Power Production," Int. J. Hydrogen Energy. (Accepted)

[4] Hasan, A., and Dincer, I., 2020, "A New Performance Assessment Methodology of Bifacial Photovoltaic Solar Panels for Offshore Applications," Energy Conversion and Management (Accepted)

I performed the majority of the synthesis, simulations, and writing of the manuscript.

List of Tables

Table of Contents

List of Figures

Nomenclature

A	Area (m^2)
CP	Coefficient of power (-)
Cp	Specific heat capacity (kJ/kg.K)
CT	Coefficient of Power
En	Energy (kJ)
Ex	Exergy (kJ)
$\dot{E}x$	Exergy rate (kW)
ex	Specific exergy (kJ/kg)
h	Specific enthalpy (kJ/kg)
h_f	Specific heat of formation (kJ/kg)
HHV	Higher heating value (kJ/kg)
I	Solar irradiance (W/m^2)
LHV	Lower heating value (kJ/kg)
$\dot{m}$	Mass flow rate (kg/s)
P	Power (kW)
P	Pressure (kPa)
PV	Photovoltaic
$\dot{Q}$	Heat rate (kW)
s	Specific entropy (kJ/kgK)
T	Temperature (^oC)
u	fluid velocity (m/s)
u	Specific internal energy (kJ/kg)
W	Work (kJ)
$\dot{W}$	Work rate (kW)
x	Mole fraction of constituent j in the flow (moles of j/moles of the total flow)

Greek letters

η	Energy efficiency
ψ	Exergy efficiency
ρ	Density (kg/m^3)

Subscripts

ch	Chemical
c	Compressor
conv	Convection
cond	Conduction
cenr	Central
d	Destruction
e	Electrical
fg	Phase change between liquid and gas
fc	Forced convection
gen	Generation
H_2	Hydrogen
HCS	Hydrogen compression system
is	Isentropic

in	Input (flowing into the system boundary)
max	Maximum
net	Net result
ov	Overall
out	Output (flowing out of the system boundary)
o	At standard conditions, outer diameter
p	Pump
RC	Rankine cycle
ST	Steam turbine
SRC	Steam Rankine cycle

Superscripts

.	Rate
HP	Hydrogen at high pressure
IO	Indian Ocean
LP	Hydrogen at low pressure
NA	North Atlantic
NP	North Pacific
SA	South Atlantic
SO	Southern Ocean
SP	South Pacific

Acronyms

CASU	Cryogenic Air Separation Unit
GFEMA	Gibbs free energy minimization approach
O/C	Oxygen content in the coal divided by the carbon content in the coal
OTEC	Ocean Thermal Energy Conversion
RC	Rankine cycle
EIA	Energy Information Agency
NREL	National Renewable Energy Laboratory

Aspen Plus terms (*italic* terms)

Cisolid	For homogeneous solids that have a defined molecular weight, with the option of entering the particle size distribution
Mixed	Material stream option in Aspen Plus modeling
NC	Nonconventional solid (for heterogeneous solids that have no defined molecular weight) with the option of entering the particle size distribution
Rstoic	Aspen Plus reactor model that carries out the reaction based on the stoichiometric balanced chemical reaction equation with a specified reactants conversion percentage
RGibbs	Aspen Plus reactor model that carries out the reaction based on Gibbs free energy minimization approach

Chapter 1: Introduction

The world fossil fuel reserves are gradually depleting, forcing humanity to find alternative sources to meet the continuously rising energy demands. Recent reports from the International Energy Agency predicted that there would be a 50% increase in the global energy demand within the next ten years [1]. The worldwide energy consumption in 2016 was an estimated 101.78 quadrillion kJ, and it is projected to increase to 112.6 quadrillion kJ by 2050 [2]. Carbon dioxide emissions reached an estimated 5,157 million metric tons in 2016, according to the Energy Information Agency (EIA). The concerns about the finite nature of fossil fuels have resulted in extensive research and development on alternative sources of energy as well as on the efficient use of fossil fuels. Furthermore, various governments have expedited the adoption of renewable energy sources integrated with energy storage mediums such as carbon-free/neutral fuels and batteries. For example, in Germany their transport sector is already converting some their trains to hydrogen. It is expected that hydrogen use will surge in 2030 by 30% [3].

1.1 Energy and Environmental Issues

Renewable energy plants need to compete with current fossil fuel-based plants to make them economically viable. Renewable energy systems need to be integrated to offer multiple commodities (see Figure 1.1), such as not limited to renewable fuels, district cooling and heating systems. An economy should be built around these commodities to further incentivize private investments. The first step in developing the conceptual system for a hydrogen production plant is to select the best possible combinations (based on developed criteria) of the required subsystems. After the four conceptual systems are proposed, Chapter 4 will analyze these concepts through both energy and exergy analyses.

Figure 1.1 shows the primary subsystems and their interactions in hydrogen production plants. The subsystems that build the hydrogen production plant are selected based on specific criteria from the literature. An essential requirement of the hydrogen produced by the hydrogen production plant is to provide high purity hydrogen that is ready to be stored, exported, filled into the H_2 fueled vehicles fuel tank, and for industrial uses.

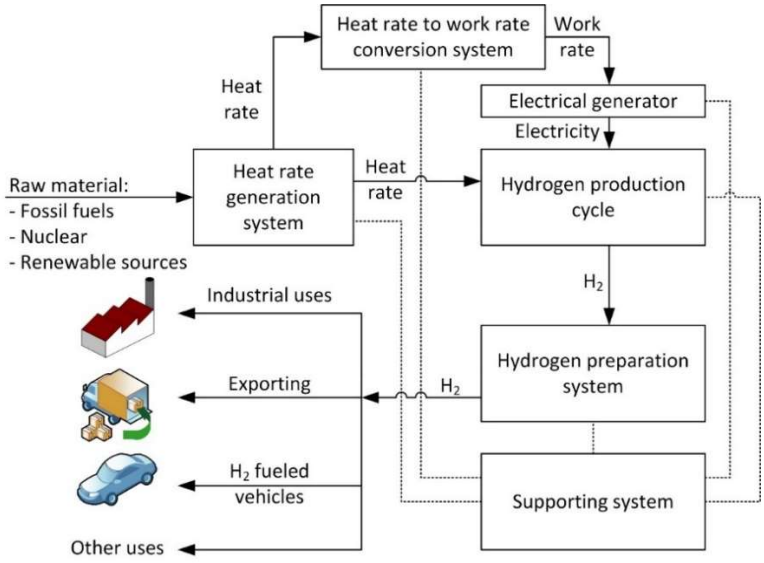

Figure 1.1 The main subsystems and their interactions in the hydrogen production plant, which produce ready to use hydrogen.

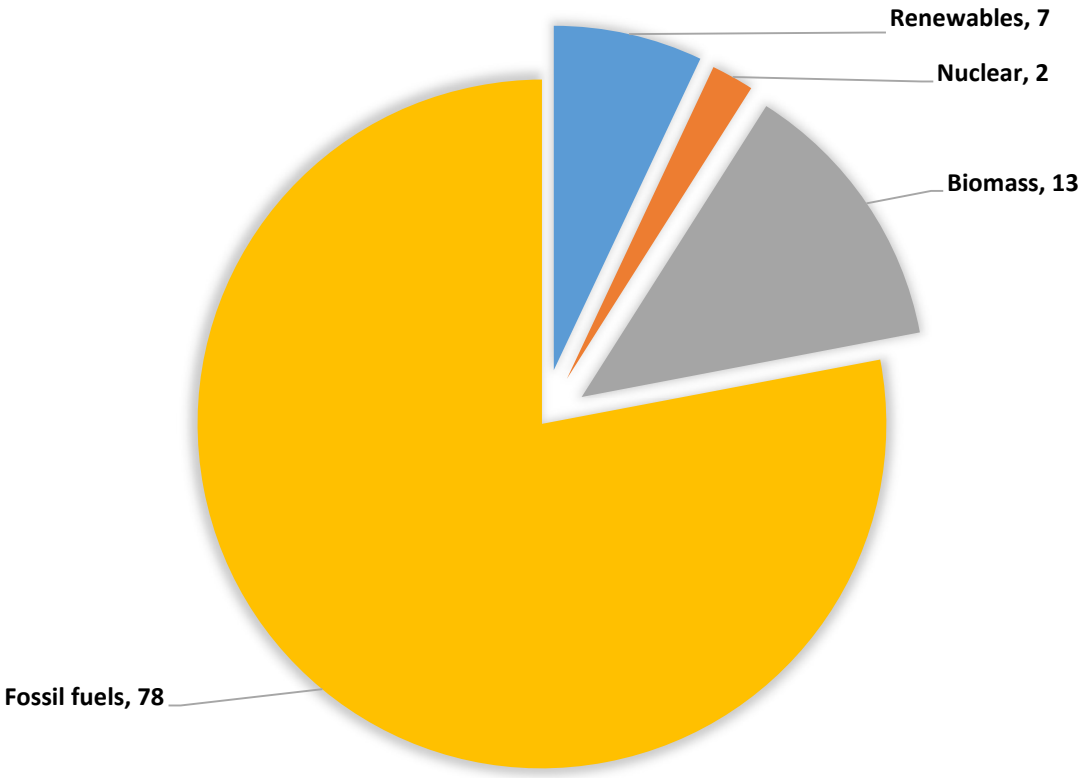

Figure 1.2 Sources of energy consumption in the world in percentage (data from [1]).

1.2 Motivation

The latest publications on the modeling and analysis of clean ammonia and carbon-neutral methanol mainly from renewable energy sources show that there is a gap in the literature in the integration of other commodities that could raise the overall efficiencies of the systems. For example, the utilization of carbon dioxide dissolved in large bodies of waters such as lakes and oceans is overlooked even though it contains more than 75 times the carbon dioxide found in the atmosphere. Furthermore, the cold water extracted at certain depths from these large bodies of water can be used for liquefaction of gaseous fuels such as ammonia or for district cooling purposes.

Finally, the motivation for working on this thesis can be summarized in the following bullet points:

- There is an immediate need to significantly reduce the environmental impact of fuel combustion in the transportation sector (to help mitigate global warming)
- A need to better understand the unexplored field of ammonia and methanol production from renewable energy sources especially constant low-temperature reservoirs
- A need to better understand the unexplored high energy content of the ocean
- Propose systems that are fully renewable but reducing the effect discontinuity of conventional renewable energy sources

1.3 Objectives

The main objective of the thesis is to conceptually develop novel integrated renewable energy systems for ammonia and methanol production. The novel systems should achieve better performances than the currently used systems and literature proposed systems. The specific objectives of the thesis can be presented in more details as follows:

- To develop novel renewable methanol and ammonia production energy systems and attain better efficiencies than the proposed systems in the literature.
- To compare the overall carbon-based emissions produced by each system to ensure carbon neutrality and effects on the environment.
- To further utilize the different renewable energy sources by-products such as the water used to provide heating/cooling the solar panels, along with the discharged condenser water from the OTEC cycle.

- To model, analyze and simulate the subsystems, such as the solar bifacial cooling system using phase change,
- To utilise the rich carbon dioxide content dissolved in the ocean to produce carbon-neutral methanol.
- To validate the developed models with existing experimental work from the literature.
- To examine the effect of various operating parameters on the performance of the subsystems and perform an optimization study using the sensitivity analysis tools.

1.4 Novelties

The main novelties that this thesis offers as the main contribution to the field is the novel integration of renewable-based energy systems with ammonia and methanol production, as well as the novel integration of a thermal management system for bifacial modules. The proposed systems are modeled, simulated, and analyzed, and the performance is compared between themselves and later with the literature proposed systems. The main finding of the research, modeling, simulation, and analyses of this thesis are summarized as follows:

In system 1, a new trigeneration OTEC based integrated energy system is proposed and investigated for development, analysis, and assessment.

- The focus will be on the utilization of the deep seawater for district cooling, ammonia, and power production.
- An OTEC system that integrates an appropriate low-temperature ammonia production system and district cooling is lacking in the literature.
- The system is able to achieve higher energy efficiencies than the unintegrated OTEC systems reported in the literature.

The main objective of this study is to develop and thermodynamically assess renewable energy-based integrated systems for remote areas that are sustainable and reliable.

- The system integrates a novel ammonia synthesis system with a PEM electrolyser powered by both wind and solar PV power.
- The system utilizes a low operating pressure ammonia production system.
- The system is able to achieve higher energy efficiencies than the unintegrated systems reported in the literature

In this study, a new OTEC-based integrated energy system is proposed and investigated for development, analysis, and assessment.

- The focus will be on the novel utilization of seawater, and the extraction of dissolved carbon dioxide in the deep seawater for district cooling, methanol, and power production.
- This will allow for the increased utilization of the cold water extracted by means of carbon dioxide extraction and cooling duty provided.
- An OTEC system that integrates carbon dioxide extraction from deep ocean waters for the purpose of the production of carbon-neutral methanol is lacking, as explained in the literature.
- The integrated system offers higher efficiencies than the unintegrated OTEC plants, which may range from 2% to 5%, respectively.

In system 4, a new bifacial PV-based integrated energy system is proposed and investigated for development, analysis, and assessment.

- The solar bifacial system integrates a thermal management system that is driven by the temperature of the surface lake water that can be as low as 4^{o}C in the winter and as high 18^{o}C in the summer.
- The thermal management system is indirectly coupled with the lake surface water using a heat exchanger, where the working heat transfer fluid is ammonia for the bifacial modules.
- The thermal management system can warm up the bifacial PV modules in the winter to temperatures above 0^{o}C, allowing for any type of precipitation to melt.
- The system integrates a novel ammonia-based heating/cooling system to melt the precipitation on the surface of the front-facing solar panel. Solar bifacial systems in the literature rely on the backward-facing solar panel to warm up the module, therefore, melting the snow. Using the proposed method in the literature will cause the system to lose quality solar irradiance during the day based on the heating provided by the backward-facing solar panel.
- The system achieved the highest energy and exergy efficiency in the literature, with the utilization of the solar irradiance reflected of the water surface.

- During hot weather seasons, the ammonia-based heating system operates as a cooling system, as it uses the lake surface water as a cold temperature reservoir. The novel ammonia-based boiling cooling mechanism is integrable with a heat engine with ammonia as a working fluid. The boiling system can be configured to operate passively.
- The proposed system offers net power-producing cooling and heating systems, unlike the systems proposed in the literature.

Chapter 2: Literature Review

In this chapter, a detailed literature review on renewable energy-based ammonia and carbon-neutral methanol production is presented. The section will first provide an overview of the available technologies and then focus on the specific methods of interest in this thesis, where the selection of these particular methods was highlighted in the earlier chapter in the motivation and objective sections.

The rest of this chapter is organized as follows: the chapter first presents a detailed literature review of the Ocean Thermal Energy Conversion (OTEC) systems, where it presents the technology and the latest scientific and commercial development. The second section will highlight the advancement in photovoltaic technologies with a special focus on bifacial modules. The third section provides a detailed literature review on the direct and indirect conversion from solar energy to fuels. The fourth section will reflect on the available technologies for commercial applications as well as the latest research and development systems in extracting and investigating the available feedstocks in the ocean. The fifth section presents the ammonia technology as a fuel, followed by section six on the methanol as a fuel.

2.1 Ocean Thermal Energy Conversion for Power and Fuel Production

Renewable energy is recognized as one of the most compelling fields as the world transitions from carbon-based fuels to carbon neutral and free fuels. The expedited process for the transition to clean energy resources is needed as the effects of greenhouse gases such as carbon dioxide are drastically affecting the planet's temperature and causing climate change. Currently, the primary attention in the renewable energy sector is solar, wind, and biomass. However, there is a rising interest in ocean energy power plants. The world's ocean covers 70% of the planet earth's surface, making it widely available to many countries [4]. There are four main methods of utilizing ocean energy that include: ocean waves, high and low tides, underwater water currents, and ocean depth temperature difference. There are offshore solar and wind plants that can also be utilized and have their advantages over conventional solar and wind. Similarly, OTEC plants can be built in an on and offshore configuration.

OTEC is a source of renewable energy, where useful electrical power is produced by utilizing temperature difference from the surface to various depths of water as the driving source of a heat engine. An OTEC plant can provide continuous power production year-round in specific geological locations. Some modifications can be performed to the cycle to make it more appealing and reliable. The OTEC process for power generation is driven by the Rankine cycle. Currently, the OTEC process is of interest in areas around the equator, where the temperature difference is highest around the world in the ocean[5]. Some of the challenges with ocean thermal currently include low energy conversion rates that range between 2-5% and the sheer size/deployment of the OTEC units [5]. The low efficiency of the system is highly due to the small temperature differences that ranges between 20-25 degrees Celsius, as well as the high energy consumption associated with the pumping of the water. These issues need to be addressed to make it competitive with other renewable energy sources. OTEC shows great potential as it continuously produces power unlike other sources of renewable energy such as wind and solar. Oceans inherently are the world's largest solar energy collector as they cover most of planet earth's surface. A large area of about 60 million km^2 of water bodies exist are located in tropical front-facing. Such a large area absorbs solar energy in the equivalence of 245 billion barrels of oil [6].

One of the possible methods to make renewables cheaper and more cost-effective is by means of smart integration. The integration of storage and subsystems allows for better returns on investments making renewables much more appealing for governments and private sectors. An emerging idea for energy export is the integration of renewable energy plants with hydrogen production. Hydrogen is an energy carrier that is carbon-free. However, hydrogen storage is a difficult task as the pressure required for storage is, in most instances, non-cost effective. Therefore, chemical storage is one of the best-suited methods for hydrogen storage. Ammonia and methanol are the two compounds that receive the most attention for hydrogen storage. In this study, ammonia will be discussed as it is one of the products of the proposed system [7].

Hasan and Dincer [8] proposed an integrated two-stage OTEC cycle for power, methanol, and district cooling production. The study utilized an Electrolytic Cation Exchange Module

(ECEM) for hydrogen and carbon dioxide production from the carbon dioxide-rich deep seawater. The carbon dioxide and hydrogen would then be used for methanol production. The discharge water from the condenser of the OTEC cycle was then used for district cooling purposes. The maximum energy efficiency cycle achieved was 8.7%. Other research articles attempted to increase the OTEC cycle efficiency via integration with higher quality thermal energy sources. Yuan et al. [9] proposed a solar-assisted combined OTEC cycle to increase the upper temperature of the OTEC cycle. Increasing the upper temperature increases the Carnot efficiency, therefore providing a more substantial potential for the energy and exergy efficiency of the cycle. The system produces both electricity and cooling for cold fishery storage. The cycle peak efficiency was found to be 7.89%, respectively. The concentrated solar thermal modules raised the temperature of the evaporator/boiler to 80ºC, therefore, increasing the Carnot efficiency. In another study by Yilmaz et al.[10] proposed a solar collector OTEC based hydrogen production and liquefaction system. The system also provided a hot and cold storage tank. The hydrogen production was performed by PEM electrolyzers powered by the OTEC cycle. The integrated system energy and exergy efficiency were found to be 43.49% and 36.49%. In another study Park et al.[11] simulated a solar-OTEC hybrid system for electrical power and fresh-water production. The authors mention that the OTEC cycle itself has a low efficiency to investment costs, as the temperature difference is low, and the pumping power is high. Furthermore, the author further mentions the costs associated with a long piping system for the cold water. The upper temperature of the solar-OTEC cycle was simulated to be 80ºC. The authors compared the base cycle with their simulated modified-hybrid cycle. In another study, several regenerative OTEC systems were simulated and analyzed [12]. The cycles utilized the discharged effluents from three nuclear powerplants in South Korea. The cycles included in this study were closed cycle, regenerative cycle, Kalina cycle, open cycle, and hybrid cycle. All five cycles were simulated under equivalent conditions but with various working fluids to accommodate the operating conditions. The highest efficiency was achieved was with a regenerative cycle with R-134a. The maximum efficiency achieved was found to be 5.21%. The corresponding net power was found to be 131 MW. In other studies, there were attempts to mitigate the pumping power effects on an OTEC cycle. A study [13] was conducted on the use of direct and indirect salinization

of surface water, causing a salinity gradient that would drive the surface water to the bottom of the ocean. The warm salinized water would pass through a heat exchanger, where it would mix with cold water which would, in turn, reduce the hot water temperature and salinity. After the salinity is reduced it travels naturally back to the surface by the means of bouncy forces. The new cold water would, in turn, cool down the OTEC cycle.

Other attempts in optimizing various OTEC cycles, used different refrigerants as they have large specific heat capacities given their application. For example, Yoon et al. [14]. Performed a study on liquid-vapor ejector based OTEC plant referred to as an EP-OTEC plant that used R152a. The maximum cycle energy efficiency was found to be 4.0%, respectively. The resultant energy efficiency is 38% higher than the base single-stage OTEC plant, with R152a as its working fluid. Yoon et al. [15] also studied the efficiency of an OTEC plant using three different cycles using R717 as a working fluid. The study found that the cycle was mostly affected by the turbine efficiency and the outlet vapor quality. The highest efficiency of the three tested cycles was found to be 2.379%, 2.361%, and 2.401% for the Uehara, Kalina, and Rankine cycle.

Other methods of optimizing an OTEC cycle is by studying the structural properties and parameters. Some of these parameters include pipe length, pipe diameter, seawater depth for cold water extraction, and the warm and cold seawater flow rates. Yeh et al.[16] studied the aforementioned parameters and found that the maximum net power out can be achieved with a larger ratio of warm to cold seawater. The study also mentions that a cold-water temperature is preferable as it provides a more significant work output.

One appealing nature of OTEC plants, is their reliability for power production, in certain geological areas. However, they do experience fluctuations in power productions depending on the temperature of the surface water due to varying seasons. To reduce the size and capital cost of these plants' energy storage is necessary. Some plants currently produce carbon-free or neutral fuels for storage—even in the case of energy export fuels such as hydrogen, ammonia, and methanol. There is current research regarding renewable energy to clean fuel [7]. The national renewable energy laboratory has a pilot wind to hydrogen plant, for energy use peak offset, and for later use if production is low [17]. The University of Minnesota is also investigating wind energy to ammonia synthesis plants

[18]. The plant is made to secure the energy needs of communities along with the production of carbon-free fuels.

In the following section, the most recent developments in bi-generation integrated OTEC cycles will be discussed. Ahmadi et al.[19] investigate the integration of a solar collector with an ocean thermal energy conversion system. The system consisted of an OTEC plant integrated with a solar collector to increase the temperature difference within the cycle. The system also included a proton exchange membrane electrolyzer for hydrogen production from the power produced. The authors reported the overall energy and exergy efficiency of 3.6% and 22.7%. The reported numbers are higher than that of other reported unenhanced OTEC systems, as the average is 2-3%. Furthermore, the net power output of the hybrid OTEC system was found to be 101.96 kW, and the hydrogen production rate was reported to be 1.2 kg/h.

Uehara et al. [20] investigate the performance of a hybrid OTEC plant that has an integrated desalination system. The design of the first system is referred to as an I-H OTEC cycle, which is a combination of a closed cycle OTEC plant integrated with a spray flash desalination plant. The system operates by evaporating the liquid ammonia using the warm seawater, the seawater then enters a flash chamber, and it evaporates. The evaporated steam then enters a condenser that is cooled by the cold seawater to produce the desalinated freshwater. The authors also optimized the system with the heat transfer area of the heat exchangers being the objective function. The results of the optimization were for a 10 MW I-H OTEC cycle with plate type heat exchangers and ammonia as a working fluid and then compared it to a J-H OTEC cycle.

From the literature, OTEC hybrids with freshwater production are currently being studied and are continuously improving. However, there is a lack of study about the utilization of the seawater being pumped as the heat source and sink of the cycle for other products. Combining OTEC-Hybrids with fuel production might make the appeal, efficiency, and return of investment more attractive for investors. There have been some studies performed to asses hydrogen production driven by OTEC plants. Jitsuhara et al. [21] stated that an offshore hydrogen production platform should be considered. The idea behind this claim is the use of a fraction of the desalinated water produced from the cycle to be used as a

feedstock for the OTEC powered fuel cells to produce hydrogen. For hydrogen to be a clean energy carrier, it needs to be produced from a greenhouse gas-free material as well as the process being powered by a renewable source. These changes will allow in accomplishing a sustainable hydrogen economy much sooner than anticipated. Hydrogen shows potential as a means of energy storage as it can be produced from various biomass and water.

Furthermore, combusting hydrogen results with a byproduct of water vapor. However, there are drawbacks to hydrogen, as it's challenging to store and requires extreme compression pressures ranging from 5,000 to 10,000 psi. There are still some difficulties in this proposal as hydrogen storage is still an issue, as most of the hydrogen storage is performed by compression, which is costly and inefficient. However, using the chemical storage of hydrogen in the forms of fuels such as ammonia and methanol is appealing as they cost less in terms of storage. Methanol is inherently in a liquid state at room temperature, and ammonia is in a gas state at room temperature. However, ammonia requires less energy for storage during compression relative to hydrogen.

Several OTEC pilot plants have been developed over time that produced 30-120kW. To increase production, the intake pipes can be made larger to handle larger flowrates. This increase in size and flow allows for power production rates of up to 100MW. Currently, the 1-20MW scale plants are being developed. The developments in the production of electricity using OTEC has been gaining traction in the tropical and coastal areas mainly. Some examples of these pilot plants include a 1 MW plant in Tarawa Island(Pacific), a 20MW plant in Qingdao(China), as well Makai plant in Hawaii (USA)[4]. The reason behind these pilot programs are the benefits that come from the byproducts of the plant. Such as nutritious water for aquaculture, desalinated water in certain configurations, and district cooling. However, such integrated systems have not been properly explored and analyzed. The increase in the utilization of cold water should be investigated as it is the highest consuming entity causing the efficiency to drop.

2.2 Cost of Renewables

The current Levelized production cost is 0.20$/kWh for OTEC plants, compared to wind and solar, which come at a cost of 0.04-0.06$/kWh (wind) and 0.10$/kWh (solar)[22].

Depending on the country and its accessibility to fossil fuels, the cost of power production from fossil fuel ranges from 0.05-0.17$/kWh [23]. In many cases, fossil fuels are cheaper than renewable-based power production at face value. Of course, one should account for the capital cost needed for a normalized power production cost, where solar, wind, and natural gas come at a cost of 2,000-3,700$/kW(commercial-residential),1200-1700$/kW, and 1,000$/kW[24]. OTEC comes at a cost of 4,000$/kW based on the price of 100MW plant [25,26], which is relatively more expensive from the other alternatives. However, one should account for the reliability of the other renewable sources of energy as OTEC can run indefinitely 24/7. The baseload power that OTEC offers can be complementary to the intermittent renewable energy sources, as they can be designed to be dispatchable, allowing it to ramp up and down power production based on the production rates. Furthermore, the potential by-products of OTEC are of interest in the agricultural, aquaculture, HVAC, and freshwater production sectors[27].

2.3 Feed Stocks Available in the Ocean

The ocean's waters are at continuous equilibrium with the atmosphere's carbon dioxide and nitrogen content. This section will investigate the variation of the concertation of such species in the ocean waters and how the proposed systems in this thesis use them to achieve the thesis and research objectives and goals.

2.3.1 Carbon Content

The ocean's waters are at continuous equilibrium with the atmosphere's carbon dioxide content. As discussed previously in this section, the ocean waters can capture the increase of carbon dioxide in the atmosphere in the form of carbonic acid. Currently, the average minimum total carbon dioxide concentration is 100 mg/L at all depths in various areas. Carbon dioxide is existent in 2-3% in the form of dissolved gas, and 97-98% is in chemically bounded state of bicarbonate and carbonate [3]. To put this into perspective, the volume of the oceans is 1.3×10^{21} L, which translates into a CO_2 content of 1.3×10^{5} gigatons, which is 175 times greater than that contained in the atmosphere [3]. According to a study by Willuar et al.[3] the concentration of carbon dioxide in the ocean in weight to volume basis was found to be 100 mg/L, which is 140 times that found in the atmosphere at 0.77 mg/L. The study also claims the benefits of using energy-efficient processes to

extract CO_2 from the ocean will indirectly reduce the CO_2 concentration in the atmosphere. Furthermore, the authors also declare that the recovery of pure CO_2 from the ocean waters would also eliminate the energy-intensive regeneration processes needed for the recovery of CO_2. The findings Willuar et al.[28,29] further assess the objective of this proposal, which is carbon neutral fuels production.

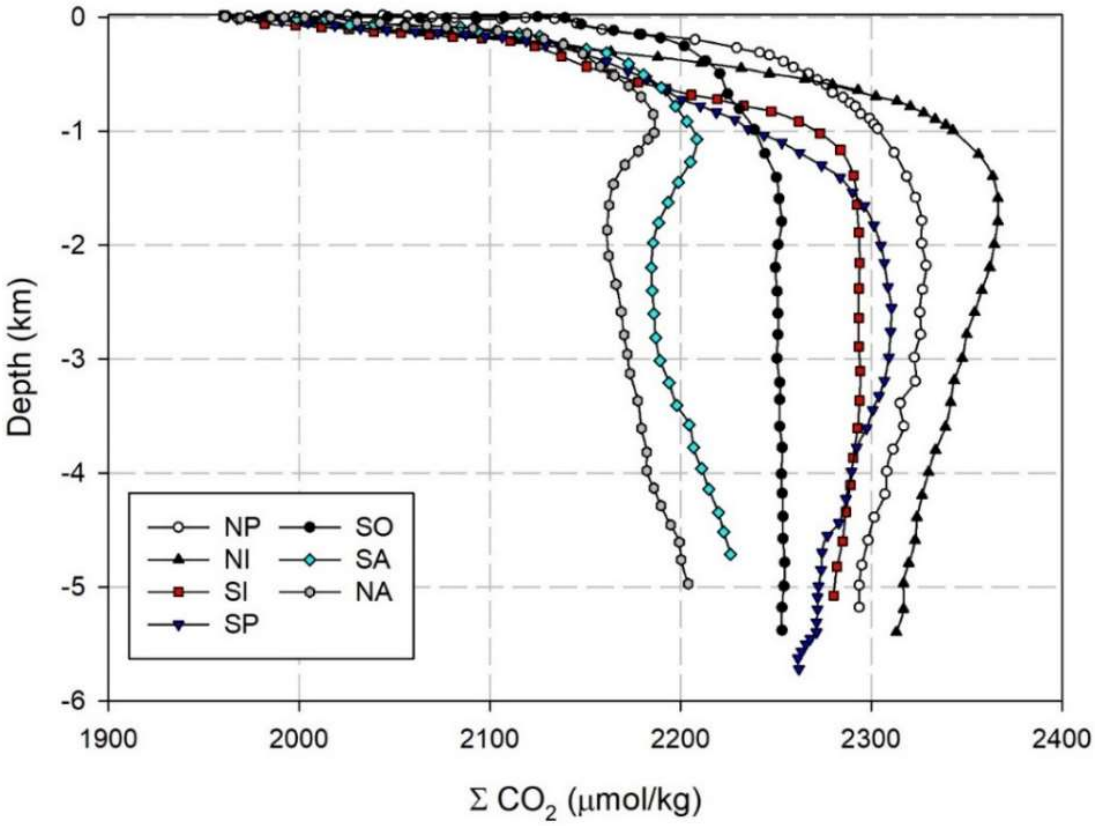

Figure 2.1 Carbon dioxide concentration profile along the depth of various oceans [30].

The carbon dioxide concentration increases as the depth increases in the ocean waters. This is convenient as the cold water extracted for the OTEC cycle can be further utilised, instead of simply cooling the condenser. The distribution of total carbon dioxide can be seen in Figure 2.1 as the depth increases the total dissolved carbon dioxide increases. This is of great potential for hybrid desalination and carbon dioxide extraction or even for ocean thermal. The total carbon dioxide as the depth of the ocean increases is shown for various areas, as seen in Figure 2.1.

2.3.2 Nitrogen Content

Another gas that is found in the ocean in mainly its diatomic form, is nitrogen. Nitrogen makes up approximately 70% of the earth's atmosphere. Recovering nitrogen from the ocean or the atmosphere is of importance as it could be used to store hydrogen in the form of ammonia. Nitrogen can be extracted at reasonable purities from the atmosphere using conventional technologies such as cryogenic air separation units and swing sorption. However, there is a lack of research on the potential nitrogen extraction from seawater as a byproduct of desalination and OTEC technologies.

In the ocean, 94% of the total nitrogen inventory is in the form of dissolved nitrogen, which translates to $1x10^7$ Tg of nitrogen. The majority of the remaining fixed nitrogen is available in the form of NO_3^-. Table 2.1 displays the mean concentration and oceanic inventory of nitrogen in the ocean.

Table 2.1: The mean concentration and oceanic inventory of nitrogen in the ocean.

Species	Mean concentration euphotic zone (mmol m^{-3})	Mean concentration Euphotic zone (mmol m^{-3})	Oceanic inventory (Tg N)
Ammonium	0.3	0.01	340
Nitrogen gas	450	575	1×10^7
Dissolved Organic N	6	4	7.7×10^4

Source:[31]

The nitrogen in the ocean can be extracted with the method proposed by Probst et al.[26]. The nitrogen extraction unit uses EDGAR semi-permeable membrane. This membrane extracts dissolved gases from water with efficiencies as high as 90% recovery. The power consumption of the unit was found to be 2400W for a flow rate of 34LPM of water. the extraction efficiency of dissolved gasses can be estimated using the following relation:

$$\frac{S_i E_i}{1 - E_i} = \frac{S_{ox} E_{ox}}{1 - E_{ox}} \tag{2.1}$$

For this system, a model developed by Ezzat and Dincer [22] was adapted to simulate the hydrogen production. As mentioned, the excess electricity previously is transferred to an electrolyzer. The electrolyzer performs electrolysis on water to produce hydrogen. The overall reaction in the electrolyzer is given below:

Reduction at the cathode:

$$2\,H+(aq)\ +\ 2e-\ \rightarrow\ H_2\,(g) \tag{2.2}$$

Oxidization at the anode:

$$2\,H_2O(l) \rightarrow\ O_2(g) +\ 4\,H^+(aq) +\ 4e- \tag{2.3}$$

Overall reaction:

$$2\,H_2O(l) \rightarrow\ 2\,H_2(g) +\ O_2(g) \tag{2.4}$$

2.4 Ammonia Storage

Most of the world's fossil fuel-based power plants use coal as fuel. Coal naturally has one of the highest emissions of carbon dioxide per energy unit relative to other fuels such as natural gas. To help in the shift in more efficient and less greenhouse emitting sources should be considered, such as renewable energy. As renewable energy is relatively more expensive to build per unit of energy produced than fossil fuel-based plants. However, to bridge the transition gap from coal and other fossil fuels, they could be used to produce ammonia, hydrogen, and electricity as energy carriers. Making the hydrogen production fully powered by a renewable source will help in accomplishing a hydrogen economy much sooner than anticipated. Hydrogen shows promising potential as an alternative fuel as it can be produced from various sources such as hydrocarbon-based fuels, ammonia, and water. Currently, hydrogen is not being used greatly in mass transportation. However, it is emerging as many car companies are producing Fuel Cell Electric Vehicles (FCEVs). One of hydrogens' characteristics as a fuel is its energy density, as a frame of reference 2.8kg of gasoline contains the same energy available from 1kg of hydrogen. Furthermore, when combusting hydrogen, the only by-product is water vapor. The storage of hydrogen currently is performed mainly using compression and metal-hydrides. The compression of H_2 is often performed at 200 bar in most countries, where the steel vessels are tested to pressures up to 300 bar [1]. There is, however, some novel high-pressure tanks that are mainly composed of composite reinforced carbon fiber that are regularly filled up to 450 bar and can withstand 600 bar of pressure. In some instances, higher storage pressure for hydrogen has been proposed. Al-Zareer et al.[32] developed two hydrogen multi-stage compression and storage systems at 700 bar. The study concluded that 921 kg of hydrogen stored at 700 bar required 12.2-15.6 GJ of energy. Hydrogen is also stored in various

chemical forms, mainly methane, methanol, and ammonia. Ammonia provides a carbon-free solution for chemical storage of hydrogen, unlike methanol, methane, etc.. Furthermore, ammonia is not a greenhouse gas (GHG), which comes as an advantage as more strict protocols to help slow down and prevent climate change [33]. Some common fuel properties are summarized in table 2.2.

Table 2.2:Various fuel properties

Fuel (storage medium)	P (bar)	HHV (MJ/kg)	LHV (MJ/kg)	Storage Temperature (◦C)
Ammonia (pressurized tank)	10	22.5	18.8	25
Ammonia (metal amines)	1	17.1	18.8	25
Methanol (liquid)	1	23.0	19.9	25
Gasoline (liquid)	1	46.7	42.5	25
Hydrogen (metal hydride)	14	142	120	25
Hydrogen (pressurized tank)	102	141.9	119.9	-253

Source: [34,35]

There are still some difficulties in this proposal as hydrogen storage is still an issue, as the majority of hydrogen storage is performed by compression, which is costly and inefficient. However, using the chemical storage of hydrogen in the forms of fuels such as ammonia and methanol is appealing as they cost less in terms of storage. Ammonia requires less energy for storage during compression relative to hydrogen. The viability of ammonia as a fuel will be discussed thoroughly.

The following section discusses NH_3 as a storage medium compared to methane and methanol will be briefly discussed. Furthermore, the use of ammonia as a fuel will also be briefly discussed.

As the case with hydrogen ammonia currently is mainly stored using compression. Ammonia, as a storage method of hydrogen, offers several advantages over their carbon-based counterparts or even pure hydrogen storage. Ammonia has a high content of hydrogen atoms per unit volume with no carbon, unlike methane r methanol. Ammonia is 17.8wt% of H_2 or in terms of moles 1:1.5 NH_3 to H_2 ratio [34]. Furthermore, NH_3 requires less energy on a hydrogen weight basis than compressing pure hydrogen. However, there some disadvantages to ammonia. If one compares the chemical reactions for ammonia and

methanol synthesis, it can be seen that the liquid physical property at STP of methanol comes at the cost of a hydrogen molecule that oxidizes to become water. The synthesis reactions are illustrated in eqs. 2.5 and 2.6 [36].

$$N_2 + 3H_2 \leftrightarrow 2NH_3 \tag{2.5}$$

$$\Delta h_{300K} = -46.19 \frac{kJ}{mol}$$

Ammonia is a highly toxic gas and poses a problem when being considered for use in sectors such as energy storage and transportation. However, ammonia safety concerns can be offset as the development of safe storage, transportation, and handling are improved. There are currently well-established procedures for processing and storing NH3 in various physical forms (gas, liquid, and solid), especially in the agriculture sector[37][38].

Metal Amines

Metal amines are an emerging method of storing hydrogen, over their metal hydride counterparts. Metal hydrides suffer from low hydrogen densities and slow hydrogen release kinetics [39]. Metal ammines release ammonia for it to be further decomposed to hydrogen. They decompose thermally as they evolve ammonia, at a temperature that is highly reliant on the composition of the storage complex. The combination of ammonia evolving complexes along with ammonia decomposition catalysts makes for a very versatile hydrogen storage device.

Metal ammines complexes that are in the form $M(NH_3)_nX_m$, where M represents the metal cation that includes and not limited to Mg, Ca, Cr, Ni, and Zn, X represents the anion which includes Cl and SO_4. Ammine complexes are commonly formed with the presence of ammonia and an anhydrous MX_m salt. The enthalpy of formation is highly dependent on M and X and usually varies between 40 and 80 $kJ.mol^{-1}$-NH_3[40]. Christensen et al. [39] performed an experimental study to characterize $Mg(NH_3)_6Cl_2$ ammonia desorption rate at various temperatures. The sample was prepared by exposing $MgCl_2$ to ammonia at a pressure of 1 bar. It can be seen that the decomposition reaction starts at approximately 350 K. About 2/3 of the ammonia is released as the temperature reaches 500 K, and the remaining 1/3 is released as the temperature reaches 620 K. Two cycles were performed to

verify the cycle, the authors reported that the $MgCl_2$ performed mostly the same proving its reversibility.

If the main objective is to extract hydrogen from the desorbed ammonia, one route would be to pass the ammonia over a catalyst that would decompose the ammonia into N_2 and H_2. Choudhary et al. [41] studied a variety of metal catalysts. The authors confirmed that Ru catalysts were found to be the most active. However, the authors noted that Ni catalysts were the least active of the catalysts. The activation energies to decompose the ammonia varied from 17 to 22 $kcal.mol^{-1}$. Table 2.3 summarizes the hydrogen formation rates from the tested metal catalysts.

Table 2.3: summary of the hydrogen formation rates from the tested metal catalysts

	10% Ni/SiO_2		65% $Ni/SiO_2/Al_2O_3$		10% Ir/SiO_2		10% Ru/SiO_2	
Temp. (K)	Conv. (%)	H_2 Form. Rate (mmol/min)	Conv. (%)	H_2 Form. Rate (mmol/min)	Conv. (%)	H_2 Form. Rate (mmol/min)	Conv. (%)	H_2 Form. Rate (mmol/min)
673	1.4	0.44	3.5	1.1	3.9	1.2	14.3	4.5
723	4.2	1.3	9.3	2.9	8.1	2.6	36.4	11.4
773	10.5	3.3	21.7	6.8	18.2	5.7	64.0	20.0
823	21.6	6.8	48.7	15.	30.4	9.5	-	-
873	36.4	11.4	79.5	24.9	56.0	17.6	97	30.3
923	70.0	21.1	97.0	30.3	-	-	99	30.9
973	-	-	-	-	98	30.6	-	-

Source: [41]

2.5 Ammonia as a Fuel

Ammonia as fuel is widely studied subject Zamfirescu, and Dincer [34] investigate ammonia as a fuel in a study. The study states the benefits of ammonia as a fuel. Some of these benefits included ammonia being a carbon-free substance, having high octane numbers, the compactness of fuel tanks on vehicles, and cost-effectiveness. The cooling effect is also mentioned in the study as it could potentially reduce the size of the cooling system of cars that run on internal combustion engines. The cost of driving a vehicle with ammonia as fuel is CN$3.2 /100 km, and the tank can be sized based on the following ratio 18L/100 km. The presented results are very appealing and comparable to the price to drive a small compact gasoline vehicle that consumes 6-7L/100km, which would cost CN$6-7/100 km.

Giddey and Kulka [42] review various electrochemical technologies and materials of ammonia production. The paper shows the potential of ammonia in the future and emerging hydrogen economy as it has 17.6% wt hydrogen compared to other fuels such as methanol, which contains 12.5 wt% of hydrogen. One of the benefits of ammonia is that it's currently mass-produced for fertilizers, and many countries have storage and transportation infrastructure in place. However, most of the world's ammonia demands are presently being met by the Haber Bosch process, which is energy-intensive and high on capital costs. In the study, electrochemical methods for ammonia production have the potential to reduce the energy input by 20%, to simplify the current reactor designs and reduce the cost of the production plants. The current electrochemical ammonia conversion rates are low in the range of $10^{-13} - 10^{-8}\ \frac{mol}{cm^2 s}$. The maximum synthesis rate was achieved by a polymer electrolyte membrane. The review concluded that electrochemical processes for ammonia production are still in the early stage. However, the low-pressure operation gives these processes merit. Furthermore, the authors also mention that more research is needed in the catalysts in the ammonia production side.

Cinti et al. [43] design and analyzed a solid oxide electrolyzer coupled with an ammonia production plant. In this paper, a concept that incorporates and SOE for hydrogen production combined with an improved Haber Bosch reactor for ammonia synthesis was presented. The authors mentioned the high potential efficiencies that SOE operate at as it could utilize high temperatures that can be recovered from the Haber Bosch Reactor. The SOE and HBR operate at 650ºC. The ammonia production for this concept has no CO_2 emissions and it consumes 40% less power than similar plants.

Sanchez and Martin [44] evaluate an ammonia production facility that uses air and water as feedstocks. The nitrogen is obtained from an air separation unit, and the hydrogen is produced from water splitting. The ammonia is then synthesized in a three-bed packed reactor. Two types of cooling were analyzed indirect and direct cooling. The ammonia recovery system is performed by condensation using cold air. As for the power that is used to drive the electrolyzer and compressor, they can be obtained for renewable sources such as solar and wind energy. To conclude, the study of solar energy as a power source was

used along with indirect cooling for ammonia production. However, the current high cost for solar panels increases the capital cost over 1.35 euro/kg of ammonia.

Al-Zareer et al. [45] propose a novel hydrogen storage system using a multistage ammonia production system. The pressurized ammonia is stored in a tanker truck that has an ammonia electrolyzer. The tanker then transports the ammonia where its decomposed to provide the stored hydrogen. The energy and exergy efficiency of the system was found to be 72.3% and 71.8%. The authors found that the system consumes 59.4kJ of work per mole of hydrogen stored and recovered. The operation parameters for the system were as follows: 21,000 liters ammonia storage tank and the ammonia were stored at 61 bar. The maximum ammonia storage was 13.2 tonnes of ammonia in a liquid state. Furthermore, the ammonia was stored in 0.518 hours.

Bicer et al. [46], comparatively assess and evaluates four different ammonia production methods, using life cycle assessments (LCA). The systems analyzed consisted mainly of an electrolyzer for hydrogen production and a Haber-Bosch plant for the ammonia synthesis and production process. The energy systems utilized in the study included the following sources: hydropower, nuclear, biomass, and municipal waste. The systems were assessed in the LCA based on their environmental impact, abiotic depletion, human toxicity, energy and exergy efficiency. It was found during the study that ammonia production using hydropower and municipal waste incineration had smaller environmental impacts than the other selected methods. The energy efficiencies of the systems proposed were calculated to be 42.7%%, 23.8%, 15.4% and 11.7% respectively for hydropower, nuclear, biomass and municipal waste-based options. The exergy efficiencies of the proposed systems were calculated to be 46.4%, 20.4%, 15.5% and 10.3%, respectively for hydropower, nuclear, biomass and municipal waste-based options. In another study Bicer and Dincer, performed an LCA study on an ammonia fueled vehicle. The study concluded that the ammonia driven vehicle has 100 g carbon dioxide equivalent per km. Gasoline and diesel driven vehicles had carbon dioxide emissions of 270g and 230g. Their study also concluded that the global warming potential of natural gas power plants can be reduced by 60% by using ammonia.

The main objective of this study is to develop a renewable energy-based integrated system for remote areas that are sustainable and reliable. The proposed systems will be modeled simulated and analyzed using mainly two software packages that include COMSOL and Aspen Plus. The overall system will undergo energy and exergy analyses for performance benchmarking and sustainable applications.

2.6 Ammonia Safety and Toxicity

Ammonia is a colourless gas at standard pressure and temperature. Ammonia is pungent and detectable by smell at 5 ppm concentration in the air. Based on the U.S safety standards, an exposure to a dosage of 300 ppm is considered dangerous and could have detrimental effects on health and liveliness. Ammonia is highly toxic in nature and is dangerous when the concentration in human blood surpasses 50 μmol/L. An increase to 100 μmol/L in concentration of ammonia in human blood could cause disturbance in consciousness. Any concentrations past 200 μmol/L could cause convulsions and a coma [47,48].

2.7 Methanol as a Fuel

Struckmann et al. [49] investigate methanol as a future form of chemical energy storage using recycled carbon dioxide. The thermodynamics and operational boundaries of methanol production are also assessed. The authors reported an observation from their thermodynamic assessment, which was that the majority of the exergy losses are associated with chemical energy being converted to electrical and vice versa. However, the authors reported great potential in the recycling process of CO_2 into methanol. The exergy efficiency of the assessed system was 83.1%, where the exergy efficiency takes the chemical exergy of hydrogen and methanol along with the exergy associated with the power input and heat released from the system. The exergetic efficiency of the overall energy conversion and storage system was reported to be 16.2% and 20%. The efficiency of the conversion and storage system is highly dependent on the conversion devices used. To conclude their study the authors stated that methanol is a great candidate as stationary energy storage, and as a transportation fuel. However, it was also stated that hydrogen as energy storage medium has a higher exergy efficiency, but the storage of hydrogen is both complex and cost-intensive.

Aresto et al. [50] investigate state of the art catalytic process to recycle carbon dioxide and convert it into various fuels and chemicals. Currently, there are two reasons for carbon dioxide recycling for the production of fuels, the first one being carbon dioxide is mainly produced from fossil fuels, and second the hydrogen needed is also produced from carbon-based fossil fuels. However, the authors mention that if the conversion process of the carbon dioxide powered by renewable sources of energy, there is great potential to convert excess carbon dioxide into non-fossil fuel-based products. Furthermore, it is expected that several GtCO2/y would be converted into non-fossil fuel-based fuels by 2050. Therefore, carbon capture unit's utilization is very important and may allow for drastic cuts to the carbon released in the earth's atmosphere.

2.8 Solar Energy for Power and Renewable Fuel Production

Solar photovoltaics (PVs) were introduced in 1983 by Charles Fritts with a 30 cm^2 PV cell made of Gold and Selenium [51]. After the introduction of PV, the next major step in the development of the PV technology happened in 1954 [52]. In 1954, at Bell Labs, Chapin, Fuller and Pearson built single silicon crystals for the use in PV cell that works on the basis of P-N junctions. Bells lab developed a PV cell that achieved an energy conversion efficiency ranging from 5% to 6%. These discoveries and improvements in the PV cell technology solidified the idea of using solar as a source of energy. The development of PV panels has been increasing as the shift to renewable energy became necessary. Nowadays, the energy efficiency of commercial PV panels has increased to an energy efficiency of 22.8% which was achieved by SunPower [53], and in addition, lab-scale PV solar efficiency reached an outstanding over 40% [54].

Part of the extensive research headed towards focusing on improving the performance of the PV cells through material enhancement and bifaciality. In a study conducted by Jia. [5] the bifacial solar cells reached an efficiency of 12.4% using mc-Si thin-film solar cells. The authors also found that a bifacial efficiency of 14% and above is realistic if installed in optimal conditions. The study concluded that the bifacial cells outperformed the mono-facial cells by 24%. Some other researchers focused on solar trackers, which as its name suggest help the solar panel to keep its face towards the solar position. It was found that the solar tracking system were able to increase the overall power produced by the solar

panel by 10% to 100% depending on the geographical conditions [55]. However, the installation cost of the solar tracking system, its various moving parts, the maintenance costs and the motorization all should be taken into consideration while considering the increase in the total power production [52]. Solar trackers can be classified into three main categories based on its working principle, passive, microprocessor, and finally, electro-optically controlled units.

The first category of solar trackers is passive, as it operates based on the difference in exposure to solar irradiance between two containers [56]. The two containers contain a heat transfer fluid, where the difference in solar irradiation between the two containers, causes a temperature difference between the fluids. The temperature difference causes the hotter fluid to travel from one container travels to go to the other container to achieve to an equilibrium between them and as a result, the solar PV panel moves. Such a system does not have to consume electrical energy and does not require a control system, which makes it the least demanding system of the other categories. However, with their low electrical consumption advantage, the system has the disadvantage of low accuracy. The microprocessor category of solar trackers is based on calculating the solar position for various points in time and driving the motors to direct the solar PV panel towards the sun [57]. The electro-optically controlled units control the motors through the difference between the lighting on two photo resistors. The third class of solar trackers is the most accurate. However, with the solar tracking system it consumes electrical energy and usually requires a very precise installation and can lead to problems in duration with cloudy days.

Another way of enhancing the operation of the solar panel is maintaining the solar panel at the optimum working temperature [58]. It was found that the solar PV efficiency is significantly affected by the panel operating temperature [59,60]. It was found that the solar PV panel is very sensitive to temperature variation, where an increase in 1^{o}C in the operating PV temperature will lead to a decrease in its conversion efficiency by an average of 0.45% [61]. Thus, researchers have focused on maintaining the solar PV panel operating temperature within the optimum operation range. Furthermore, other researchers, including Ref. [13], have focused on integrated PV based applications where they can use the heat extracted from the PV system for use in various applications, such as heating, drying and

HVAC applications. One of the most expensive cooling technology applied to solar PV panels is the water spray technology, which is also applied to clean the surface of the panels [62,63]. Researchers achieved an increase in the total power production of the solar panels of 15% [64], 17% [62] and up to 60% [63].

As for solar energy to fuel system, a study conducted by Joshi et al. [2] found that hydrogen as a fuel option could be one of the viable solutions for the current energy and environmental problems. However, the source of which the hydrogen is produced from is highly important for it to be an environmentally benign and sustainable fuel. In the study of solar thermal (high temperature and low temperature), photovoltaic, photo-electrolysis, bio-photolysis etc. were evaluated for hydrogen production. The methods were evaluated based on the overall exergy efficiency and sustainability factor. The paper concluded that water electrolysis is the most mature technology currently, and with use of photovoltaics, it is a sustainable method. Photo-electrolysis, however, is at its early stages of the development cycle, as the materials cost for hydrogen production is not viable as of now. As for photo biological processes it was found they have low conversion rates to hydrogen and are not ready for mass production. High-temperature processes were also assessed, and it was found that more research was needed in the materials and heat exchanger areas for it to be more viable.

With all the proposed technologies and methods of enhancing the solar PV panel efficiencies, none of the proposed systems applies a technology to increase the area utilization of the available panels. This paper proposes the use of bifacial photovoltaic solar panel for offshore power production, which is novel and has not been discussed and investigated in the literature. The proposed bifacial photovoltaic solar panel consists of having two conventional solar panels fixed back-to-back where the backward-facing solar panel takes advantage of the reflected solar radiation from the sea surface. The performance of the bifacial system (with the added advantage) is assessed through simulating a single set of bifacial photovoltaic solar panel mounted on floater covered with aluminum sheets floating on the waters surface. The proposed system is then modeled and simulated on COMSOL Multiphysics software. The specific objective of this study is to develop a methodology for assessing the performance of the novel use of a bifacial PV module for

offshore energy production by considering the gain in performance from the reflected irradiance from the water to the back of the bifacial PV module. The model is then simulated under various design and operating conditions, including the variation of the solar radiation direction, water conditions, and module orientation. Furthermore, this allows for the characterization of the performance of bifacial modules for offshore purposes, which is technically lacking in the literature [65].

Even with improvements in the efficiency of PV cells, there is still a need to increase the electrical power production per unit area for PV to be more competitive with thermal power plants [66]. One concept for PV that is being investigated and implemented is bifaciality [67]. Bifacial PV technology has received raising attention in recent years due to their ability to yield more energy per unit area than the conventional mono facial counterpart. Bifacial PV attracted increasing attention in 2010 in the global market, where companies such as PVG solutions, LG and others started the commercialization of the bifacial PVs, which were based on various c-Si structures. c-Si Bifacial PV cell structures come in various forms such as the passivated emitter rear contact, passivated emitter rear locally-diffused, interdigitated back contact, passivated emitter rear totally diffused and heterojunction with intrinsic thin layer [68]. Interest in bifacial PV modules is rising in the energy sector, as they increase the output of electricity per area. Bifacial modules exhibit some of the highest efficiencies per area in the industry. The higher yields and efficiencies are highly due to their capability to absorb light from both sides [69]. Some commercial and residential applications have reported a 10-20% increase in energy production when using bifacial rather than single face PV modules [70]. An example of the use of bifacial modules is the use of a reflective white thermoplastic polyolefin roofing membrane, which reflects the solar irradiance to the backside of the module allowing for the potential of a 20% increase in production [71]. The efficiency of bifacial modules varies from 19.4% [72] to 24.7% [73] for the front face and 16.7% [74] to 24.7% [73] for the back face of the bifacial module.

The research trends in improving the performance of PV cells through material enhancement and bifaciality can be seen in the literature. Jia et al. [75] demonstrated that a bifacial solar cell reached an efficiency of 12.4% using mc-Si thin solar film. That study

also confirmed that an efficiency of 14% is possible if the solar module is placed under optimal operating conditions. The authors found that there was a 24% gain in energy conversion efficiency for bifacial cells was experienced relative to mono-facial solar cells of the same material. Another issue regarding solar panels relates to their position throughout the day [75]. Many solar panels are placed in optimized positions and are fixed throughout the day in order to reduce the capital and installation costs. However, solar tracking can be implemented with PV panels to permit them to produce electricity more efficiently throughout the day [76]. Solar tracking has been found to have a dramatic effect on the performance of solar panels. In one study [55], an overall increase of 10-100% in electrical power production was achieved by implementing solar tracking. However, the high installation and maintenance costs of solar tracking remain problematic.

Thermal management of photovoltaics is also important for the longevity of the operation of the cell and, more critically, the operating efficiency of the PV cell [60,77]. Solar panels are sensitive to temperature changes. Most solar panels operate best at a nominal cell temperature of 25^{o}C [78]. It was found that for every 1^{o}C increase in the PV operating temperature the conversion efficiency decreases by an average of 0.45% [61]. Colder temperatures have not been found to have major effects on the efficiency of PV cells [79]. Of course, the integration PV cells with other systems that can utilise the thermal energy produced by the PV systems can be beneficial and complement the efficiency of the overall system [80].

In [81] the reserachers found that bifacial solar PV panels were able to achieve higher utilization of the solar PV panel area. In addition, recently as well [68] simulated bifacial PV panels under different solar irradiance incident angles accounting for the variation of the solar incident throughout the day. However, the models are based on view factors. In this thesis, an accurate ray incident and density-based simulation of the performance of two PV faces system, and compared with a single bifacial PV panel is simulated on a water surface at the city of Ottawa, Canada. The performance of the two faces PV system is assessed in terms of the total power production at the specified location for the two seasonal weather extremes of Ottawa, Canada. The selection of the month January is to investigate the performance of the considered system in a month with low radiation intensity (northern

hemisphere), during the month of May for the performance in high radiation intensity. The first is in May, the month with year average solar radiation and the second is January, the month with the lowest solar radiation and solar hours [82]. The actual solar position and the solar intensity are simulated based on the specified time of year and the specified location on earth using COMSOL Multiphysics.

Chapter 3: Systems Development

This chapter will introduce the proposed systems and the detailed descriptions of each system and its subsystems to their components level. System 1 and 2 integrate renewable-based energy that includes wind, solar and OTEC with ammonia production. As for system 3 and 4 they integrate a bifacial solar and a closed OTEC cycle with a carbon-neutral methanol production system.

3.1 Development of various ammonia production systems

Two systems are proposed in this section, and their development will be discussed thoroughly. System 1 integrates a closed-loop OTEC plant with an ammonia production system. System 2 integrates both offshore wind turbines and solar PV, with an integrated ammonia production system.

3.1.1 System 1 (OTEC integrated with ammonia)

The first developed concept for an ammonia production system integrates an OTEC based plant that utilizes the temperature difference of the ocean's surface and deep water. The subsystems of the main plant include the following:

- The Proton Exchange Membrane electrolyzer for hydrogen production. The hydrogen is produced at a pressure of 1 bar and operates at current industry standards. As for the oxygen produced, it is disposed to the atmosphere.
- The Cryogenic Air Separation Unit (CASU) is the system which is responsible for providing the nitrogen to the ammonia synthesis system. The CASU produces nitrogen with a purity of more than 95%. The nitrogen is then fed to the ammonia synthesis system at its operating pressure. The CASU was fed air at ambient conditions, which in this case, was taken at STP. The ambient air compressor operates at a pressure of 8 bar.
- The compressed air exchanges heat with the separated oxygen and nitrogen to a temperature of -146ºC. A distillation column is placed in the cycle to separate the liquified gases. The simulations for ammonia synthesis and CASU related selected parameters for the simulations in Aspen Plus are summarized in the system description.

- The Aspen Plus Simulation Operating Conditions for the ammonia reactors were set to a pressure of 1 bar.
- The ammonia reactors were based on the Gibbs free energy minimization approach in accordance with the literature. The system consists of 5 ammonia reactors, and the heat recovery Rankine cycle operates within 400 kPa (maximum) and 3 kPa (minimum).
- Three-stage hydrogen compression system consisting of multiple compression stages with intercoolers. The intercoolers generate a cooling capacity, which reduces the overall power requirements of the compression system.
- Three-stage carbon dioxide compression system consisting of multiple compression stages with intercoolers. The intercoolers cool down the compressed gas at every stage, which reduces the overall power requirements of the compression system.
- Single-stage Closed OTEC ammonia-based system for power production. Uses a baseline cycle that can produce the required baseload required. The cycle utilizes a single-stage ammonia-based Rankine cycle.
- The evaporator and the condenser use the same warm and cold-water lines of the OTEC cycle. A separate heat exchanger is used to provide cooling duties for various applications
- Two seawater pumping systems are available to provide seawater from the surface and the deep ocean water
- The condenser water discharge is used for cooling output that could be used for district cooling purposes

In the proposed system, an integrated closed-cycle OTEC plant is proposed. The OTEC plant operates with a single-stage ammonia Rankine cycle. The OTEC cycle, as mentioned previously, uses the warm surface ocean water to superheat the ammonia in the evaporator of the cycle. The cold deep ocean water is supplied to the cycle to condense the ammonia in the cycle. The cycle operates on the given temperature differences. The OTEC plant in this study was adopted from information from the NREL and Hasan and Dincer [5,8]. The baseline Rankine cycle produces a net of 10 MW and uses ammonia as a working fluid for

the cycle. The author also discusses that there are other potential working fluids that include refrigerants. However, there are currently working plants and heat exchangers that allow the use of ammonia as a working fluid. As for the operation parameters, they were obtained from the Makai OTEC powerplant operating in Hawaii [83,84]. The model was validated based on the Makai OTEC plant. The operation parameters used in the ASPEN plus simulation are summarised in Table 3.1.

In order to increase the efficiency of the cycle, the discharged cold water from the condenser is further utilised for cooling purposes. As most of these plants will work in tropical and near the equator areas, cooling is needed for most of the year. The discharge water temperature was heated up to 12ºC to characterize the cooling duty. A temperature of 12ºC was used as it is the recommended discharge temperature with the least environmental implications according to the literature. The surface water temperature was taken at 26 ºC, which is also the average temperature of the surface in the summer. As for the cold deep ocean water, it was taken at 4.5ºC. The cold water in the deep ocean exists at 4ºC, as water is most dense at that temperature, but 4.5ºC was taken to accommodate for the heat gain from the cold water traveling through the thermocline. The overall system schematic and Aspen flowsheet can be seen in Figures 3.1[85].

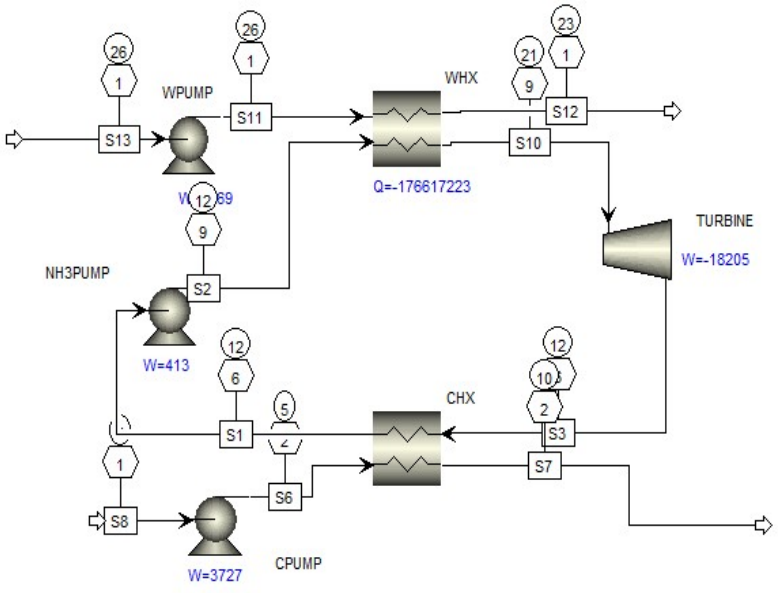

Figure 3.1: Single stage OTEC cycle Aspen Plus flowsheet

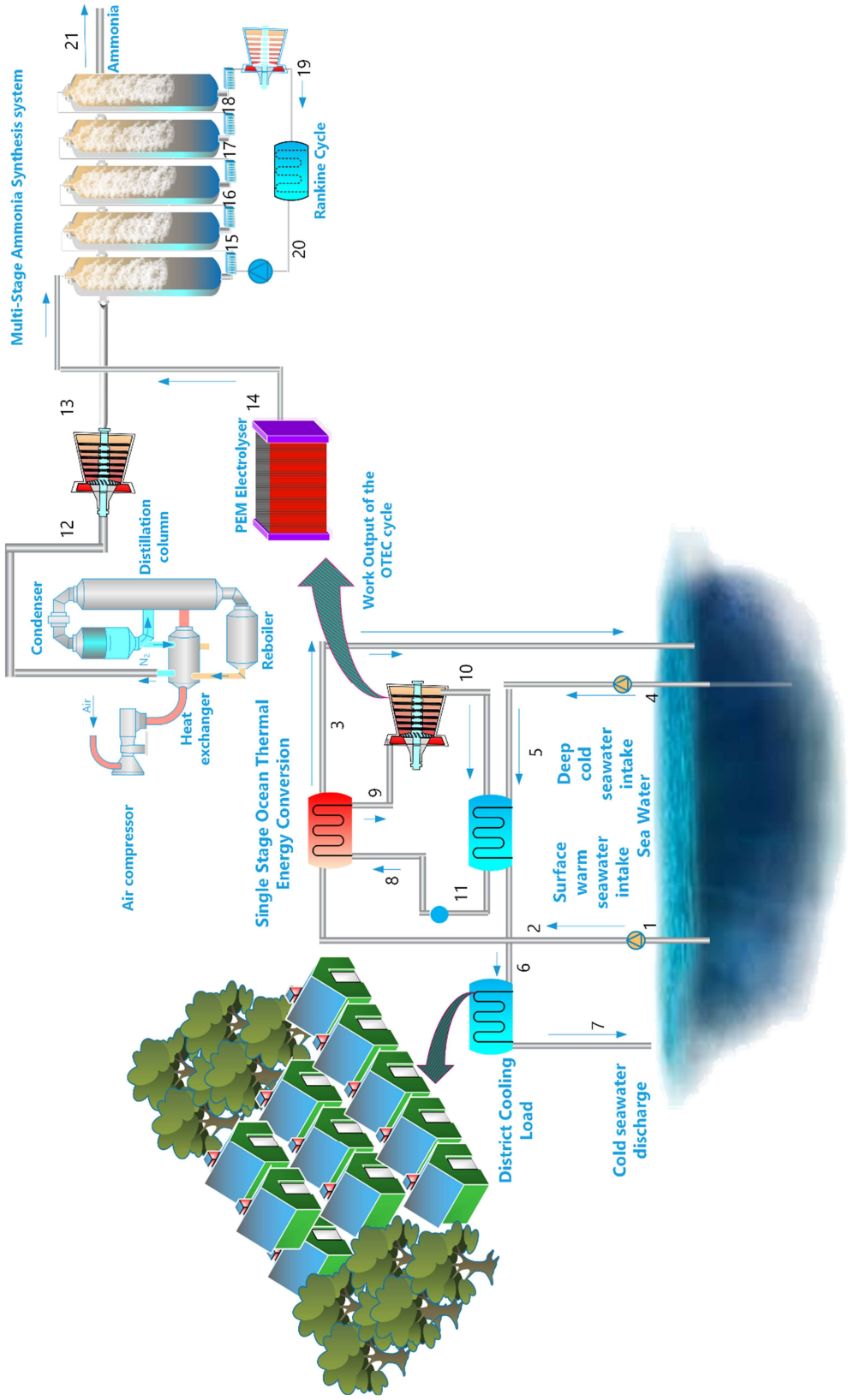

Figure 3.1: System 1 overall schematic

The operating flowrate for the working fluid, cold and warm water was varied to endure optimum operating conditions. After the OTEC cycle produces electricity, 50% of the power is used to produce hydrogen using a Proton Exchange Membrane electrolsyser. The hydrogen is then fed to the ammonia synthesis system, as suggested by Al-Zareer et al.[45]. The nitrogen needed for the ammonia synthesis was provided from a cryogenic air separation unit. Ammonia is the selected method of energy storage, as it is a carbon-free fuel and requires less energy in terms of compression relative to hydrogen.

Table 3.1: OTEC operation parameters

Resource conditions	Value	Units
Warm water temperature	26	(° C)
Flow rate	50,000	(kg/s)
Coldwater temperature	4.5	(° C)
Flow rate	28,450	(kg/s)
Working fluid	NH_3	(---)
Efficiencies		
Water pumps	0.72	(-)
Working fluid pumps	0.72	(-)
Power turbine	0.75	(-)
Generator	0.94	(-)

The ammonia is produced for the purpose of offsetting seasonal electric demands or energy export. The ammonia can be later decomposed to hydrogen and nitrogen. The hydrogen would then be used as fuel for the PEM fuel cell to produce electricity based on the demand. According to a study by Boggs and Botte [86], it was found that the decomposition of ammonia to hydrogen would require 1.55 $W_e h$ of power for every gram of hydrogen produced. The overall reaction for the ammonia synthesis process is given by:

$$N_2(g) + 3H_2(g) \leftrightarrow 2NH_3(g) \tag{3.1}$$

The ammonia reactors in the Aspen Plus simulation operate at a pressure of 1 Bar. The ammonia reactors operate under the Gibbs free energy minimization approach, and heat losses were assumed to be zero (well insulated) to be recovered by a Rankine cycle, which is based on the literature [45]. The ammonia synthesis reaction is exothermic; therefore, a heat recovery Rankine cycle was put in place to recover the heat. The Rankine cycle operates between 400kPa (Upper limit) and 3 kPa (Lower limit). As for the Cryogenic Air

Separation Unit (CASU), it was fed air at standard temperature and pressure. The Aspen flow sheet of the ammonia synthesis system is shown in Figure 3.3. The simulation parameters for the ammonia synthesis system summarized in Table 3.1, which were selected from reference [87].

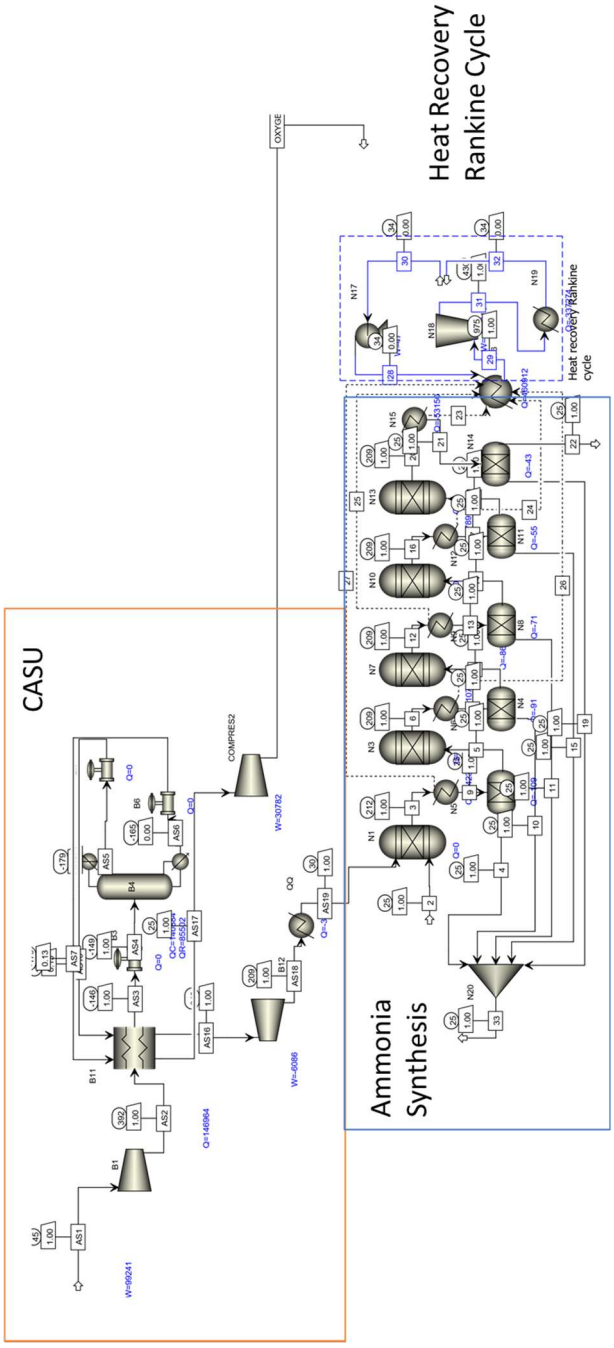

Figure 3.2: Overall Aspen Plus flow sheet of the ammonia synthesis system and CASU

Table 3.2: Ammonia synthesis and CASU operation parameters

Parameter	Value	Unit
Ratio of nitrogen to the hydrogen mole flow rate entering the system	2.17	$\frac{\text{mol } H_2}{\text{mol } N_2}$
Discharge pressure of the CASU	61	bar
Isentropic efficiency of the compressors	72	%
Heat losses in reactors	0	$\frac{\text{kJ}}{\text{mol. } NH_3}$
Specific work to produce Nitrogen (CASU)	458.4	$\frac{\text{kW}}{\text{kg}}$

3.1.2 System 2 (Offshore wind and solar)

The proposed bi-generation system consists of wind turbines, PV units, and an electrolyzer/fuel cell. The proposed system is designed based on the hourly demands of Ontario, Canada, for over 12 months. The peak demand in Ontario is approximately 19 MW in most days. The power demand was scaled down by the same trends to have a peak of 6 MW. The system consists of two GE 1.5xle wind turbines, which are popular models currently and in use in some wind power generation facilities in Ontario. The total wind power potential is 3 MW, as each of the GE 1.5xle produces a maximum of 1.5MW at wind speeds of 11m/s [88,89]. Furthermore, the system also integrates solar PV panels. The model chosen for the PV cells was a thin film first solar 6420 cells. The total potential for the integrated, installed PV modules is 3 MW [90,91]. The power generation units (wind turbines and solar PV) are designed to meet most of the demands and have excess during the off-peak hours. During the off-peak hours, the system is designed to provide power and water to PEM electrolyzers for hydrogen production. For this system, an electrolyser model developed by Ezzat and Dincer [92] was adopted to simulate the hydrogen production. As mentioned previously, the excess electricity is transferred to an electrolyzer. The electrolyzer performs electrolysis on the water to produce hydrogen. The overall reaction in the electrolyzer is written as follows:

Reduction at the cathode:

$$2H^+(aq) + 2e^- \rightarrow H_2(g) \tag{3.2}$$

Oxidization at the anode:

$$2\,H_2O(l) \rightarrow\ O_2(g) +\ 4\,H^+(aq) +\ 4e^- \tag{3.3}$$

Overall reaction:

$$2\,H_2O(l) \rightarrow\ 2\,H_2(g) +\ O_2(g) \tag{3.4}$$

The hydrogen is then used as feedstock for a multistage ammonia synthesis plant, as suggested by Al-Zareer et al.[32]. The CASU feeds the ammonia synthesis system nitrogen. Ammonia is the selected method of storage for the hydrogen produced as it is a carbon-free fuel and has a higher lower heating value than hydrogen by about 30% on a molar basis. The heat released from the exothermic reaction of the ammonia synthesis is recovered by a Rankine cycle to produce electricity, which is mostly provided to run the CASU. The produced ammonia is stored in a compressed tank, and when peak power cannot be met by the wind and solar plant, the ammonia is decomposed into nitrogen and hydrogen. The hydrogen is then used to power a PEM fuel cell to meet the power demands of the community. According to a study by Boggs and Botte [93], it was found to decompose ammonia to hydrogen; it requires 1.55 Wh of electrical power per gram of hydrogen produced. The overall reaction for the ammonia synthesis process is given by

$$N_2(g) + 3H_2(g) \leftrightarrow 2NH_3(g) \tag{3.5}$$

The Aspen Plus simulation Operating Conditions for the Ammonia Reactors were taken as follows: Operational pressure was 1 Bar, the ammonia reactors were based on the Gibbs free energy minimization approach in accordance with the literature [45], the system consists of 5 ammonia reactors and the heat recovery Rankine cycle operates within 400 kPa (maximum) and 3 kPa (minimum). The CASU was fed air at ambient conditions. The Aspen flowsheet is shown in Figure 3.4. The simulations for ammonia synthesis and CASU related selected parameters for the simulations in Aspen Plus are summarized in Table 1, which were selected from reference [32].

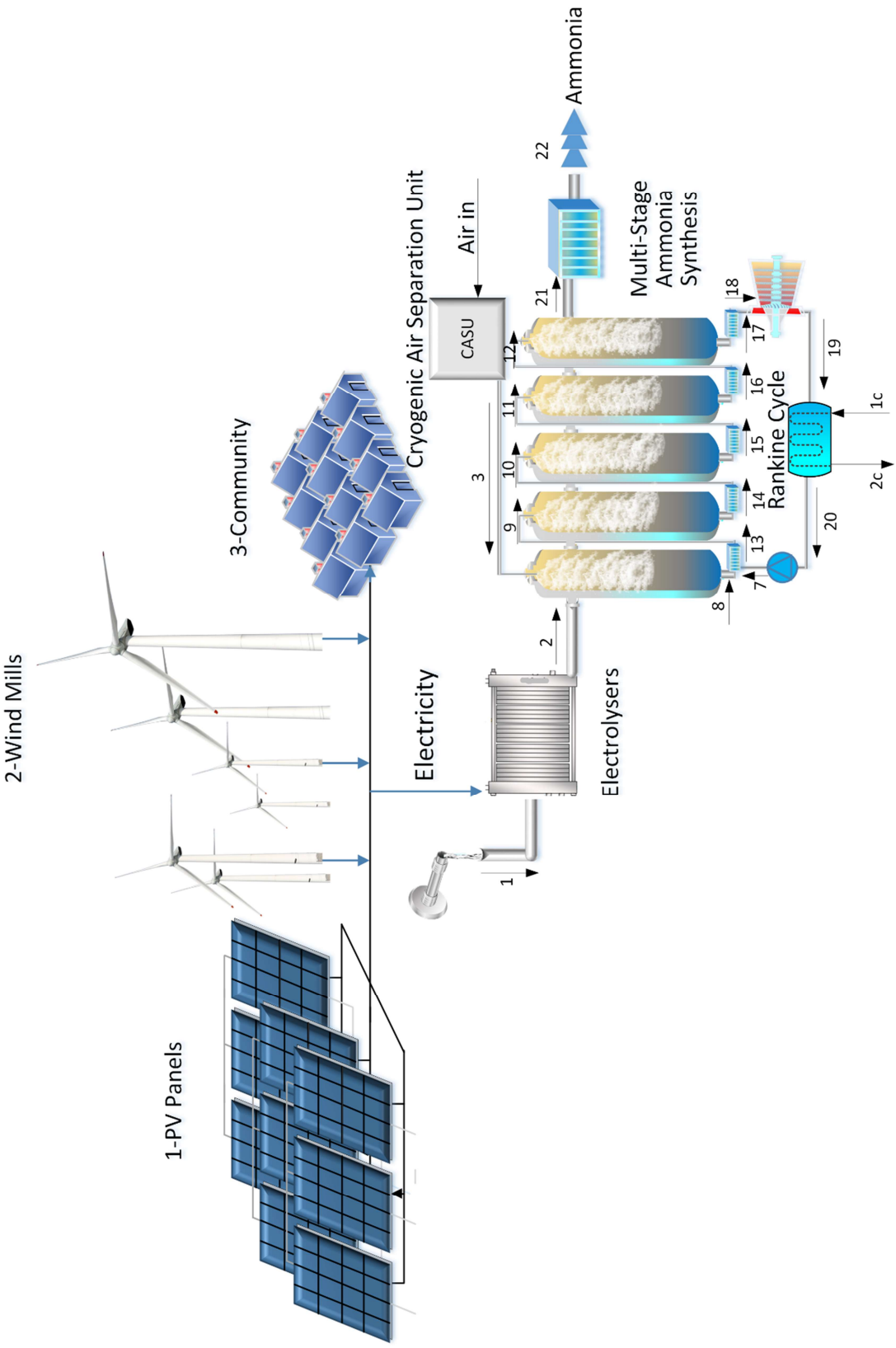

Figure 3.3: System 2 overall schematic

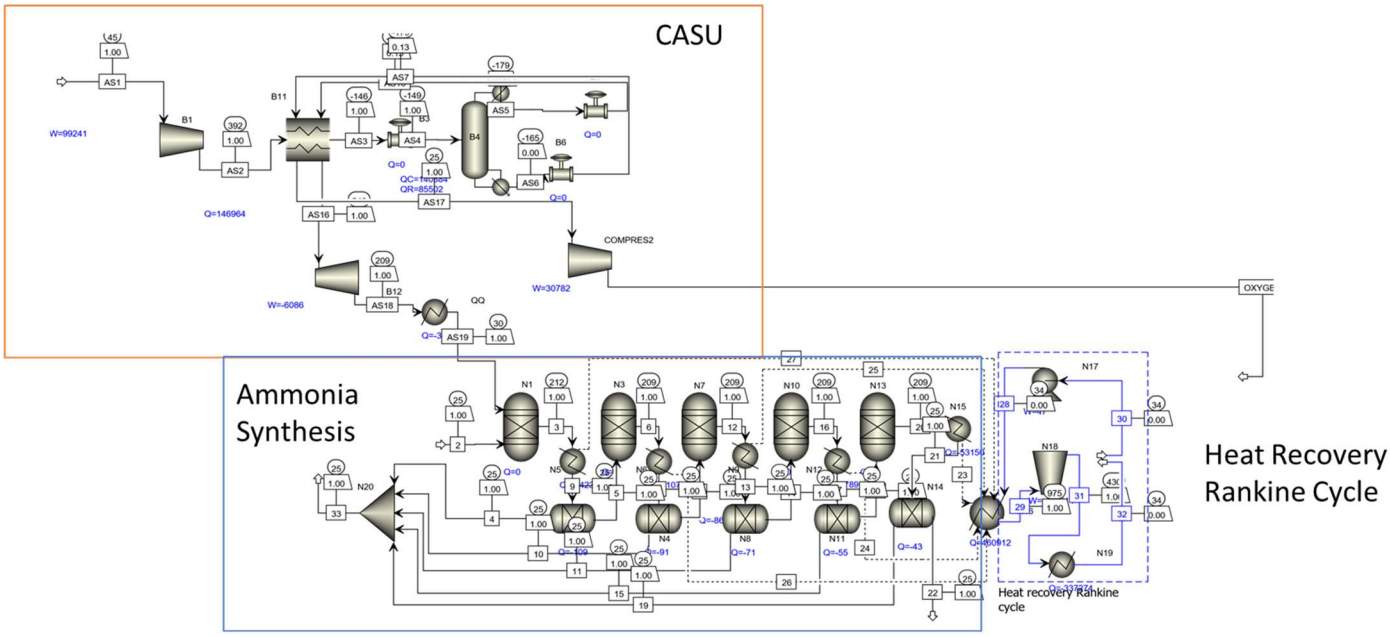

Figure 3.4: The ASPEN flow sheet of the ammonia synthesis system and CASU.

Table 3.3:Ammonia synthesis and CASU operation parameters

Parameter	**Value**	**Unit**
Ratio of nitrogen to the hydrogen mole flow rate entering the system	2.17	$\frac{\text{mol } H_2}{\text{mol } N_2}$
Discharge pressure of the CASU	61	bar
Isentropic efficiency of the compressors	72	%
Heat losses in reactors	0	$\frac{kJ}{mol.NH_3}$

Note that the heat losses from the reactors were assumed to be zero as they are well insulated [1].

3.2 Development of the various methanol production systems

In this thesis, several OTEC-based integrated energy systems are proposed and investigated for development, analysis, and assessment. The focus will be on the utilization of seawater, and the extraction of dissolved carbon dioxide in the deep seawater for district cooling, methanol, and power production. This will allow for the increased utilization of the cold water extracted by means of carbon dioxide extraction and cooling duty provided. An OTEC system that integrates carbon dioxide extraction from deep ocean waters for the purpose of the production of carbon-neutral methanol is lacking, as explained in the literature. Furthermore, the aim is to achieve higher energy efficiencies than that reported in the literature of unintegrated OTEC plants, which range from 2% to 5% [9], respectively.

3.2.1 System 3 (OTEC integrated with methanol)

The first developed concept for a methanol production OTEC based plant that utilizes the temperature difference of ocean's surface water and the following:

- The main source of continuous renewable energy is the constant temperature of the ocean at a certain depth, which is done using the OTEC system for the goal of methanol production. While the other main subsystems that are integrated to deliver the utilized ocean energy to produce power and methanol are as follows:
- Electrolytic Cation Exchange Module (ECEM) for carbon dioxide and hydrogen production. The ECEM reactor recovers the carbon dioxide from the ocean water as it electrolyzes the water to produce hydrogen.
- Multistage hydrogen and carbon dioxide compression system consists of a three-stage hydrogen compression system coupled with intercoolers for optimized performance. The intercoolers use the water discharged from the system's condenser, which reduces the overall power requirements of the compression system.
- The carbon dioxide-based methanol synthesis system produces methanol from the extracted carbon dioxide from the deep ocean water that is highly concentrated with bicarbonates. The main reaction occurs in the presence of Cu/ZnO2/Al2O3 catalysts in the large-scale production of methanol
- The methanol production system also consists of a reverse water gas shift reactor in the inter steps of the methanol production, followed with the final steps of methanol and water separation to ensure the purity of the methanol.
- Single-stage closed OTEC ammonia-based system for power production, which is designed to produce the required baseload of 16MW, at the lowest temperature differentials in the water.
- The evaporator and the condenser use the same warm and cold-water lines of the OTEC cycle. A separate heat exchanger is used to provide cooling duties for various applications, such as district cooling.
- Two seawater pumping systems are available to provide seawater from the surface and the deep ocean water.

- The condenser water discharge is used for cooling output that could be used for district cooling purposes.

The suggested system in this thesis is powered by an Ocean Thermal Energy Conversion (OTEC) plant that is combined with an ECEM reactor, a district cooling system, and a multistage methanol production system. The main feedstock of this system is the carbon dioxide found in the seawater and hydrogen produced from the electrolyzed seawater. The ECEM reactor will produce both the hydrogen and carbon dioxide required to feed the methanol production system. The system is a tri-generation system as it produces the following commodities: power, methanol, and cooling. Figure 3.4 displays the layout of the proposed system. It should be noted that carbon dioxide and hydrogen can be produced using other technologies. For example, a cryogenic air separation unit can be used to produce carbon dioxide in the system or even flue gases from local industrial and power plants. As for the hydrogen, it could be produced from a biomass feedstock, or from water by using a photocatalytic reactor. However, in this system, the commodities found in the ocean will be used for the analysis. As for the district cooling system, the rejected ocean cold water that was used to cool the condensers of the 2-stage ammonia Rankine cycle was used to cool 6000 average Florida homes, as such a system will be possible in such a climate. The cooling load of the system was calculated to be 69 MW and is fixed in all scenarios and cases during the study, at a temperature of 13°C.

The OTEC plant was adopted from the National Renewable Energy Laboratory (NREL) research developed by Bharathan [5]. The baseline Rankine cycle produces a net of 10 MW and uses ammonia as a working fluid for the cycle. The author also discusses that there are other potential working fluids that include various refrigerants such as R-134a. However, there are currently working plants and heat exchangers that allow the use of ammonia as a working fluid.

Several OTEC pilot plants have been developed over time that produced 30-120kW. To increase production, the intake pipes can be made larger to handle larger flowrates. This increase in size and flow allows for power production rates of up to 100MW. Currently, the 1-20MW scale plants are being developed. The developments in the production of electricity using OTEC has been gaining traction in the tropical and coastal areas mainly.

Some examples of these pilot plants include a 1 MW plant in Tarawa Island(Pacific), a 20MW plant in Qingdao(China), as well Makai plant in Hawaii (USA)[4]. The reason behind these pilot programs are for the benefits that come from the byproducts of the plant. Such as nutritious water for aquaculture, desalinated water in certain configurations, and district cooling. However, such integrated systems have not been properly explored and analyzed. Especially in the case of increasing the utilization of cold water, which is the highest consuming entity causing the efficiency to drop.

As for the methanol production system was modeled and validated with Struckmann et al. [49], as the authors reported great potential in the recycling process of carbon dioxide into methanol. The exergy efficiency of the assessed system was 83.1%, where the exergy efficiency takes the chemical exergy of hydrogen and methanol along with the exergy associated with the power input and heat released from the system. The exergetic efficiency of the overall energy conversion and storage system was reported to be 16.2% and 20%. The efficiency of the conversion and storage system is highly dependent on the conversion devices used. The conversion from carbon dioxide to methanol was calculated from the Aspen simulation at 71.2% .

The carbon dioxide concentrations increases as the depth increases in the ocean waters. This is convenient as the cold water extracted for the OTEC cycle can be further utilised, instead of simply cooling the condesner. The distribution of total carbon dioxide can be seen in Figure 2.1. as the depth increases the total dissolved carbon dioxide increases. This is of great potential for hybrid desalination and carbon dioxide extraction or even for ocean thermal.

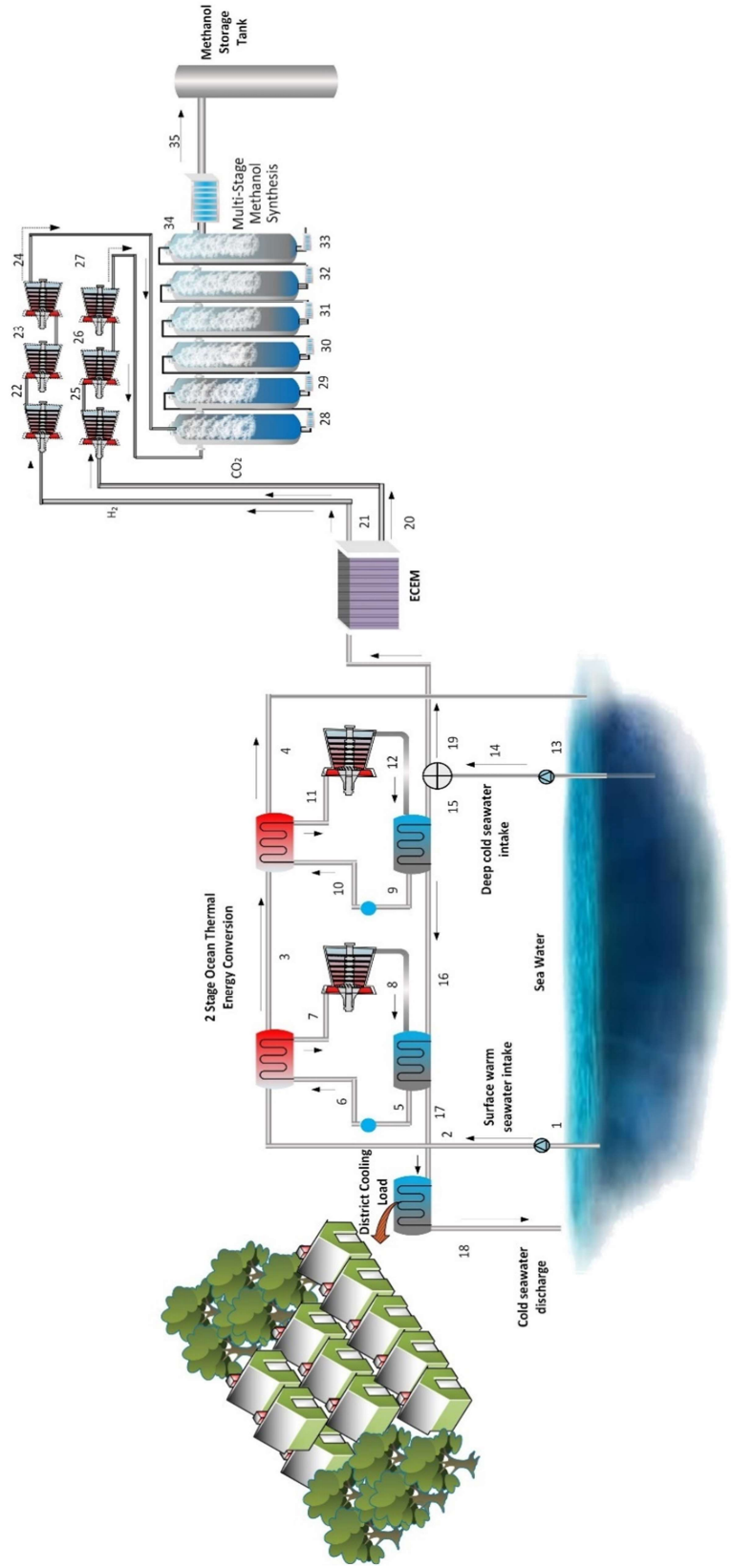

Figure 3.5: System 3 overall schematic

The methanol production system is based on a validated Aspen Plus model [49]. The model was developed to produce methanol from exhaust captured carbon dioxide. However, in this proposal, the carbon dioxide is produced from the ocean water. The model follows the following overall reactions to produce the methanol from carbon dioxide and hydrogen:

$$CO_2 + 3H_2 \leftrightarrow CH_3OH + H_2O \tag{3.5}$$

$$\Delta h_{300K} = -49.16 \frac{kJ}{mol}$$

The inter-step reaction that occurs displays the reverse water gas shift reaction which produces CO and H_2O.

$$CO + H_2O \leftrightarrow CO_2 + H_2 \tag{3.6}$$

$$\Delta h_{300K} = 41.16 \frac{kJ}{mol}$$

As for the final step the reaction occurs between CO and H_2 to produce methanol. The reaction takes place with the presence of the following catalysts: Cu/ZnO2/Al2O3.

$$CO + 2H_2 \leftrightarrow CH_3OH \tag{3.7}$$

$$\Delta h_{30} = -90.77 \frac{kJ}{mol}$$

The molar ratio of hydrogen to carbon dioxide that was used for feed was set to 3:1 during the simulation. The highest reactor pressure was set to 5 MPa with a 25 kPa pressure drop set at every reactor stage. The feed after all the reactor stages is then flashed at a pressure of 1.2MPa where the unreacted carbon monoxide, carbon dioxide, and hydrogen are compressed to 5 MPa and returned to the feed. The compressor's efficiency was set to 0.8 isentropic and 0.9 a mechanical efficiency. Furthermore, the hydrogen and carbon dioxide go through a triple compression process from atmospheric pressure to 0.4MPa, 0.4 to 1.2MPa, and finally 1.2 to 5 MPa. If the recycling of the feed is factored in, the system has a carbon dioxide to methanol conversion efficiency of 96.8%. The Aspen flowsheet is shown in Figure 3.7.

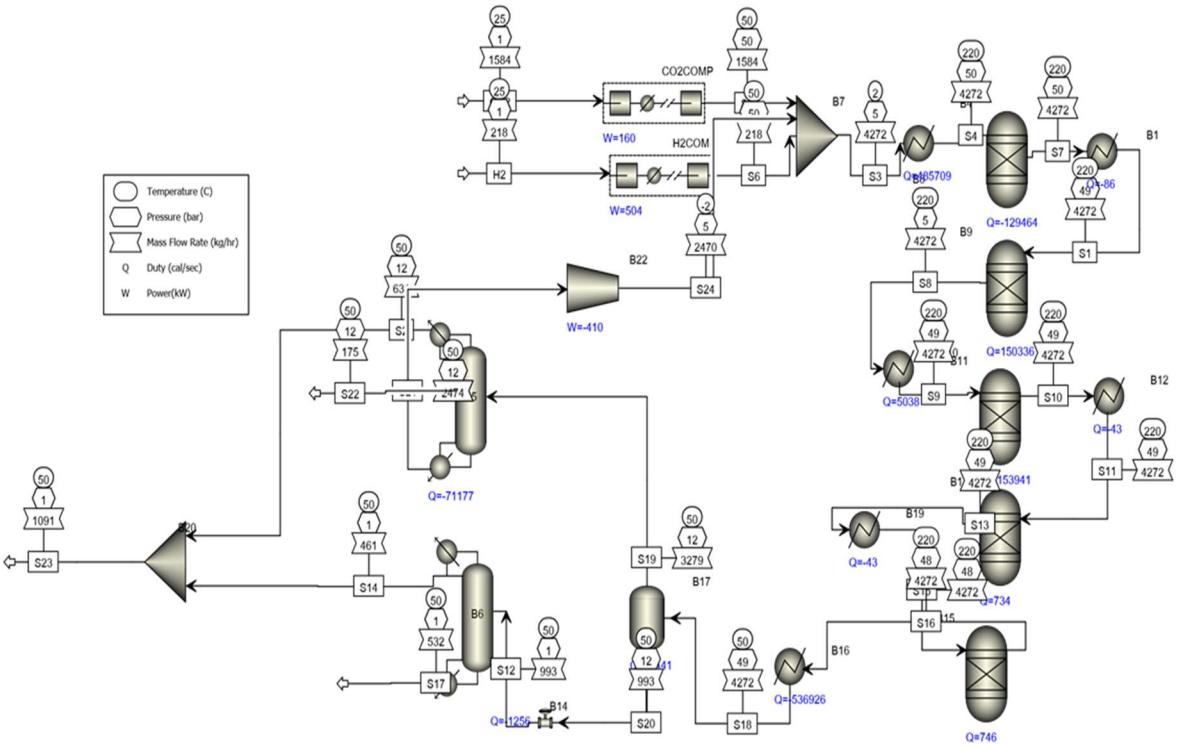

Figure 3.6: Aspen Plus flow sheet of the carbon dioxide to methanol conversion

The OTEC plant was validated NREL [5]. The baseline double stage Rankine cycle produces a net of 16.7 MW and uses ammonia as a working fluid for the cycle. The author also discusses that there are other potential working fluids that include various refrigerants such as R-134a. However, there are currently working plants and heat exchangers that allow the use of ammonia as a working fluid. The model was validated based on the Makai OTEC plant. The operation parameters used in the Aspen plus simulation are summarized in Table 3.4. A two-stage ammonia Rankine cycle is shown in figure 3.8, along with an integrated district cooling system that utlises the rejected cold sea water to cool down at a rate of 69.0MW. This is possible as the mass flow rate of the cold water is 28,450 kg/h. As for the cold-water inlet, it was found that the most recent development for the OTEC cold water pipes are vacuum insulated using hollow fiberglass material to build the OTEC pipes. According to Hasan and Dincer [94,95], vacuum insulation and air insulation were found to be very good thermal insulators and could be built at cost-effective rates. Therefore, the temperature effects of the high flow rate of cold seawater as it travels from the deep sea to the surface are very small. According to the NREL [5] the temperature increase is 0.5°C.

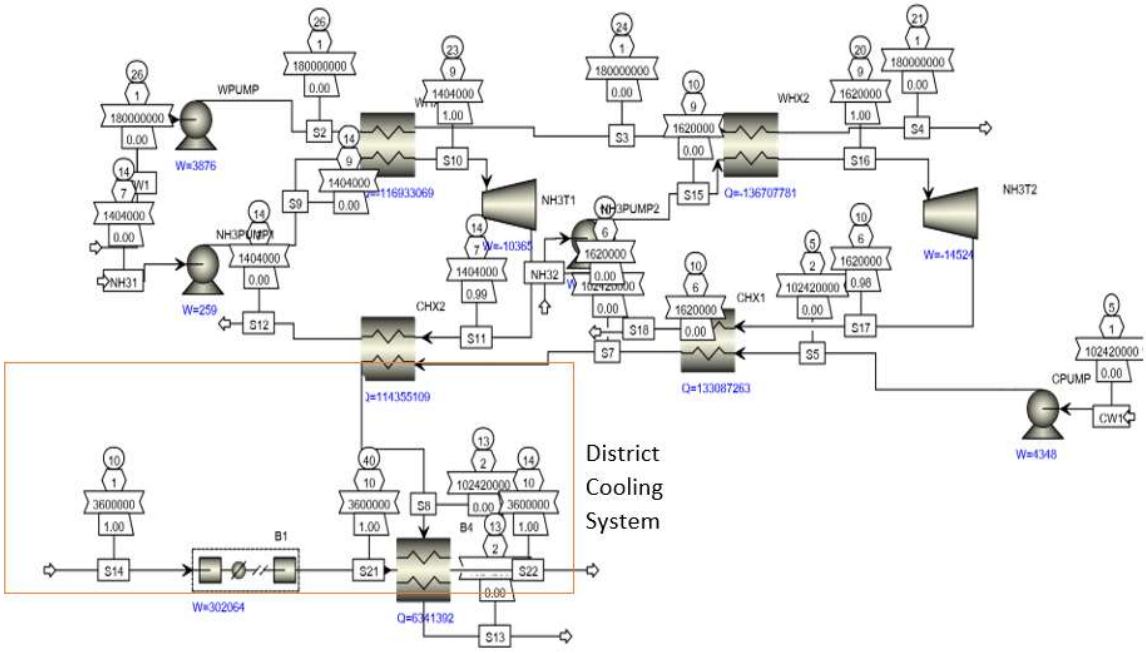

Figure 3.7: Aspen Plus flowsheet of the power production Rankine cycle of the OTEC.

Table 3.4: Operation parameters of the OTEC plant

Resource conditions	Value	Units
Warm water temperature	26	(°C)
Flow rate	50,000	(kg/h)
Cold water temperature	4.5	(°C)
Flow rate	28,450	(kg/h)
Working fluid	NH_3	(---)
Efficiencies		
Water pumps	0.72	(-)
Working fluid pumps	0.72	(-)
Power turbine	0.75	(-)
Generator	0.94	(-)

Source:[5]

3.2.2 System 4 (Methanol integrated with solar bifacial)

In the following section, the system development process and basis of the proposed system will be discussed. The offshore bifacial PV based system is integrated with an organic Rankine cycle. The offshore bifacial system's main purpose is to increase energy production by capturing the reflection of the surface of the water and ice. The system has a series of heat exchangers that use the surface lake/ocean water to warm/cool down the

working fluid (ammonia) depending on the season. The surface lake water in the winter is known to be coldest at 4ºC. The ammonia is warmed up to temperatures above 0ºC, that in turn warms up the PV panels to melt any precipitations that has accumulated ahead of sunrise. After the snow is melted, the bifacial solar panels are warmed up from the negative ambient temperature to a steady-state of the lake surface temperature. As the solar irradiance intensity increases, the cell temperature increases as well based on its Nominal Operating Cell Temperature (NOCT). It was estimated that a cell temperature of 18-27ºC is possible, at solar intensities ranging between 450-700 W/m^2 (winter solar irradiances considered). The positive cell temperatures will allow for the boiling of the ammonia working fluid which can then be used to run an organic Rankine cycle. The heat transfer rate and the temperature is increased by having the area of the bifacial modules much larger than the area where the ammonia heat transfer area. This causes a concentration effect without the use of any lenses. The case is similar in the summer with positive temperatures, as the solar intensity increases a cell temperature of 45-50ºC is possible based on a solar irradiance range of 700-1,000 W/m^2 (summer solar irradiances considered). The solar cells can be cooled down to increase their efficiency, to the temperature of the lake surface temperature of 21-23ºC. The ammonia will again boil, and in turn cools= down the PV modules, and operating an organic Rankine cycle. This configuration will allow for a similar approach to OTEC in tropical countries but in colder countries such as Canada. Even in the days where the temperatures are too low to run the thermal plant the solar panels are still operational given that there is solar irradiance, while gaining the benefit of the reflection of the solar rays off the surface water, therefore increasing the yield per area of the solar cell. The excess heating/cooling, depending on the cycle can then be used to for various domestic uses such as a preheater/cooler for air-conditioning. The systems excess power can be optimized based on the location of deployment to produce methanol for seasonal energy storage that can be used when needed. The methanol production system will use an ECEM reactor for the extraction of carbon dioxide in lake water, and hydrogen from the electrolysis of the water.

The bifacial PV cells allow for the utilization of the solar radiation reflected from the water surface leading to an increase in energy production. The surface area utilization also increases, which in turn reduces the fault detection and problems of solar farm size.

Another advantage of the proposed system is that it increases the energy density per unit area of the solar farm. A schematic diagram of the considered solar panel used for offshore power production is shown in Figure 3.9. As shown in Figure 3.9, the solar-based offshore power production used the conventional structure and build of conventional solar panels, around on average half a day of available useable solar irradiance (which varies based on the season and inclination of the solar panel. As shown in Figure 3.9, the problem of the solar panels heating up is dealt with by proposing the integration of heat pipes or a heat exchanger embedded in between the two opposing panels.

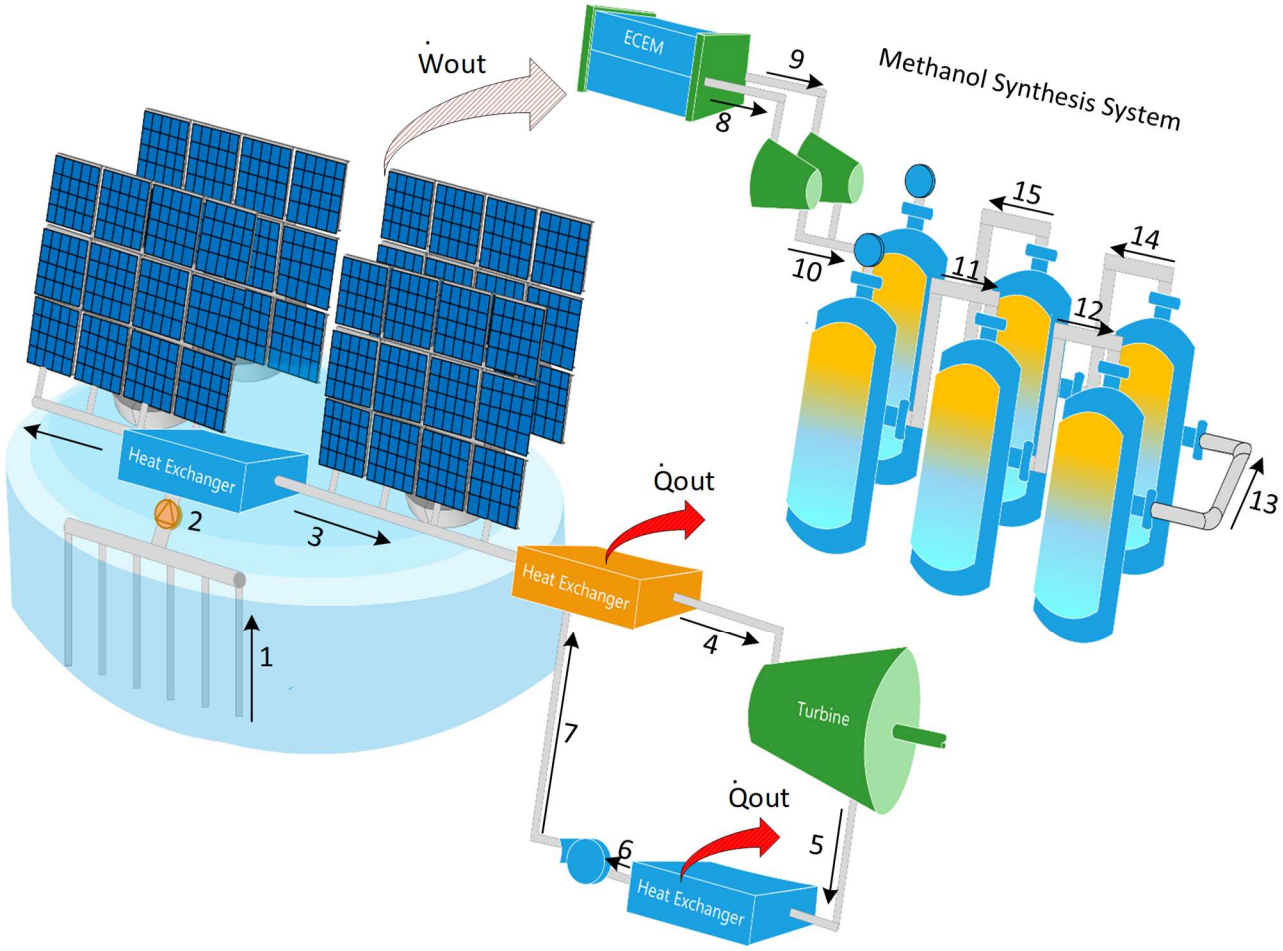

Figure 3.8: System 4 overall schematic

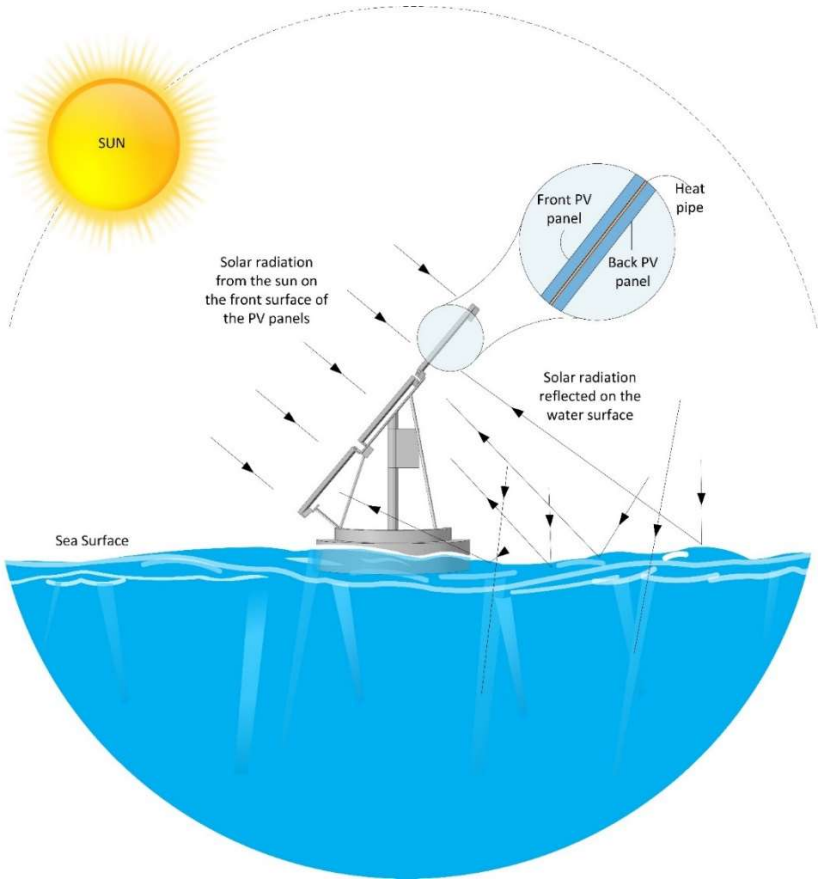

Figure 3.9: Schematic diagram of the proposed bifacial solar panel floating on a water feature showing the incident solar radiation at a moment in time as well as those radiations that are reflected from water surface as well as other surfaces.

The increase in power production through solar PV is also of importance. This system will investigate the performance of using the proposed structure of bifacial solar panels in comparison to single face solar panels with the exact same structure and simulated for the same operation and design conditions. The water domain will be simulated using two different conditions, which include still and wavy water. The wavelength of the water wave was chosen to be 4m and with an amplitude of 0.2m. The dimensions of the proposed bifacial solar photovoltaic panels are shown in Figure 3.9, where each set is mounted on a floater covered with sheets of aluminum to enhance the performance of the system, which has a diameter of 2 m and a height of 0.38 m. The solar panels are at a height of 1.65 m and it has a 3 × 4 panels configuration, where each panel is 1 × 1 m^2 area panel.

In order to investigate the performance of the proposed offshore power production system two models are developed and integrated to simulate a problem with multi-physics

properties. As mentioned earlier, the three-dimensional radiation model is developed and simulated in COMSOL Multiphysics software. The solar irradiance received by the solar panels is integrated over the area giving the solar incident power received by the bifacial module. The incident power received by the front and back of the PV panel modules can be used to show the effectiveness of the offshore bifacial solar module.

Chapter 4: Analysis and Optimization Study

In this chapter, the detailed thermodynamic analysis of the four proposed systems will be presented, plus the main assumptions made during the simulation and the calculations of the thermodynamic parameters.

4.1 Thermodynamic and Heat Transfer Analyses

This section presents the development of the three-dimensional heat and mass transfer analysis for mainly system 4. For systems 1-4 the thermodynamic correlations and modeling are presented as well.

4.1.1 System 1

Some assumptions are made for the analyses of the system components as follows:

- The ammonia production plant operates at steady-state conditions
- The ammonia production plant start-up period is not considered
- The kinetic and gravitational potential energies changes are neglected throughout the plant
- All gases in the system are treated as real gases (exception for this assumption is for the gases in the chemical exergy equation, they are treated as ideal gases)
- The electrical generator thermal efficiency is $\eta_{gen} = 95\%$

The property sources used in Aspen Plus simulation are given as follows:

For H_2O:

- The 1984 NBS/NRC: Steam table correlations for thermodynamic properties are used for H_2O.
- The International Association for Properties of Steam (IAPS) correlations for transport properties for H_2O (Aspen Plus property method: STEAMNBS for the temperature range of 273.15 K to 2000 K at a maximum pressure of over 10,000 bar) are used.

In this section the analysis method of the results will be discussed thoroughly. To begin with, the overall energy and exergy efficiency equations were derived for the system as follows:

$$\eta_{OTEC} = \frac{\sum \dot{W}_{Turb} + \dot{W}_{CWPump} + \dot{W}_{WWPump} + \dot{W}_{NH_3Pump}}{\dot{E}_{in}} \quad (4.1)$$

where $\dot{W}_{Turb}$ represents the power produced by the turbine, $\dot{W}_{CWPump}$ represents the cold water pumping power, $\dot{W}_{WWPum}$ represents the warm water pumping power and $\dot{W}_{NH_3Pump}$ represents the ammonia pumping power.

As for the energy being inputted to the system through the warm surface water, it can be described as follows:

$$\dot{E}_{in} = \dot{m}_{WW} \times (h_{inlet} - h_{outlet}) \times \varepsilon \quad (4.2)$$

Here, $\dot{E}_{in}$ represents the energy inputted from the warm water from the ocean. The specific enthalpy difference is from the inlet and outlet of the warm water is represented by $h_{inlet} - h_{outlet}$. As for ε, it represents the effectiveness of the heat exchanger used in the system.

$$\psi_O = \frac{\dot{W}_{Turb} + \dot{W}_{CWPump} + \dot{W}_{WWPump} + \dot{W}_{NH_3Pump}}{\dot{E}x_{in}} = \frac{\eta_O}{\eta_{Carnot}} \quad (4.3)$$

where $\dot{W}_{net}$ represents the net power produced by the OTEC plant, $\dot{E}x_{in}$ exergy inputted from the warm water from the ocean. Another method for calculating the exergy efficiency is by dividing the energy efficiency of the system by the Carnot efficiency (η_{Carno}).

$$\eta_{Carnot} = 1 - \frac{T_L}{T_H} \quad (4.4)$$

The general specific exergy destruction can be calculated from the following relation

$$Ex_d = (1 - \psi_0) \times Ex_{in} \quad (4.5)$$

The following section represents the general balance equations. The left and right side of eq.4.6 represents the sum of all mass flow rates entering and leaving the system. The mass is conserved throughout the process.

$$\sum \dot{m}_{in} = \sum \dot{m}_{out} \quad (4.6)$$

The left and the right side of eq.4.7 represent the energy leaving and entering the system. There are several types of energy entering and leaving the system. Some of the forms of

energy represented in the energy balance equation include the work rate, thermal energy rate, the energy associated with the mass flowing through the system.

$$\dot{Q}_{in} + \dot{W}_{in} + \sum \dot{m}_{in}\left(h + \frac{v^2}{2} + gz\right)_{in} = \dot{Q}_{out} + \dot{W}_{out} + \sum \dot{m}_{out}\left(h + \frac{v^2}{2} + gz\right)_{out} \quad (4.7)$$

The left and the right side of eq. 4.8 represent the exergy leaving and entering the system. Some of the forms of exergy represented in the energy balance equation include the work rate, thermal exergy rate and the exergy associated with the mass flowing through the system.

$$\sum \dot{E}x_{\dot{Q}_{in}} + \sum \dot{E}x_{\dot{W}_{in}} + \sum \dot{E}x_{flow_{in}} = \sum \dot{E}x_{\dot{Q}_{out}} + \sum \dot{E}x_{\dot{W}_{out}} + \sum \dot{E}x_{flow_{out}} + \dot{E}x_d \quad (4.8)$$

4.1.2 System 2

Some assumptions are made for the analyses of the system components as follows:

- The ammonia production plant operates at steady-state conditions
- The ammonia production plant start-up period is not considered
- The kinetic and gravitational potential energies changes are neglected throughout the plant
- All gases in the system are treated as real gases (exception for this assumption is for the gases in the chemical exergy equation, they are treated as ideal gases)
- The electrical generator thermal efficiency is $\eta_{gen} = 95\%$

The property sources used in Aspen Plus simulation are given as follows:

For H_2O:

- The 1984 NBS/NRC: Steam table correlations for thermodynamic properties are used for H_2O.
- The International Association for Properties of Steam (IAPS) correlations for transport properties for H_2O (Aspen Plus property method: STEAMNBS for the temperature range of 273.15 K to 2000 K at a maximum pressure of over 10,000 bar) are used.

The performance of the overall system was evaluated using the first and second laws of thermodynamics. The system is evaluated under steady-state conditions but modeled dynamically for transient operation.

The assumptions made for the systems analysis are as follows: (a) the system operates at a steady-state and (b) all gases behave as ideal gases.

The wind turbines chosen for this system were the GE 1.5XLE, as mentioned previously. To give an accurate representation of the power output of the wind turbine, the power curve of the wind turbine was obtained from GE. The data points were then used in the Eureqa, which is an AI-based software that provides regression fittings based on various modeling equations. The regression obtained was 0.9999 (R^2), and the model obtained from Eureqa is shown below in Eq.4.14. However, a less accurate representation of the power output of any wind turbine can be defined by equations 4.9-4.12, and 4.15-4.30. [96–99]

The kinetic energy inputted to the wind turbine can be modeled by taking into account the mass flow rate and the speed of the wind as follows:

$$P_{kinetic} = \frac{1}{2} \times \dot{m} \times V^2 \tag{4.9}$$

Here, $\dot{m}$ is the mass flow rate of air and V $\left(\frac{m}{s}\right)$, is the wind speed of air at the inlet of the turbine

$$\dot{m} = V \times A \times \rho \tag{4.11}$$

where A is the area of the turbine rotor and ρ $\left(\frac{kg}{m^3}\right)$, is the density of air

The power output from the wind turbine considers the kinetic energy captured and the conversion efficiency of the turbine into electricity. The power output can be modeled as follows:

$$P_{wind} = P_{kinetic} \times C_p \tag{4.12}$$

The power coefficient of any horizontal axis is limited by the Betz limit, which is 0.593. The Cp of a horizontal axis turbine could be estimated using the following relation [100]:

$$C_p = \frac{P}{\rho \times A \times \frac{V_\infty^3}{2}} = 4a\,[1-a]^2 \tag{4.13}$$

However, the Cp value of the GE 1.5xle can be modeled using the following equation obtained from Eureqa fitting of the Cp actual values to the Eq.4.14 [101,102]:

$$\begin{aligned} C_P &= 0.00775V^2 + 35.48 \times sqrt(0.00779V) + 0.001486V \times sin(0.3547V) \\ &+ 0.0293 \times tan(6.2723 + sin(0.3547V) - 0.0009984V^2) - 3.435 \\ &- 0.682V \end{aligned} \tag{4.14}$$

The model in comparison to the actual data, can be seen in the results and discussion section. The accuracy/error that the correlation provides relative to the actual data and the complexity of the correlation obtained from the Eureqa software is shown in Figure 4.1. Furthermore, the graph represents each iteration of the correlation and the level it provides relative to its complexity.

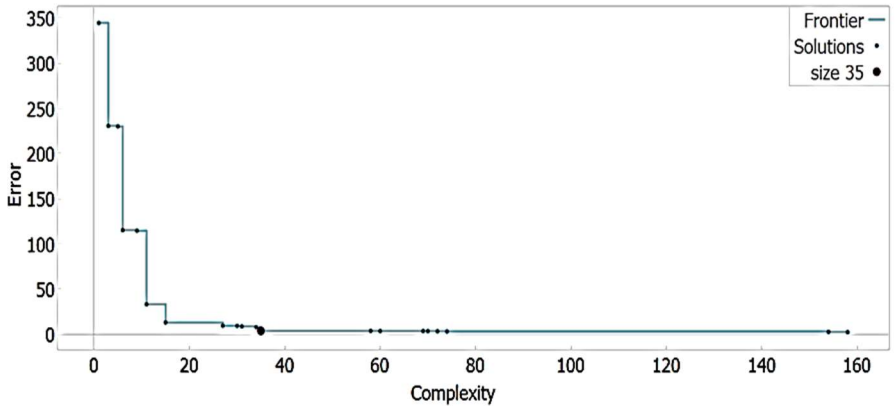

Figure 4.1: Solution plotted accuracy vs complexity of modeling equation obtained from the Eureqa.

The energy and exergy efficiency of the wind turbine is modeled as follows:

$$\eta_{\text{wind}} = \frac{\text{P}_{\text{wind}}}{\text{P}_{\text{kinetic}}} \tag{4.15}$$

$$\psi_{\text{wind}} = \frac{\text{P}_{\text{wind}}}{\dot{\text{Ex}}_{\text{in}}} \tag{4.16}$$

The exergy analysis of a wind turbine is based on the electric output from the electromechanically genrated power provided by the wind turbine. The exergy input of the wind turbine can be defined by the potential useful work that can be defined by the pressure

drop across the wind turbine [101,102]. The following equation can define the exergy input of the horizontal axis turbine used:

$$\dot{E}x_{in} = W_u = \frac{\Delta P \times \dot{m}}{\rho} \tag{4.17}$$

The pressure drop across the wind turbine can be estimated with the use of the actuator disk model. The disk model simplifies the rotors of the wind turbine by assuming it is a porous actuator disk. The pressure drop across the wind turbine can be estimated based on the Actuator disk model. The pressure drop model is shown in equation 4.18:

$$\Delta P = \frac{T}{A} = \frac{C_T \times \rho \times U_\infty^2}{2} \tag{4.18}$$

where the C_T is the coefficient of thrust, ρ is the density of air, U_∞ is the undisturbed velocity of the wind, and T is thrust force.

The final pressure drop can also be also calculated based at the speed at the hub of the rotor based on the Betz theory by calculating the axial induction factor. The axial induction factor based on the Betz theory is shown as follows:

$$a = \frac{1}{2}\left(1 - \sqrt{1 - C_T}\right) \tag{4.19}$$

where the final pressure drop can be calculated as follows:

$$\Delta P = \frac{C_T \times \rho \times \left(\frac{1}{1-a} V_1\right)^2}{2} \tag{4.20}$$

The thrust coefficient for the wind turbine rotor can be calculated as follows:

$$C_T = \frac{\frac{F}{\rho \times A \times V_\infty^2}}{2} = 4a(1-a) \tag{4.21}$$

where F is the axial force on the turbine and A is the area of the rotor.

Here, C_T isn't widely available for all wind turbines. However, it can be derived using the more widely available coefficient of performance. The relation was found to be as follows:

$$C_T = \frac{C_P}{1-a} \tag{4.22}$$

However, if a is unknown, it could be found using equation 4.23.

$$C_P = \left(1 - \left(\frac{1}{2}\left(1 - \sqrt{1 - C_T}\right)\right)\right) \times C_T \tag{4.23}$$

As for the inlet and outlet temperature of the turbine, they can be estimated by assuming that the air acts as an ideal gas. The temperature at the entry and exit of the turbine is calculated using the following relation:

$$T_{1,2} = \frac{P_{1,2}}{\rho \times R_{air}} \tag{4.24}$$

where P is the pressure at the inlet and outlet of the wind turbine and R is the ideal gas constant.

The pressure at the inlet and outlet of the wind turbine can be estimated using the following relation:

$$P_{1,2} = P_{atm} + (\rho V) \tag{4.25}$$

As for the PV system, First Solar thin-film was chosen. The power output of the PV was simulated in SAM simulator, based on the average hourly solar irradiance conditions in a year in Toronto, Ontario. SAM simulates each PV cell based on its performance graphs and efficiency variations along with temperature and irradiance. This information was then used as the operating parameters of the solar field using Eq.4.26-4.29.

The power produced from the PV cells are modeled as follows:

$$\mathrm{P_{PV}} = \eta_{\mathrm{PV}} \times \mathrm{I} \times \mathrm{A_{PV}} \tag{4.26}$$

where η_{PV} is the efficiency of the PV cell and I is the solar irradiance in $(\frac{W}{m^2})$ and $\mathrm{A_{PV}}$ is the area of the PV cell in (m^2) . The area of the solar system was chosen to produce 3 MW of power at a solar irradiance of 1,000 W/m^2. The area of the solar field equates to 17,650 m^2, respectively.

Here, η_{PV} is the electrical efficiency of the PV cell, I is the solar irradiance received by the PV/T unit, and $\mathrm{A_{PV}}$ is the area of the PV cells. The PV energy and exergy efficiency can be calculated as follows:

$$\eta_{\mathrm{PV}} = \frac{\mathrm{P_{PV}}}{\mathrm{I_{solar}} \times \mathrm{A_{PV}}} \tag{4.27}$$

$$\psi_{PV} = \frac{P_{PV}}{(1 - \frac{T_0}{T_{Sun}})(I_{solar}(A_{PV}))} \tag{4.28}$$

The following section represents the general balance equations.

The sum of all mass flow rate entering the system is represented on the left and the right the sum mass rate exiting the system is represented. The mass is conserved throughout the process.

$$\sum \dot{m}_{in} = \sum \dot{m}_{out} \tag{4.29}$$

The left side of the energy balance equation represents the thermal energy rate entering the system, the work rate entering the control volume, and the energy associated with the mass entering the system. The right side represents the exergy associated with the mass exiting the control volume, the thermal energy rejected by the system, the work rate exiting the system.

$$\dot{Q}_{in} + \dot{W}_{in} + \sum \dot{m}_{in}\left(h + \frac{v^2}{2} + gz\right)_{in} = \dot{Q}_{out} + \dot{W}_{out} + \sum \dot{m}_{out}\left(h + \frac{v^2}{2} + gz\right)_{out} \tag{4.30}$$

The left side of the exergy balance equation represents the thermal energy rate entering the system, the work rate entering the control volume, and the exergy associated with the mass entering the system. The right side represents the exergy associated with the mass exiting the control volume, the thermal energy rejected by the system, the work rate exiting the system, and the exergy destruction rate.

$$\sum \dot{E}x_{\dot{Q}_{in}} + \sum \dot{E}x_{\dot{W}_{in}} + \sum \dot{E}x_{flow_{in}} = \sum \dot{E}x_{\dot{Q}_{out}} + \sum \dot{E}x_{\dot{W}_{out}} + \sum \dot{E}x_{flow_{out}} + \dot{E}x_d \tag{4.31}$$

The analysis includes the overall exergy destruction rates, exergy, and energy efficiencies for the system. The thermodynamic analysis for the overall systems analysis was taken at steady-state conditions. The wind turbine analytical assumptions included: the pressure drops through the wind turbine are neglected, the temperature of the air at that height was taken at 15℃, the rotor of the turbines is 77m in diameter, and All heat loss were neglected. The operational PV assumptions were taken as follows: The PV cell temperature was found

SAM simulator to be 46℃, the ambient temperature was taken at 25℃, and the electrical efficiency of the PV cell is 17%.

The energy and exergy analysis of the overall system considers the net power produced from the Rankine cycle and the ammonia produced. Table 4.7 presents the balance equations of the integrated system. The overall energy and exergy efficiencies of the proposed system are written as follows:

$$\eta_{\text{overall}} = \frac{\text{P}_{\text{wind}} + \text{P}_{\text{PV}} + \dot{\text{m}}_{\text{NH}_3} \times \text{LHV}_{NH_3} + \dot{\text{W}}_{Rankine}}{\text{P}_{\text{kinetic}} + \text{I}_{\text{solar}} \times \text{A}_{\text{PV}}} \tag{4.32}$$

$$\psi_{\text{overall}} = \frac{\text{P}_{\text{wind}} + \text{P}_{\text{PV}} + \dot{\text{m}}_{\text{NH}_3} \times ex_{\text{NH}_3} + \dot{\text{W}}_{Rankine}}{\dot{\text{E}}\text{x}_{\text{in}_{\text{wind}}} + \left(1 - \frac{\text{T}_0}{\text{T}_{\text{Sun}}}\right) \text{I}_{\text{solar}} * \text{A}_{\text{PV}}} \tag{4.33}$$

4.1.3 System 3

Some assumptions are made for the analyses of the system components as follows:

- The methanol production plant operates at steady-state conditions
- The methanol production plant start-up period is not considered
- The kinetic and gravitational potential energies changes are neglected throughout the plant
- All gases in the system are treated as real gases (exception for this assumption is for the gases in the chemical exergy equation, they are treated as ideal gases)
- The electrical generator thermal efficiency is $\eta_{\text{gen}} = 95\%$

The integrated balance equations are presented in Table 4.9. The property sources used in Aspen Plus simulation are given as follows:

For H_2O:

- The 1984 NBS/NRC: Steam table correlations for thermodynamic properties are used for H_2O.
- The International Association for Properties of Steam (IAPS) correlations for transport properties for H_2O (Aspen Plus property method: STEAMNBS for the

temperature range of 273.15 K to 2000 K at a maximum pressure of over 10,000 bar) are used.

Note that the carbon-capturing technologies will be discussed in the following section. According to Willhauer et al.[28] the energy required to recover carbon dioxide from the ocean water is based on the energy required to electrolyze the desalinated water. This comes as the carbon dioxide is a by-product of the ECEM electrolysis reaction. The electrical energy requirement per liter of carbon dioxide was found to be 49 kWh/m^3-H_2. The general relation for the work required to produce the hydrogen was found to be as follows:

$$\dot{W}_{ECEM} = w_{ECEM} \times \dot{V}_{H_2}(T_O, P_O) \tag{4.34}$$

where the w_{ECEM} is the specific work relative to the volume of hydrogen produced and $\dot{V}_{H_2}$ is the volumetric flow rate of hydrogen produced at a certain temperature and pressure.

The required mass flow rate of carbon dioxide being extracted can be found using the following relation:

$$\dot{m}_{CO_2} = \dot{V}_{SW}\left(\eta_{CO_2} \times 0.1\right) \tag{4.35}$$

where η_{CO_2} is the efficiency of the carbon dioxide which is 92% and the carbon dioxide content in the seawater was assumed to be 0.1kg-CO_2/m^3.

The following section represents the general balance equations. The sum of all mass flow rate entering the system is represented on the left and the right the sum mass rate exiting the system is represented. The mass is conserved throughout the process.

$$\sum \dot{m}_{in} = \sum \dot{m}_{out} \tag{4.36}$$

Here, $\dot{m}$ denotes the mass flow rate, where the subscripts in and out refer to the mass entering and leaving the boundary of the open system. The left side of the energy balance equation represents the thermal energy rate entering the system, the work rate entering the control volume, and the energy associated with the mass entering the system. The right side represents the exergy associated with the mass exiting the control volume, the thermal energy rejected by the system, the work rate exiting the system.

$$\dot{Q}_{in} + \dot{W}_{in} + \sum \dot{m}_{in}\left(h + \frac{v^2}{2} + gz\right)_{in} = \dot{Q}_{out} + \dot{W}_{out} + \sum \dot{m}_{out}\left(h + \frac{v^2}{2} + gz\right)_{out} \quad (4.37)$$

Here, $\dot{Q}$ denotes the heat rate, $\dot{W}$ denotes the power, h denotes specific enthalpy, V denotes velocity, g denotes the gravity acceleration and z denotes the elevation. Finally, equation 4.38 displays the overall energy efficiency equation of the proposed system.

$$\eta_{Ov} = \frac{\dot{m} \times LHV_{CH_3OH} + \sum \dot{W}_{turbine} - \sum \dot{W}_{Aux}}{\dot{E}_{in}} \quad (4.38)$$

Here, $\dot{E}_{in}$ is defined as the enthalpy difference between the inlet and outlet of the warm sea water after it enters the first heat exchanger and leaves after the second heat exchanger. As for $\sum \dot{W}_{turbine}$ it represents the work rate output of the turbine and $\sum \dot{W}_{Aux}$ represents of the summation of all the auxiliary components such as pumps that consume power. $\dot{E}_{in}$ is shown in eq.4.39.

$$\dot{E}_{in} = \dot{m}(h_{inlet} - h_{outlet}) = \dot{m} \times C_p \times \Delta T \quad (4.39)$$

4.1.4 System 4

Some assumptions are made for the analyses of the system components as follows:

- The methanol production plant operates at steady state conditions
- The methanol production plant start up period is not considered
- The kinetic and gravitational potential energies changes are neglected throughout the plant
- All gases in the system are treated as real gases (exception for this assumption is for the gases in the chemical exergy equation, they are treated as ideal gases)
- The electrical generator thermal efficiency is $\eta_{gen} = 95\%$

The integrated balance equations are presented in Table 4.10. The property sources used in Aspen Plus simulation are given as follows:

For H_2O:

- The 1984 NBS/NRC: Steam table correlations for thermodynamic properties are used for H_2O.
- The International Association for Properties of Steam (IAPS) correlations for transport properties for H_2O (Aspen Plus property method: STEAMNBS for the temperature range of 273.15 K to 2000 K at a maximum pressure of over 10,000 bar) are used

4.1.4.1 Radiation distribution model

The radiation distribution model simulated domain is shown in Figure 4.2 as well as the selected boundary conditions used to setup the simulation, which is built and simulated in COMSOL Multiphysics as mentioned earlier. The shown set boundary conditions in Figure 4.2 are for the case where the bifacial solar panel is floating on a water surface, where the water is deep enough so that the water feature is considered opaque rather than transparent.

The Geometric Optics module in COMSOL is used to simulate the performance of the bifacial model through simulating the solar rays and their interaction with the developed bifacial PV panel. The material properties, including the refractive index of the water, ice, and the PV panel are presented in Table 4.2. The distance between the earth and the sun is far enough to assume the solar rays to be parallel. Simulating the solar incident rays is done through introducing the rays through a plane square surface on a distance of 10 m from the sea surface, as shown in Figure 4.2. The set boundary conditions are presented in Figure 4.1, where the solar rays are introduced through an illuminated surface. The density of rays is selected as the initial position of the illuminated surface with a total number of rays passing through the window is 6000 rays. The 6000 rays are selected based on the ray independence study, which is presented later in the results and discussion section of the system.

The ray property specification is based on a vacuum wavelength of 660 nm. The water surface boundary condition has the properties of diffusion scattering wall with an absorption coefficient (refer to Table 4.1 for all the material properties). The upper and lower surfaces of the PV panels are selected to be a ray freeze wall equipped with deposited ray power, where each surface has it is own boundary wall conditions.

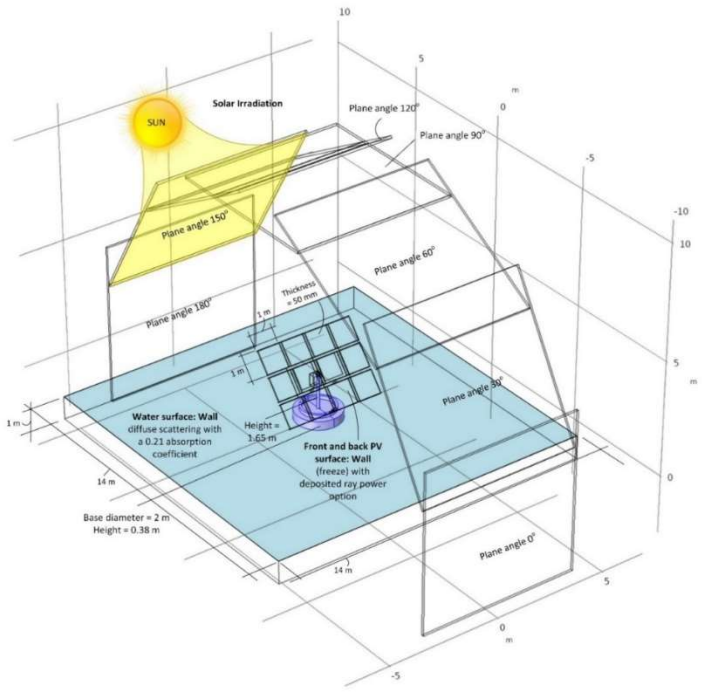

Figure 4.2: The radiation distribution model selected boundary conditions.

Table 4.1: Refractive index of the simulation materials and their absorption coefficients

Material	Refractive index, real part	Refractive index, imaginary part	Absorption coefficient	Ref.
Water	1.3310	1.876×10^{-8}	0.210	[103]
Silicon	3.8365	0.015380		[104]
Air	1	1	0	[64]

The refractive index are at vacuum wave length of 660 nm

4.1.4.2 Wave front Ray Tracing Method Governing Equations

The ray tracing method was used in the simulated model, which couples the firs order differential equations for the instantaneous ray's positions q and wave vector k. The coupled equations are similar the Hamiltonian formulation in classical mechanics. Here, the angular frequency is represented by ω.

$$\frac{\delta q}{\delta t} = \frac{\delta \omega(k)}{\delta k} \tag{4.40}$$

$$\frac{\delta k}{\delta t} = \frac{\delta \omega(k)}{\delta q} \tag{4.41}$$

As for the incident power ratio, it considers the total irradiance power received by the backward facing PV panel relative to the front facing PV panel. This is performed by integrating the solar irradiance received by both the working areas of the front and back

PV faces of the bifacial module. The relations of incident power ration can be represented as presented in equation 4.41.

$$Incident\ Power\ Ratio = \frac{\int I_{front}\ dA}{\int I_{back}\ dA} \tag{4.42}$$

Here, I_{front} denotes the solar irradiance received by the front surface of the bifacial PV solar panel, and I_{back} denotes the solar irradiance received by the back surface of the bifacial panel.

The incident power received can then be used to calculate the power produced by the bifacial module. This is due to the solar irradiance being dependent on the working area of the bifacial PV module. A conversion efficiency of 17% was chosen in this study based on the PV operating parameters of Hasan and Dincer [19]. The power produced from the PV cells are modeled as follows:

$$\mathrm{P_{PV}} = \eta_{\mathrm{PV}} \times \mathrm{I_{solar}} \times \mathrm{A_{PV}} \tag{4.43}$$

where η_{PV} is the efficiency of the PV cell obtained, $\mathrm{A_{PV}}$ is the area of the PV cell in (m^2) and I is the solar irradiance $(\frac{W}{m^2})$ received by the module. The energy efficiency of the bifacial module can be defined based on the power produced divided by the total irradiance power received by the working surfaces of the module.

$$\eta_{\mathrm{PV}} = \frac{\mathrm{P_{PV}}}{\mathrm{I_{solar}} \times \mathrm{A_{PV}}} \tag{4.44}$$

The refractive index of the simulation materials and their absorption coefficients are summaries and presented in Table 4.2.

Table 4.2: Refractive index of the simulation materials and their absorption coefficients

Material	Refractive index, real part	Refractive index, imaginary part	Absorption coefficient	Ref.
Water	1.3310	1.876×10^{-8}	0.210	[103]
Silicon	3.8365	0.015380	*	("Silicon (Si) - University of Reading,")
Air	1	1	0	[64]

* No value is selected since the photo-electrochemical model considers the absorption efficiency of the PV panel surface.

4.1.5 Fluid Flow and Heat Transfer Models

In this section, the fluid and heat transfer model used to simulate how the proposed system maintains the surface of the solar bifacial module temperature to operate within the optimum operation range will discussed.

The system performance is simulated by using COMSOL Multiphysics simulation software. Figure 4.3 shows the system boundary conditions. The first is being the inlet condition for the flow into the tubes in the cold plate sandwiched between the two bifacial panels as shown in Figure 4.3. The inlet is set as a mass flow rate. The outlet is set to as an outlet pressure boundary condition. Aluminum is the material of selection for the cold plate material. Solar radiation is imported from the ray model where it considers the variation of the solar direction. The heat generated in the panel is the result of the integrated model of the ray and the electrochemical solar based efficiency model. One should note that the number of pipes seen in figure 4.3 will vary in the optimization study. It was found that ideally a single pipe should be used to increase the concertation factor.

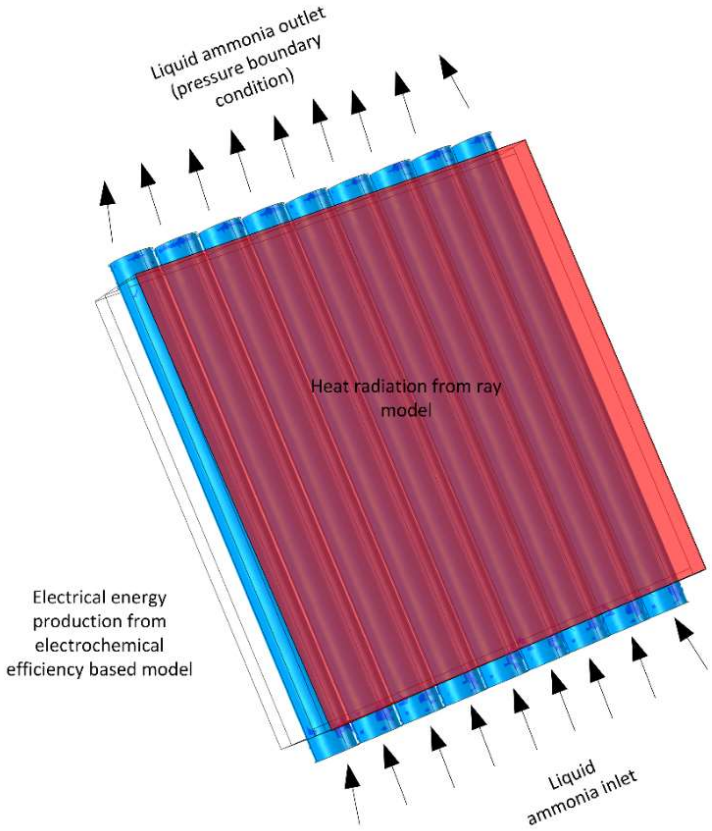

Figure 4.3: Fluid and heat boundary conditions

4.2 Optimization study

Ocean Thermal Energy conversion (OTEC) is a method of reliable renewable energy production. The process makes use of the temperature differential that exists from the warm surface water and the cold deep ocean water. In many tropical or near equator land masses near an ocean OTEC plants can operate 24/7, unlike other forms of renewable energy such as solar and wind. OTEC offers a sustainable energy solution that could be scaled large levels of energy. Currently, OTEC is being implemented in a commercial level in tropical island communities that currently rely on fossil fuel-based energy production. In such communities, ' land is a commodity that needs to persevere for other uses such agriculture, tourism, or housing. OTEC, on a large scale can be deployed offshore and will not compete for land. Furthermore, according to MAKAI engineering group 1 offshore commercial plant, it prevents bringing roughly 1.3 million barrels of oil each year, which prevents 0.5 million tons per year of CO_2 emissions [27]. The current levelized production cost is 0.20$/kWh for OTEC plants, compared to wind and solar which come at a cost of 0.04-0.06$/kWh (wind) and 0.10$/kWh (solar)[22]. Depending on the country and its accessibility to fossil fuels, the cost of power production from fossil fuel ranges from 0.05-0.17$/kWh [23]. In many cases fossil fuels are cheaper than renewable-based power production at face value. Of course, one should account for the capital cost needed for a normalised power production cost, where solar, wind and natural gas come at a cost of 2,000-3,700$/kW(commercial-residential),1200-1700$/kW, and 1,000$/kW[24]. OTEC comes at a cost of 4,000$/kW based on the price of 100MW plant [25,26], which is relatively more expensive from the other alternatives. However, one should account for the reliability of the other renewable sources of energy as OTEC can run indefinitely 24/7. The baseload power that OTEC offers can be complimentary to the intermittent renewable energy sources, as they can be designed to be dispatchable, allowing it to ramp up and down power production based on the production rates. Furthermore, the potential by-products of OTEC are of interest in the agricultural, aquaculture, HVAC and freshwater production sectors[27].

An OTEC plant must be optimized based on the objective and the revenue streams targeted which includes various scenarios, as OTEC plants could have several by-products. However, in this thesis the main purpose of the optimization is power production

efficiency. In this section some detailed studies related to OTEC optimization will be discussed. Sinama et al.[105] presented a thermodynamics analysis of a closed OTEC Rankine cycle, using the concept of equivalent Gibbs system. The equivalent Gibbs system links the mass, energy, and entropy by using the Gibbs equations. The entropy production can be represented using fluxes and related forces. According to the authors, this an ideal method to find which component needs to be optimized. The authors then used the generic optimization program to optimize the parameters of the 10MW OTEC plant.

There are four different proposed systems, where part of these are developed to produce clean ammonia from various renewable energies while the others are proposed to produce carbon-neutral methanol. Due to the various operating principles each system has its own objective function and they are listed as follows:

In Table 4.3 the objectives of the optimization for all the proposed systems are presented as well as the main constrains of each system. Note that more details regarding each system is presented and discussed further in the coming sections and subsections Table 4.4.

4.2.1 Optimization of System 1

In this system an integrated closed-cycle OTEC plant is proposed. The OTEC plant operates with a single-stage ammonia Rankine cycle. The OTEC cycle as mentioned previously, uses the warm surface ocean water to superheat the ammonia in the evaporator of the cycle. The cold deep ocean water is supplied to the cycle to condense the ammonia in the cycle. The cycle operates on the given temperature differences. The baseline Rankine cycle produces a net of 10 MW and uses ammonia as a working fluid for the cycle. The author also discusses that there are other potential working fluids that include refrigerants. However, there are currently working plants and heat exchangers that allow the use of ammonia as a working fluid. As for the operation parameters, they were obtained from the MAKAI OTEC powerplant operating in Hawaii [83,84]. After the OTEC cycle produces electricity, 50 % of the power is used to produce hydrogen uing a Proton Exchange Membrane electrolsyser. The hydrogen is then fed to the ammonia synthesis system. Ammonia is the selected method of energy storage, as it is a carbon-free fuel and requires less energy in terms of compression relative to hydrogen.

Table 4.3:The upper and lower bounds of the variables of system 1 along with constraints and the objectives of the optimization study.

System	Objectives	Constraints
System 1 and 2	- Energy efficiency - Exergy efficiency - Pumping power consumption - ammonia production rate - Cooling output -Cost of Ammonia	- Warm water temperature (21-26 ^{o}C) - Cold water temperature (4.5 ^{o}C) - Warm water flow rate (32,000-55,000 kg/s) - Cold water flow rate (19,000-35,000 kg/s)

4.2.2 Optimization of System 2

The proposed bi-generation system consists of a wind turbine, PV units, and an electrolyzer/fuel cell. The proposed system is designed based on the hourly demands of Ontario, Canada for over 12 months. The system consists of two GE 1.5xle wind turbines. The total wind power potential is 3 MW, as each of the GE 1.5xle produces a maximum of 1.5MW at wind speeds of 11m/s [21]. Furthermore, the system also integrates solar PV panels. The model chosen for the PV cells was a thin film first solar 6420 cell. The total potential for the integrated, installed PV modules is 3 MW [22]. The power generation units (wind turbines and solar PV) are designed to meet most of the demands and have excess during the off-peak hours. During the off-peak hours, the system is designed to provide power to water PEM electrolyzers. The electrolyzer performs electrolysis on water to produce hydrogen.

The hydrogen is then used as feedstock for a multistage ammonia synthesis plant as suggested. The CASU feeds the ammonia synthesis system nitrogen. Ammonia is the selected method of storage for the hydrogen produced as it is a carbon-free fuel and has a higher lower heating value than hydrogen by about 30% on a molar basis. The produced ammonia is stored in a compressed tank and when peak power cannot be met by the wind and solar plant the ammonia is decomposed into nitrogen and hydrogen. The hydrogen is then used to power a PEM fuel cell to meet the power demands of the community.

Table 4.4:The upper and lower bounds of the variables of systems 2 an along with constraints and the objectives of the optimization study.

System	Objectives	Constraints
System 1 and 2	- Exergy efficiency - Pumping power consumption - ammonia production rate - Cooling output -Cost of Ammonia	- Solar irradiance (200-1,200 W/m^2) - Wind speed (0-25 m/s)

4.2.3 Optimization of System 3

The suggested system in this thesis is powered by an Ocean Thermal Energy Conversion (OTEC) plant that is combined with an ECEM reactor, a district cooling system, and a multistage methanol production system. The main feedstock of this system is the carbon dioxide found in the seawater and hydrogen produced from the electrolyzed seawater. The E-CEM will produce both the hydrogen and carbon dioxide required to feed the systems. The system is a tri-generation system as it produces the following commodities: power, methanol, and cooling. As for the district cooling system, the rejected ocean cold water that was used to cool the condensers of the 2-stage ammonia Rankine cycle was used to cool 6000 average Florida homes, as such a system will be possible in such a climate. The cooling load of the system was calculated to be 69 GW and is fixed in all scenarios and cases during the study, at a temperature of 13°C, respectively.

Table 4.5:The upper and lower bounds of the variables of systems 3 and 4 along with constraints and the objectives of the optimization study.

System	Objectives	Constraints
System 3 and 4	- Exergy efficiency - Pumping power consumption - Methanol production rate - Cooling output - PV power to area ratio - Cost of Methanol	- Warm water temperature (21-26 ^{o}C) - Cold water temperature (4.5 ^{o}C) - Warm water flow rate (32,000-55,000 kg/s) - Cold water flow rate (19,000-35,000 kg/s) - Solar irradiance (200-1,200 W/m^2) - Wind speed (0-25 m/s)

4.2.4 OTEC Optimization Methodology

The OTEC was optimized using previously simulated systems that included single and double stage configurations. In this subsection, a triple-stage OTEC plant was optimized

on Aspen Plus. The Cycle was optimized using various warm and cold seawater flow rates. Furthermore, the cycle pressure was varied as well, to find the optimum pressure. It should be noted that an initial optimization study was performed to optimize the lowest pressure in the cycle. It was found any pressure lower than 6.5 bar yielded very low efficiencies. This mainly due to the low pressure changing the saturation temperature of the ammonia, which requires a larger cold-water flow rate in the condenser. The sensitivity analysis module on Aspen Plus was used to optimize the system using the parameters seen in Table 4.9.

Table 4.6. The upper and lower bounds of the variables of the triple stage OTEC cycle.

Variable	Lower limit	Upper limit	Units
Warm temperature	21	26	ºC
Cold water temperature	4.5	-	ºC
Warm water flow rate	32,000	55,000	kg/s
Cold water flow rate	19,000	35,000	kg/s
Ammonia Flow Rate	590	620	kg/s
Cycle Max. Pressure	8.5	9.25	bar

Figures 4.4 and 4.5 display the sensitivity analysis result for the energy efficiency of the cycle while varying the maximum pressure of the cycle from 8.5 to 9.25 bar. The working fluid flow rate was also varied between 590 and 620 kg/s. The energy and exergy efficiency of the cycle peaked at 2.02% and 28.1%. It should be noted that the warm and cold-water flow rate were varied as well. However, it was found that the maximum efficiency was achieved at a flow rate of 50,000 kg/s and 27,000 kg/s for the warm and cold sweater flow rates. The maximum energy efficiency occurred at a working fluid pressure of 9.25 bar. Figure 4.6-4.8 displays two of the optimization steps for a three-stage OTEC cycle. The cycle steps represent the stages of the cycle, that the working fluid is undergoing. At a pressure of 9.25 bar regardless of the flow rate, the cycle was able to extract larger amounts of energy (step 4). The higher energy production, after the superheated fluid passes the first turbine in step 4, corresponding to a lower temperature at the exit allowing for further utilization of the warm seawater pumped.

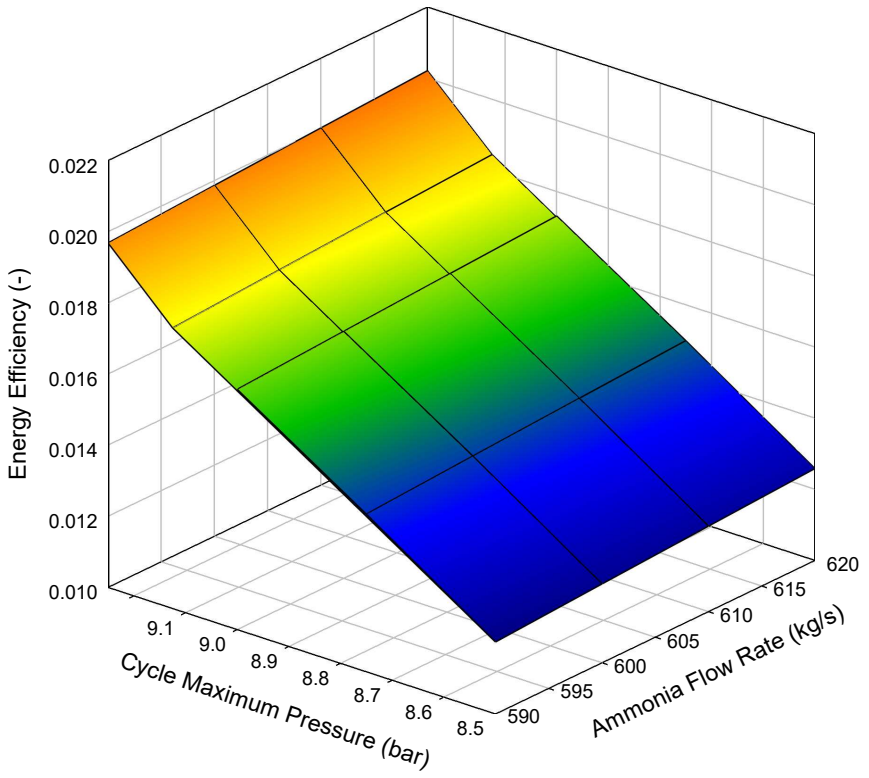

Figure 4.4: Energy efficiency of the triple stage OTEC with varying maximum cycle pressure and ammonia flow rate

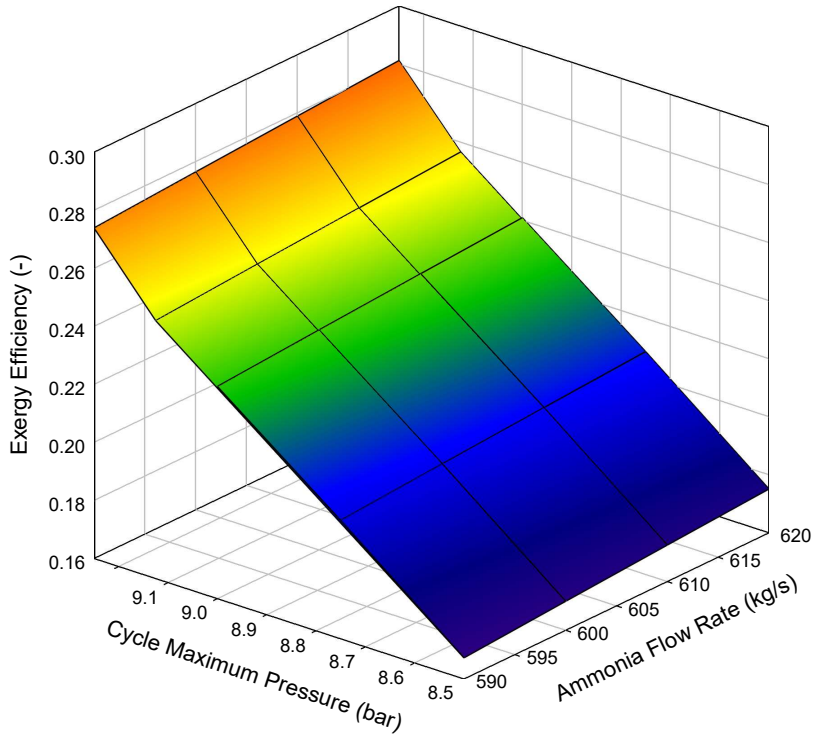

Figure 4.5: Exergy efficiency of the triple stage OTEC with varying maximum cycle pressure and ammonia flow rate

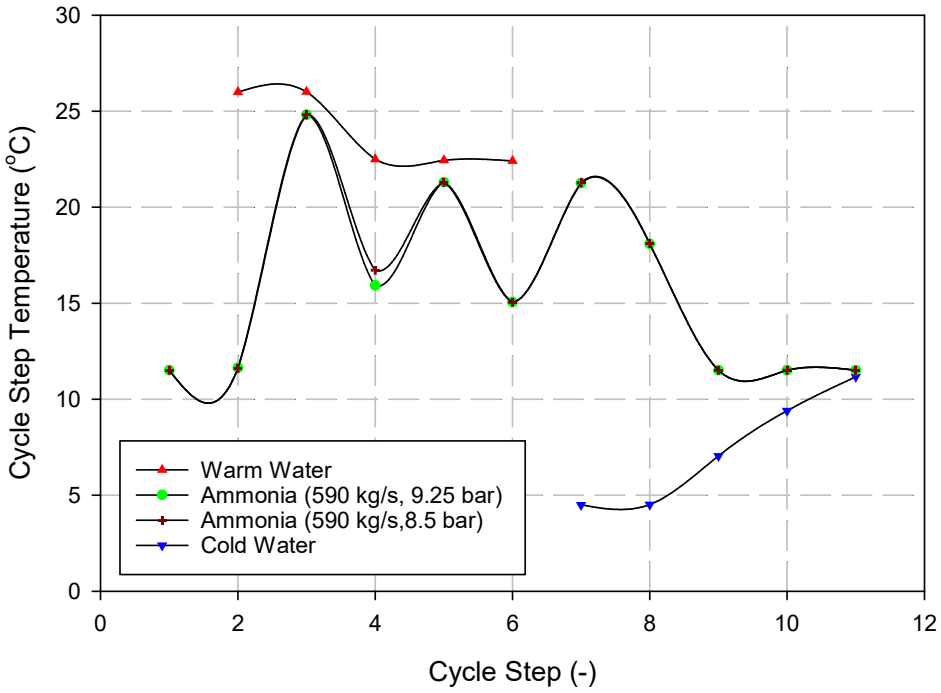

Figure 4.6: Cycle step temperature in independent steps in the cycle

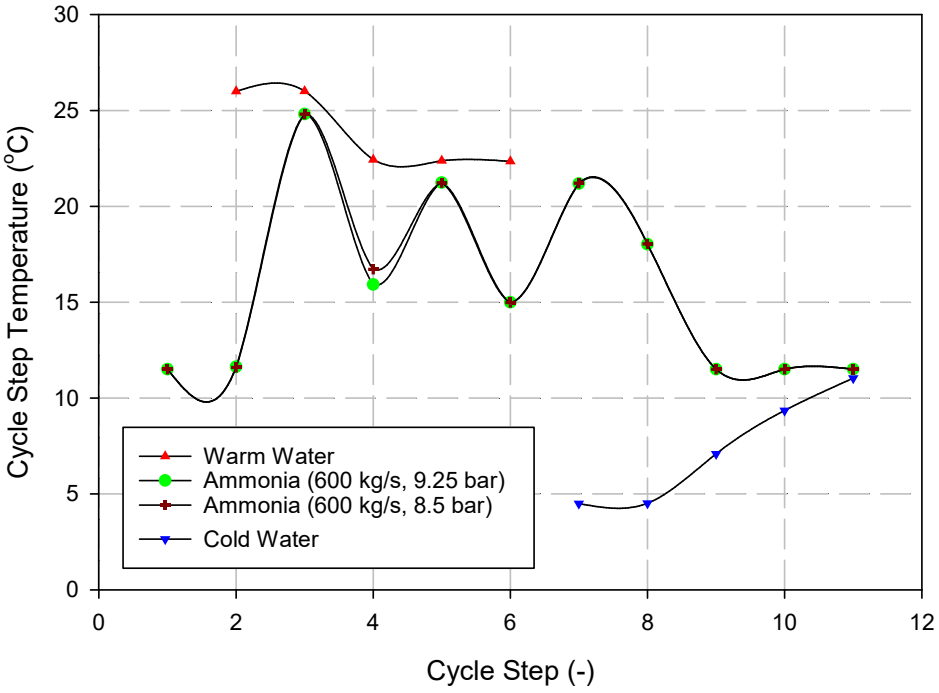

Figure 4.7: Cycle step temperature in independent steps in the cycle

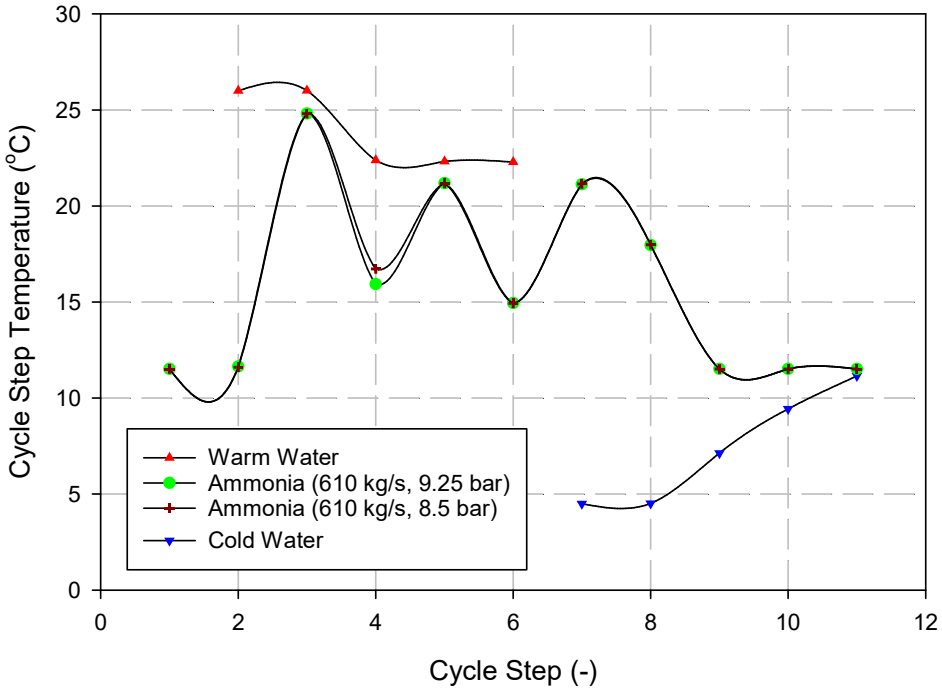

Figure 4.8: Cycle step temperature in independent steps in the cycle

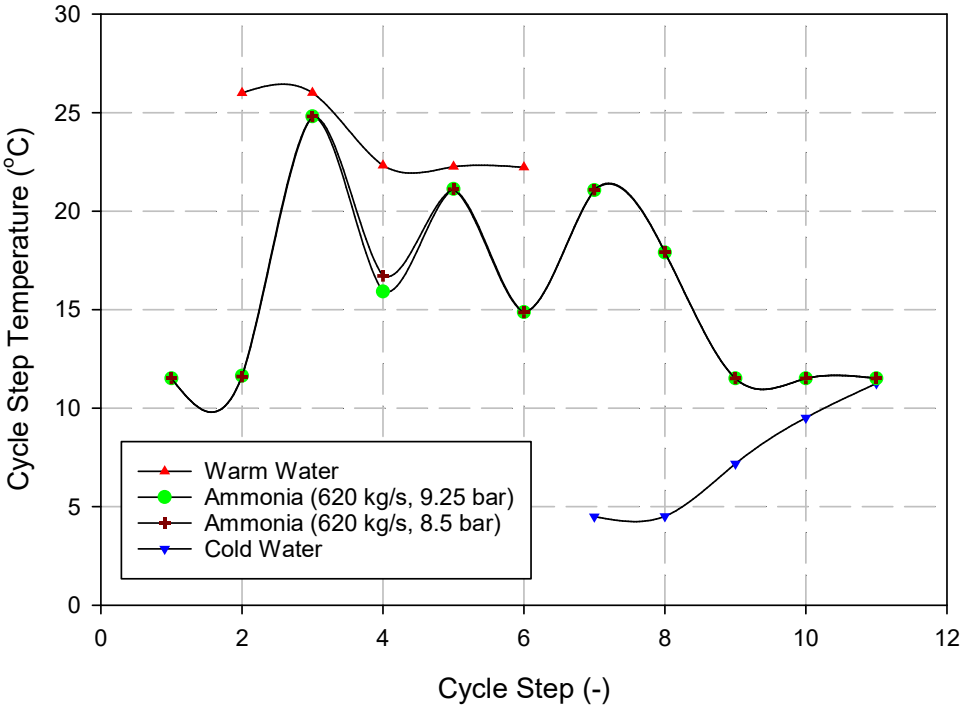

Figure 4.9: Cycle step temperature in independent steps in the cycle

Table 4.7: System 1 balance equations

Component	Balance Equations
Pump 1	MBE: $\dot{m}_1 = \dot{m}_2$ EBE: $\dot{m}_1 h_1 + \dot{W}_{pump} = \dot{m}_2 h_2 + \dot{W}_{loss}$ ENBE: $\dot{m}_1 s_1 + \dot{s}_{gen} = \dot{m}_2 s_2$ EBE: $\dot{m}_1 ex_1 + \dot{W}_{pump} = \dot{m}_2 ex_2 + \dot{W}_{loss} + E\dot{x}^Q + E\dot{x}^D$
Pump 2	MBE: $\dot{m}_4 = \dot{m}_5$ EBE: $\dot{m}_4 h_4 + \dot{W}_{pump} = \dot{m}_5 h_5$ ENBE: $\dot{m}_4 s_4 + \dot{s}_{gen} = \dot{m}_5 s_5$ EBE: $\dot{m}_4 ex_4 + \dot{W}_{pump} = \dot{m}_5 ex_5 + E\dot{x}^D$
Pump 3	MBE: $\dot{m}_{11} = \dot{m}_8$ EBE: $\dot{m}_{11} h_{11} + \dot{W}_{pump} = \dot{m}_8 h_8$ ENBE: $\dot{m}_{11} s_{11} + \dot{s}_{gen} = \dot{m}_8 s_8$ EBE: $\dot{m}_{11} ex_{11} + \dot{W}_{pump} = \dot{m}_8 ex_8 + E\dot{x}^D$
Heat Exchanger 1	MBE: $\dot{m}_2 = \dot{m}_3, \dot{m}_8 = \dot{m}_9$ EBE: $\dot{m}_2 h_2 + \dot{m}_8 h_8 = \dot{m}_3 h_3 + \dot{m}_9 h_9 + \dot{Q}_{loss}$ SBE: $\dot{m}_2 s_2 + \dot{m}_8 s_8 + \dot{s}_{gen} = \dot{m}_3 s_3 + \dot{m}_9 s_9 + \dot{Q}_{loss}/T_s$ EBE:$\dot{m}_2 ex_2 + \dot{m}_8 ex_8 = \dot{m}_3 ex_3 + \dot{m}_9 ex_9 + E\dot{x}^Q + E\dot{x}^D$
Heat Exchanger 2	MBE: $\dot{m}_5 = \dot{m}_6, \dot{m}_{10} = \dot{m}_{11}$ EBE: $\dot{m}_5 h_5 + \dot{m}_{10} h_{10} = \dot{m}_6 h_6 + \dot{m}_{11} h_{11} + \dot{Q}_{loss}$ SBE: $\dot{m}_5 h_5 + \dot{m}_{10} h_{10} + \dot{s}_{gen} = \dot{m}_6 s_6 + \dot{m}_{11} s_{11} + \dot{Q}_{loss}/T_s$ EBE:$\dot{m}_5 ex_5 + \dot{m}_{10} ex_{10} = \dot{m}_6 ex_6 + \dot{m}_{11} ex_{11} + E\dot{x}^Q + E\dot{x}^D$
Heat Exchanger 3	MBE: $\dot{m}_6 = \dot{m}_7$ EBE: $\dot{m}_6 h_6 = \dot{m}_7 h_7 + \dot{Q}_{Load} + \dot{Q}_{loss}$ SBE: $\dot{m}_6 s_6 + \dot{s}_{gen} = \dot{m}_7 s_7 + \dot{Q}_{Load}/T_s + \dot{Q}_{loss}/T_s$ EBE:$\dot{m}_6 ex_6 = \dot{m}_7 ex_7 + Ex^{\dot{Q}_{load}} + E\dot{x}^Q + E\dot{x}^D$
Turbine	MBE: $\dot{m}_9 = \dot{m}_{10}$ EBE: $\dot{m}_9 h_9 = \dot{m}_{10} h_{10} + \dot{W}_{turbine} + \dot{Q}_{Loss}$ ENBE: $\dot{m}_9 s_9 + \dot{s}_{gen} = \dot{m}_{10} s_{10} + \dot{Q}_{loss}/T_s$ EBE: $\dot{m}_9 ex_9 = \dot{m}_{10} ex_{10} + E\dot{x}^Q + E\dot{x}^D + \dot{W}_{turbine}$
PEM electrolyser	MBE: $\dot{m}_{water} = \dot{m}_{14}$ EBE: $\dot{m}_{water} h_{water} + \sum \dot{W}_{in} = \dot{m}_{14} h_{14} + \dot{W}_{loss}$ ENBE: $\dot{m}_{water} s_{water} + \dot{s}_{gen} = \dot{m}_{14} s_{14}$ EBE: $\dot{m}_{water} ex_{water} + \sum \dot{W}_{in} = \dot{m}_{14} ex_{14} + \dot{W}_{loss} + E\dot{x}^D$
Reactor series	MBE: $\dot{m}_{14} + \dot{m}_{13} = \dot{m}_{21}$ EBE: $\dot{m}_{14} h_{14} + \dot{m}_{13} h_{13} = \dot{m}_{21} h_{21} + \dot{Q}_{out}$ ENBE: $\dot{m}_{14} s_{14} + \dot{m}_{13} s_{13} + \dot{s}_{gen} = \dot{m}_{21} s_{21} + \dot{Q}_{out}/T_s$ EBE: $\dot{m}_{14} ex_{14} + \dot{m}_{13} ex_{13} = \dot{m}_{21} ex_{21} + E\dot{x}^Q + E\dot{x}^D$
CASU	MBE: $\dot{m}_{Air} = \dot{m}_{13}$ EBE: $\dot{m}_{Air} h_{Air} = \dot{m}_{13} h_{13} + \dot{Q}_{out}$ ENBE: $\dot{m}_{Air} s_{Air} + \dot{s}_{gen} = \dot{m}_{13} s_{13} + \dot{Q}_{out}/T_s$ EBE: $\dot{m}_{Air} ex_{Air} = \dot{m}_{13} ex_{13} + E\dot{x}^Q + E\dot{x}^D$
Turbine	MBE: $\dot{m}_{19} = \dot{m}_{20}$ EBE: $\dot{m}_{19} h_{19} = \dot{m}_{20} h_{20} + \dot{W}_{turbine} + \dot{Q}_{Loss}$ ENBE: $\dot{m}_{19} s_{19} + \dot{s}_{gen} = \dot{m}_{20} s_{20} + \dot{Q}_{loss}/T_s$ EBE: $\dot{m}_{19} ex_{19} = \dot{m}_{20} ex_{20} + E\dot{x}^Q + E\dot{x}^D + \dot{W}_{turbine}$
Expander	MBE: $\dot{m}_{12} = \dot{m}_{13}$ EBE: $\dot{m}_{12} h_{12} = \dot{m}_{13} h_{13} + \dot{W}_{Expander} + \dot{Q}_{Loss}$ ENBE: $\dot{m}_{12} s_{12} + \dot{s}_{gen} = \dot{m}_{13} s_{13} + \dot{Q}_{loss}/T_s$ EBE: $\dot{m}_{12} ex_{12} = \dot{m}_{13} ex_{13} + E\dot{x}^Q + E\dot{x}^D + \dot{W}_{Expander}$

Table 4.8: System 2 balance equations

Component	Balance Equations
Pump	MBE: $\dot{m}_{20} = \dot{m}_7$ EBE: $\dot{m}_{20}h_{20} + \dot{W}_{pump} = \dot{m}_7 h_7 + \dot{W}_{loss}$ ENBE: $\dot{m}_{20}s_{20} + \dot{s}_{gen} = \dot{m}_7 s_7$ EBE: $\dot{m}_{20}ex_{20} + \dot{W}_{pump} = \dot{m}_7 ex_7 + \dot{W}_{loss} + E\dot{x}^Q + E\dot{x}^D$
Heat Exchanger 1	MBE: $\dot{m}_8 = \dot{m}_{18}$ EBE: $\dot{m}_8 h_8 + \dot{Q}_{in} = \dot{m}_{18}h_{18} + \dot{Q}_{loss}$ SBE: $\dot{m}_8 s_8 + \dot{s}_{gen} + \dot{Q}_{in}/T_s = \dot{m}_{18}s_{18} + \dot{Q}_{loss}/T_s$ EBE:$\dot{m}_8 ex_8 = \dot{m}_{18}ex_{18} + E\dot{x}^Q + E\dot{x}^D$
Heat Exchanger 2	MBE: $\dot{m}_{21} = \dot{m}_{22}$ EBE: $\dot{m}_{21}h_{21} = \dot{m}_{22}h_{22} + \dot{Q}_{out}$ SBE: $\dot{m}_{21}s_{21} + \dot{s}_{gen} = \dot{m}_{22}s_{22} + \dot{Q}_{out}/T_s$ EBE:$\dot{m}_{21}ex_{21} = \dot{m}_{22}ex_{22} + E\dot{x}^Q + E\dot{x}^D$
Turbine	MBE: $\dot{m}_{18} = \dot{m}_{19}$ EBE: $\dot{m}_{18}h_{18} = \dot{m}_{19}h_{19} + \dot{W}_{turbine} + \dot{Q}_{Loss}$ ENBE: $\dot{m}_{18}s_{18} + \dot{s}_{gen} = \dot{m}_{19}s_{19} + \dot{Q}_{loss}/T_s$ EBE: $\dot{m}_{18}ex_{18} = \dot{m}_{19}ex_{19} + E\dot{x}^Q + E\dot{x}^D + \dot{W}_{turbine}$
PEM electrolyser	MBE: $\dot{m}_1 = \dot{m}_2$ EBE: $\dot{m}_1 h_1 + \sum \dot{W}_{in} = \dot{m}_2 h_2 + \dot{W}_{loss}$ ENBE: $\dot{m}_1 s_1 + \dot{s}_{gen} = \dot{m}_2 s_2$ EBE: $\dot{m}_1 ex_1 + \sum \dot{W}_{in} = \dot{m}_2 ex_2 + \dot{W}_{loss} + E\dot{x}^D$
Reactor series	MBE: $\dot{m}_2 + \dot{m}_3 = \dot{m}_{21}$ EBE: $\dot{m}_2 h_2 + \dot{m}_3 h_3 = \dot{m}_{21}h_{21} + \dot{Q}_{out}$ ENBE: $\dot{m}_2 s_2 + \dot{m}_3 s_3 + \dot{s}_{gen} = \dot{m}_{21}s_{21} + \dot{Q}_{out}/T_s$ EBE: $\dot{m}_2 ex_2 + \dot{m}_3 ex_3 = \dot{m}_{21}ex_{21} + E\dot{x}^Q + E\dot{x}^D$
CASU	MBE: $\dot{m}_{Air} = \dot{m}_3$ EBE: $\dot{m}_{Air}h_{Air} = \dot{m}_3 h_3 + \dot{Q}_{out}$ ENBE: $\dot{m}_{Air}s_{Air} + \dot{s}_{gen} = \dot{m}_{13}s_{13} + \dot{Q}_{out}/T_s$ EBE: $\dot{m}_{Air}ex_{Air} = \dot{m}_{13}ex_{13} + E\dot{x}^Q + E\dot{x}^D$

Table 4.9: System 3 balance equations

Component	Balance equation
Pump 1	MBE: $\dot{m}_1 = \dot{m}_2$ EBE: $\dot{m}_1 h_1 + \dot{W}_{pump} = \dot{m}_2 h_2 + \dot{W}_{loss}$ ENBE: $\dot{m}_1 s_1 + \dot{s}_{gen} = \dot{m}_2 s_2$ EBE: $\dot{m}_1 ex_1 + \dot{W}_{pump} = \dot{m}_2 ex_2 + \dot{W}_{loss} + E\dot{x}^Q + E\dot{x}^D$
Pump 2	MBE: $\dot{m}_{13} = \dot{m}_{14}$ EBE: $\dot{m}_{13} h_{13} + \dot{W}_{pump} = \dot{m}_{14} h_{14}$ ENBE: $\dot{m}_{13} s_{13} + \dot{s}_{gen} = \dot{m}_{14} s_{14}$ EBE: $\dot{m}_{13} ex_{13} + \dot{W}_{pump} = \dot{m}_{14} ex_{14} + E\dot{x}^D$
Pump 3	MBE: $\dot{m}_5 = \dot{m}_6$ EBE: $\dot{m}_5 h_5 + \dot{W}_{pump} = \dot{m}_6 h_6$ ENBE: $\dot{m}_5 s_5 + \dot{s}_{gen} = \dot{m}_6 s_6$ EBE: $\dot{m}_5 ex_5 + \dot{W}_{pump} = \dot{m}_6 ex_6 + E\dot{x}^D$
Pump 4	MBE: $\dot{m}_9 = \dot{m}_{10}$ EBE: $\dot{m}_9 h_9 + \dot{W}_{pump} = \dot{m}_{10} h_{10}$ ENBE: $\dot{m}_9 s_9 + \dot{s}_{gen} = \dot{m}_{10} s_{10}$ EBE: $\dot{m}_9 ex_9 + \dot{W}_{pump} = \dot{m}_{10} ex_{10} + E\dot{x}^D$
Heat Exchanger 1	MBE: $\dot{m}_2 = \dot{m}_3$, $\dot{m}_6 = \dot{m}_7$ EBE: $\dot{m}_2 h_2 + \dot{m}_6 h_6 = \dot{m}_3 h_3 + \dot{m}_7 h_7 + \dot{Q}_{loss}$ SBE: $\dot{m}_2 s_2 + \dot{m}_7 s_7 + \dot{s}_{gen} = \dot{m}_3 s_3 + \dot{m}_7 s_7 + \dot{Q}_{loss}/T_s$ EBE:$\dot{m}_2 ex_2 + \dot{m}_7 ex_7 = \dot{m}_3 ex_3 + \dot{m}_7 ex_7 + E\dot{x}^Q + E\dot{x}^D$
Heat Exchanger 2	MBE: $\dot{m}_3 = \dot{m}_4$, $\dot{m}_{10} = \dot{m}_{11}$ EBE: $\dot{m}_3 h_3 + \dot{m}_{10} h_{10} = \dot{m}_4 h_4 + \dot{m}_{11} h_{11} + \dot{Q}_{loss}$ SBE: $\dot{m}_3 s_3 + \dot{m}_{10} s_{10} + \dot{s}_{gen} = \dot{m}_3 s_3 + \dot{m}_{11} s_{11} + \dot{Q}_{loss}/T_s$ EBE:$\dot{m}_3 ex_3 + \dot{m}_{10} ex_{10} = \dot{m}_4 ex_4 + \dot{m}_{11} ex_{11} + E\dot{x}^Q + E\dot{x}^D$
Heat Exchanger 3	MBE: $\dot{m}_5 = \dot{m}_8$, $\dot{m}_{16} = \dot{m}_{17}$ EBE: $\dot{m}_5 h_5 + \dot{m}_{16} h_{16} = \dot{m}_8 h_8 + \dot{m}_{17} h_{17} + \dot{Q}_{loss}$ SBE: $\dot{m}_5 s_5 + \dot{m}_{16} s_{16} + \dot{s}_{gen} = \dot{m}_8 s_8 + \dot{m}_{17} s_{17} + \dot{Q}_{loss}/T_s$ EBE:$\dot{m}_5 ex_5 + \dot{m}_{16} ex_{16} = \dot{m}_8 ex_8 + \dot{m}_{17} ex_{17} + E\dot{x}^Q + E\dot{x}^D$
Heat Exchanger 3	MBE: $\dot{m}_{12} = \dot{m}_9$, $\dot{m}_{15} = \dot{m}_{16}$ EBE: $\dot{m}_{12} h_{12} + \dot{m}_{15} h_{15} = \dot{m}_9 h_9 + \dot{m}_{16} h_{16} + \dot{Q}_{loss}$ SBE: $\dot{m}_{12} s_{12} + \dot{m}_{15} s_{15} + \dot{s}_{gen} = \dot{m}_9 s_9 + \dot{m}_{16} s_{16} + \dot{Q}_{loss}/T_s$ EBE:$\dot{m}_{12} ex_{12} + \dot{m}_{15} ex_{15} = \dot{m}_9 ex_9 + \dot{m}_{16} ex_{16} + E\dot{x}^Q + E\dot{x}^D$
Turbine	MBE: $\dot{m}_7 = \dot{m}_8$ EBE: $\dot{m}_7 h_7 = \dot{m}_8 h_8 + \dot{W}_{turbine} + \dot{Q}_{Loss}$ ENBE: $\dot{m}_7 s_7 + \dot{s}_{gen} = \dot{m}_8 s_8 + \dot{Q}_{loss}/T_s$ EBE: $\dot{m}_7 ex_7 = \dot{m}_8 ex_8 + E\dot{x}^Q + E\dot{x}^D + \dot{W}_{turbine}$
Turbine	MBE: $\dot{m}_{11} = \dot{m}_{12}$ EBE: $\dot{m}_{11} h_{11} = \dot{m}_{12} h_{12} + \dot{W}_{turbine} + \dot{Q}_{Loss}$ ENBE: $\dot{m}_{11} s_{11} + \dot{s}_{gen} = \dot{m}_{12} s_{12} + \dot{Q}_{loss}/T_s$ EBE: $\dot{m}_{11} ex_{11} = \dot{m}_{12} ex_{12} + E\dot{x}^Q + E\dot{x}^D + \dot{W}_{turbine}$
Hydrogen Compression	MBE: $\dot{m}_{21} = \dot{m}_{24}$ EBE: $\dot{m}_{21} h_{21} + \sum \dot{W}_{Comp} = \dot{m}_{24} h_{24} + \dot{Q}_{loss}$ ENBE: $\dot{m}_{21} s_{21} + \dot{s}_{gen} = \dot{m}_{24} s_{24} + \dot{Q}_{loss}/T_s$ EBE: $\dot{m}_{21} ex_{21} + \sum \dot{W}_{Comp} = \dot{m}_{24} ex_{24} + \dot{W}_{loss} + E\dot{x}^D$
Carbon Dioxide Compression	MBE: $\dot{m}_{20} = \dot{m}_{27}$ EBE: $\dot{m}_{20} h_{20} + \sum \dot{W}_{Comp} = \dot{m}_{27} h_{27} + \dot{Q}_{loss}$ ENBE: $\dot{m}_{20} s_{20} + \dot{s}_{gen} = \dot{m}_{27} s_{27} + \dot{Q}_{loss}/T_s$ EBE: $\dot{m}_{20} ex_{20} + \sum \dot{W}_{Comp} = \dot{m}_{27} ex_{27} + E\dot{x}^Q + E\dot{x}^D$
Reactor series	MBE: $\dot{m}_{28} = \dot{m}_{33}$ EBE: $\dot{m}_{28} h_{28} = \dot{m}_{33} h_{33} + \dot{Q}_{out}$ ENBE: $\dot{m}_{28} s_{28} + \dot{s}_{gen} = \dot{m}_{33} s_{33} + \dot{Q}_{out}/T_s$ EBE: $\dot{m}_{28} ex_{28} = \dot{m}_{33} ex_{33} + E\dot{x}^Q + E\dot{x}^D$
ECEM	MBE: $\dot{m}_{19} = \dot{m}_{21} + \dot{m}_{20}$ EBE: $\dot{m}_{19} h_{19} + \dot{W}_{in} = \dot{m}_{20} h_{20} + \dot{m}_{21} h_{21} + \dot{W}_{loss}$ ENBE: $\dot{m}_{19} s_{19} + \dot{s}_{gen} = \dot{m}_{20} s_{20}$ EBE: $\dot{m}_{19} ex_{10} + \dot{W}_{in} = \dot{m}_{20} ex_{20} + \dot{W}_{loss} + E\dot{x}^D$

Table 4.10: System 4 balance equations

Component	Balance Equations
ECEM	MBE: $\dot{m}_7 = \dot{m}_8 + \dot{m}_9$ EBE: $\dot{m}_7 h_7 + \sum \dot{W}_{in} = \dot{m}_8 h_8 + \dot{m}_9 h_9$ ENBE: $\dot{m}_7 s_7 + \dot{s}_{gen} = \dot{m}_8 s_8 + \dot{m}_9 s_9$ EBE: $\dot{m}_7 ex_7 + \sum \dot{W}_{in} = \dot{m}_8 ex_8 + \dot{m}_9 ex_9 + E\dot{x}^D$
Hydrogen Compression	MBE: $\dot{m}_9 = \dot{m}_{10}$ EBE: $\dot{m}_9 h_9 + \sum \dot{W}_{Comp} = \dot{m}_{10} h_{10} + \dot{Q}_{loss}$ ENBE: $\dot{m}_9 s_9 + \dot{s}_{gen} = \dot{m}_{10} s_{10} + \dot{Q}_{loss}/T_s$ EBE: $\dot{m}_9 ex_9 + \sum \dot{W}_{Comp} = \dot{m}_{10} ex_{10} + \dot{W}_{loss} + E\dot{x}^D$
Carbon Dioxide Compression	MBE: $\dot{m}_8 = \dot{m}_{11}$ EBE: $\dot{m}_8 h_8 + \sum \dot{W}_{Comp} = \dot{m}_{11} h_{11} + \dot{Q}_{loss}$ ENBE: $\dot{m}_8 s_8 + \dot{s}_{gen} = \dot{m}_{11} s_{11} + \dot{Q}_{loss}/T_s$ EBE: $\dot{m}_8 ex_8 + \sum \dot{W}_{Comp} = \dot{m}_{11} ex_{11} + E\dot{x}^Q + E\dot{x}^D$
Reactor series	MBE: $\dot{m}_{11} + \dot{m}_{10} = \dot{m}_{16}$ EBE: $\dot{m}_{11} h_{11} + \dot{m}_{10} h_{10} = \dot{m}_{16} h_{16}$ ENBE: $\dot{m}_{11} s_{11} + \dot{m}_{10} s_{10} + \dot{s}_{gen} = \dot{m}_{16} s_{16}$ EBE: $\dot{m}_{11} ex_{11} + \dot{m}_{10} ex_{10} = \dot{m}_{16} ex_{16} + E\dot{x}^Q + E\dot{x}^D$
Pump 1	MBE: $\dot{m}_{1w} = \dot{m}_{2w}$ EBE: $\dot{m}_{1w} h_{1w} + \dot{W}_{pump} = \dot{m}_{2w} h_{2w} + \dot{W}_{loss}$ ENBE: $\dot{m}_{1w} s_{1w} + \dot{s}_{gen} = \dot{m}_{2w} s_{2w}$ EBE: $\dot{m}_{1w} ex_{1w} + \dot{W}_{pump} = \dot{m}_{2w} ex_{2w} + \dot{W}_{loss} + E\dot{x}^Q + E\dot{x}^D$
Pump 2	MBE: $\dot{m}_5 = \dot{m}_6$ EBE: $\dot{m}_5 h_5 + \dot{W}_{pump} = \dot{m}_6 h_6$ ENBE: $\dot{m}_5 s_5 + \dot{s}_{gen} = \dot{m}_6 s_6$ EBE: $\dot{m}_5 ex_5 + \dot{W}_{pump} = \dot{m}_6 ex_6 + E\dot{x}^D$
Heat Exchanger (PV/T)	MBE: $\dot{m}_2 = \dot{m}_3$ EBE: $\dot{m}_2 h_2 + \dot{Q}_{in} = \dot{m}_3 h_3$ SBE: $\dot{m}_2 s_2 + \dot{Q}_{in}/T_s + \dot{s}_{gen} = \dot{m}_3 s_3$ EBE:$\dot{m}_2 ex_2 + E\dot{x}^Q = \dot{m}_3 ex_3 + E\dot{x}^D$
Heat Exchanger	MBE: $\dot{m}_4 = \dot{m}_5, \dot{m}_{1c} = \dot{m}_{2c}$ EBE: $\dot{m}_4 h_4 = \dot{m}_5 h_5 + \dot{Q}_{out}$ SBE: $\dot{m}_4 s_4 + \dot{s}_{gen} = \dot{m}_5 s_5 + \dot{Q}_{out}/T_s$ EBE:$\dot{m}_4 ex_4 = \dot{m}_4 ex_4 + E\dot{x}^Q + E\dot{x}^D$
Turbine	MBE: $\dot{m}_3 = \dot{m}_4$ EBE: $\dot{m}_3 h_3 = \dot{m}_4 h_4 + \dot{W}_{turbine} + \dot{Q}_{Loss}$ ENBE: $\dot{m}_3 s_3 + \dot{s}_{gen} = \dot{m}_4 s_4 + \dot{Q}_{loss}/T_s$ EBE: $\dot{m}_3 ex_3 = \dot{m}_4 ex_4 + E\dot{x}^Q + E\dot{x}^D + \dot{W}_{turbine}$

Chapter 5: Results and Discussion

In this chapter, the results of the simulation and the thermodynamic analysis of the four proposed ammonia and methanol production plants are presented. Each ammonia and methanol production plant has a separate section in this chapter, which includes specific results.

5.1 Results of System 1

In this section, the result of the system will be discussed thoroughly. There are mainly two cases of operation in terms of outputs. Case 1 considers that 50% of the net power produced is provided to an electrolyzer that provides hydrogen to the ammonia synthesis system. Case two considers only power being produced. Figure 5.1 displays the results of the energy efficiency for both cases. One can derive from Figure 5.1 for case 2 yields higher energy efficiency, as it does not send the power produced for further processing causing more irreversibility's similar to case 1. The energy efficiency in both cases increases as the working fluid mass flow rate increases. This is a result of warm water containing enough thermal energy to provide to the working fluid at higher flow rates (573 kg/s). The lower working fluid flow rates experience a phase change to a superheated state. However, as there is a significantly large supply of warm water, most of the energy transferred is stored in its sensible form. Larger working fluid flow rates can store more latent thermal energy, which is desired as it stores more thermal energy at its saturation temperature, which in this case is 21^{o}C.

The warm water flow rate was fixed at a rate of 19,310.34 kg/s, meaning the heat source potential is fixed based on this flow rate. Therefore, the relation between the efficiency of both cases will be affected by the cooling water flow rates. The cycle experienced a negative change in efficiency as the cold-water flow rates passed the base cold-water flow rate for each case of working fluid flow rates. The base cold-water flow rate was selected for each working fluid flow rate based on the cooling load needed for the working fluid to experience a phase change to saturated liquid as it leaves the condenser. As for the limitation of the higher cooling rates values, they will eventually yield to network consumption of the system and in some cases the working fluid will require larger amounts than provided to experience a phase change to a superheated state.

The highest energy efficiencies experienced by the cycle in case 1 and 2 are found to be 1.37% and 1.83%. The highest energy efficiency in both cases was found at a cold-water flow rate of 23,862 kg/s and a working fluid flow rate of 573 kg/s. The ratio of the warm water to the cold water flow rate is 1:1.25 ratio, where the cold ratio of the warm to cold to working fluid ratio was found to be

42:34:1. As for the lowest energy efficiency values, they were found to be at the lowest working fluid flow rate of 100 kg/s, where the cold flow rate was 14,916 kg/s. The corresponding energy efficiency for case 1 and 2, are found to be 0.0108% and 0.0144%. The lowest efficiency corresponds to the rising pumping work required for the cold water, which directly affects the energy efficiency for both case 1 and 2. However, in case 1 the CASU also requires more work input to match the mass flow rate of nitrogen gas needed to feed the ammonia synthesis system; at the optimal energy efficiency of case 2 the energy efficiency is about 25.1% larger than case 1 energy efficiency. As the cold-water flow rate increases the difference between the efficiencies decreases in all working fluid flow rate cases, as seen in the figure.

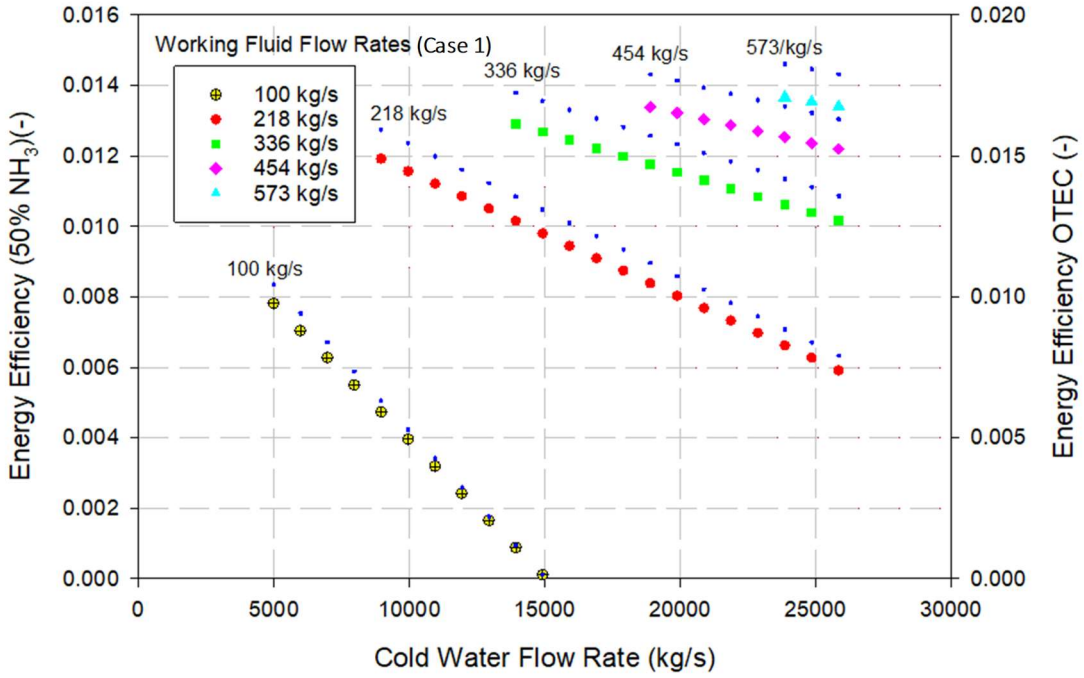

Figure 5.1: Energy efficiency of the two analyzed cases with varying to cold water and ammonia flow rates

The highest exergy efficiencies experienced by the cycle in case 1 and 2 are found to be 56.17% and 78.02%. The highest energy efficiency in both cases was found a cold-water flow rate of 23,862 kg/s and a working fluid flow rate of 573 kg/s. The ratio of the warm water to the cold water flow rate is 1:1.25 ratio, where the cold ratio of the warm to cold to working fluid ratio was found to be 42:34:1. As for the lowest exergy efficiency values, they were found to be at the lowest working fluid flow rate of 100 kg/s, where the cold flow rate was 14,916 kg/s. The corresponding exergy efficiency for case 1 and 2, are found to be 0.44% and 0.62%. Again, like the energy efficiency study, the lowest efficiency corresponds to the rising pumping work required for the cold water,

which directly effects the exergy efficiency. At the optimal exergy efficiency of case 2 is about 28.00% larger than that of case 1. As the cold-water flow rate increases, the difference between the efficiencies increases in all working fluid flow rate cases, in this case, the difference between the lowest exergy efficiency for both cases of 29.03%, as seen in the figure.

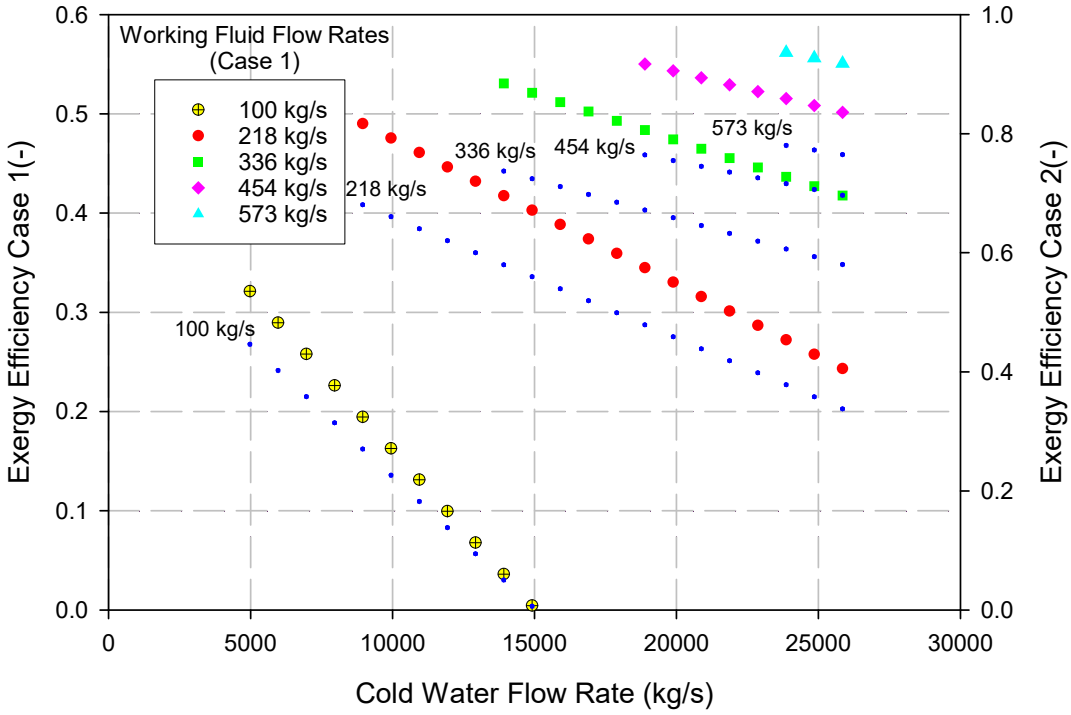

Figure 5.2: Exergy efficiency of the two analyzed cases with varying to cold water and ammonia flow rates

Figure 5.3 displays the relationship between cold water and working fluid flow rates. The parametric study was performed to using the same 5 working fluid flow rates for each step of change of cold-water flow rate. The highest net power production was achieved at the highest working fluid flow rate of 573 kg/s and a cold flow rate of 23,862 kg/s. The maximum power production was 6,611.7 kW and 13,223.5 kW for case 1 and 2. The maximum net power production rates were achieved at the highest energy and exergy efficiency of the cycle through all the cases performed in the parametric study. As for the lowest net power production in both cases in this study, they were achieved at the lowest energy and energy and exergy efficiency. This is highly due to the excessive power consumed by the cold-water flow rate pumping. Similar to the case with the energy and exergy efficiency study, the declining efficiencies were a result of lack of working fluid to absorb the thermal energy available and/or the increasing pumping power consumed by the

excessive cooling rates of the cycle. The lowest net power production was found to be 9.12 kW and 18.22 kW for case 1 and 2. One should note that at the lowest power production rates the cooling duty was found to be 358.4GW, which isn't the highest cooling duty. However, the condenser discharge temperature was lowest at 6.43°C, making it higher quality in terms of cooling. One should also note that the cooling water and working fluid rates were 14,916 kg/s and 100 kg/s.

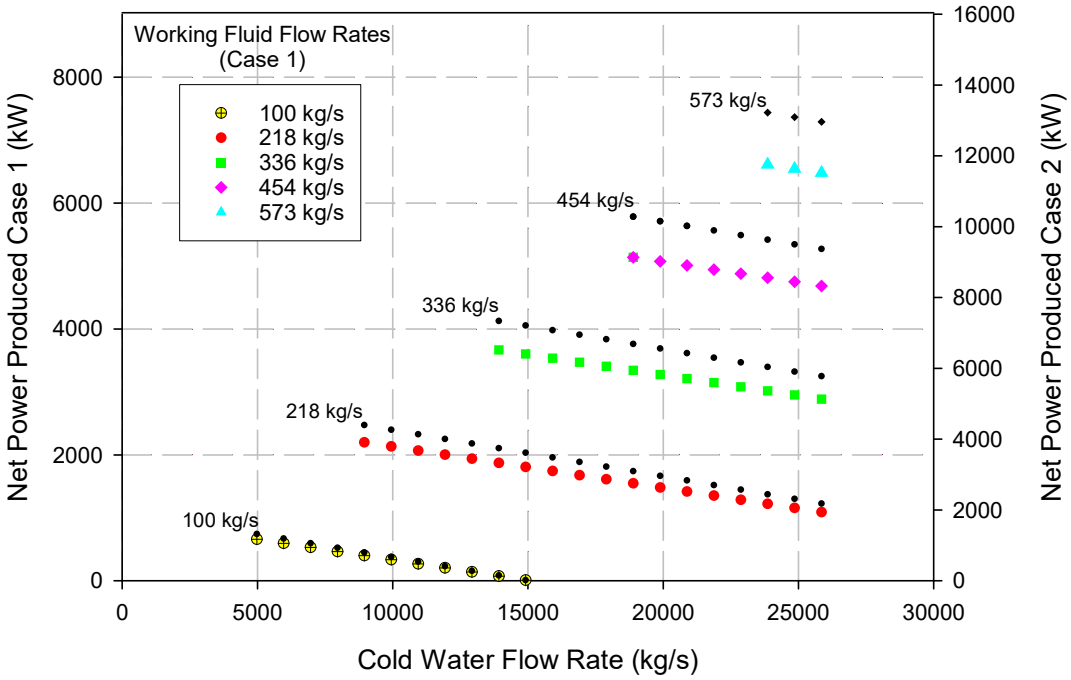

Figure 5.3: Net power produced of the two analyzed cases with varying to cold water and ammonia flow rates

To quantify the irreversibility's in the system, an exergy destruction study was performed. Figure 5.4 displays the relationship between the cold water and the working fluid flow rate. Case 1 and 2 in this case do not have similar trends. The trends due to the irreversibility associated with the chemical reaction of the synthesis of ammonia. The maximum exergy destruction rate is more than double in case 1 compared to case 2. Case 2 has the highest quality of exergy as it only produces electrical power, unlike case 1 where 50% of the power is converted into ammonia. The maximum exergy destruction rate for case 1 was 7,615.5 kW, where the cold water and working fluid flow rates were found to be 25,850kg/s and 573 kg/s. this is the result of high-quality exergy being transformed into chemical energy in the form of ammonia and as it is the largest cold water flow rate in that parametric

study pumping power is wasted high-quality electrical power. As for case 2 the highest exergy destruction rate was found to be 4,276.4 kW, where the cold water and working fluid flow rate were 25,850 kg/s and 573 kg/s.

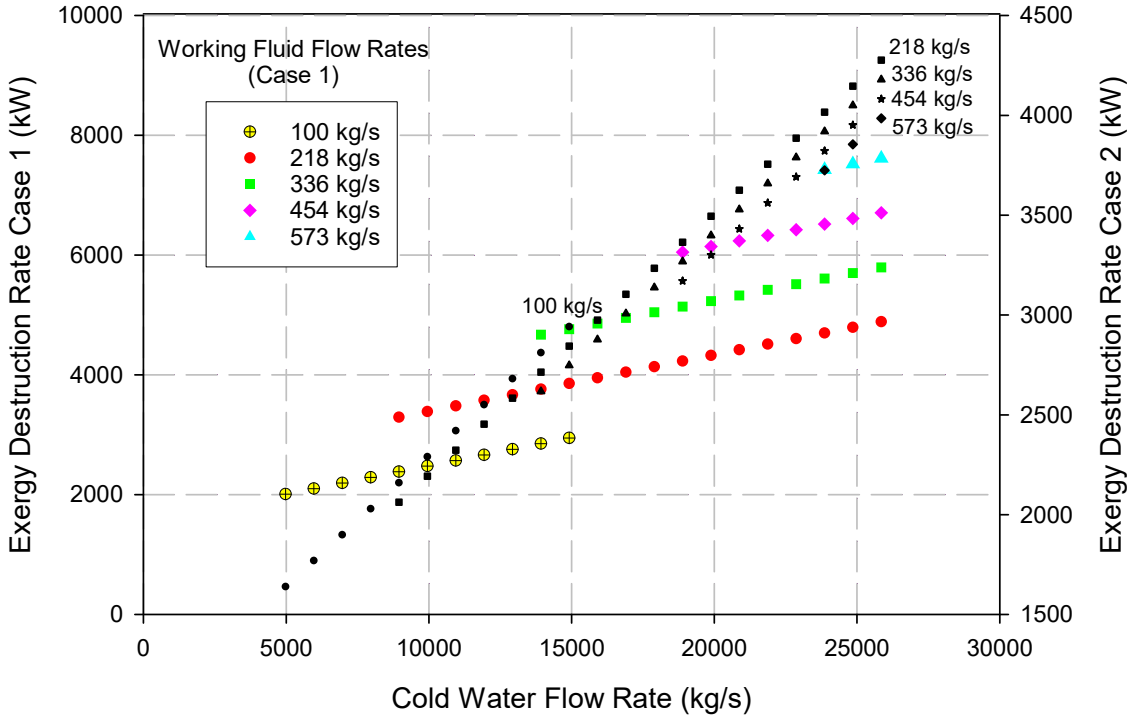

Figure 5.4: Exergy destruction rate of the two analyzed cases with varying to cold water and ammonia flow rates

The exergy destruction rate for case 1 was highest at peak energy and exergy efficiency, as in this point of the study, the most heat was absorbed as it has the highest working fluid flow rate. Furthermore, 1.83% was converted to power from a potential of 7.2% based on the Carnot efficiency of the cycle, causing a large amount of exergy destruction. The lowest exergy destruction rate was found to be 2,008.72 kW and 1,639.02 kW at a cold water and working fluid flow rate of 4,976 kg/s and 100 kg/s. In the case of lowest exergy destruction rate the exergy destruction is mainly due to the wasted thermal energy absorbed by the cycle and the inability of the cycle to utilize the heat. Figure 5.5 shows the relationship of the hydrogen production rate relative to the cold water and working fluid flow rate. Similar to the relation seen in figures 5.1 and 5.2 the relation is linear and decreasing as the cold flow rate increases in all cases of the working fluid flow rates.

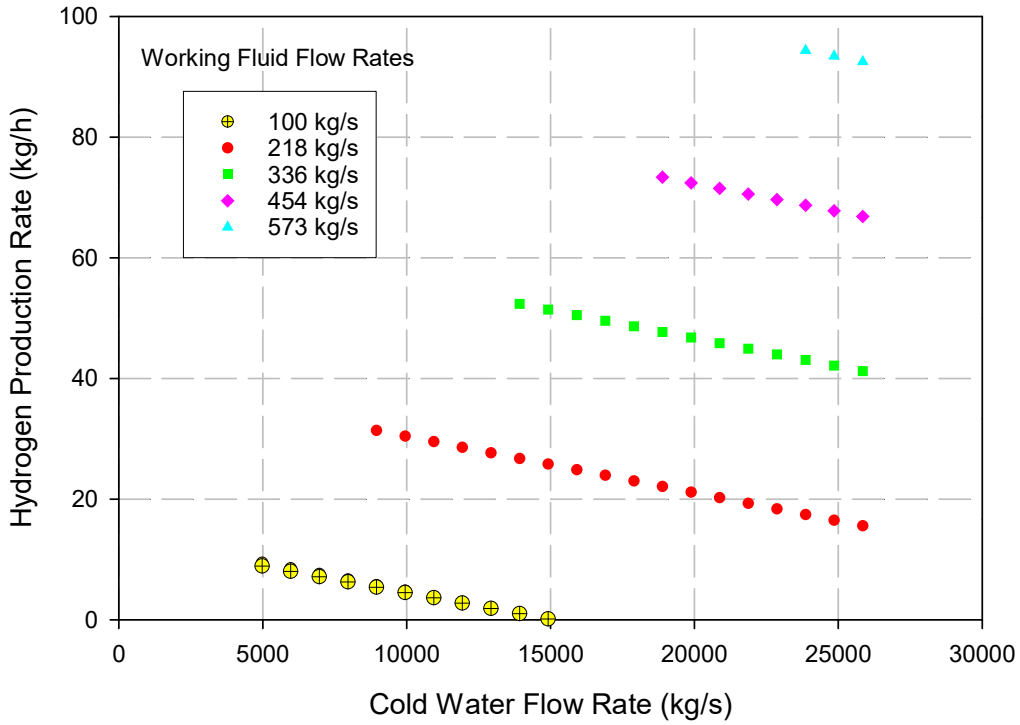

Figure 5.5: Hydrogen production rate with varying to cold water and working fluid flow rates

The reason being the pumping power is increasing because of the rising cold-water flow rate, which decreases the net power available for hydrogen production. Furthermore, the numerator of the energy and exergy efficiency is the useful outputs of the system, which is power, which has a direct relationship with the hydrogen. The maximum hydrogen production rate was found to be 94.35 kg/h, where the cold water and working fluid flow rates were 23,862 kg/s and 573 kg/s. As for the lowest hydrogen production rate, it was found to be 0.13 kg/h, the corresponding cold water and working fluid flow rates were found to be 14,916 kg/s and 100 kg/s. As for figure 5.6 displays the ammonia production rate relative to the cold water and working fluid flow rate. The ammonia production rate is directly related to the hydrogen production rate as the ammonia synthesis system was previously optimized and can be adjusted for various hydrogen. Furthermore, the molar ratio between the nitrogen was fixed at 2.17. Therefore, the reaction is always completed with excess nitrogen. The maximum and minimum ammonia production rate was found to be 534.65 kg/h and 0.74 kg/h. The corresponding cold water and working fluid flow rates were as follows 23,862 kg/s and 573 kg/s (Maximum production) and 14,916 kg/s and 100 kg/s (Minimum production).

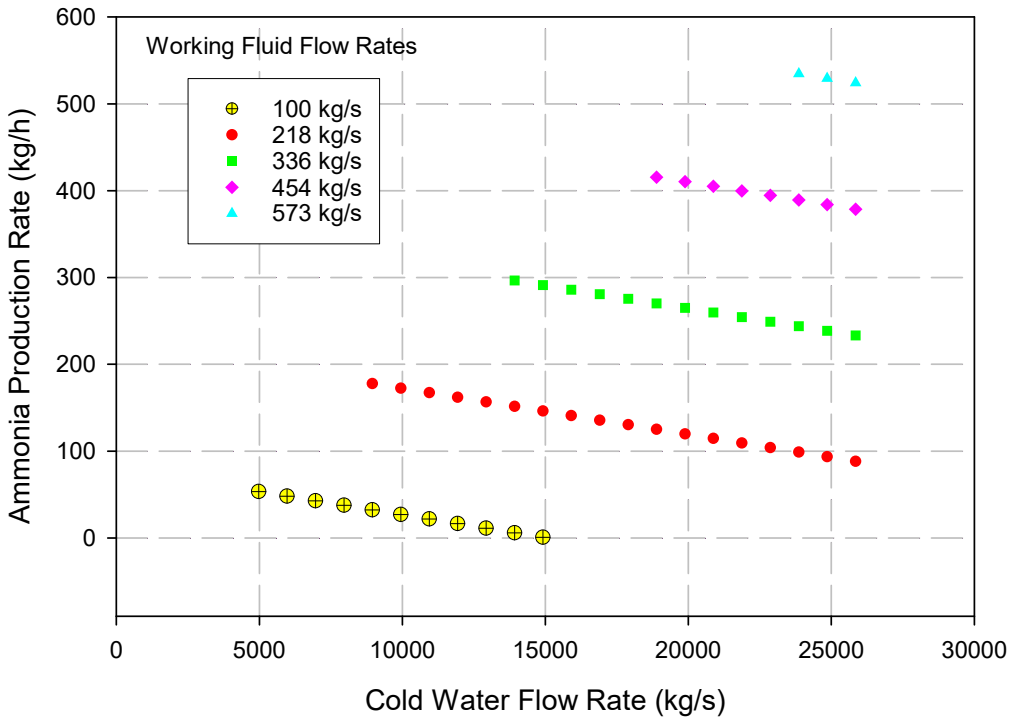

Figure 5.6: Ammonia production rate with varying to cold water and working fluid flow rates

Figure 5.7 displays the relationship between the cooling duty and condenser discharge temperature relative to the cold water and working fluid flow rates. The cooling duty increases for each working fluid flow rate as the cold-water flow rate increases. This occurs as the cold-water flow rate is more than that's needed to cool the working fluid to its saturation point in the condenser. Furthermore, the cooling duty is measured based on its temperature increase from its condenser discharge temperature to a final discharge temperature of 12ºC to the ocean; therefore, the temperature of the condenser discharge directly increases the cooling load as it decreases and vice versa. The temperature parametric study shows a logarithmic relation as the cold-water flow rate increases. This is due to the heat transfer relations between the two fluids. If the cold-water rate keeps increasing, the system will mainly produce cooling. The maximum cooling duty was achieved at a working fluid flow rate of 218 kg/s, where the cold-water flow rate was found to be 25,850 kg/s, which corresponds to a cooling duty of 565.7 GW at a condenser temperature of 6.92ºC. The lowest cooling duty of 20.1 GW was also achieved at a working

fluid of 218 kg/s at the lowest cold-water flow rate of 8,952 kg/s for that study where the condenser discharge temperature was 11.48ºC.

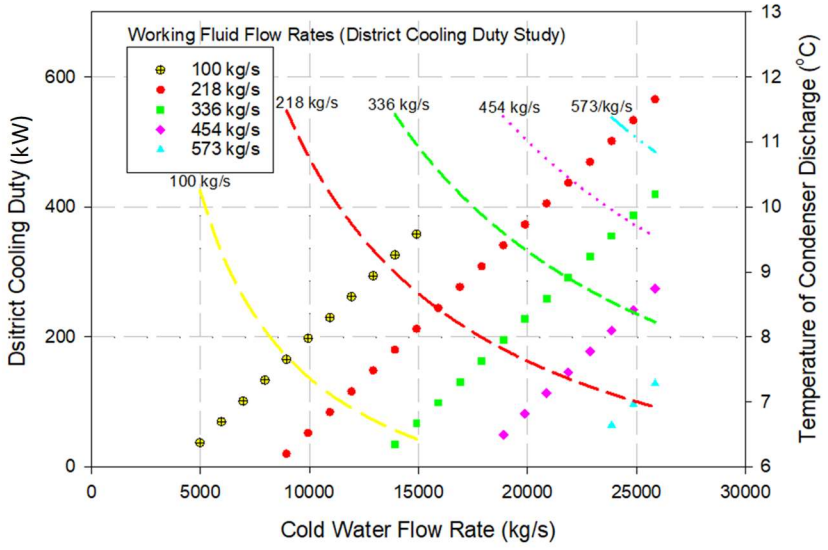

Figure 5.7: Ammonia production rate with varying to cold water and working fluid flow rates

Table 5.1. Single stage OTEC cycle state points (based on the Aspen Plus flow sheet fig. 3.1)

From	To	Temperature	Pressure	Specific enthalpy	Specific entropy	Enthalpy rate	Mass flow rate	Specific exergy
		ºC	bar	kJ/kg	kJ/kgK	kW	1000 kg/h	kJ/kg
	CPUMP	4.5	1.0	-15959.7	-9.4	367073.7	828000	3.2
CPUMP	CHX	4.5	1.7	-15959.6	-9.4	3670707.8	828000	3.3
CHX		5.2	1.0	-15956.5	-9.4	3670003.3	828000	2.9
	NH3PUMP	11.5	6.5	-3999.1	-11.3	2239.5	2016.0	323.5
NH3PUMP	WHX	11.6	9.0	-3998.4	-11.3	2239.1	2016.0	324.0
WHX	TURB	21.7	9.0	-2733.8	-7.0	1530.9	2016.0	307.9
TURB	CHX	11.5	6.5	-2765.6	-6.9	1548711.8	2016.0	265.1
CHX		6.2	6.5	-4023.6	-11.4	2253216.3	2016.0	324.9
	WPUMP	26.0	1.0	-15867.5	-9.1	793375.5	180000	0.0
WPUMP	WHX	26.0	1.3	-15867.5	-9.1	793372.7	180000	0.0
WHX		22.7	1.0	-15881.6	-9.1	794080.9	180000	0.0

The cooling duty at the maximum energy and exergy efficiency 64.4GW where the condenser temperature was found to be 11.38ºC. If the final discharge temperature to the ocean was increased to a value larger than 12ºC a larger cooling duty can be obtained. However, for ecological reasons, the cooling water temperature was limited to 12ºC as it

was recommended based on the literature. A note to the readers, the cooling duty of the cycle was not placed in the efficiency study as it will yield high efficiencies that might be misleading. This comes as with the case of drilling for oil the reservoir is available, and the system is not producing; however, extracting it. The state points for the OTEC cycle and Ammonia production system are presented in Tables 5.1 and 5.2.

Table 5.2. Ammonia production system state points

From	To	Temperature	Pressure	Specific enthalpy	Specific entropy	Energy rate	Mass flow rate	Exergy rate
		°C	kPa	kJ/kg	kJ/kgK	kW	kg/s	kW
	N1	25.0	100	-0.2	0.0	-0.3	1.5	-1.8
	N1	25.0	200	1.4	-2.8	0.1	0.1	55.7
N1	N5	183.6	100	-0.2	0.5	-0.3	1.6	72.5
N2	N20	25.0	100	-2699.5	-5.8	-377.7	0.1	-0.3
N2	N3	25.0	100	-0.1	0.3	-0.2	1.4	-2.3
N3	N6	169.5	100	-0.1	0.4	-0.2	1.4	49.8
N6	N4	25.0	100	-194.4	-0.1	-280.5	1.4	-2.1
N4	N7	25.0	100	-0.2	0.2	-0.2	1.3	-1.9
N5	N2	25.0	100	-238.5	-0.1	-377.5	1.6	-2.6
N4	N20	25.0	100	-2699.5	-5.8	-280.6	0.1	-0.2
N8	N20	25.0	100	-2699.5	-5.8	-197.1	0.1	-0.1
N7	N9	146.6	100	-0.2	0.3	-0.2	1.3	30.1
N9	N8	25.0	100	-147.2	-0.1	-197.1	1.3	-1.8
N8	N10	25.0	100	-0.2	0.1	-0.3	1.3	-1.6
N11	N20	25.0	100	-2699.5	-5.8	-116.2	0.0	-0.1
N10	N12	107.8	100	-0.2	0.2	-0.3	1.3	12.1
N12	N11	25.0	100	-91.9	-0.1	-116.4	1.3	-1.5
N11	N13	25.0	100	-0.2	0.0	-0.3	1.2	-1.5
N14	N20	25.0	100	-2699.5	-5.8	-36.4	0.0	0.0
N13	N15	53.2	100	-0.2	0.1	-0.3	1.2	0.2
N15	N14	25.0	100	-29.9	0.0	-36.6	1.2	-1.4
N14		25.0	100	-0.2	0.0	-0.3	1.2	-1.4
N17	N16	46.0	400	-15755.5	-8.7	-6144.6	0.4	1.1
N16	N18	179.2	400	-13173.9	-2.4	-5137.8	0.4	274.0
	N17	45.9	10	-15755.9	-8.7	-6144.8	0.4	1.0
N18	N19	45.9	10.0	-13582.8	-1.9	-5297.3	0.4	56.6
N19		45.9	10	-15755.9	-8.7	-6144.8	0.4	1.0

5.2 Results of System 2

In this section, the results of the developed system are presented. The results include energy and exergy performance assessments and various renewable fuel production rates. The wind turbine (GE 1.5 XLE) was modeled using Eureqa as mentioned previously in the Analysis and Assessment section. The results of the model and its validation are shown below in Figure 5.8. The correlation coefficient obtained from the regression analysis was 0.9999 (R^2) for the model relative to the actual data [88].

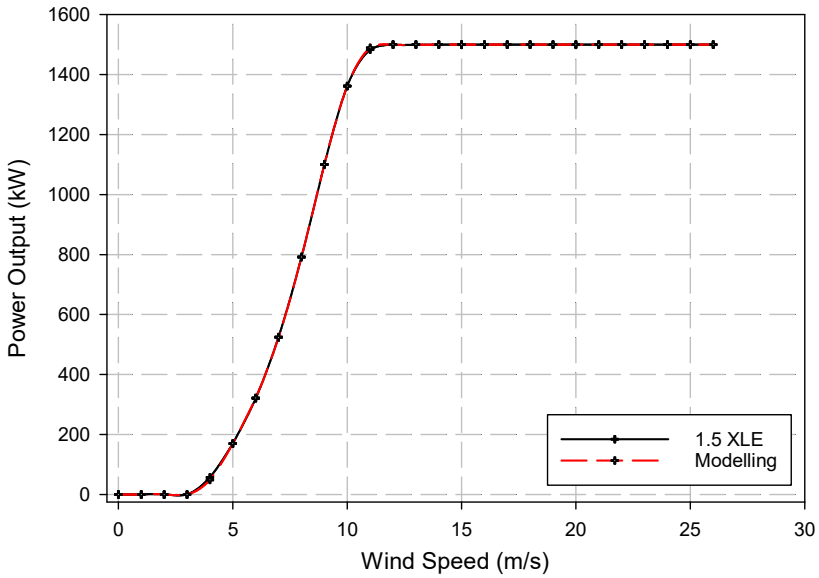

Figure 5.8: Power output of the turbine relative to the wind speed for both the experimental data and theoretical model

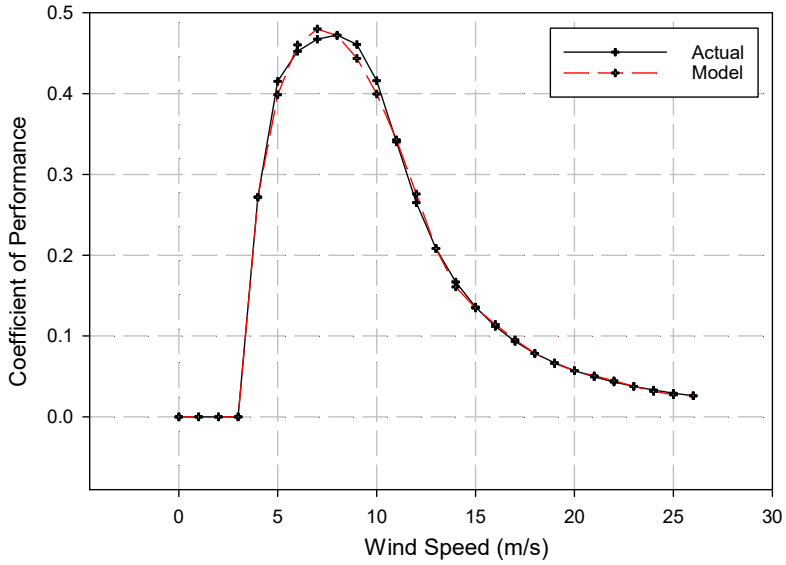

Figure 5.9: Power coefficient for 1.5XLE calculated and modeled

The power coefficient was obtained from GE for the wind turbine and was then modeled using Eureqa. The peak power coefficient value was found to be 47.3% in the Eureqa model, which is very close to the 48% that General Electric reported for the 1.5 XLE wind turbine [81,82]. Figure 5.9 displays the values calculated from actual data provided by GE using eq 2. The fitted model for the coefficient of performance is also shown in Figure 5.9. The average error between the actual and modeled is 2.18%.

The exergy destruction rate peak was found to be 54.9 GW, which is mainly due to the speed limitation of the wind turbine as the power production stays constant after 11.5 m/s. The wind turbine is unable to convert the kinetic energy provided from the wind to electrical power at speeds past 11.5 m/s. The reported exergy destruction is for one turbine. The exergy efficiency of the wind turbine peaks at 47.2% which was achieved at 8m/s. This is a result of the maximum conversion rate relative to wind speed. The results of the study are shown Figure 5.10.

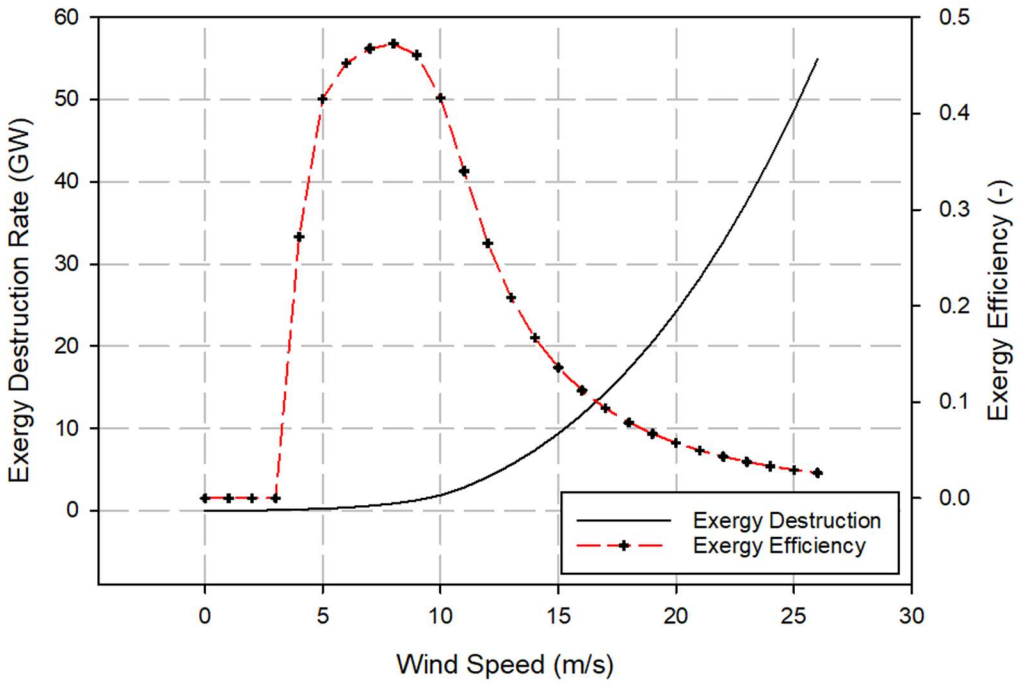

Figure 5.10: Exergy destruction and efficiency of a GE 1.5 xle

As mentioned previously, the first solar FS 6420 parameters of operations were used for this case study. The reported nominal efficiency at $1{,}000\ W/m^2$ is 17%. An exergy analysis was performed on a module level for the FS 6420. The results of the exergy efficiency and exergy destruction can be seen in Figure 5.10. The peak exergy destruction rate occurred at 1200 W/m^2, where the corresponding value was 2396.8 W. the reason for the exergy destruction being the highest at 1200 W/m^2 is due to the inability of the PV module to output more than 420 W past 1,000 W/m^2. As for the exergy efficiency, it stays constant relative to the solar irradiance up until the irradiance surpasses 1,000 W/m^2. The lowest exergy efficiency was 14.9% at 1200 W/m^2.

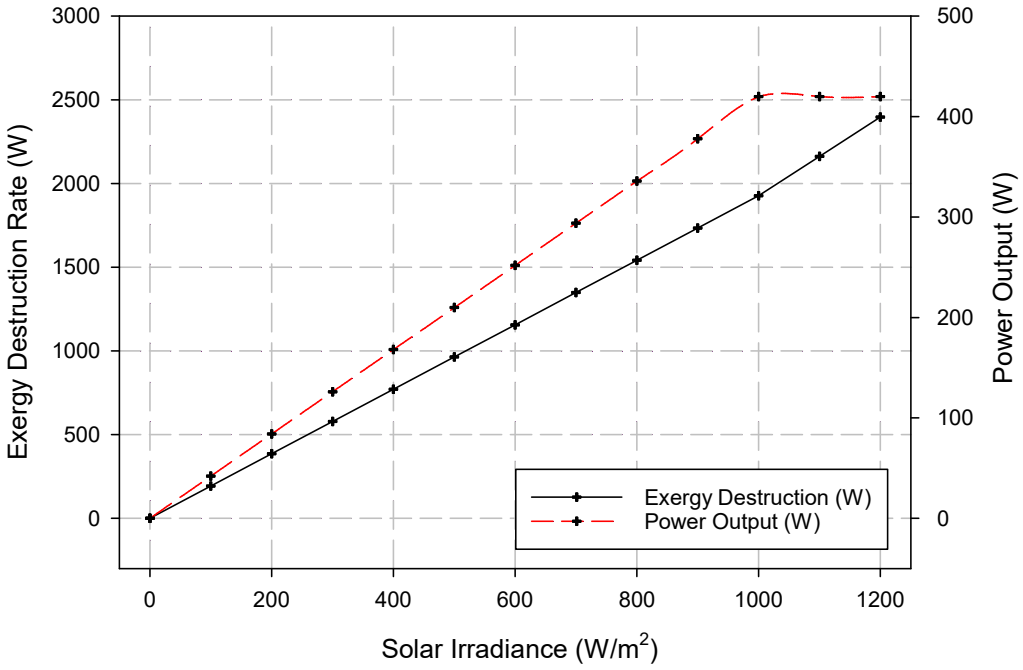

Figure 5.11: Power output and exergy destruction rate of the FS 6420 relative to solar irradiance

Figure 5.11 displays the relation between the hydrogen production rate and varying solar irradiance. The hydrogen production rate and irradiance have a direct and increasing relationship. The relation comes as the hydrogen production rate is directly related to the amount of power provided to the electrolyzer is supplied by the wind turbines that are running at 6,8,10 and 12 m/s and the PV unit with a varying solar irradiance. The electrolyzers utilize the excess power from the wind and PV plant that supplies power to the community. As mentioned previously in the design parameter, therefore, as the solar

irradiance increases, the more excess power the electrolyzer receives. The peak hydrogen production rate was found to be 85.65 kg/h at a solar irradiance of 1,000 W/m^2 and a wind speed of 12m/s. The ammonia production rate from the PMAPS system was also modeled and is shown in Figure 5.12. The ammonia production irradiance has a direct and increasing relation. The relation comes as the ammonia production rate is directly related to the amount of power provided to the electrolyzers to produce more hydrogen. The electrolyzers mentioned in the system is provided by the wind turbines that are operating at a wind speed of 6,8,10 and 12 m/s and the PV unit with a varying solar irradiance. The ammonia produced is then stored in a tank at a pressure of. The peak ammonia production rate was found to be 194.13 kg/h at a solar irradiance of 1,000 W/m^2 and a wind speed of 12 m/s.

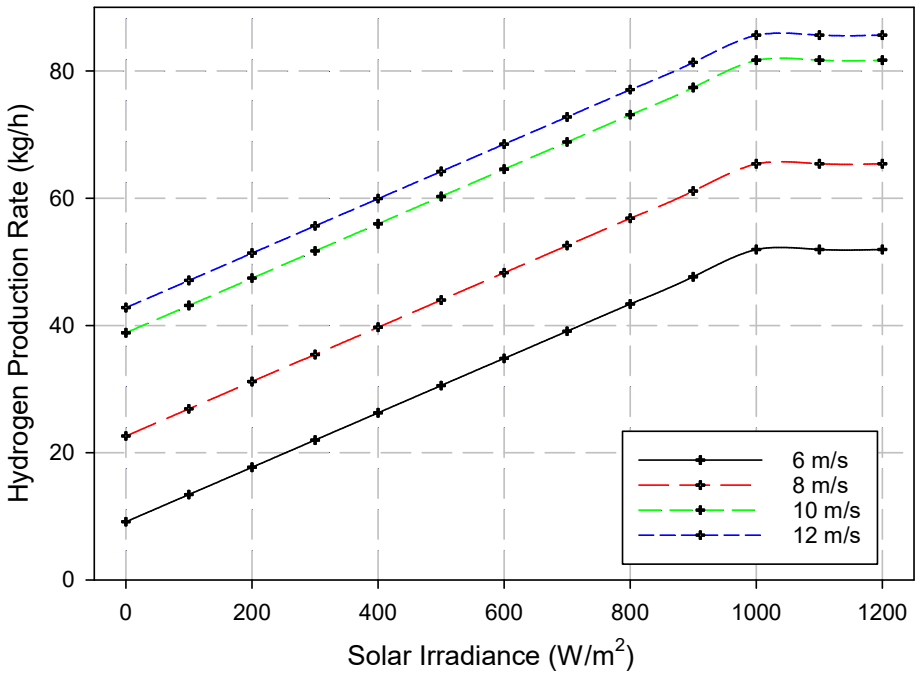

Figure 5.12: hydrogen production rate with a varying solar irradiance

The exergy destruction rate of the electrolyzer is shown below in Figure 5.13. The exergy destruction rate has a linear relation to the increasing solar irradiance. This is due to the increasing power provided to the electrolyzer and with more power reaching the electrolyzer the higher the exergy destruction rate becomes. The main cause of the exergy destruction is the high irreversibility's associated with the dissociation of the water to oxygen and hydrogen. Like the previous scenarios, the parametric study included wind turbines that are operating at a wind speed of 6,8,10 and 12 m/s and the PV unit with a

varying solar irradiance. The maximum exergy destruction rate achieved was 933.14 kW when the wind speed was 12 m/s and solar irradiance of 1,000 W/m^2. After the value of the solar irradiance of 1,000 W/m^2 is achieved the exergy destruction rate remains constant as the power output of the PV cells achieve peak performance at 1,000 W/m^2 and remain constant thereafter.

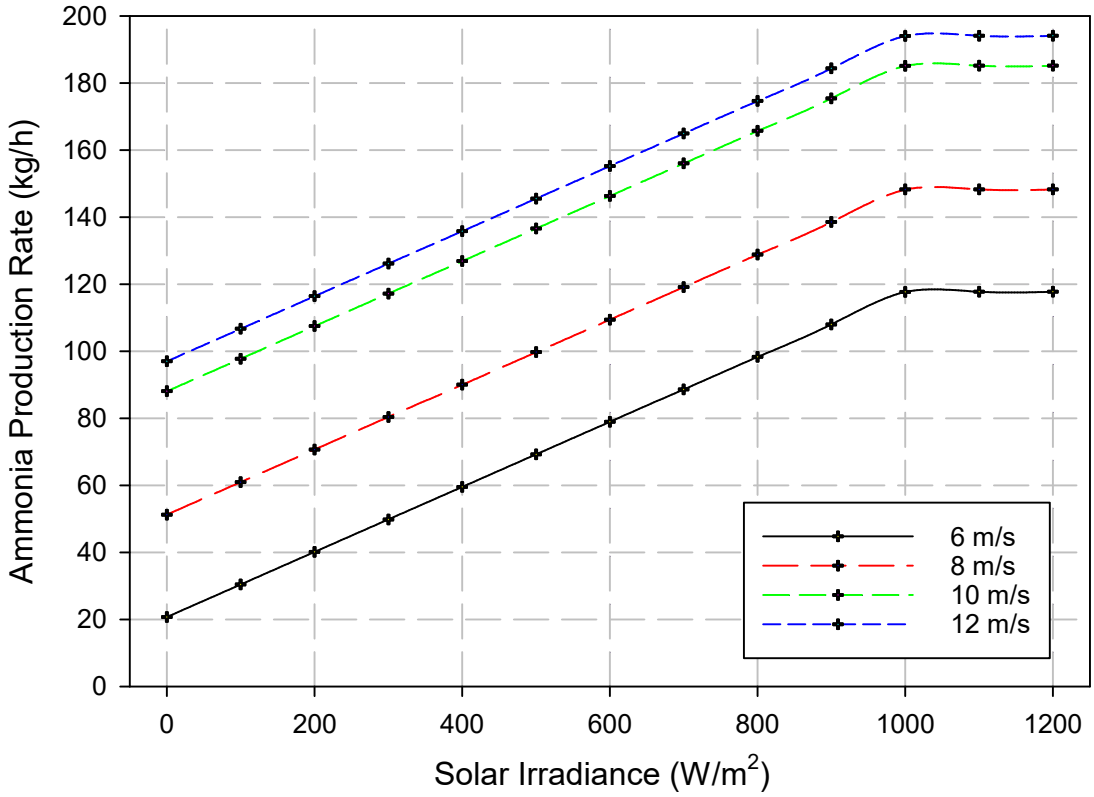

Figure 5.13: Ammonia production rate relative to a varying solar irradiance

In Figure 5.14, a parametric study was performed using three fixed solar irradiances of 600, 800 and 1,000 W/m^2 with a varying wind speed. As mentioned previously two GE 1.5 xle were modeled for this system and the results for the hydrogen produced from the PEM water electrolyser are shown in the figure. The relation is highly reliant on the power curve that the wind turbines experience. The peak hydrogen production starts to occur at 12m/s and an irradiance of 1,000 W/m^2, The maximum hydrogen production was found to be 80.5 kg/h. However, as seen in the figure, the hydrogen production remains constant

after a wind speed of 12m/s. This is due to the inability of the wind turbine to convert the kinetic energy of into power at such high speeds.

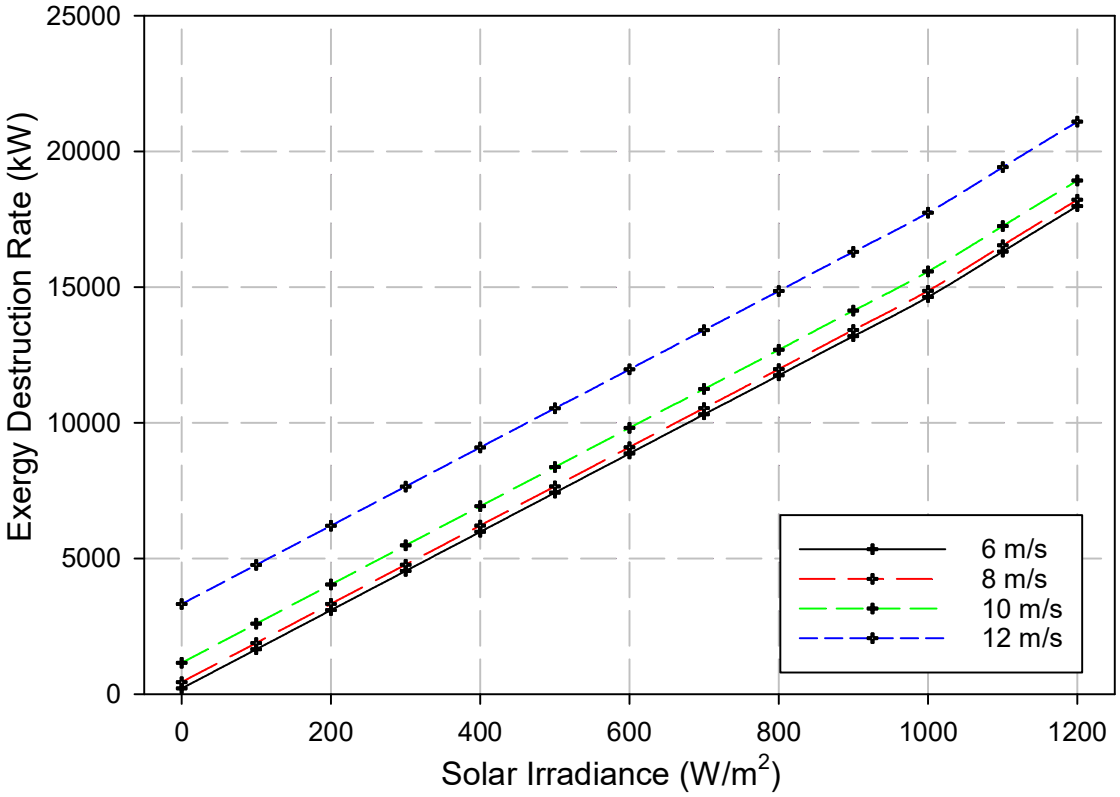

Figure 5.14: Exergy destruction rate of the electrolyzer hydrogen production rate with a varying solar irradiance

The ammonia production rate from the PMAPS system was also modeled and is shown in Figure 5.15. The ammonia production rate and wind speed have a direct and increasing relation. The relation comes as the ammonia production rate is directly related to the amount of power provided to the electrolyzer as it produces more hydrogen. The electrolyzer power as mentioned in Figure 5.15 is supplied by the wind turbines that are operating at a variable rate and the PV units operating at 600,800, and 1,000 W/m^2 of irradiance. The peak ammonia production rate was found to be 456.1 kg/h at a solar irradiance of 1,000 W/m^2 and a wind speed of 12m/s.

The exergy destruction rate of the electrolyzer is shown below in Figure 5.15. The exergy destruction rate has an increasing with increasing wind speed. This is due to the increasing power provided to the electrolyzer and with more power reaching the electrolyzer the higher the exergy destruction rate becomes. The main cause of the exergy destruction is

the high irrevisbilties associated with the dissociation of the water to oxygen and hydrogen. Like the previous scenarios, the parametric study included wind turbines that are operating at a variable rate and the PV units operating with 600,800, and 1,000 W/m^2 of irradiance. The maximum exergy destruction rate achieved was 1.5 GW when the wind speed was 12 m/s and a solar irradiance of 1,000 W/m^2. After the value of the solar irradiance of 1,000 W/m^2 is achieved the exergy destruction rate remains constant as the power output of the wind turbines achieve peak performance at 11m/s and remain constant thereafter.

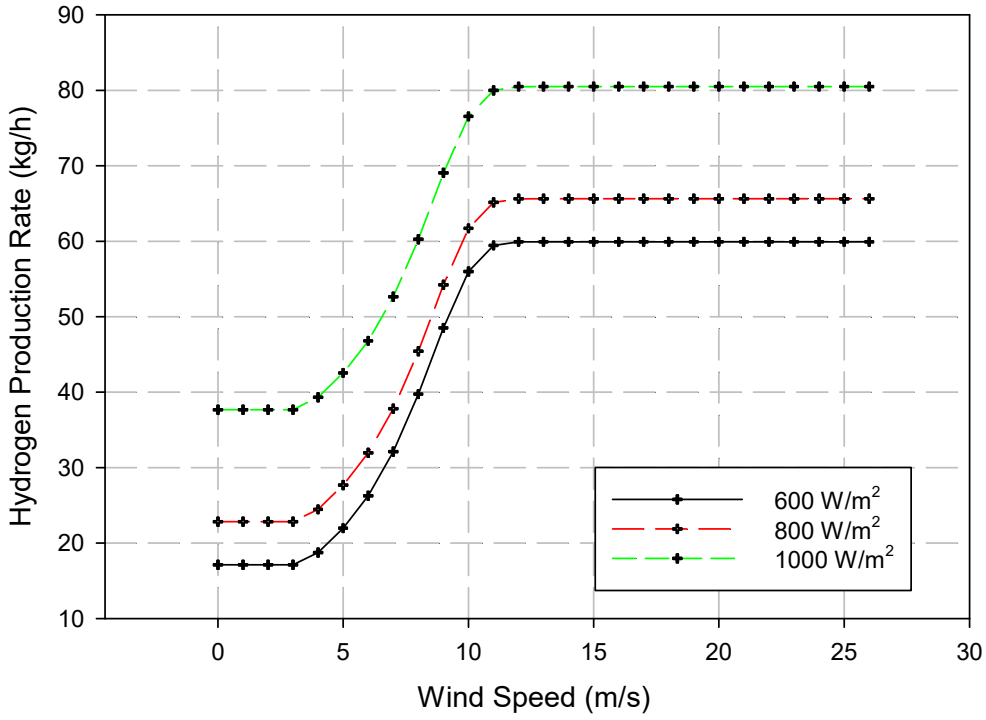

Figure 5.15: hydrogen production rate with a varying wind speed

A parametric study with the same variations as in Figure 5.16 was performed to find the effects of the operation parameters on the energy and exergy efficiency of the overall system in Figures 5.15 and 5.16. It was found the peak energy and exergy efficiency of the overall system was reached when the wind speed was 8m/s and the solar irradiance was 0 W/m^2 and the corresponding efficiencies were 75.8% and 73.6%. The reason behind this result is due to the high exergy destruction associated with the inability of the solar panel to convert the majority of the solar irradiance. This is the reason why the highest efficiency was achieved at a solar irradiance of 0 W/m^2. However, at the maximum power output (3MW) from the solar field, the maximum exergy and energy efficiency of the

overall system was found to be 18.8% and 19.1%. It should be noted that solar energy is an overall more reliable source of renewable energy than wind.

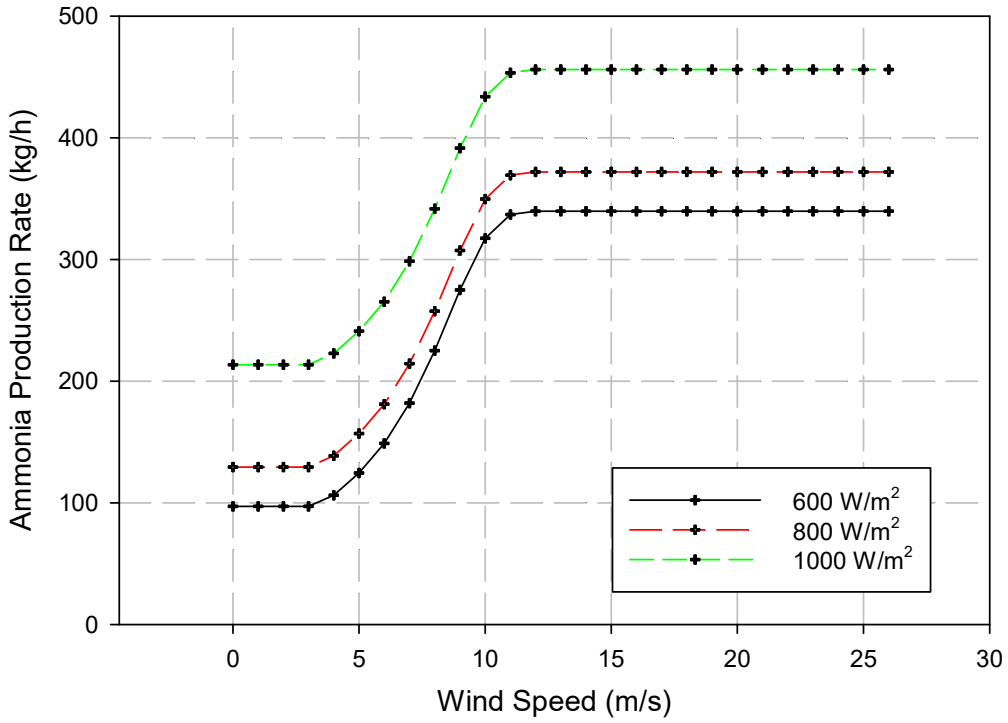

Figure 5.16: Ammonia production rate relative to a varying wind speed

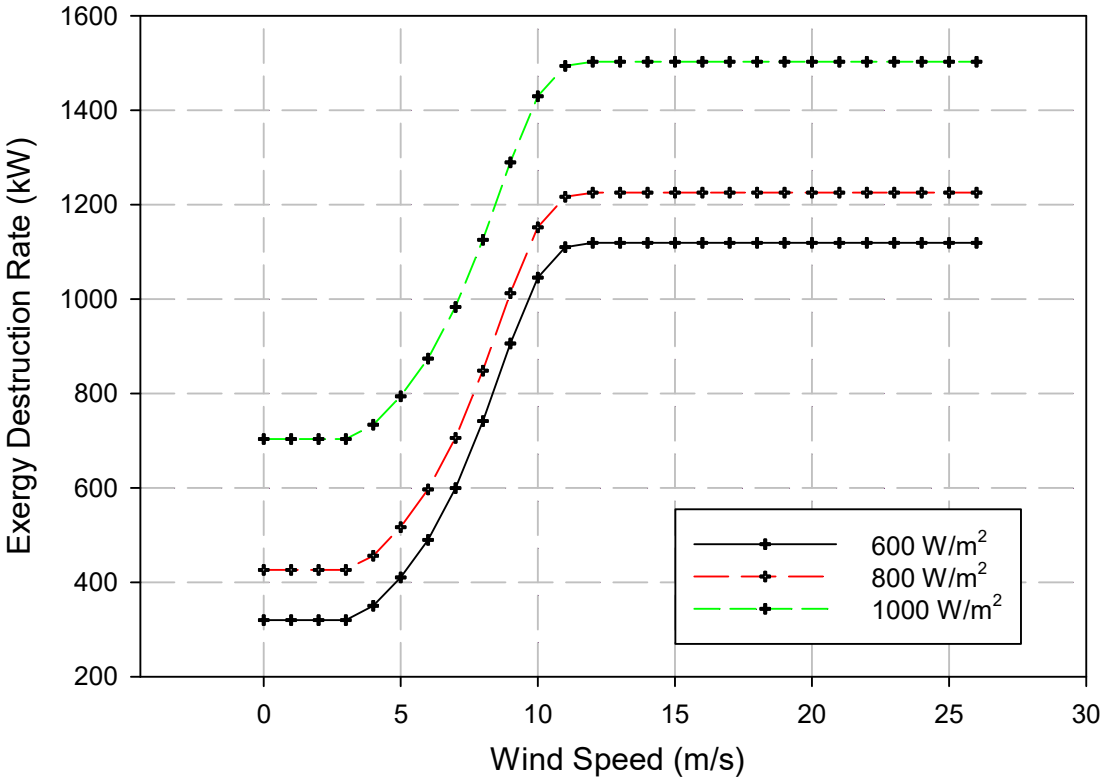

Figure 5.17: Exergy destruction rate of the electrolyzer hydrogen production rate with a varying wind speed

Furthermore, the main reason behind the lower efficiencies when solar was the dominant source of energy, is highly due to the low power output relative to the high solar influx. It should be also noted that solar panels still have the potential to have an increase in energy and exergy efficiency as the technologies mature. The state points of the ammonia production cycle is given in Table 5.2.

A parametric study was performed where the wind turbines are operating at 6,8,10 and 12 m/s and the PV unit with varying solar irradiance. The maximum overall exergy destruction rate achieved was 21.1 GW when the wind speed was 12 m/s and solar irradiance of 1,000 W/m^2. The lowest exergy destruction rate was found to be 18.0 GW at 6m/s wind speed and 1,000 W/m^2.

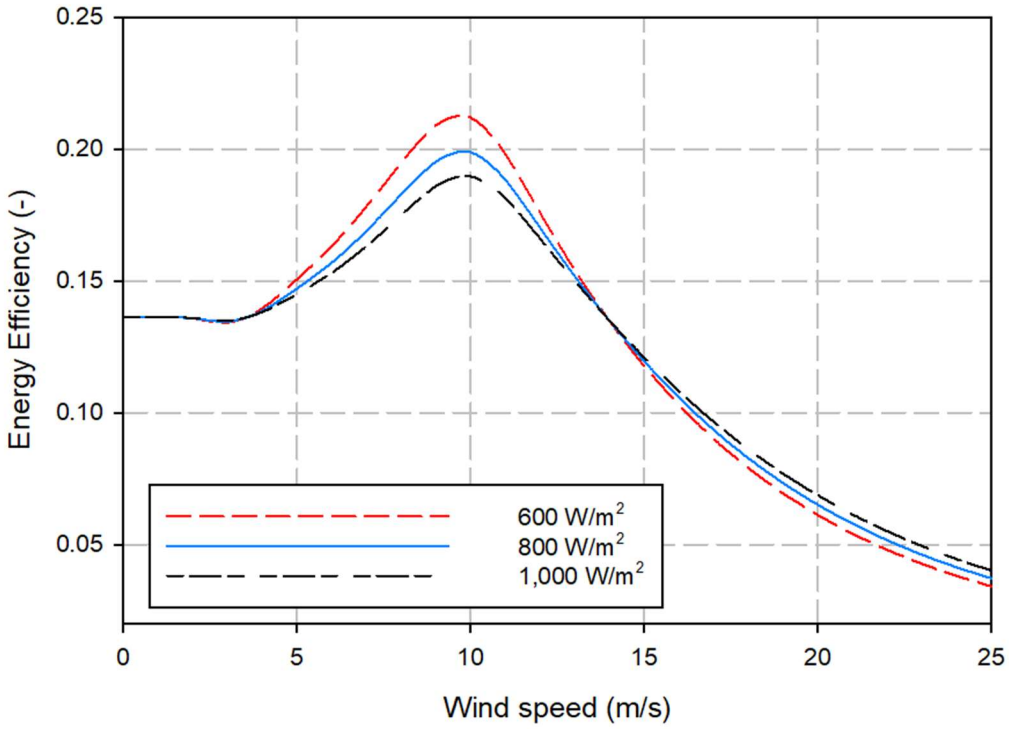

Figure 5.18: Overall energy efficiency with fixed wind speeds and varying solar irradiances

However, at a wind speed of 8 m/s and 1,000 W/m^2 the exergy destruction rate was found to be 18.2 GW which isn't significantly higher than the exergy destruction rate found at 6 m/s and 1,000 W/m^2. These findings correlations are heavily affected by the wind speed

as the wind speeds entering the wind turbine determines the coefficient of performance. As the coefficient of performance decreases, the exergy destruction rate increases giving them an inversely proportional relationship. Table 5.3 displays all the state points within the ammonia production systems Aspen Plus flow sheet.

Table 5.3. Ammonia production system state points

State	Temperature	Pressure	Specific enthalpy	Specific entropy	Energy rate	Mass flow rate	Exergy rate
	ºC	kPa	kJ/kg	kJ/kg-K	kW	kg/s	kW
1	25.0	100	-0.2	0.0	-0.3	1.5	-1.8
2	25.0	200	1.4	-2.8	0.1	0.1	55.7
3	183.6	100	-0.2	0.5	-0.3	1.6	72.5
4	25.0	100	-2699.5	-5.8	-377.7	0.1	-0.3
5	25.0	100	-0.1	0.3	-0.2	1.4	-2.3
6	169.5	100	-0.1	0.4	-0.2	1.4	49.8
7	25.0	100	-194.4	-0.1	-280.5	1.4	-2.1
8	25.0	100	-0.2	0.2	-0.2	1.3	-1.9
9	25.0	100	-238.5	-0.1	-377.5	1.6	-2.6
10	25.0	100	-2699.5	-5.8	-280.6	0.1	-0.2
11	25.0	100	-2699.5	-5.8	-197.1	0.1	-0.1
12	146.6	100	-0.2	0.3	-0.2	1.3	30.1
13	25.0	100	-147.2	-0.1	-197.1	1.3	-1.8
14	25.0	100	-0.2	0.1	-0.3	1.3	-1.6
15	25.0	100	-2699.5	-5.8	-116.2	0.0	-0.1
16	107.8	100	-0.2	0.2	-0.3	1.3	12.1
17	25.0	100	-91.9	-0.1	-116.4	1.3	-1.5
18	25.0	100	-0.2	0.0	-0.3	1.2	-1.5
19	25.0	100	-2699.5	-5.8	-36.4	0.0	0.0
20	53.2	100	-0.2	0.1	-0.3	1.2	0.2
21	25.0	100	-29.9	0.0	-36.6	1.2	-1.4
22	25.0	100	-0.2	0.0	-0.3	1.2	-1.4
23	46.0	400	-15755.5	-8.7	-6144.6	0.4	1.1
24	179.2	400	-13173.9	-2.4	-5137.8	0.4	274.0
25	45.9	10	-15755.9	-8.7	-6144.8	0.4	1.0
26	45.9	10.0	-13582.8	-1.9	-5297.3	0.4	56.6
27	45.9	10	-15755.9	-8.7	-6144.8	0.4	1.0

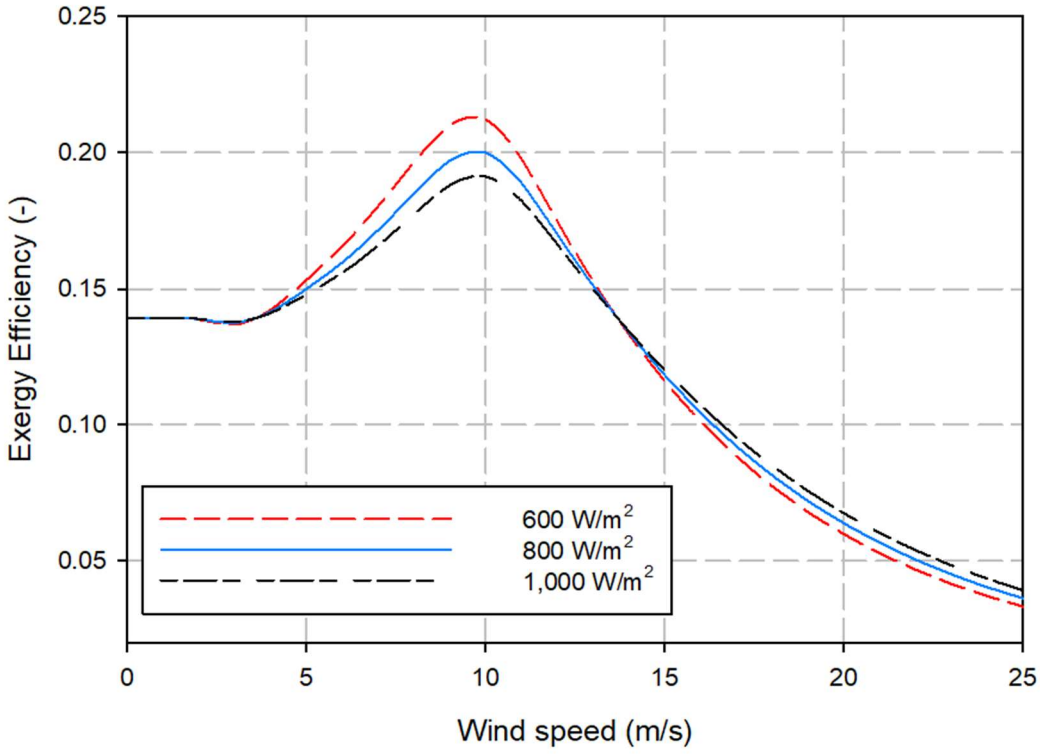

Figure 5.19: Overall exergy efficiency with fixed wind speeds and varying solar irradiances

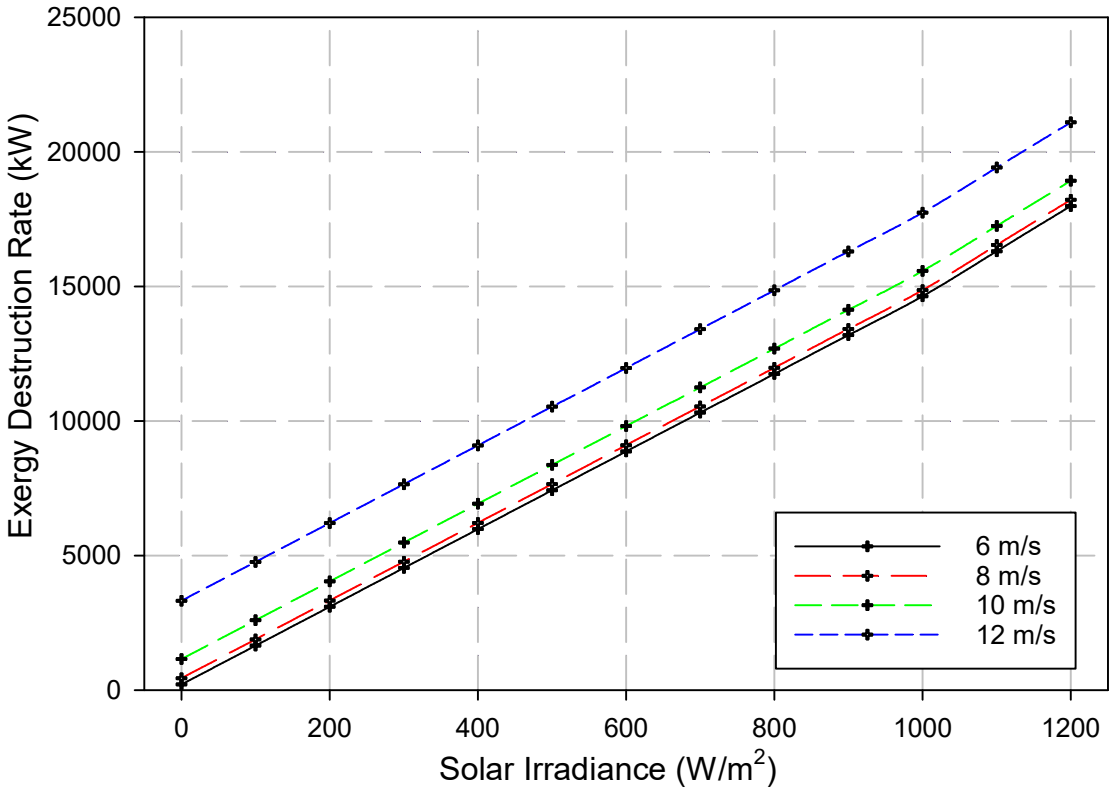

Figure 5.20: Overall exergy destruction rate with fixed wind speeds and varying solar irradiances

5.3 Results of System 3

In the following section, parametric studies along with an energy analysis, will be presented for the proposed system Figure 5.21 displays the net power output from the 2 stage OTEC cycle by varying the mass flow rates of ammonia for the first and second OTEC stages. It was found that the peak net power output with the fixed ocean water flow rates of 28,450 kg/s (cold water) and 50,000kg/s (Warm water) was found to be 55.1 MW. However, the baseload cycle was rated to be 16.2 MW. Baseload cycle means that power can be provided continuously without interruption apart from maintenance or weather-related issues.

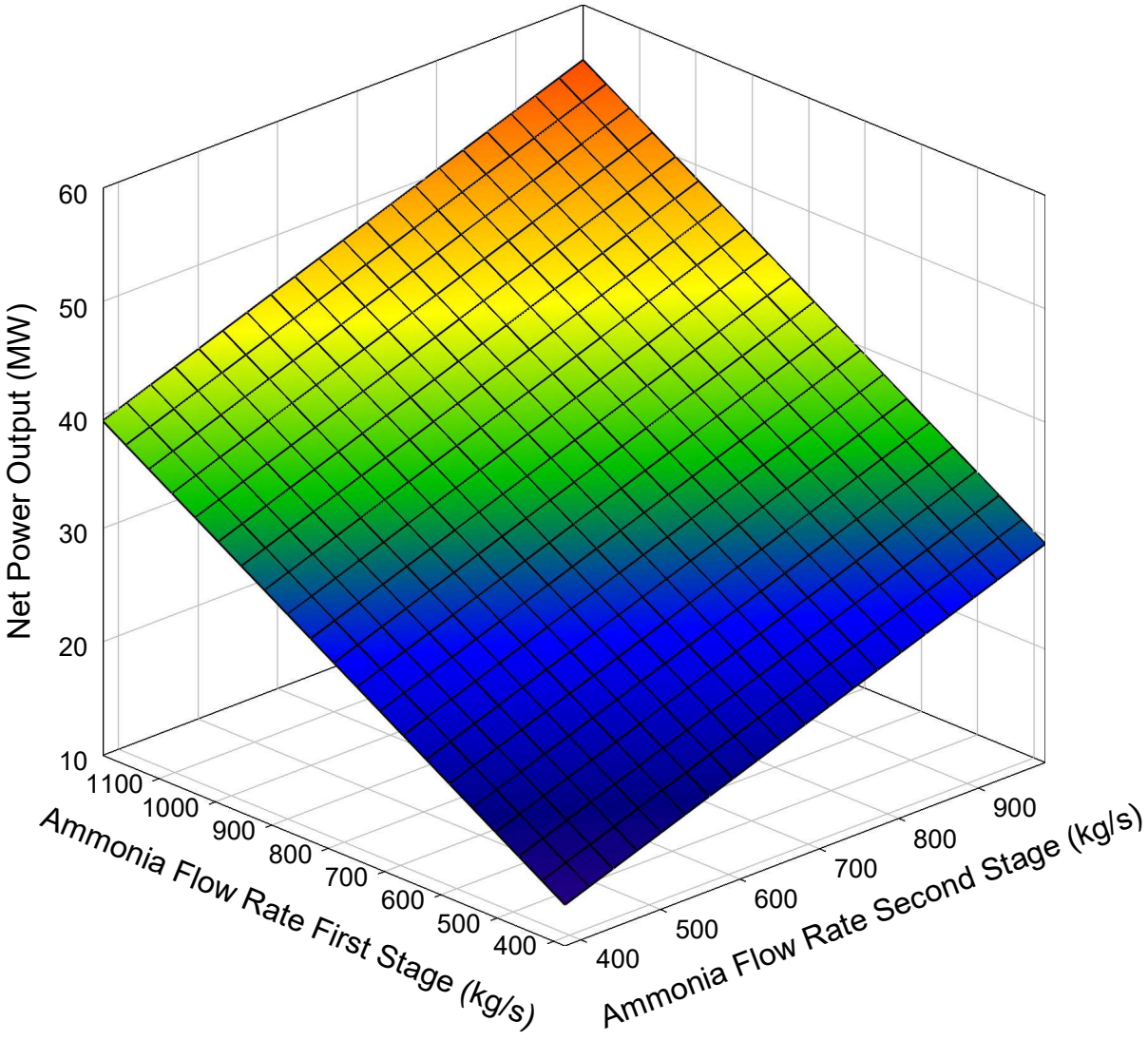

Figure 5.21: Net power output of the OTEC plant with varying ammonia flow rates for stages 1 and 2.

The ammonia flow rates for the maximum net power output were as follows 1200 kg/s for stage 1 and 984 kg/s for stage 2 of the OTEC plant. It was observed that the second stage runs at an 18% lower ammonia flow rate as the warm surface water temperature dropped along with the cold-water temperature increased.

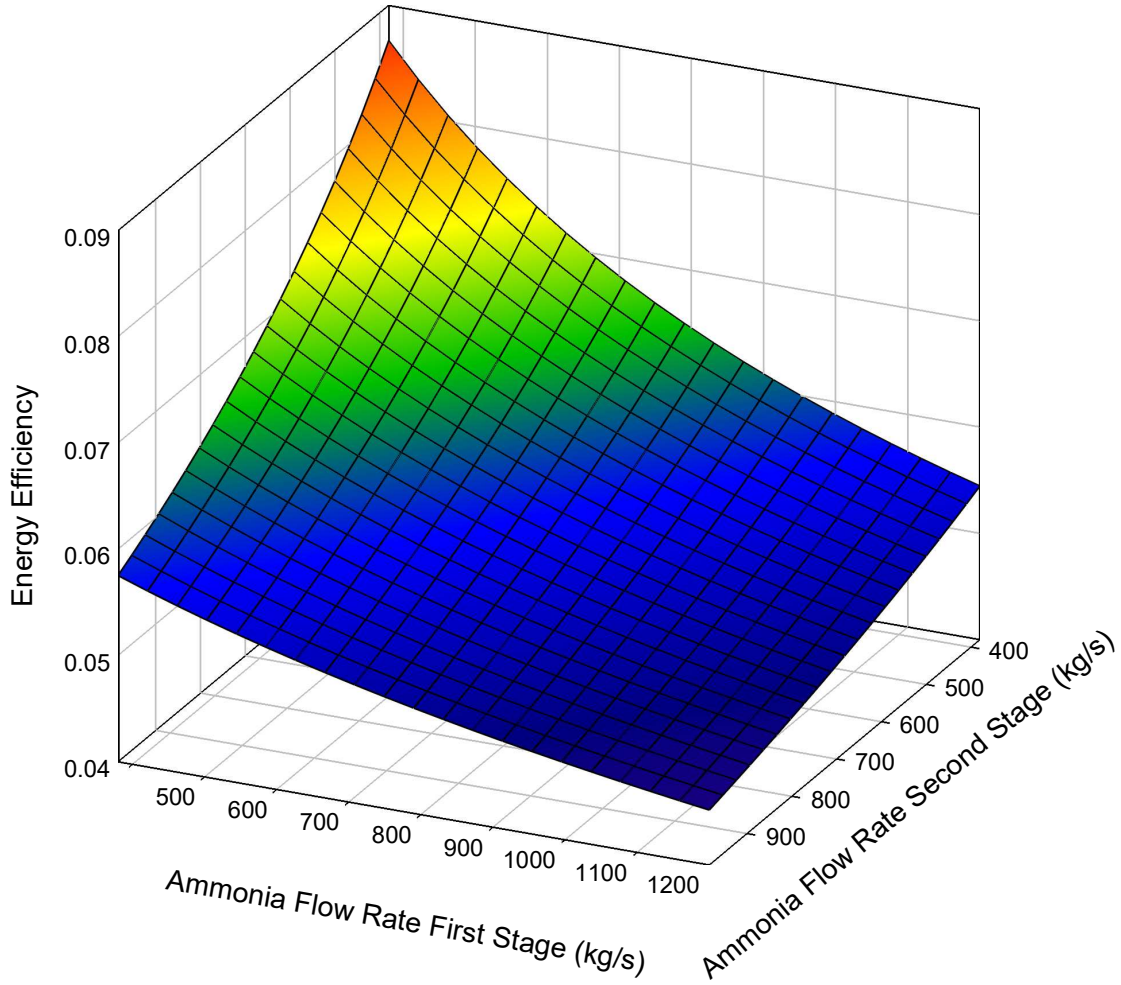

Figure 5.22: Overall energy efficiency of with varying ammonia flow rates for stages 1 and 2

Figure 5.24 displays the overall energy efficiency of the system when all the power produced is provided to the E-CEM reactor for carbon dioxide and hydrogen production. The hydrogen and carbon dioxide are then used as feedstocks for the methanol production plant. The efficiency of 0.36kg/s, which is more than 10.8 times the amount previously reported at peak production. The corresponding power output from the cycle was found to be 13.6 GW at the reported maximum energy efficiency. The reason behind this efficiency

is due to the fixed cold-water flow rate that can provide a very large cooling load that is fixed at 69MW.

The ECEM reactor used was based on the lab-scale unit developed by NREL [4,14]. The peak overall energy efficiency was found to be 7.50%, where the methanol production was found to be 0.12 kg/s. The corresponding power provided from the OTEC was 13.6 MW at ammonia flow rates of 380 kg/s for stage 1 and 380 kg/s for stage 2. The peak efficiency of the overall system was achieved at much lower ammonia flowrates than when peak power production and energy efficiency of the OTEC plant was obtained. The reason being the conversion of the power to methanol is being done at a constant rate, and as the heat inputted increases from the heat exchanger's, the overall efficiency will decrease with higher power rates. Furthermore, in all the parametric studies, a cooling load of 69.0 MW which has the potential to cool 6,000 Florida homes.

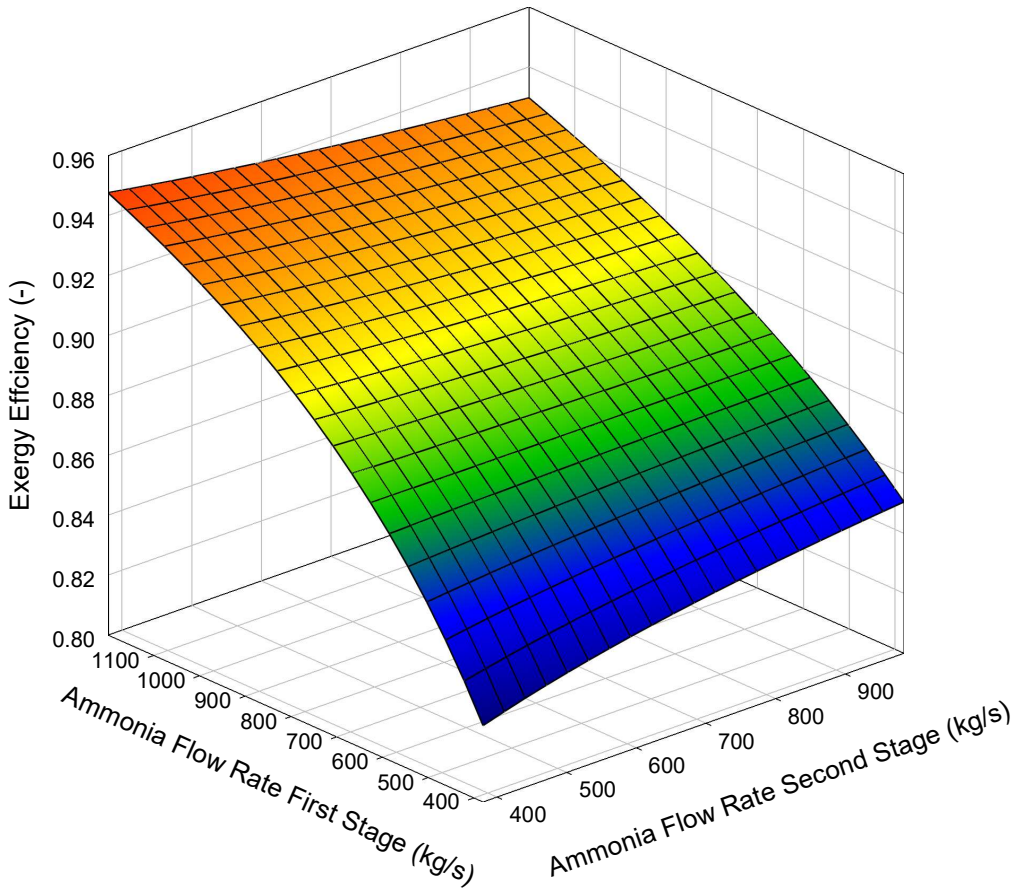

Figure 5.23: Exergy efficiency of the cycle with varying stage working fluid flow rates

Figure 5.23 displays the relation between the output of the cycle, which in this case is power and cooling. The cycle achieves high exergy efficiencies at any given flow rate of working fluid in both stages. The reason being that the cooling duty is fixed at 69.6 GW, which raises the utilization of the cycle, as shown previously in figure 5.9. The cooling output utilizes the cold-water discharge of the cycle, which in most cases, would be treated as waste. The highest exergy efficiency was 94.8%.

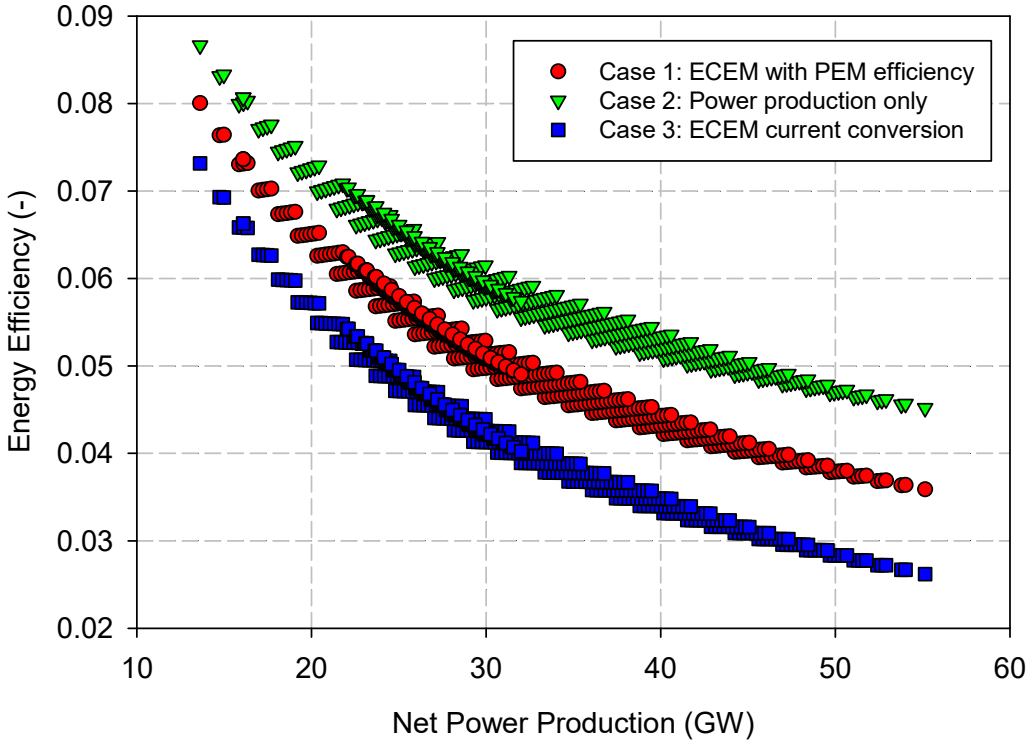

Figure 5.24: A case study for various operating parameters for the proposed system and their effect on energy efficiency with varying net power production from the OTEC plant

However, with the results shown in Figure 5.24 (overall efficiency) can be improved based on the development of the ECEM reactor. According to the literature, the achievement of Proton Exchange Membrane (PEM) electrolyzer is possible for the ECEM. Therefore, another parametric study was performed using various operating conditions for the overall all system vs. the net power produced from the OTEC plant as shown in Figure 5.24. Where the first case assumes the ECEM hydrogen conversion efficiency is that of a PEM electrolyzer (4.5 kWh/m^3), the second case has no fuel production (only power production and district cooling are considered), and the third and the final case assess the overall

efficiency based on the current status of the ECEM reactor. The maximum overall energy efficiency of the cycle was found to be 8.0, 8.6, and 7.3% for cases 1,2, and 3. The corresponding net power output of the cycle was found to be 13.6GW, with a cooling capacity of 69.0 GW.

In Figures 5.25 and 5.26 the energy and exergy efficiency of the OTEC cycle with no cooling or methanol production is shown. The sensitivity analysis was performed to by varying the ammonia flow rate of both stages, operating within a warm and cold-water flow rate of 50,000 kg/s and 28,450 kg/s. It was found that the peak performance of the cycle was achieved at an ammonia flow rate of 1200 kg/s (first stage) and 984 kg/s (second stage).

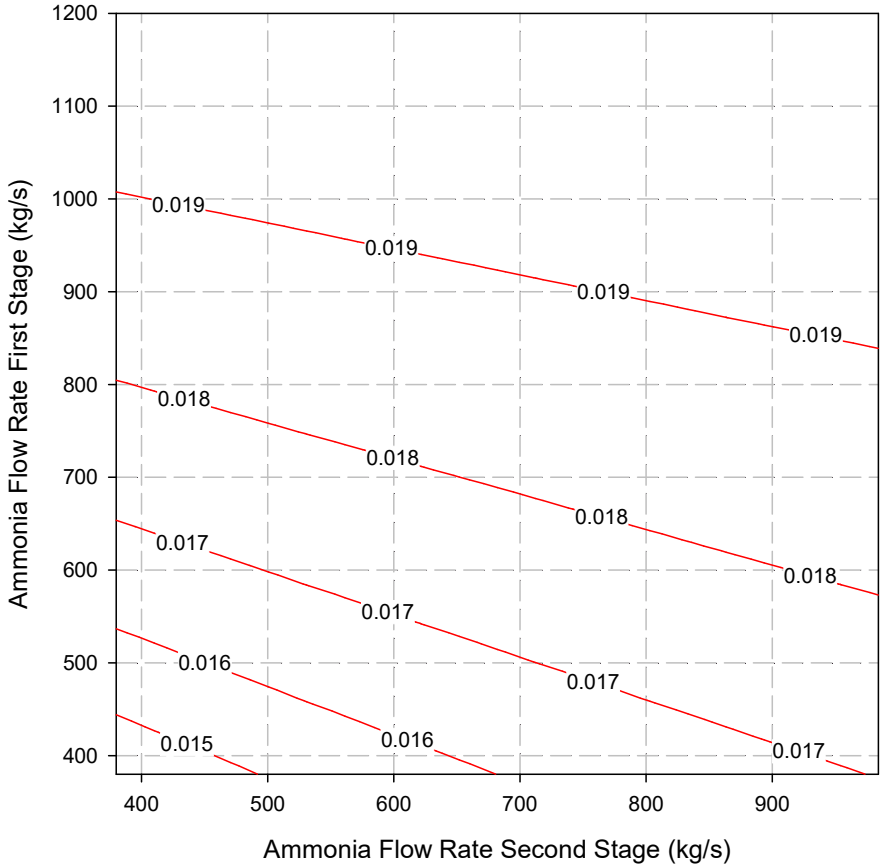

Figure 5.25: Results of the parametric study on ammonia flow rates and their effect on the OTEC energy efficiency

The corresponding energy and exergy efficiency were found to be 1.998% and 27.78%. the net power produced from the cycle at the peak performance point was 55.1 MW of

electricity. This comes as the working fluid in both stages of the OTEC plant are operating at the maximum flow rate that could experience a phase change into superheated gas. As expected, the first stage could operate at a higher flow rate than that of the second stage, as the temperature of the warm water decreases after heating the working fluid in the first stage. However, one should also note that the second stage is operating at 82.0% of the flow rate of the first stage. The counterflow arrangement of the warm and cold-water flow allows for the slightly lower second stage flow rate, as the cold water enters through the second stage condenser, which provides larger cooling duty than that for the second stage.

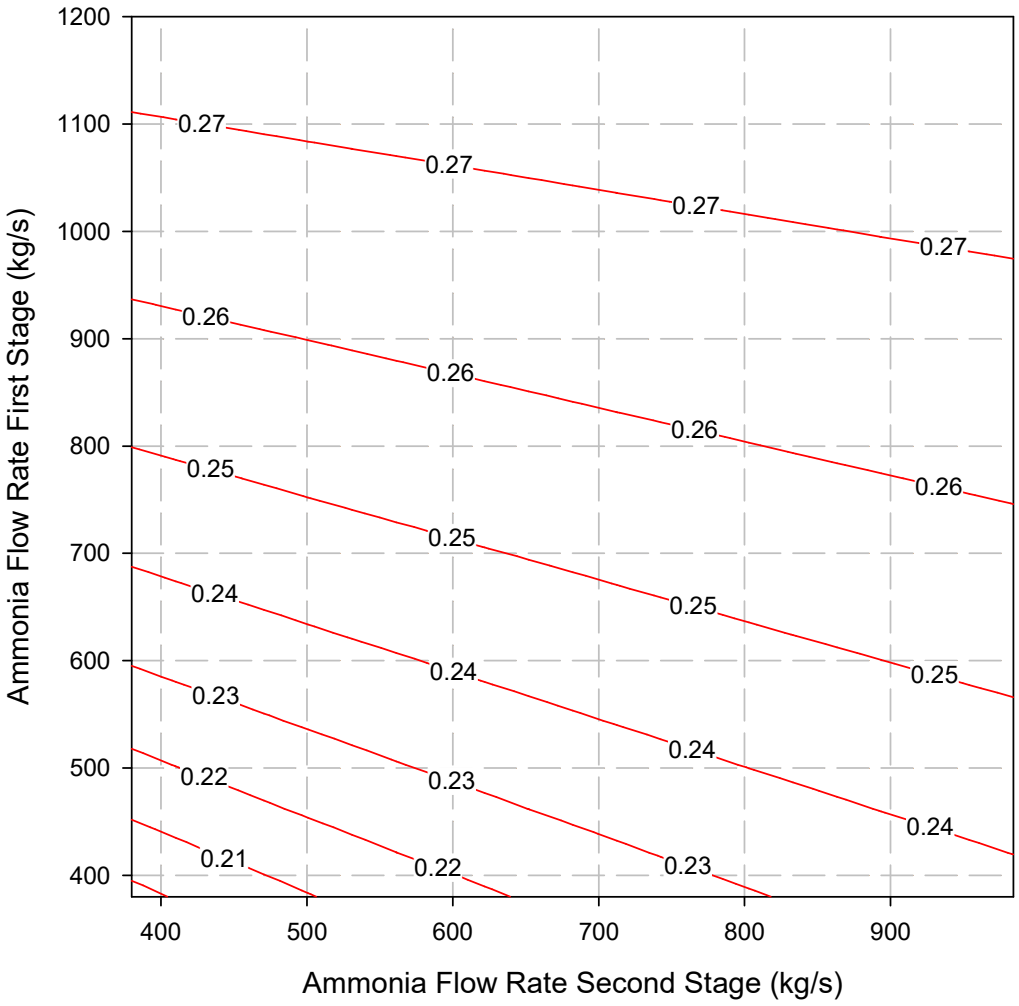

Figure 5.26: Results of the parametric study on ammonia flow rates and their effect on the OTEC exergy efficiency

In Figure 5.27 a parametric study was performed on the carbon dioxide output by varying the ECEM reactor conversion efficiency from its current status to its possible future status of PEM conversion efficiency. The peak hydrogen and carbon dioxide production rates were as follows 2.08kg/s and 0.28 kg/s at a PEM conversion rate of 4.5 kWh/m^3-H_2 [15]. The corresponding power production rate from the OTEC plant was found to be 55.1 GW. This shows the potential energy efficiency of the proposed system as ECEM reactors' conversion efficiency increases with more research and development.

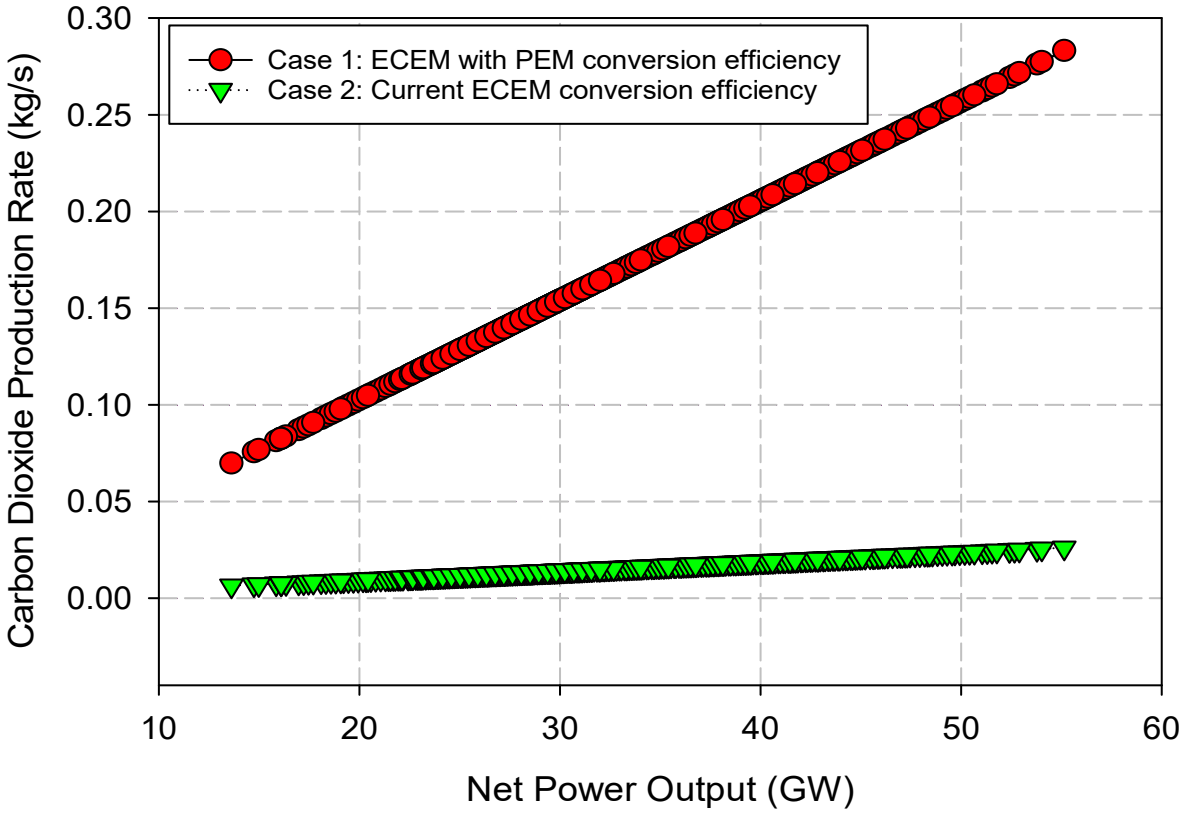

Figure 5.27: Carbon dioxide production rates by varying the ECEM reactor conversion efficiency from its current status to its future possible status of PEM

Figure 5.28 displays the methanol production rate as the OTEC net power output increases at two different ECEM hydrogen conversion efficiencies (49 and 4.5 kWh/m^3-H_2 [15]). It was found that the methanol production was found to be 0.37 kg/s and 0.034kg/s at an ECEM hydrogen conversion efficiency of 49 and 4.5 kWh/m^3-H_2 at a power input from the OTEC plant of 13.6 GW. The maximum methanol production was found to be 1.48 kg/s and 0.14 kg/s at an ECEM hydrogen conversion efficiency of 49 and 4.5 kWh/m^3-H_2 at a

power input from the OTEC plant of 55.1 GW. The results will scale linearly as the ECEM production rate is linear to the power input from the OTEC plant.

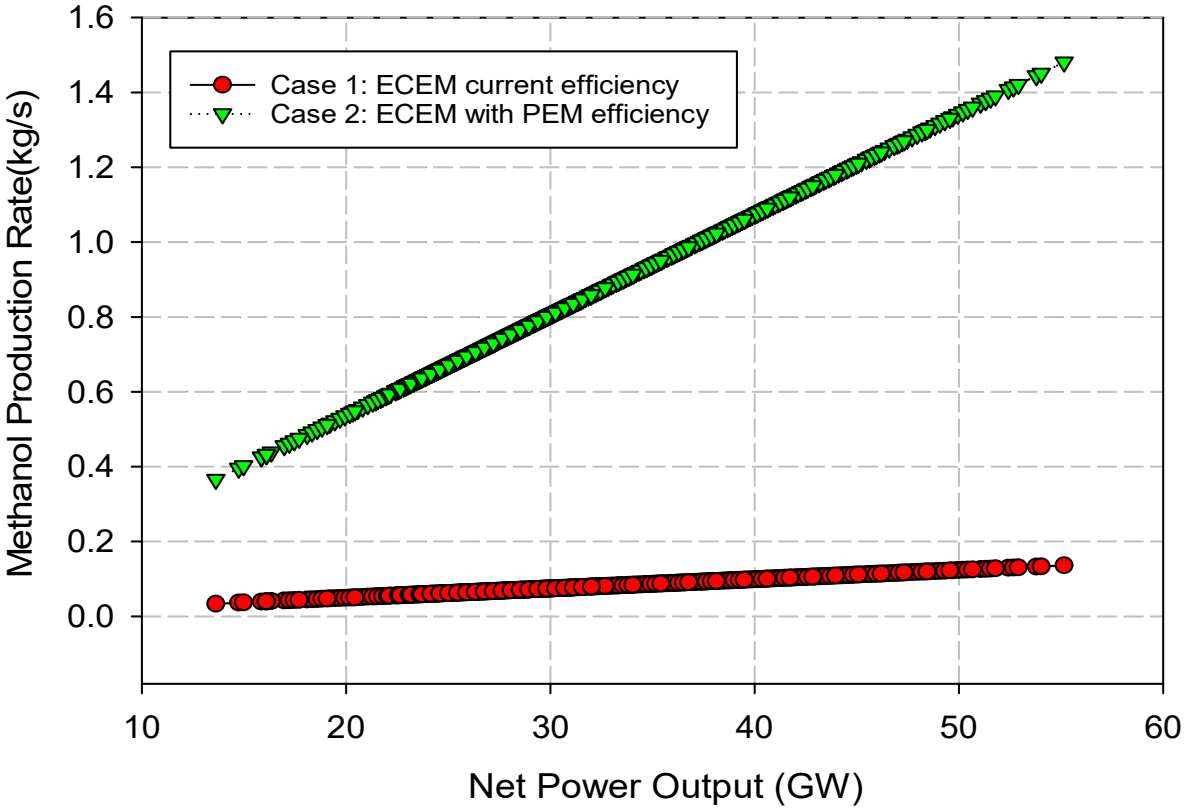

Figure 5.28: Methanol production rate as the OTEC net power output increases at two different ECEM hydrogen conversion efficiencies

In Figure 5.29, a parametric study is shown, with various temperatures and volume flow rates of warm air entering the heat exchanger to be cooled. The heat exchanger outlet temperature in all cases was fixed to 14°C. The warm air temperatures ranged from 25 to 45°C using 5°C increments in temperature for each study. In all the cases the rejected cold seawater flow rate was fixed at 22,500kg/h and was being rejected at a temperature of 13°C after the two-stage Rankine cycle. As for the warm air pressure, it was fixed at 5 bar throughout the parametric study. The maximum cooling duty in the heat exchanger was found to be 459.6 GW of potential cooling capacity. The maximum cooling capacity assumed a warm air temperature inlet of 45°C at a volume flow rate of 1,000,000,000 cum/min. As for the methanol production system and the OTEC plant state points they are presented in Tables 5.4 and 5.5 .

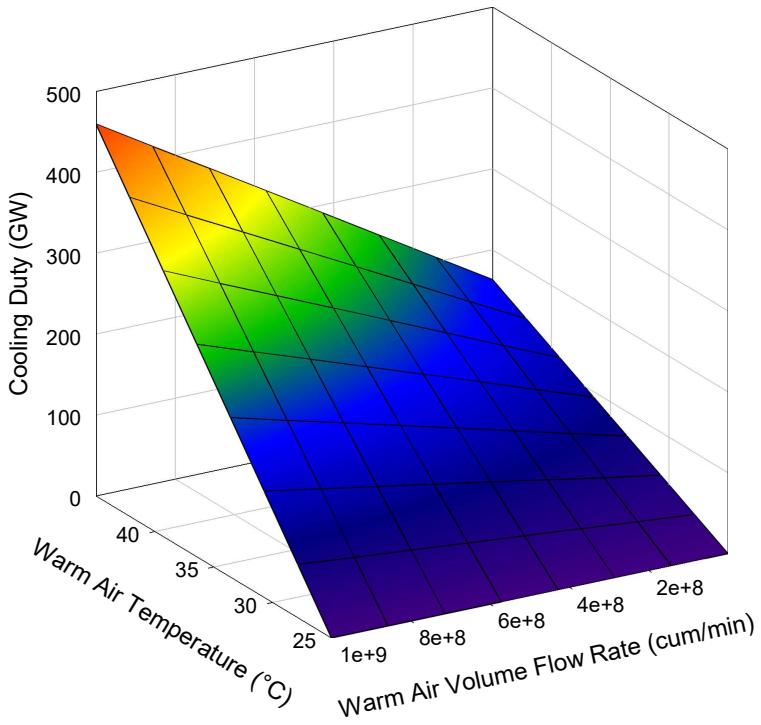

Figure 5.29: The parametric study results of district cooling duty with varying warm air inlet temperatures and volume flow rates

Table 5.4. Methanol production system state points (Based on the Aspen plus flow sheet fig. 3.7)

From	To	Temperature	Pressure	Specific enthalpy	Specific entropy	Energy rate	Mass flow rate
		°C	bar	kJ/kg	kJ/kg-K	MW	kg/s
	CO2COMP	25.0	1.0	-8,942.3	0.06	-3.94	0.44
	H2COMP	25.0	1.0	0.6	0.00	0.00	0.06
B1	B9	219.9	49.0	-7,678.3	-1.38	-3.84	0.50
B7	B8	39.0	49.8	-7,837.2	-2.09	-3.92	0.50
B8	B4	219.9	50.0	-7,358.2	-0.88	-3.68	0.50
CO2COMP	B7	49.9	49.8	-8,967.3	-0.71	-3.95	0.44
H2COMP	B7	49.9	49.8	387.0	-14.93	0.02	0.06
B4	B1	219.9	50.0	-7,678.5	-1.40	-3.84	0.50
B9	B10	219.9	5.0	-7,279.9	0.87	-3.64	0.50
B10	B11	219.9	49.0	-7,279.5	-0.65	-3.64	0.50
B11	B12	219.9	49.0	-7,672.1	-1.37	-3.84	0.50
B12	B13	219.9	48.5	-7,672.0	-1.37	-3.84	0.50
B13	B19	219.9	48.5	-7,668.8	-1.36	-3.84	0.50
B16	B17	49.9	48.5	-8,538.4	-3.57	-4.27	0.50
B17		49.9	12.0	-7,639.3	-1.06	-2.90	0.38
B17	B14	49.9	12.0	-11,154.7	-8.00	-1.34	0.12

Table 5.5. Double stage OTEC cycle state points (based on the Aspen plus flow sheet fig. 3.8)

From	To	Temperature	Pressure	Specific enthalpy	Specific entropy	Mass flow rate	Specific energy
		°C	bar	kJ/kg	kJ/kgK	kg/s	kJ/kg
	NH3PUMP	11.5	6.5	-3999.3	-11.3	400.0	323.5
TURBINE	WHX2	15.9	7.5	-2751.9	-7.0	400.0	284.4
CPUMP	CHX	4.5	1.7	-15959.6	-9.4	19310.3	3.3
	CPUMP	4.5	1.0	-15959.7	-9.4	19310.3	3.2
WHX	TURBINE	21.4	9.0	-2734.4	-7.0	400.0	307.9
WPUMP	WHX	26.0	1.3	-15867.5	-9.1	23862.0	0.0
WHX	WHX2	21.0	1.3	-15888.6	-9.1	23862.0	0.2
	WPUMP	26.0	1.0	-15867.5	-9.1	23862.0	0.0

5.4 Results of System 4

In the following section, parametric studies, along with an energy analysis, will be presented for the proposed system bifacial solar system integrated with a lake-based Rankine cycle. The preliminary results of an offshore bifacial system, and the increase of energy production by capturing the reflection of the surface of the water.

5.4.1 Results of the Bifacial System

The performance of the proposed bifacial solar panel for offshore or cold isolated areas power production is assessed and discussed under various operating conditions. In the following section, an assessment of the actual performance of the bifacial solar panels and how it stands in comparison to the single face panel will be discussed. All the cases are ran as discussed earlier for 7 hours with a constant solar radiation intensity of 200 $W/m^{2,}$ which is the average of the entire selected month.

5.4.1.1 Results of the Gird Independence Study

A mesh independent study was performed to observe the effect of the number of elements on the incident power received from the sun on both surfaces of the Bifacial PV panel. In the case of the front upwards facing surface the incident power received for the last two mesh intervals (1.57 and 2.77×10^6) was simulated to be 8,227.1 and 8,124.2W. The change in the last two intervals was calculated to be 1.25%. As for the downward-facing surface, the last three mesh intervals reported an incident power being reflected from the surface of the water as follows 2322.6, 2322.6 and 1935.5W at mesh intervals of 1.22, 1.58, 2.77×10^6 elements. The percent change for the last two intervals were calculated to be 0 and 16.6%.

from the reported mesh independent study, it can be seen that as the mesh is transformed from 1.58×10^6 elements to 2.77×10^6 elements, the resulting incident power on the PV panel surfaces have less drastic changes and become steady. For example, for the upward-facing panel when the mesh is transformed from 3.62×10^4 elements to 1.18×10^5 elements there was a 20.2% change in results. A similar case was found with the downward-facing where the rate of change was calculated as 30, 57.1, 33.3, and 50% for the first 4 intervals in the mesh independent study. This drastic change could be related to the optics module in the simulation module. This comes as the reflection was performed using 6000 rays and as the mesh becomes finer, more of these rays would be reflected.

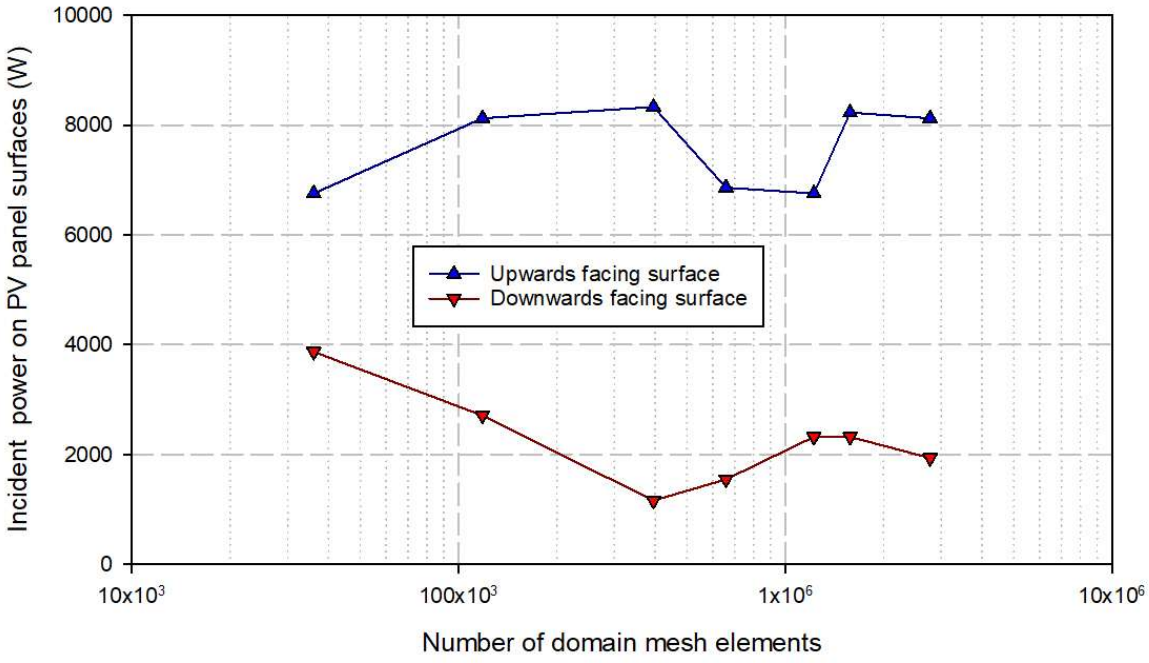

Figure 5.30: Mesh independent study for the incident power on PV panel for the front and rear surface

5.4.1.2 Number of Rays Independence Study

An incident ray independent study was performed to observe the effect of the number of incident rays on the incident power received from the sun on both surfaces of the Bifacial PV panel. In the case of the front upwards facing surface, the incident power received for 6000 and 7000 rays was simulated to be 7872.8 and 7877.4W. A 0.58% change was experienced when increasing the number of rays from 6000 to 7000 rays; the smallest

change experienced throughout the study on the upward-facing surface. The average rate of change throughout the study on the upward-facing surface was calculated to be 1.43%, where the maximum change was found to be 2.8% when increasing the rays from 3000 to 4000 rays. As for the downward-facing panels, there was a higher average rate of change throughout the study than that of the upward-facing panels. In the case of the downwards facing surface, the incident power received for 6000 and 7000 rays was simulated to be 2480.7 and 2435.9W. The average reported change was calculated to be 10.4%, where the maximum rate of change was calculated as 22.2% when the number of rays increased from 4000 to 5000. The lowest rate of change was found to be 1.84% when the number of rays increased from 6000 to 7000. It can be seen in both cases upward and downward facing surfaces, stop experiencing any drastic change past 6000 rays. The number of incident rays throughout the assessment of an offshore PV panel was kept constant at 6000 incident rays, as no significant changes where experienced after that.

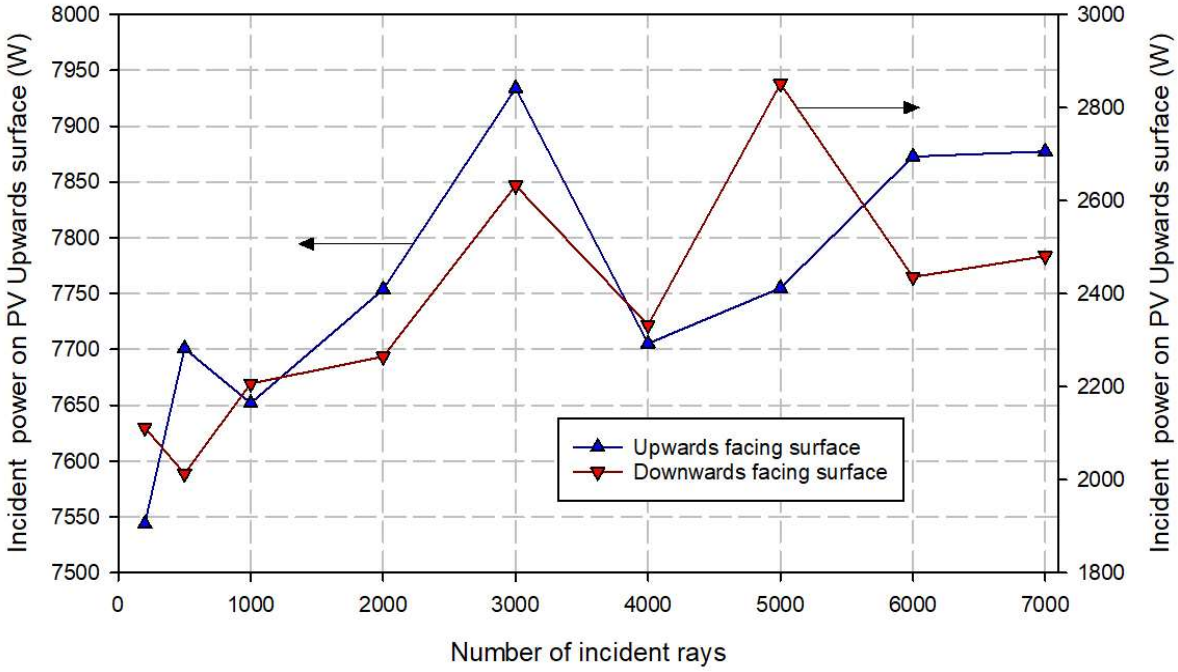

Figure 5.31: Ray independent study for the incident power on PV panel for the front and rear surface.

A study was performed to analyze the incident power ratio for an east/west facing solar panel. The incident power ratio allows for the assessment of the effectiveness of a bifacial module at varying solar positions throughout the day relative to a single face solar module.

The readers should note that the single facing module shares the same geometry and position as the bifacial module. The incident power ratio considers the total irradiance power received by the backward-facing PV panel relative to the front-facing PV panel. The results of the incident power ratio are shown in figure 5.32. When the suns position is at 30° a 13% increase in power is experienced by the bifacial module. The module's power output continues to increase by 31% when the suns position is at 90°. However, after the sun's positions passes 90° the backward-facing PV module receives more solar irradiance power than the front. At 120° the backward-facing module is producing 183% more power than the front. Finally, at 150° the backward-facing module is producing approximately 600% more power than the front module. The drastic increase in power is due to the low irradiance power received by the front-facing module as the suns position passes 90°.

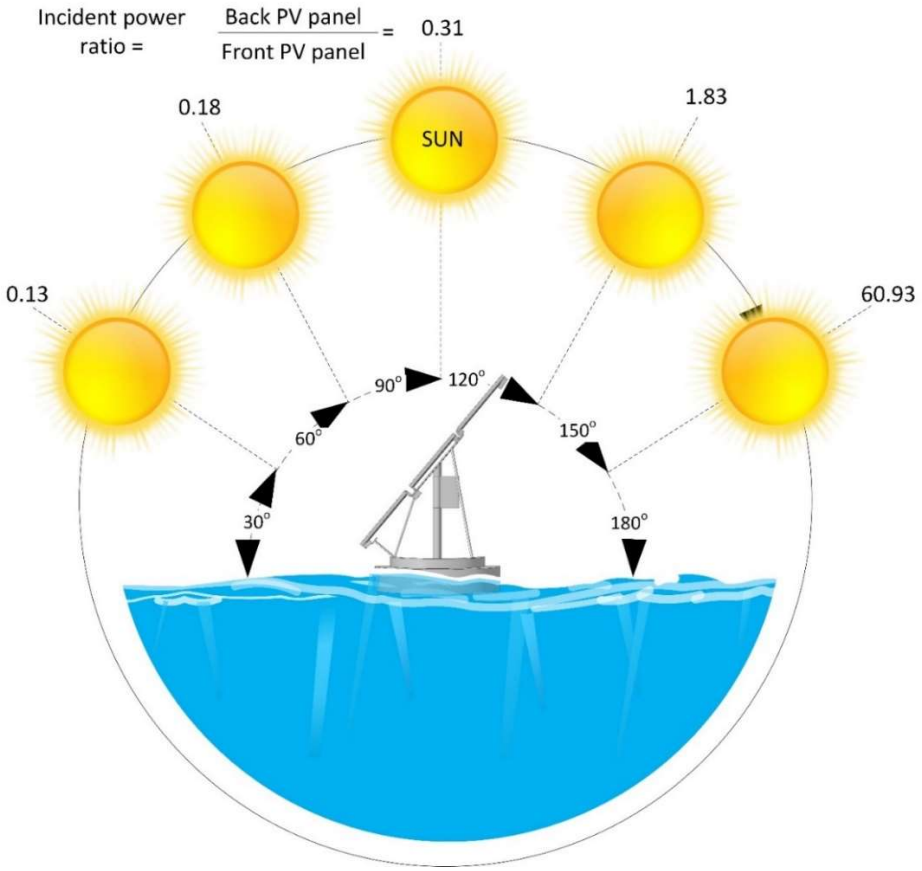

Figure 5.32: Variation of the incident power ratio with the variation of the sun angle on an east facing solar panel for six various incident angles.

Another study was performed to analyze the incident power ratio for a north/south facing solar panel. The study was performed to assess the incident power ratio effectiveness of a

bifacial module that is facing north/south in comparison to east/west throughout the day. The incident power ratio considers the total irradiance power received by the backward-facing PV panel relative to the front-facing PV panel. The results of the incident power ratio are shown in Figure 5.33. When the suns positions is at 30° a 55% increase in power was experienced by the bifacial module compared to the 13% from the east/west facing module. The modules incident ratio continues to decrease to 25% when the suns position is at 90°compared to 31% in the previous study. However, after the suns positions passes 90° the incident power ratio continues to increase to 55% at 150°. The north/south facing module performed better than the east/west as both sides of the module received solar irradiance throughout the simulation. The east/west facing module front-facing panel were receiving negligible amounts of solar irradiance when the suns position passed 90°. It is recommended when such modules are deployed in the northern hemisphere, they should be facing the north/south positions.

A study was performed to analyze the incident power ratio for a east/west facing solar panel with a wavy water surface. This assessment was performed to accommodate for the ripples that occur in the water as the tide changes in the waters. The wavy waters will create the incident rays to scatter therefore affecting the module incident power ratio. The readers should note that the geometry is identical in all the studies for the bifacial module. The results of the incident power ratio are shown in Figure 5.34. When the suns positions is at 30° a 13% increase in power is experienced by the bifacial module, which is similar to that of the still water results. The module's power output continues to increase by 33% when the suns position is at 90°, which is a 3% gain in incident power ratio relative to the still water results. However, after the suns positions passes 90° the backward-facing PV module receives more solar irradiance power than the front. At 120° the backward-facing module is producing 116% more power than the front. Finally, at 150° the backward-facing PV module is producing approximately 269% more power than the front module. The drastic increase in power is due to the low irradiance power received by the front-facing module as the suns position passes 90°. It should be noted that the effect of the wavy water on the incident power ratio is negative past 90° relative to that of the still water. However, the overall performance is still in favor of that of a bifacial module rather than a single face module.

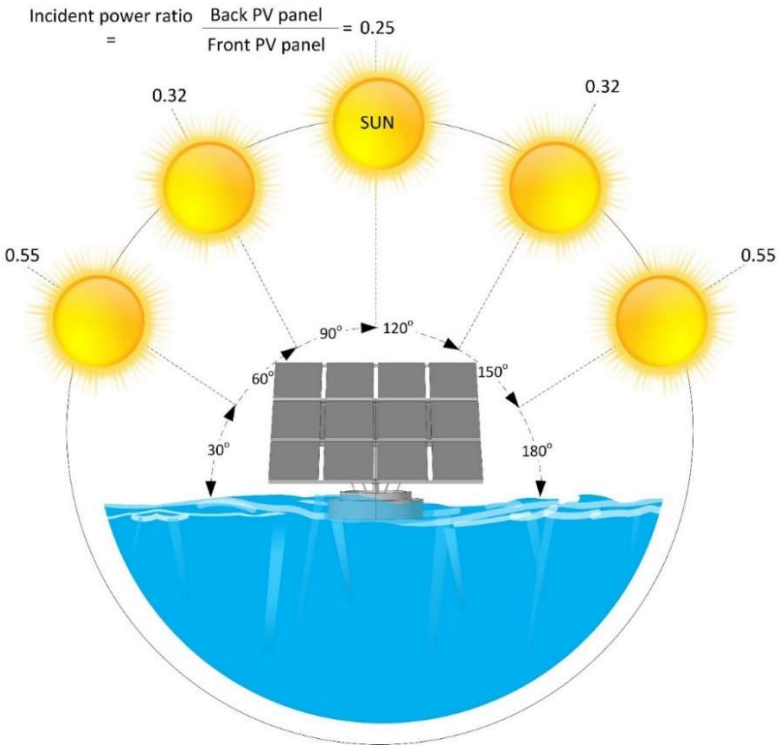

Figure 5.33: Variation of the incident power ratio with the variation of the sun angle on a north facing solar panel for six various incident angles.

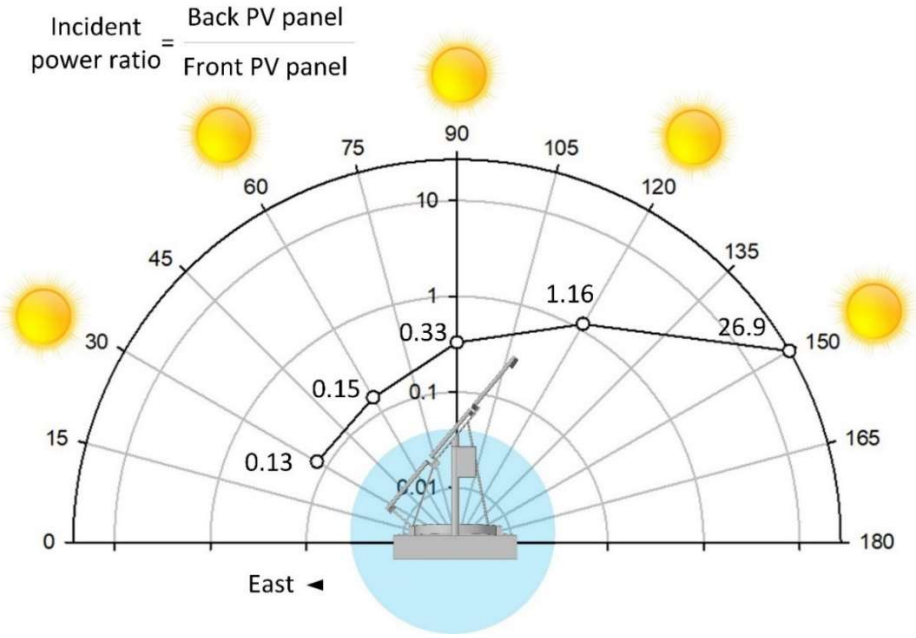

Figure 5.34: Variation of the incident power ratio with the variation of the sun angle on an east facing solar panel for six various incident angles.

Another study was performed to analyze the incident power ratio for a north/south facing solar panel with wavy water. The study was performed to assess the incident power ratio

effectiveness with wavy waters with a bifacial module that is facing north/south in comparison to east/west throughout the day. The results of the incident power ratio are shown in Figure 5.35. When the suns positions is at 30° a 49% increase in power was experienced by the bifacial module compared to the 13% from the East/West facing module with wavy water. The modules incident ratio continues to decrease to 30% when the suns position is at 90°compared to 33% in the previous study. However, after the suns positions passes 90° the incident power ratio continues to increase to 49% at 150°, similar with the case with the still water. even with the wavy waters the north/south facing module still performed better than the east/west facing module. This is mainly because the East/West facing module front-facing panel were receiving negligible amounts of solar irradiance when the suns position passed 90°, as mentioned previously.

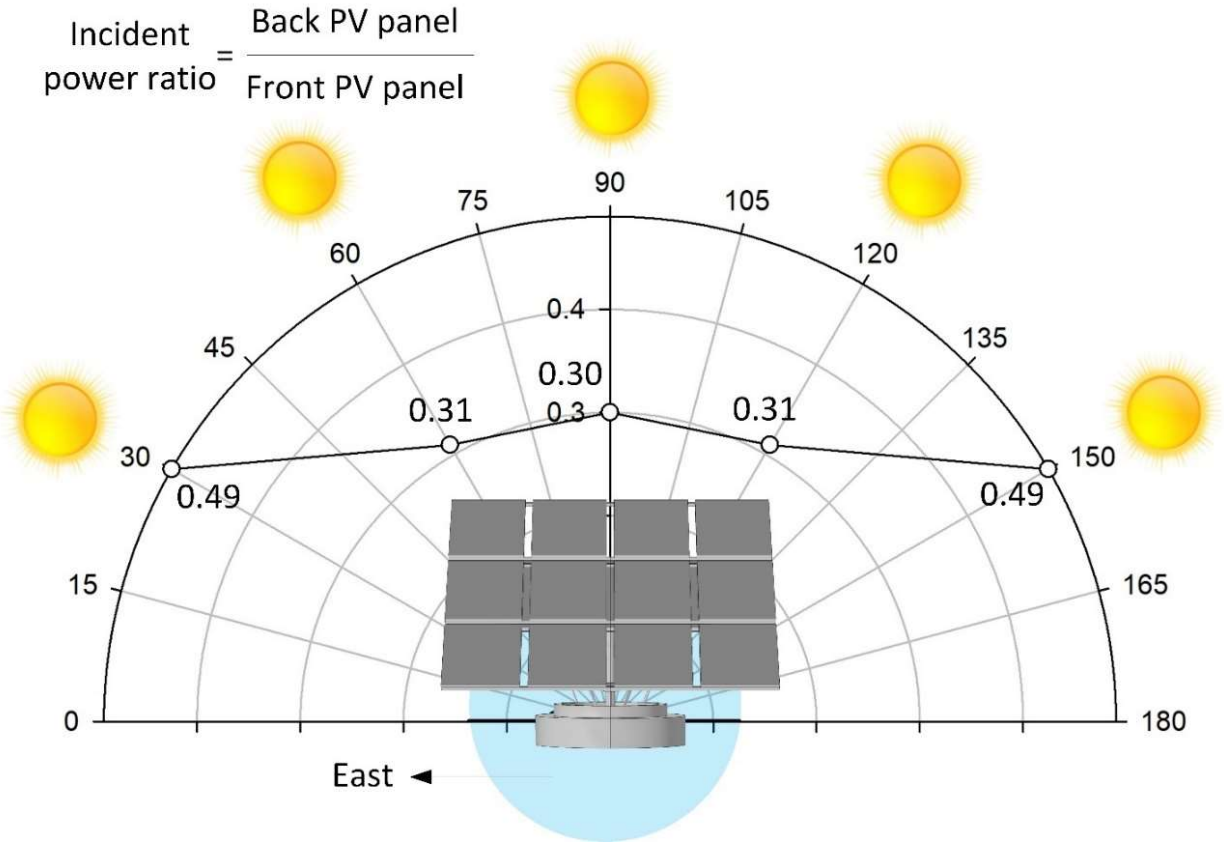

Figure 5.35: Variation of the incident power ratio with the variation of the sun angle on the north/south facing solar panel for six various incident angles.

In a study, the energy efficiency of a bifacial PV module was assessed relative to a mono-facial PV module. In Figure 5.36a, the energy efficiency of an east/west facing module was

assessed. The maximum energy efficiency achieved was 25.3% at an angle of 30°. At 90° the efficiency was calculated to be 20.2%. However, as the angle of the sun passes the 90° position, the efficiency of the bifacial module drops to 11.5% and 11.9% at the 60° and 30° positions. Throughout all the suns positions, the east/west configuration achieved a maximum of 11.9% gain in energy efficiency, mainly due to the backward-facing PV panels, capturing the reflected solar irradiance at the 30° position. A similar case can be seen in Figure 5.36b as the maximum energy efficiency was calculated as 18.6% at the 90° position with a 3.5% gain over the mono-facial module. The maximum gain in efficiency was achieved at the 60° position, where the gain was calculated as 4.6%. In this study, it can be seen that the overall the bifacial module achieved efficiency gains in all positions and orientations over the mono-facial module.

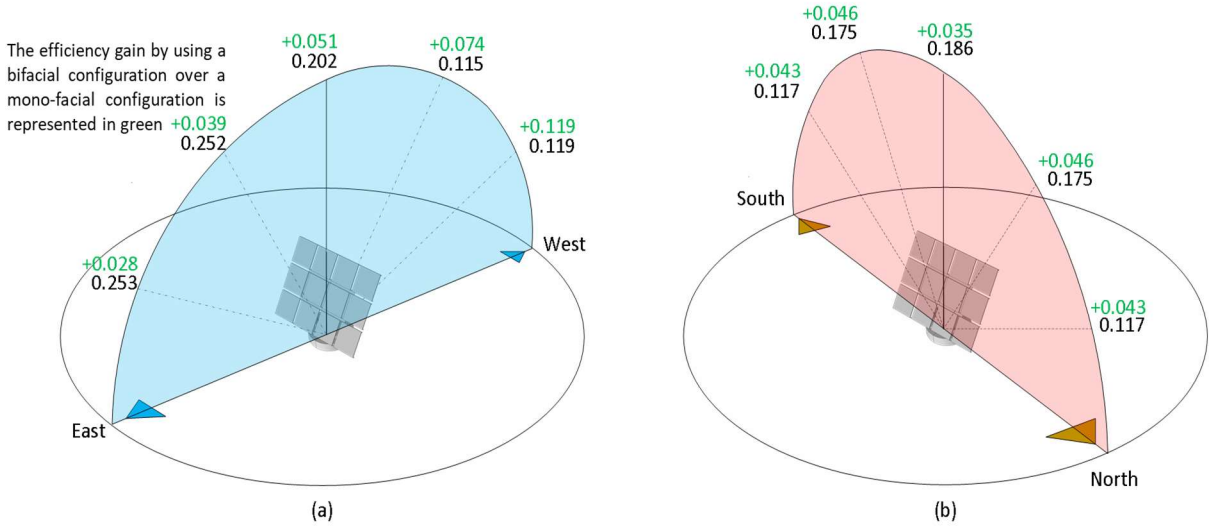

Figure 5.36: Variation of the energy efficiency and efficiency gain with the variation of the suns angles as well as the module orientations: (a) east/west (b) north/south.

5.4.1.3 Solar Bifacial System

Two orientations of the bifacial solar panel are considered, the first with the upward face facing north and the second facing east. In order to ensure the results produced by the model are independent of the mesh size and number of simulated rays by the simulated window from the sun an independence study for each is conducted and discussed in the coming sections.

5.4.1.4 Grid Orientation and Independent Study

A mesh independent study was performed to see the effects of the number of mesh elements on the simulation results. The study was also performed to ensure that the results of the simulation are independent from mesh size. The result of the study is shown in figure 5.37. The study tests the mesh quality of the total incident power received by the bifacial solar PV module. The figure shows that an increase from 4.0×10^5 to 6.0×10^5 mesh elements resulted in a 2.3% change for the upward-facing panel, and a 3.9% change for the backward-facing panel. In another case when the number of elements increased from 12,000 to 26,000 elements, the total incident ray received by the front panel experienced a lower change than the last step in the study. However, the backward facing panel experienced a 5% increase. For the remainder of the studies a mesh size of 4.0×10^5 elements.

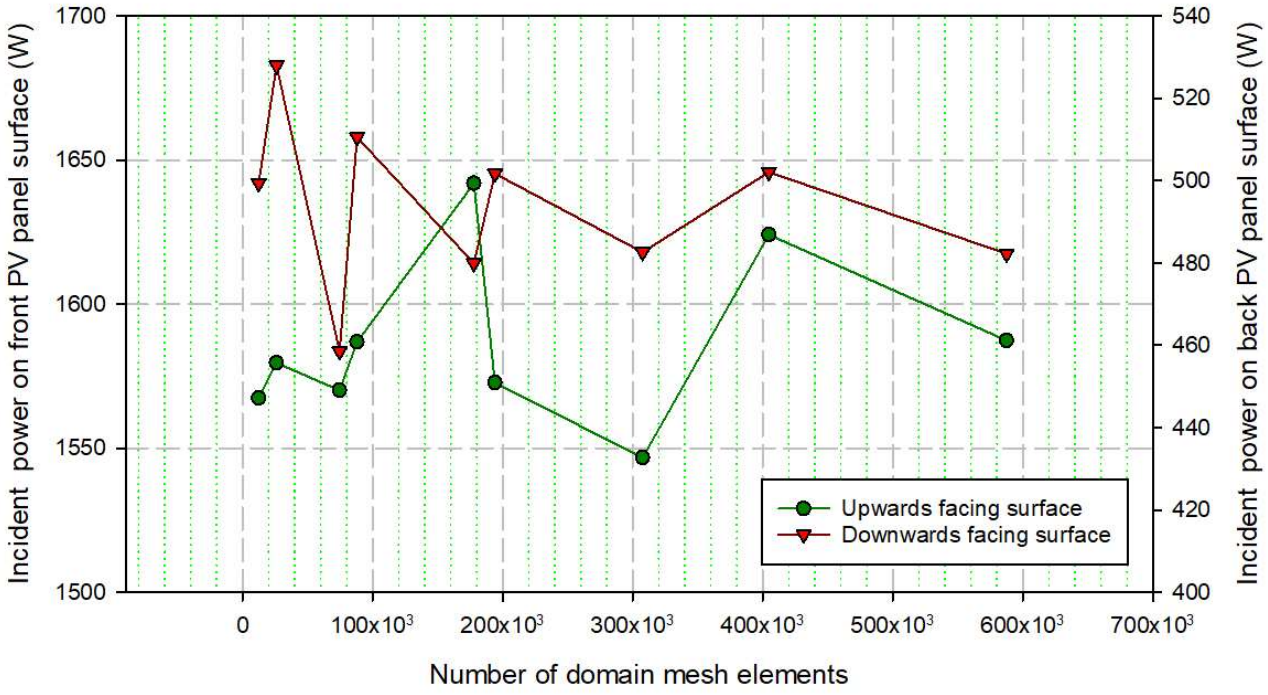

Figure 5.37: Mesh independence study of the proposed model simulating the incident radiation rays on the surface of the PV panel and the wavy sea surface and their refraction, absorption and reflection to the bifacial solar PV panel faces.

5.4.1.5 Number of rays' independence study

A ray's independence study was performed for the number of simulated solar rays as it is directly proportional to the incident power that the surfaces of the bifacial PV modules

experience. As seen in figure 5.38 it can be seen that when the rays increase from 0 to 6000 rays that the change with the incident power is significant for both upward and downward facing panels. However, when the rays increase from 7000 to 8000 rays for both PV surfaces. For the front-facing panel, the incident power changes by 1.3% with an increase from 7000 to 8000 rays for an area of 196 m^2. For the backward-facing panel, the incident power experienced a change of 1%. For the remainder of the study, 7000 rays were used, which translates to 35 rays/m^2.

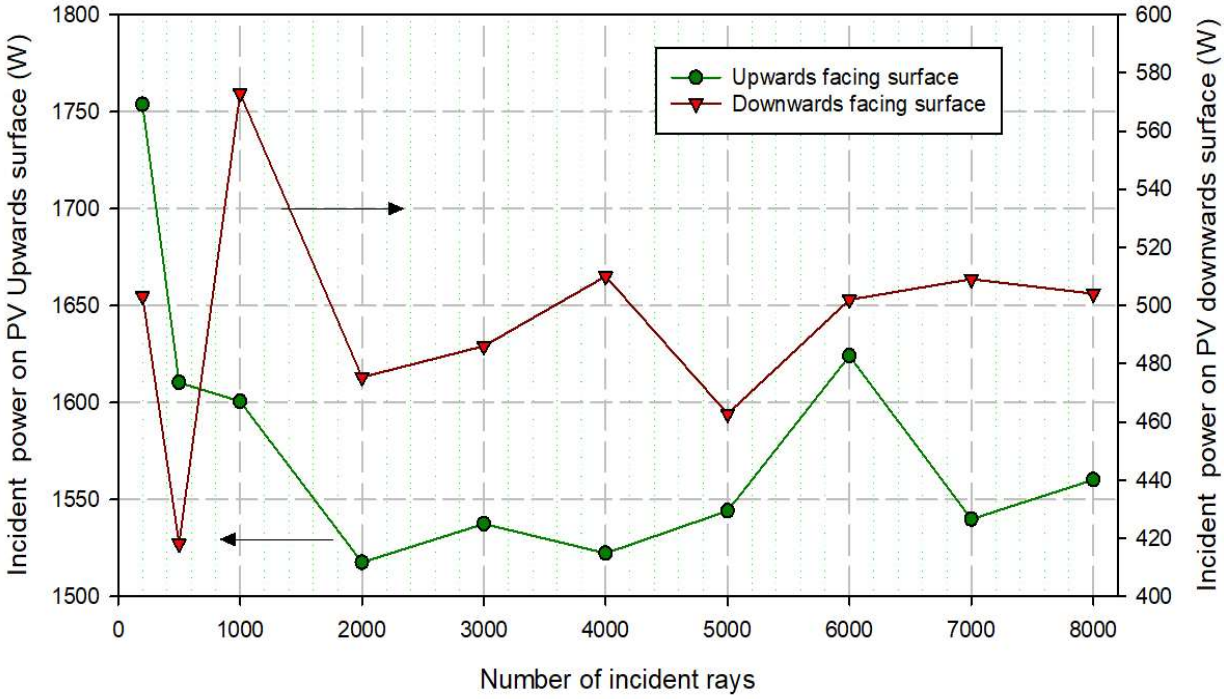

Figure 5.38: Ray independence study of the proposed model simulating the incident radiation rays on the surface of the PV panel and the wavy sea surface and their refraction, absorption and reflection to the bifacial solar PV panel faces.

A grid independence study was performed on the heat transfer aspect of the bifacial module using a various number of mesh elements. It can be seen based in Figure 5.39 that the change in the various elements sizes yields very small changes even when using a coarser mesh. The difference in change between the coarsest mesh and the finest mesh is 0.09%. However, when using small pipes, one should consider using a finer mesh to capture the geometry of the small pipe found within the heat exchanger.

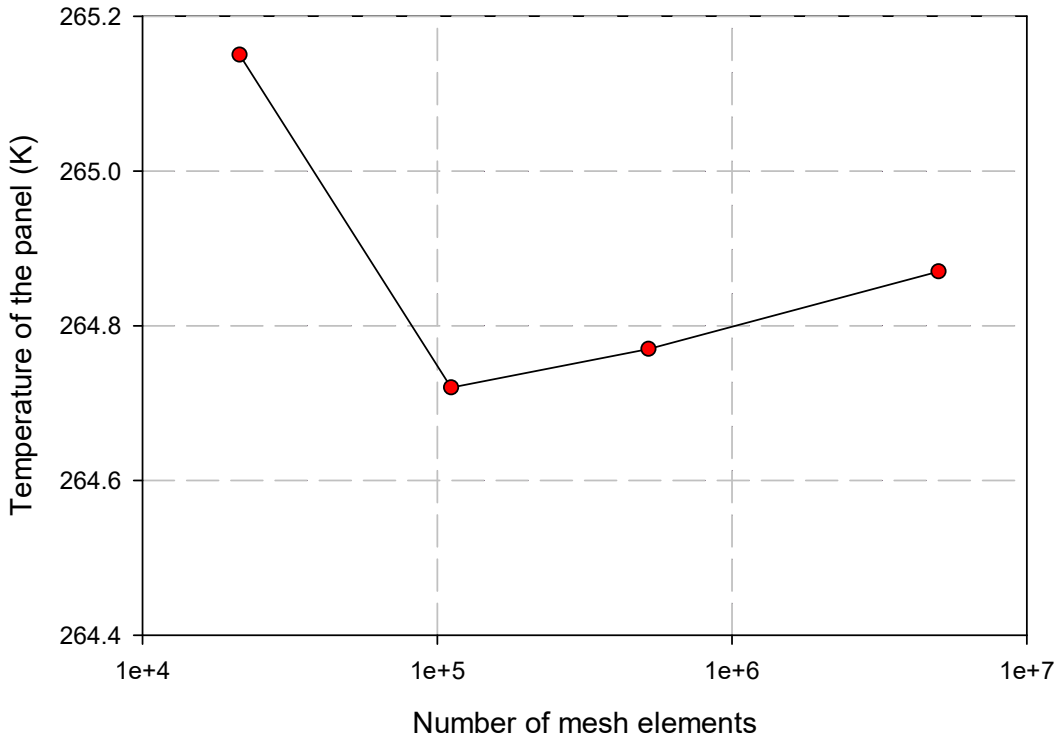

Figure 5.39: Grid independence study of the proposed model simulating the heat transfer physics within the simulation, where the temperature of the panel is considered.

5.4.1.6 Results for the Month of May

In this study, the performance of the bifacial PV module is tested based on the geological location of Ottawa, Ontario. The module was tested in two orientations east/west and north/south facing. The solar irradiance values and simulation takes place in the month of May. The assessment method for the performance of the bifacial module assesses the additional power generation from the back PV panel relative to just having a mono facial arrangement. It should be noted that the mono and bifacial PV panels are positioned over a large body of water such as a lake. Figure 5.39 displays the results of an east-facing front PV panel. The maximum amount of power for the east-facing front panel was produced at 10 am and 1 pm. At 10 am, the majority of the incident rays mainly hit the front panel. The front panel produces about 80%, and the back panel produces 20%. However, at 1 pm, the case is different as the suns angle and location is different. It was found that at 1 pm that the front and back of the module produce the power at a 50:50 ratio. As the sun moves further west at 2 pm, the backward-facing panel starts to produce more power than the front, where 70% of the power is produced from the back, and the remaining 30% is produced by the front panel. It's very clear that the power production is dominantly the

backward panel after 1 pm, as the azimuth angle and location of the suns caters to the back panel. The power production increasingly becomes from the back panel, as seen in figure 5.39. At 3 pm, the back panel is responsible for 87% of the power production, and further increases to 91% by 5 pm. To conclude this section of the case study, the bifacial module eliminated the need for tracking, while increasing the power produced per area relative to a mono facial panel.

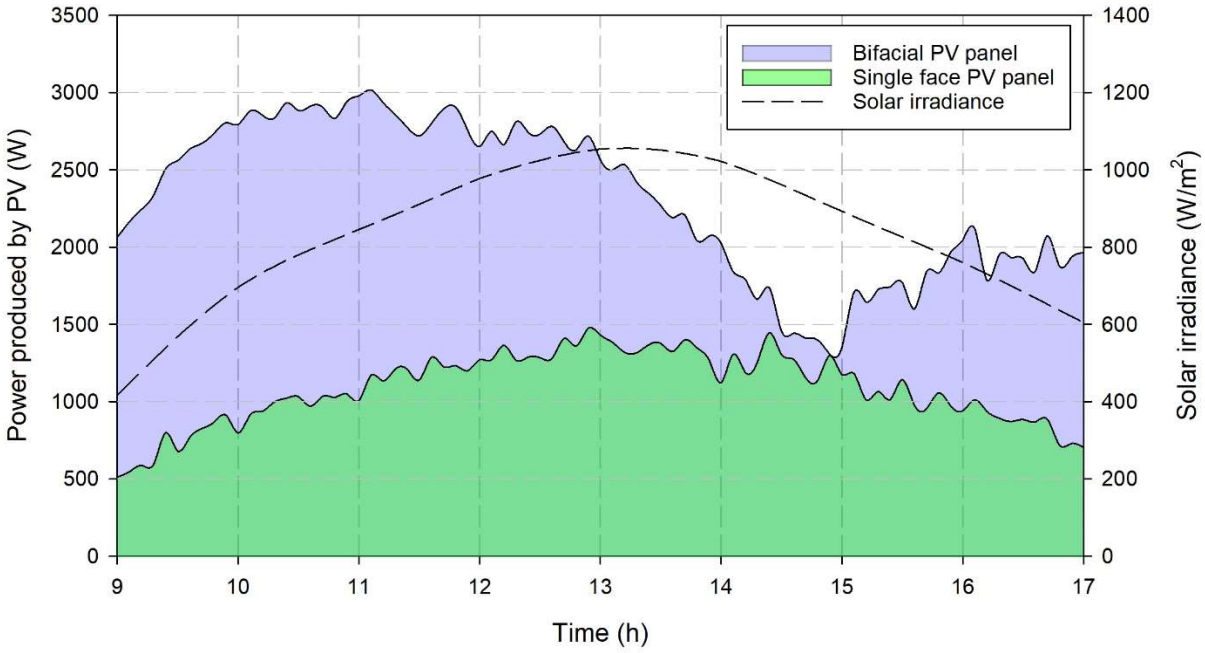

Figure 5.40: Variation of the solar irradiance, and the power production by a single face and bifacial PV solar panels throughout a day in month of May in Ottawa, Canada, with the solar panel facing east (time step: 0.1 h).

Again, like the previous study the effects on the orientation of the bifacial module is tested. In this section, a north-facing bifacial module is assessed. Figure 5.40 shows the total power produced by the north-facing bifacial module. Again, the module is assessed with a mono facial module with the same area and geometry. The solar irradiance and sun position in during the day is based on the month of May in Ottawa, Canada. Furthermore, the bifacial body is floating in a large body of water such as a lake. The case with the north-facing module varies significantly from the east facing module where the front face only accounts for 56% of the power produced at the beginning of the simulation time compared to the previous 80% in the case of east facing. Throughout the day the front facing panel remains to produce the majority of the power production, except the last hour of the day,

where it produces 36% of the total power produced. Comparing the east and north facing bifacial modules, on a total power produced basis, shows that the east facing bifacial module produces 24% over the day, relative to the north facing bifacial module.

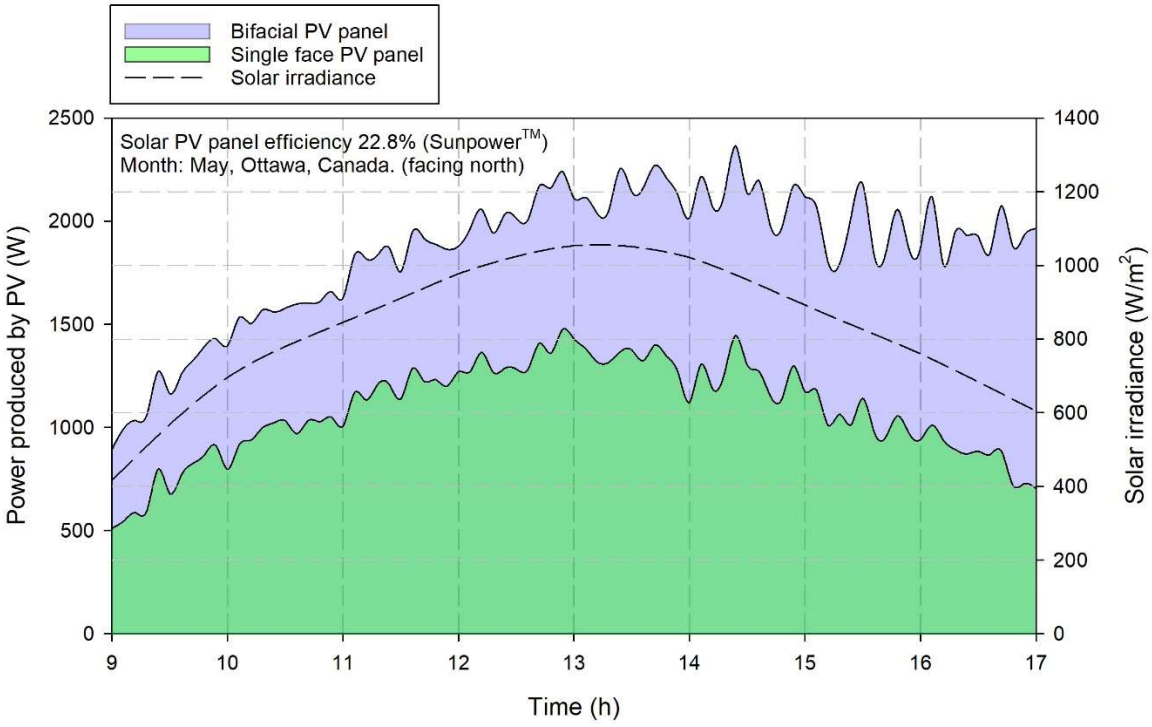

Figure 5.41: Variation of the solar irradiance, and the power production by a single face and bifacial PV solar panels throughout a day in month of May in Ottawa, Canada, with the solar panel facing north (time step: 0.1 h).

In order to conclude the case study for the month of May, the east-facing bifacial PV module yielded a 24% increase overall in power production. In the case of the north-facing bifacial modules, the front panel was utilized more than the back panel and yielded less power production as the previous statement indicates.

5.4.1.7 Results for the month of January

In this case study, the performance of a bifacial module is tested under the conditions of the month of January. January was chosen as it has the lowest solar irradiance values, where the solar irradiance during the day peaks at 450 W/m^2 on average and can on less frequent instances peak at 620 W/m^2. Again, the position of the sun during the day is taken based on an average day (January) in Ottawa, Canada. Figure 5.41 displays the results of the simulation of an east-facing bifacial PV module along with a mono facial PV panel for an assessment of the performance of the bifacial module. At the beginning of the day, the

power production is dominantly produced by the front PV panel, which generates 100% of the total power till 9 am. However, the back PV panel starts to generate noticeable power around 10 am, where it contributes 7% of the total power produced. As the day goes on, the dominance of the front panel decreases drastically as it passes 1 pm where the power production of the bifacial module starts to increase while the mono facial configuration is decreasing to 0% production. The front-facing panel nears 0% of the total power production as the time approaches 3 pm. According to the assessment of the bifacial panel relative to the mono facial configuration, shows that there is a 38% increase in total power production relative to the mono facial configuration in the month of January. Overall, there was a 66% decrease in total power production of the bifacial module relative to the month of May in Ottawa, Canada. This is highly due to the average maximum solar irradiance being significantly less in the month of January than it is in the month may, as well the day being shorter in the month of January, than the month of May. The maximum solar irradiance in the month of January is 58% less than it is in the month of May.

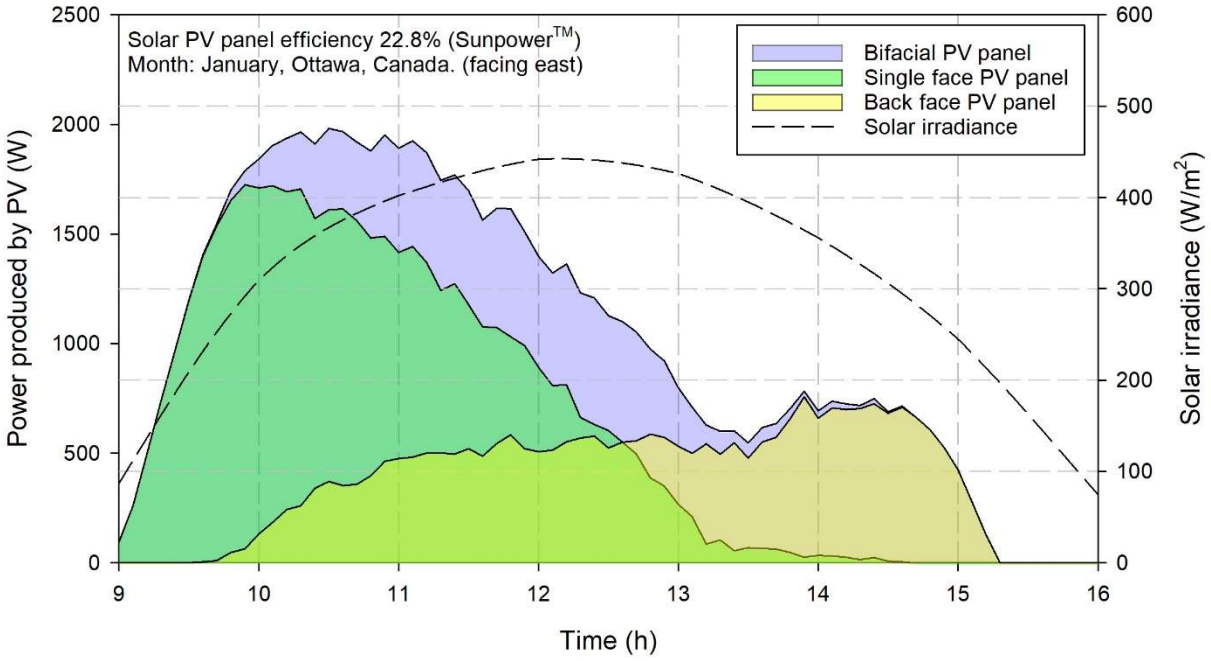

Figure 5.42: Variation of the solar irradiance, and the power production by a single face and bifacial PV solar panels throughout a day in month of January in Ottawa, Canada, with the solar panel facing east (time step: 0.1 h).

The orientation of the modules from this study is a very important factor in the case of total power produced. The assessment was made for the two orientations so the positioning can

be optimized for maximum power production. In the final study in this case the bifacial module was assessed in the north-facing orientation for the month of January. Figure 5.42 presents the results of the study of the total power produced throughout the day. Similar to the month of May the backward-facing PV panel in the bifacial module produced 97% of the total power. However, the total power produced increases by 28% in the month of January highly due to the presence of a front-facing PV panel. The total power produced is 57% lower than it is in the month of January than may.

To conclude this section of the study the minimum increase in power production when assessing the bifacial to the mono facial arrangement is 38% for the month of January. When assessing the orientation aspect of the study, the bifacial PV module produced 89% in the north-facing orientation than it did in the east-facing. In the case of orientation, the same conclusion can be made for the mono facial PV arrangement. The north-facing orientation yielded 62% of what was produced in the east-facing orientation.

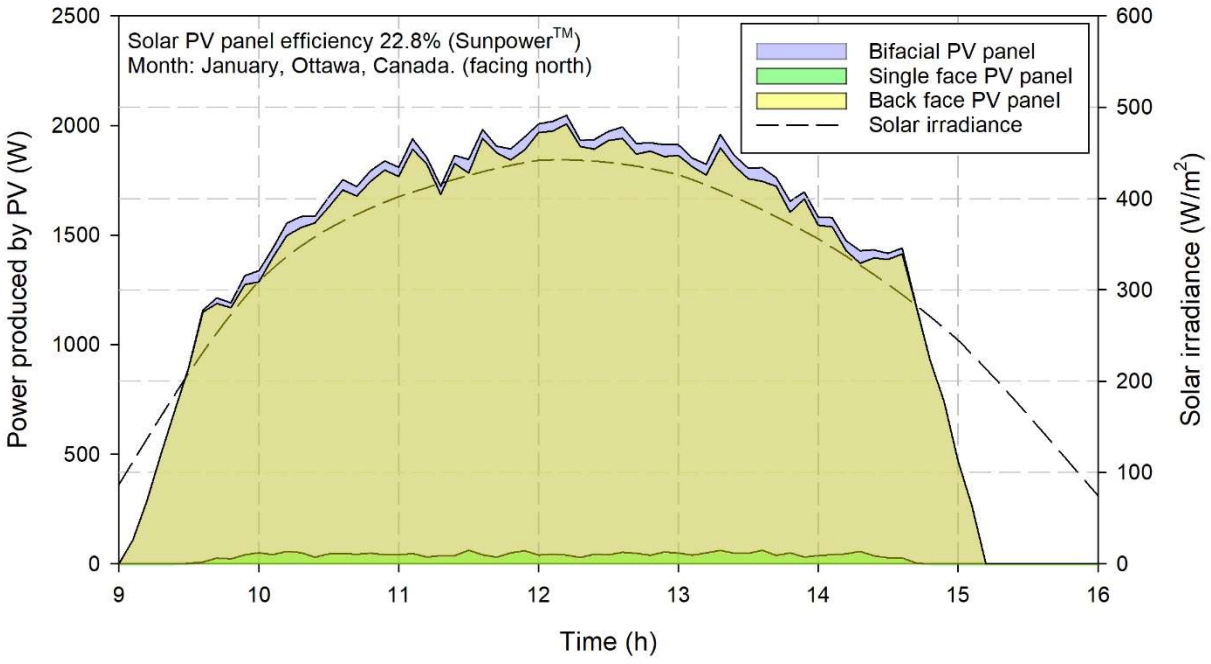

Figure 5.43: Variation of the solar irradiance, and the power production by a single face and bifacial PV solar panels throughout a day in month of January in Ottawa, Canada, with the solar panel facing north (time step: 0.1 h).

5.4.1.8 Results for an integrated heat exchanger with the bifacial PV module

In this case study, a north-facing bifacial module is being tested for its viability to be combined with a thermal power plant (Ammonia Rankine Cycle). The conditions are based on the average winter (January) temperature and maximum solar irradiance of Ontario, Canada. The average maximum solar irradiance and the average temperature in January were taken at 620 W/m^2 and -5^{o}C. The simulation assesses the concentration of heat transfer towards the center of the bifacial module, as shown in figure 5.32. The reasoning behind this system is to ensure operation under winter snow and ice conditions. The liquid ammonia is circulated through the panels, after being preheated by the lake water which remains at a minimum of 4^{o}C. The panels slowly over the night hours raises the temperature of the panels from -5^{o}C to an operational temperature of above 0^{o}C. The heating prevents ice or snow accumulation, which would prevent the panel from producing power at peak irradiance hours to its fullest potential. The module operational warm-up has no effect on the conversion efficiency of the solar panels, as they are rated for an operational temperature of 25^{o}C. Any lower temperature from 25^{o}C has no effect on the solar panel, respectively. The warmup of the panel from ambient temperatures allows the panel's nominal operational cell temperature to rise more than it would with the ambient temperature, which is taken at -5^{o}C (Average January temperature). The operational temperature under the ambient conditions would have led to an operational temperature of a maximum of 15^{o}C. However, with the use of the preheating method, the nominal operational temperature can range from 20-27^{o}C. These temperatures can cause the working fluid (Ammonia) to boil at a pressure and temperature of 9.25 bar and 21.5 ^{o}C. The superheated ammonia can then be used as the working fluid in a Rankine cycle. The simulated cycle was designed to perform similarly to an ocean thermal energy conversion plant, but for locations where the temperatures are cold. The results from the simulation will be discussed thoroughly in this section.

In Figure 5.43 a and b display the results for a bifacial module with an aluminum heat exchanger with a working fluid channel diameter of 10 cm. The working fluid is flowing at a mass flow rate of 0.0002 kg/s, the results are displayed for the peak solar irradiance period based on the previous sections results from the January case study for the north-facing bifacial module. The front panel receives 620 W/m^2, while the back panels only

receive 30% of the solar irradiance of the front panel. The maximum surface temperature for the bottom front panel reaches a steady-state temperature of 27.51ºC while the coldest temperature was in the center of the panel as the working fluid is actively boiling at a temperature of 21.5ºC which led to a temperature of 24.81ºC. The middle front panel achieved a similar steady-state temperature to the bottom front panel where the maximum steady-state temperature achieved was 27.12ºC. The minimum panel temperature was 24.38ºC. As for the top panel it achieved the lowest temperature of all the panels where the maximum and minimum surface temperature were simulated to be 26.05ºC and 23.28ºC. The temperature of the panels gradually drops as the ammonia vaporizes at the entry of the first panel and the thermal conductivity of the vaporized ammonia decreases as it passes through the other panels. Furthermore, this causes a cooling effect from the ambient conditions that cause a temperature decrease at each level of panels. As for the back facing panels, they experienced significantly lower temperature distributions than the front-facing panels. This is highly due to the lower amount of solar irradiance experienced by the backward-facing panels, which is only 30% of that experienced by the front-facing panels. The bottom back panel achieved the highest temperature distribution of any of the other back panels. The bottom panel experienced a maximum and minimum temperature of 21.86ºC and 19.92ºC. The middle panel experienced a maximum and minimum temperature of 21.20ºC and 19.26ºC. As for the top panel maximum and minimum temperature of 20.11ºC and 18.20ºC. It could be clearly seen that center of the modules is experiences that largest heat transfer rate due to the heat transfers cooling effect.

Figure 5.44 displays the vapor fraction results of the bifacial module at peak solar irradiance during the noontime, like the case of the temperature distribution graph. It could be seen that the ammonia vaporizes in the bottom section of the module. However, the colder backward-facing panels in the middle and top of the module, causes the ammonia to condensate back to its liquid state. The ammonia's boiling temperature is 21.85ºC at a pressure of 9.25 bar, which is the pressure used in this simulation. However, when observing the front-facing panel vapor fraction it could be seen that the ammonia a is still in its vapor state throughout the module. In this case another stage of heating

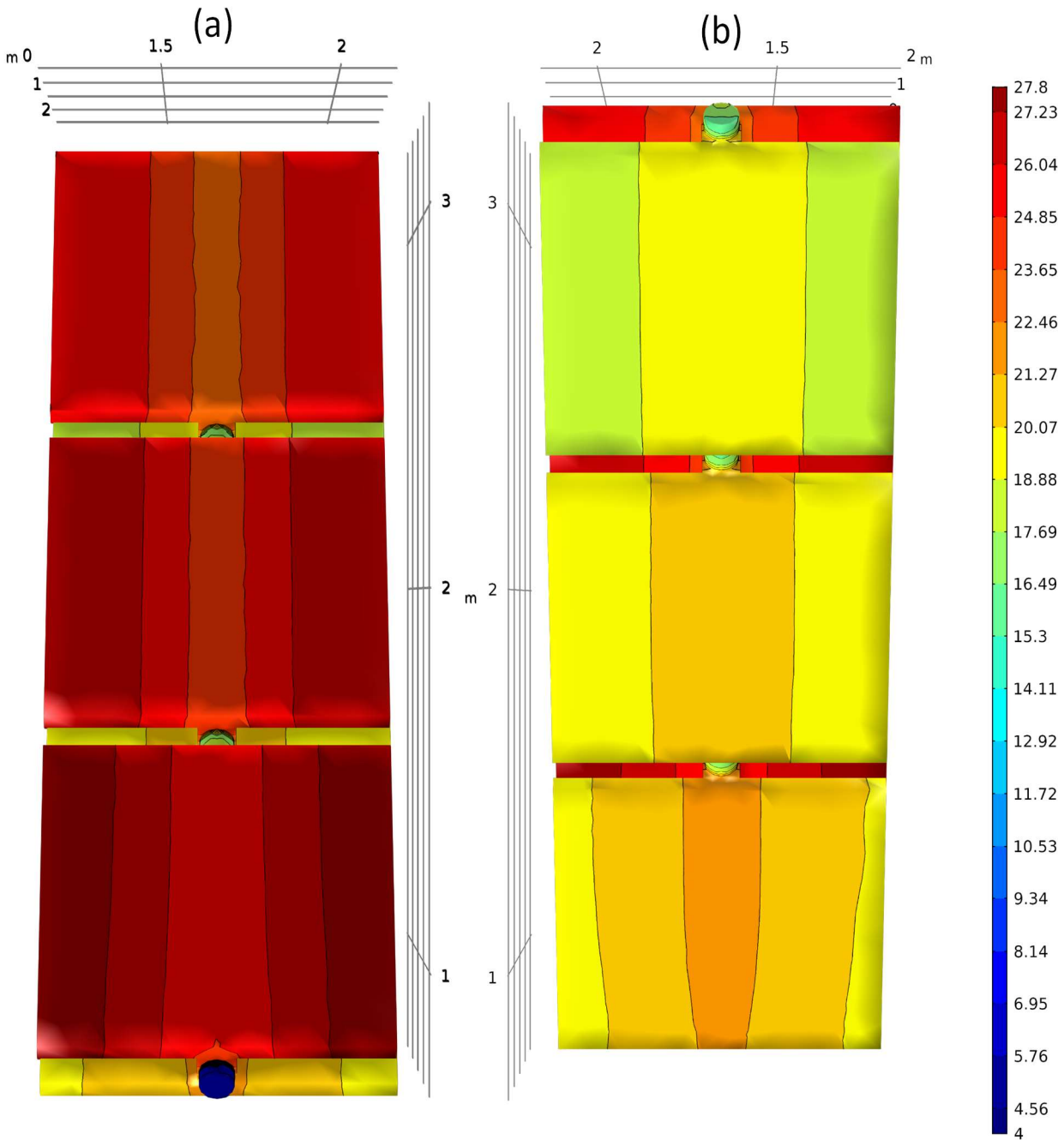

Figure 5.44: Panel surface temperature distribution at a time step of 1h. (a) Front facing (b) backward facing

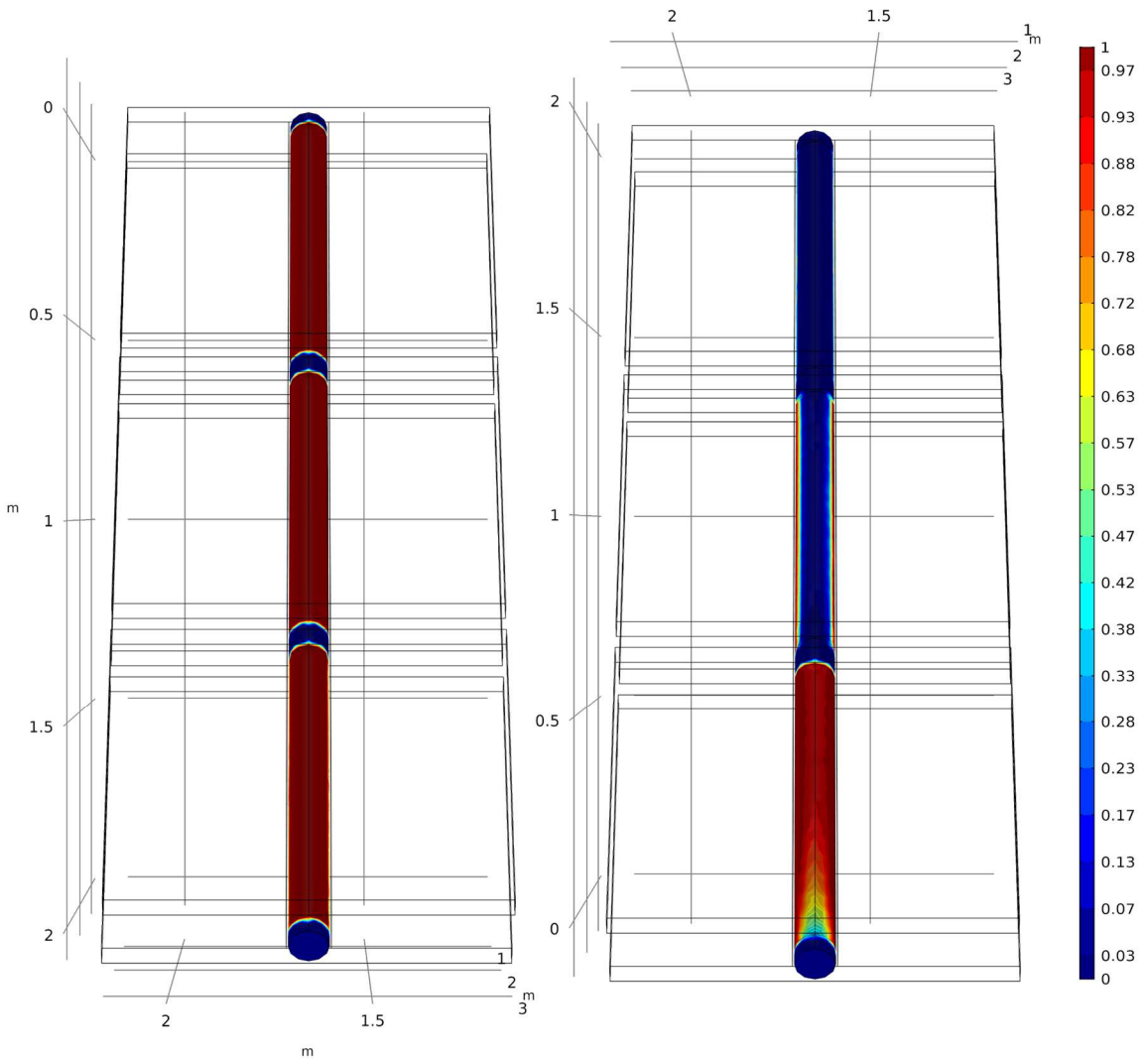

Figure 5.45*:* Vapor fraction distribution within the heat exchanger channel at a time step of 1h. (a) Front facing (b) backward facing

Figure 5.45 displays the maximum cell temperatures of the solar PV panels. The figure shows that all continue the solar panels continue to rise as they are exposed to the solar irradiance over the period which was set one hour at noon. The maximum cell temperature was achieved by the bottom front panel at 27.75ºC. As for the middle and top panel, they had a final temperature of 27.12ºC and 26.05ºC. The top, middle and bottom panels at the beginning of that hour were at the following temperatures 20.73, 22.39 and 23.49ºC. The bottom, middle and top panels gained 4.26, 4.73 and 5.32 degrees. The top panel experienced the largest temperature gain as the heat transfer rate is dependent on the temperature differential. Furthermore, the working fluid also in this case helps the top facing panels to gain some the thermal energy gained by the working fluid from the bottom

and middle panel. This conclusion can be made as the ammonia boiling temperature (21.5°C) is lower than the front bottom and middle panel temperature at the beginning of the hour. As for the backward-facing panels the results is similar in terms of the bottom panel achieving the highest cell temperature. The bottom, middle, and top backward-facing panels started at a cell temperature of 9.27,8.81, 6.51°C. The corresponding final maximum cell temperatures for the bottom, middle and top panels were found to be 21.75, 21.10, 20.02°C. The colder bottom panel temperatures cause the ammonia to re condensate back its liquid phase in the middle and top panels. The temperature of the middle and top panels is lower than that of the ammonias boiling temperature by 0.4 and 1.48 degrees. The temperature gain by the backward-facing panels are much higher than the front-facing panels. The reason being the top panels transfer some of their thermal energy to the bottom panels. This can be noticed in figure 5.45 as it shows the front panels experience a brief decline in temperatures up to the time period of 0.2h.

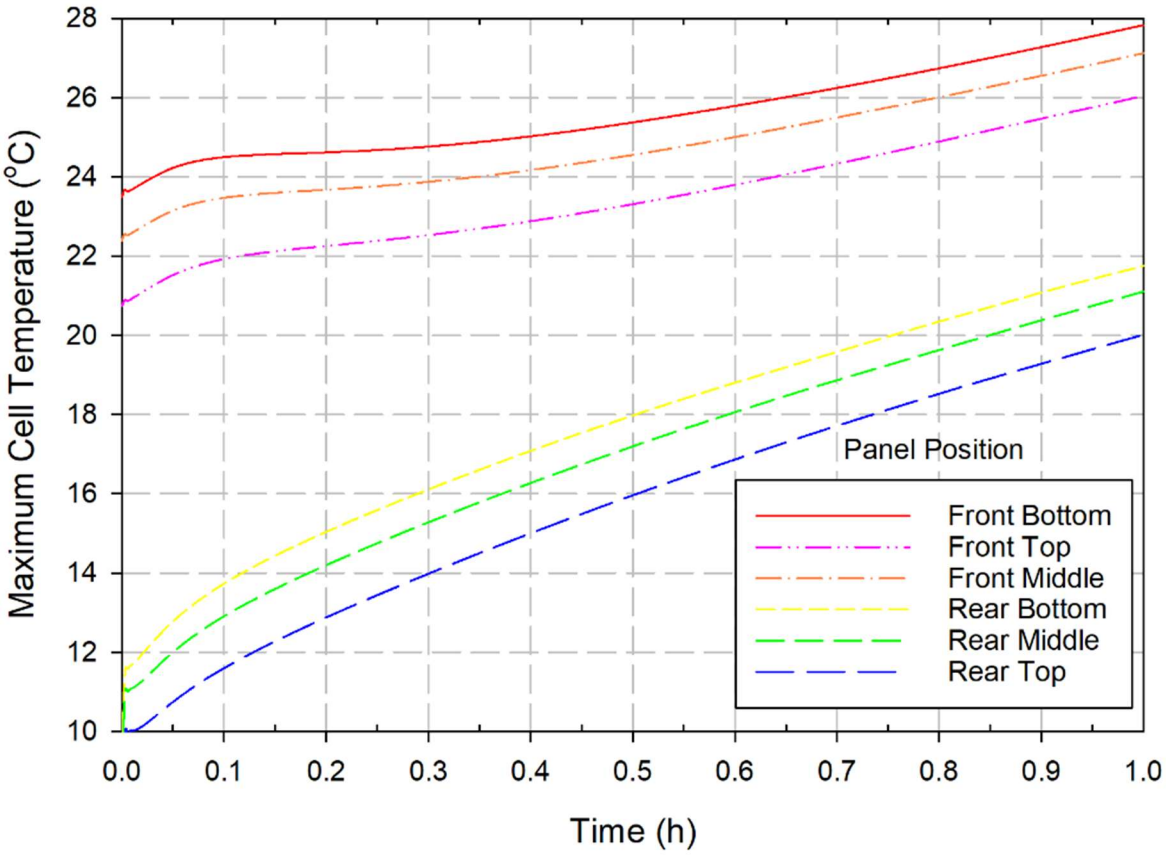

Figure 5.46: Maximum panel surface temperature through a 1 hour period

Figure 5.46 displays the minimum cell temperatures of the solar PV panels. The figure shows that all the solar panels continue to rise as they are exposed to the solar irradiance over the period, which was set one hour at noon. The front-facing panels lowest panel temperature was achieved by the top panel which had a temperature of 23.28^{o}C. as for the middle and bottom panel temperatures, they achieved a minimum cell temperature of 23.38 ^{o}C and 24.82^{o}C. The temperature gain by the top, middle and bottom front-facing panels, was 2.55, 0.99, and 1.33 degrees. The temperature gain relation is different than that of the maximum cell temperature relation. The middle panel experienced the lowest temperature gain, unlike the maximum cell temperature relation where the temperature gradually decreased as the heat transfer traveled to the top panel. As for the backward-facing panels, the lowest minimum cell temperature was achieved by the top panel at 18.21^{o}C. As for the middle and bottom panel, they had a final temperature of 19.26 ^{o}C and 19.86^{o}C. The bottom, middle and top panels gained 10.01, 11.68, and 12.06 degrees. The top panel experienced the largest temperature gain as the heat transfer rate is dependent on the temperature differential. Furthermore, the working fluid also in this case helps the top facing panels to gain some of the thermal energy gained by the working fluid from the front-facing bottom and middle panel. This conclusion can be made as the ammonias boiling temperature (21.5^{o}C) is higher than the front bottom and middle panel temperature at the beginning of the hour. The colder bottom panel temperatures cause the ammonia to re condensate back its liquid phase in the middle and top panels. Even though the temperature of the back-bottom panel is lower than the boiling temperature of the ammonia, however the heat transfer rate of the bottom panel compensates for that loss. The temperature of the bottom, middle and top panels are lower than that of the ammonias boiling temperature by 1.65, 2.25 and 3.3 degrees. It could be concluded that the front panels provide thermal energy and increase the temperature increase rate of the backward-facing panels. One should note that the front panels and back panels experience a coupled heat transfer relationship through the heat transfer fluid and the aluminum heat exchanger.

Figure 5.47 displays the temperature difference within each of the panels over a period of 1 hour. The temperature difference within all the panels increases until time step 0.10h. After that the temperature difference within the panels starts to decrease. The panels are slowly reaching a uniform surface panel temperature. However, because the changing

conditions with the solar irradiance, the back panels warming up from the heat transfer from the front-facing panels and the boiling of the working fluid it's not possible to reach a fully isothermal state for each panel. The highest temperature difference was found to be experienced by the front-facing bottom panel. The panel experienced a peak of 4.44 degrees difference within the panel. The lowest temperature difference experience was by the bottom back panel at a temperature difference of 3.54 degrees. However, as the operation of the module continues the panels temperature difference keep decreasing the heat transfer rate starts to stagnate. At the end of the hour the temperature differences experienced by the front-facing bottom, middle and top panel are 3.01, 2.74 and 2.77 degrees. As for the backward-facing panels the bottom, middle and top panel experienced a surface temperature difference of 1.89,1.84 and 1.81 degrees. The surface temperature difference was much lower than that of the front panels.

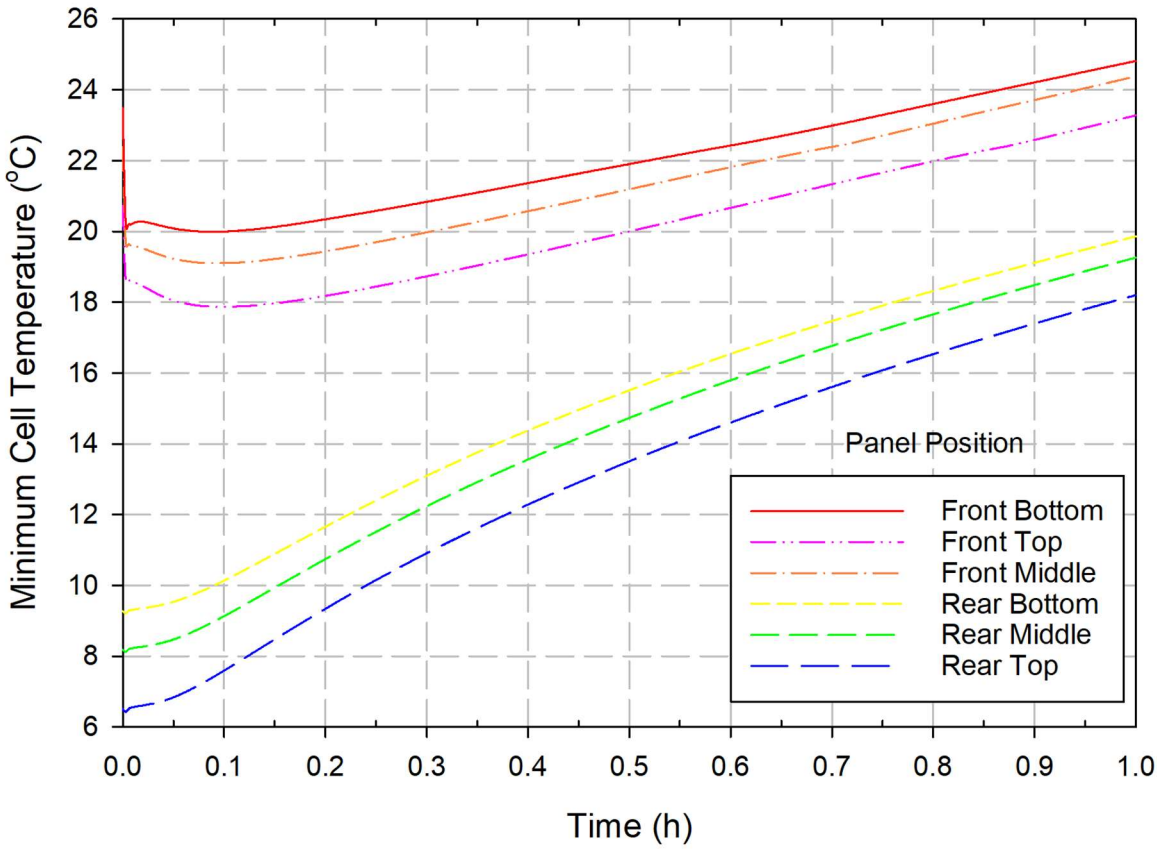

Figure 5.47: Minimum panel surface temperature through a 1 hour period

Figure 5.48 displays the heat generation rate of the bottom front and back panels along with heat rate gained by the working fluid. The heat generation experienced by the afront-facing panel, does not vary significantly over the hour. The maximum, heat generation rate was found to be 354.91W at the time step of 0.08h. The heat generation rate decreases as the simulation continues towards the hour and reaches a steady state heat rate of 331.65W. As for the backwards facing bottom panel the maximum heat generation rate experienced by was 101.29W at a time step of 0.0025h. However, in the case of the backward facing panel the heat generation decreases drastically to a steady state heat generation rate of 31.08 W. The bottom pipe experiences a maximum and minimum net heat gain of 88.31W and 8.12 W towards the end of the simulation.

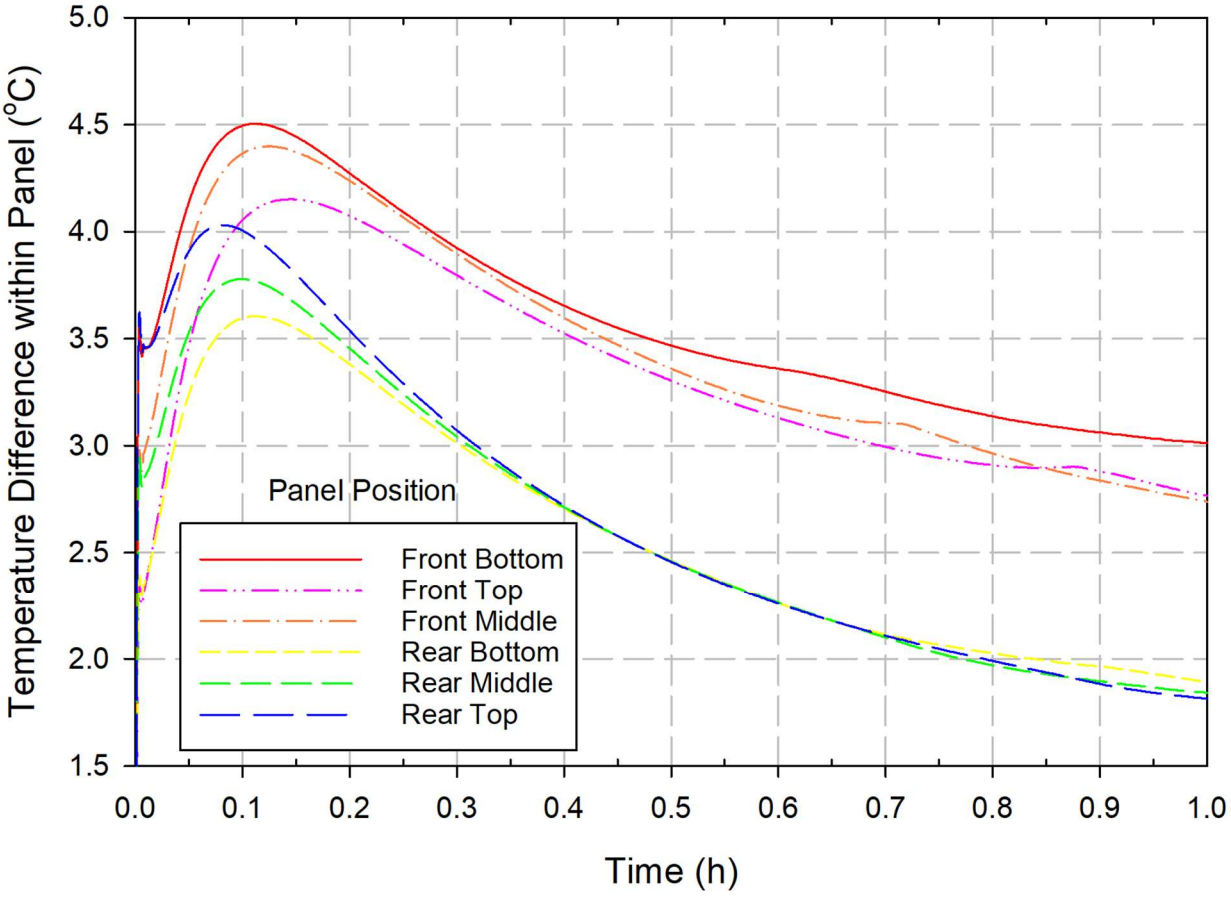

Figure 5.48: Panel surface temperature difference through a 1 hour period

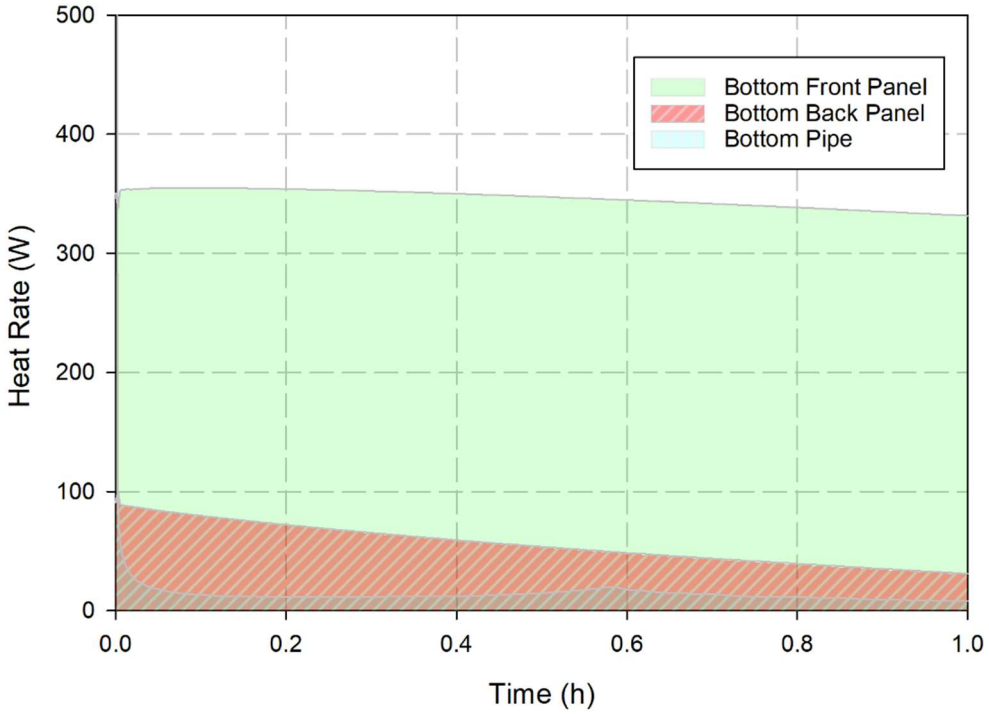

Figure 5.49: Bottom front and back panel heat generation rate and working fluid net heat gain through a 1 hour period

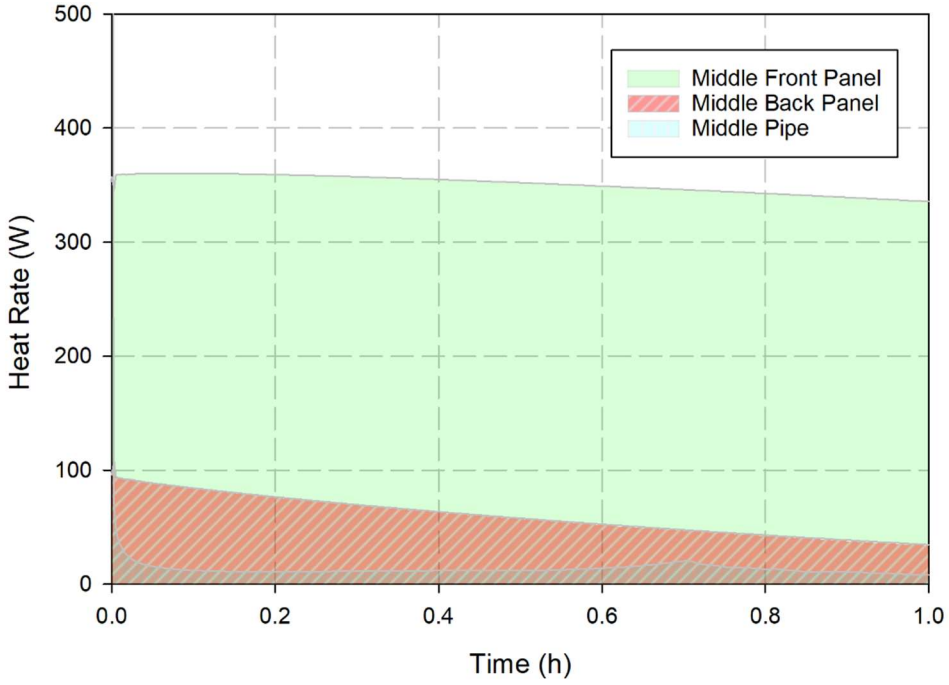

Figure 5.50: Middle front and back panel heat generation rate and working fluid net heat gain through a 1-hour period

Figure 5.49 displays the heat generation rate of the bottom front and back panels along with heat rate gained by the working fluid. The heat generation experienced by the front facing panel, does not vary significantly over the hour. The maximum, heat generation rate was found to be 360.37W at the time step of 0.075h. The heat generation rate decreases as the simulation continues towards the hour and reaches a steady state heat rate of 335.66W. As for the backwards facing bottom panel the maximum heat generation rate experienced by was 108.93W at a time step of 0.0025h. However, in the case of the backward facing panel the heat generation decreases drastically to a steady state heat generation rate of 34.60 W. The bottom pipe experiences a maximum and minimum net heat gain of 48.33W and 8.02 W towards the end of the simulation. The final heat gain rate is similar to that of the bottom section of the pipe.

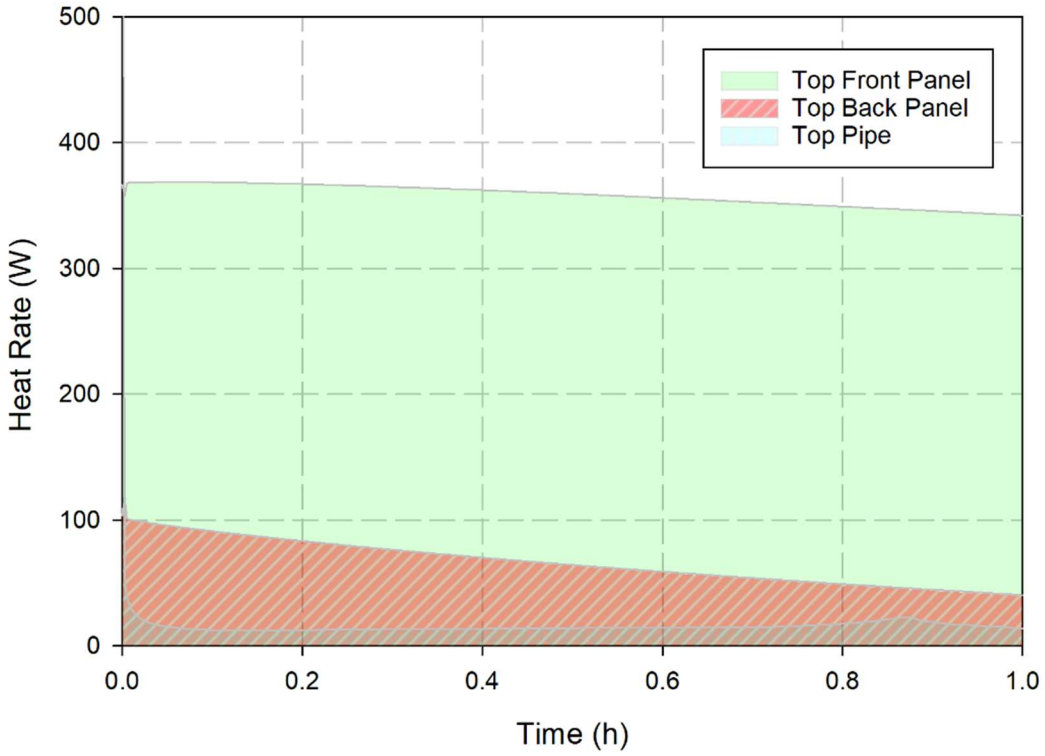

Figure 5.51: Top front and back panel heat generation rate and working fluid net heat gain through a 1 hour period

Figure 5.50 displays the heat generation rate of the bottom front and back panels along with heat rate gained by the working fluid. The heat generation experienced by the front facing panel, does not vary significantly over the hour. The maximum, heat generation rate was found to be 368.28W at the time step of 0.015h. The heat generation rate decreases as

the simulation continues towards the hour and reaches a steady state heat rate of 342.12W. As for the backwards facing bottom panel the maximum heat generation rate experienced by was 101.15W at a time step of 0.005h. However, in the case of the backward facing panel the heat generation decreases drastically to a steady state heat generation rate of 40.56W. The bottom pipe experiences a maximum and minimum net heat gain of 53.77W and 13.78W towards the end of the simulation.

In Figure 5.43 a and b display the results for a bifacial panel with an aluminum heat exchanger with a working fluid channel diameter of 5 cm. The working fluid is flowing at a mass flow rate of 0.0001 kg/s, the results are displayed for the peak solar irradiance period based on the previous sections results from the January case study for the north facing bifacial module. The front panel receives 620 W/m^2, while the back panels only receive 30% of the solar irradiance of the front panel. The maximum surface temperature for the bottom front panel reaches a steady state temperature of 28.3ºC while the coldest temperature was in the center of the panel as the working fluid is actively boiling at a temperature of 21.5ºC which led to a temperature of 23.65ºC. The middle front panel achieved a similar steady state temperature to the bottom front panel where the maximum steady state temperature achieved was 27.54ºC. The minimum panel temperature was 24.89ºC. As for the top panel it achieved the lowest temperature of all the panels where the maximum and minimum surface temperature were simulated to be 26.31ºC and 23.65ºC. The temperature of the panels gradually drops as the ammonia vaporises at the entry of the first panel and the thermal conductivity of the vaporised ammonia decreases as it passes through the other panels. Furthermore, this causes a cooling effect from the ambient conditions that cause a temperature decrease at each level of panels. As for the back facing panels, they experienced significantly lower temperature distributions than the front facing panels. This is highly due to the lower amount of solar irradiance experienced by the backward facing panels, which is only 30% of that experienced by the front facing panels. The bottom back panel achieved the highest temperature distribution of any of the other back panels. The bottom panel experienced a maximum and minimum temperature of 23.15ºC and 20.55ºC. The middle panel experienced a maximum and minimum temperature of 22.36ºC and 20.55ºC. As for the top panel maximum and minimum temperature of 21.13ºC and 18.68ºC. It could be clearly seen that center of the modules is experiences that largest heat transfer rate due to the heat transfers cooling effect.

Figure 5.44 displays the vapor fraction results of the bifacial module at peak solar irradiance during the noon time like the case of the temperature distribution graph. It could be seen that the ammonia vaporizes in the bottom section of the module. However, the colder backward facing panels in the middle and top of the module, causes the ammonia to condensate back to its liquid state. The ammonia's boiling temperature is 21.51^{o}C at a pressure of 9.25 bar, which is the pressure used in this simulation. However, when observing the front facing panel vapor fraction it could be seen that the ammonia a is still in its vapor state throughout the module. In this case another stage of heating is needed to fully boil the ammonia, for it to be directly used in a thermal power plant.

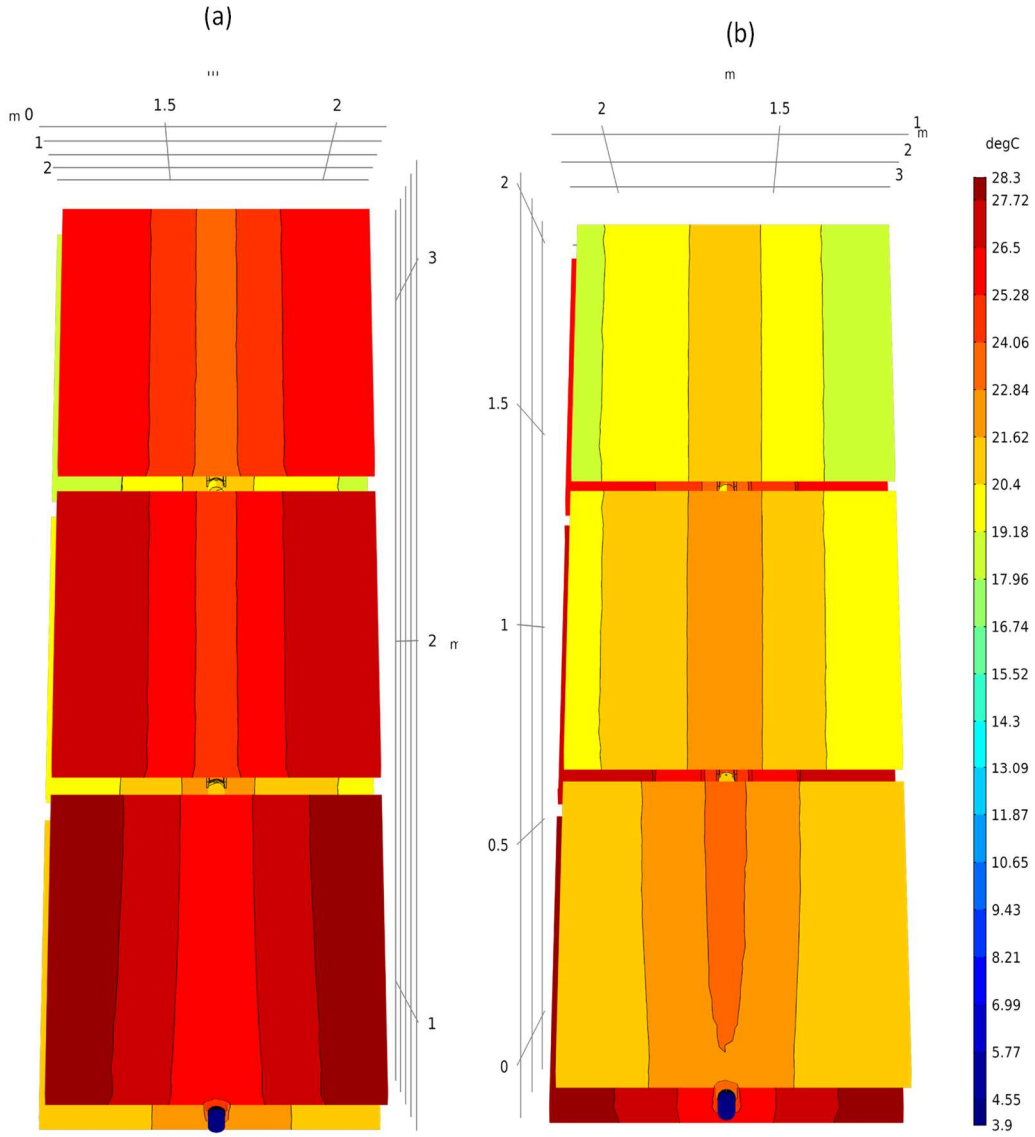

Figure 5.52: Panel surface temperature distribution at a time step of 1h. (a) Front facing (b) backward facing

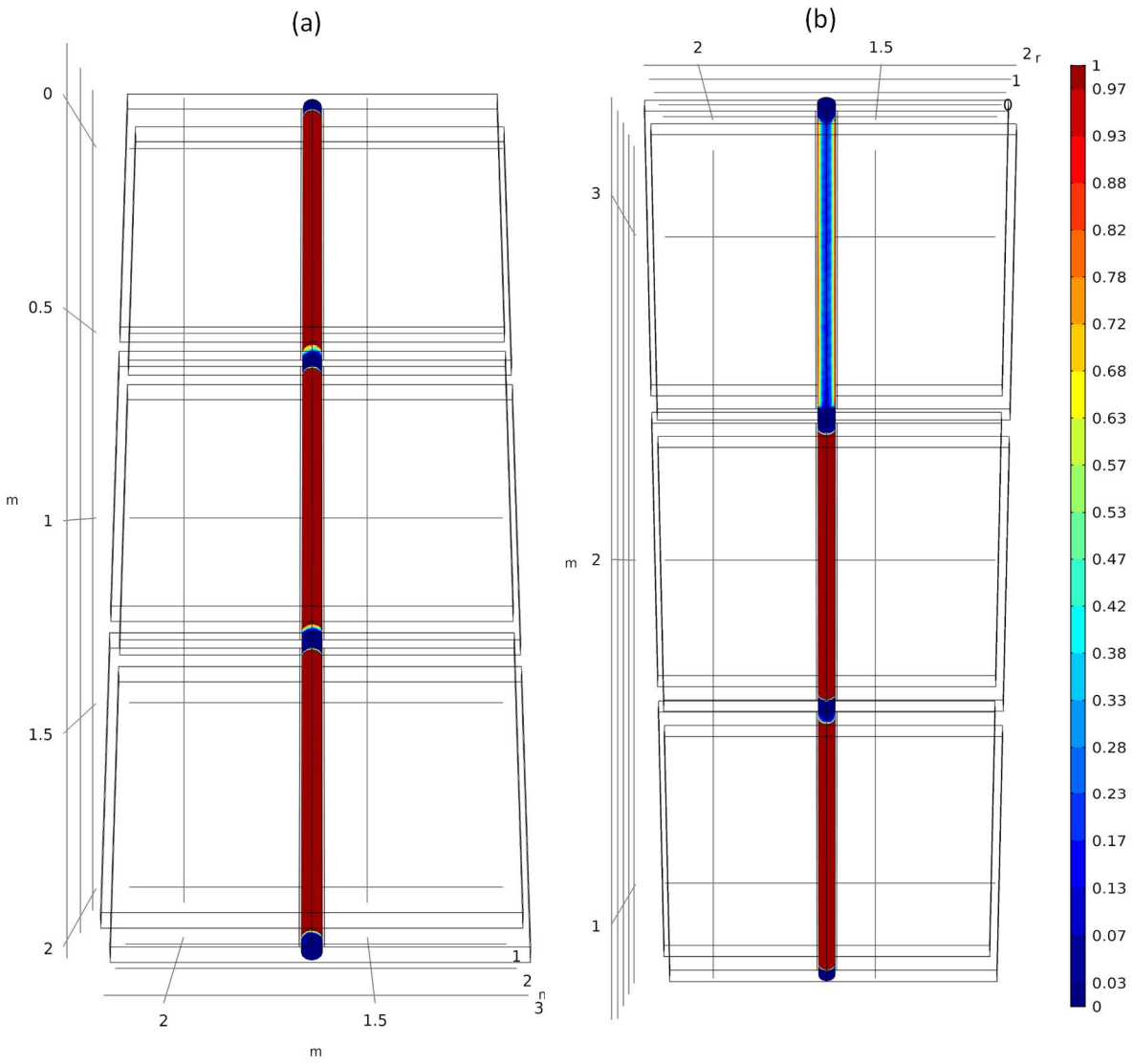

Figure 5.53: Vapor fraction distribution within the heat exchanger channel at a time step of 1h. (a) Front facing (b) backward facing

Figure 5.45 displays the maximum cell temperatures of the solar PV panels. The figure shows that all continue the solar panels continue to rise as they are exposed to the solar irradiance over the period which was set one hour at noon. The maximum cell temperature was achieved by the bottom front panel at 28.3°C. As for the middle and top panel they had a final temperature of 27.54°C and 26.31°C. The top, middle and bottom panels at the beginning of that hour were at the following temperatures 20.73, 22.39 and 23.49°C. The bottom, middle and top panels gained 4.81, 5.15 and 5.58 degrees. The top panel experienced largest temperature gain as the heat transfer rate is dependent on the temperature differential. Furthermore, the working fluid also in this case helps the top

facing panels to gain some the thermal energy gained by the working fluid from the bottom and middle panel. This conclusion can be made as the ammonias boiling temperature (21.5°C) is lower than the front bottom and middle panel temperature at the beginning of the hour. As for the backward facing panels the results is similar in terms of the bottom panel achieving the highest cell temperature. The bottom, middle, and top backward facing panels started at a cell temperature of 9.27,8.81, 6.51°C. The corresponding final maximum cell temperatures for the bottom, middle and top panels were found to be 23.15, 22.36, 21.13°C. The colder bottom panel temperatures cause the ammonia to re condensate back its liquid phase in the middle and top panels. The temperature of the top panel is lower than that of the ammonias boiling temperature 0.37 degrees. The temperature gain by the backward facing panels are much higher than the front facing panels. The reason being the top panels transfer some of their thermal energy to the bottom panels. This can be noticed in figure 5.53 as it shows the front panels experience a brief decline in temperatures up to the time period of 0.2h.

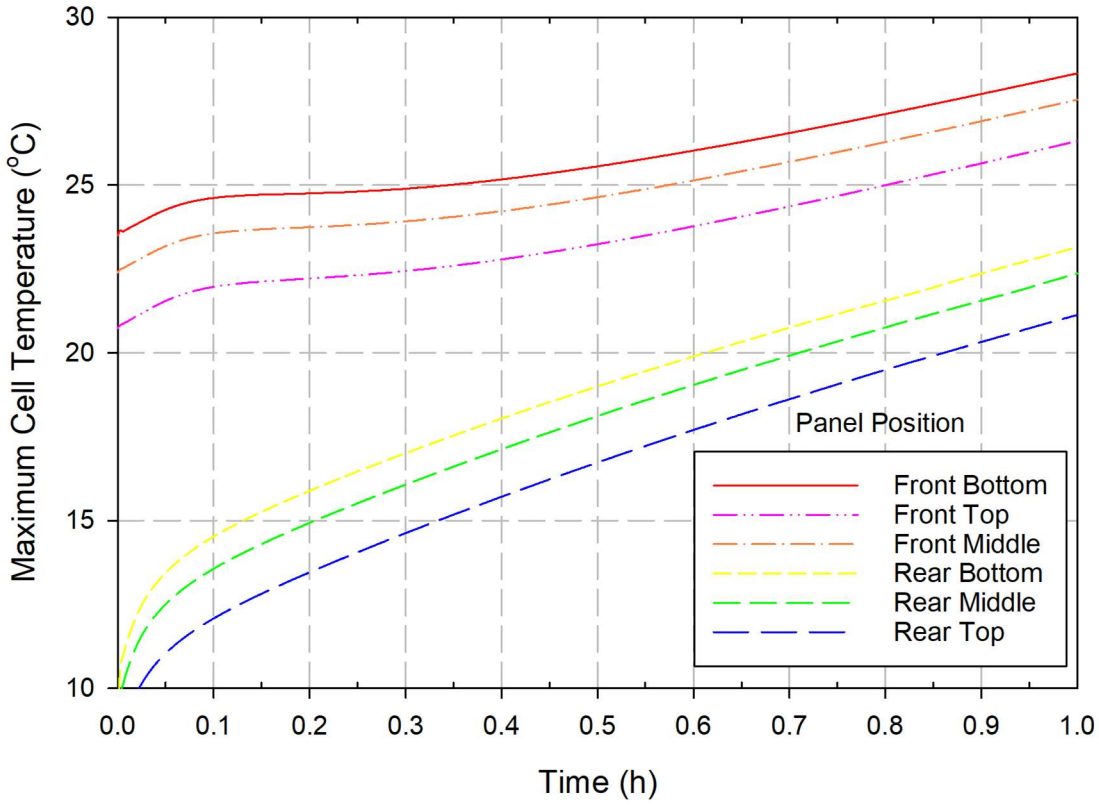

Figure 5.54: Maximum panel surface temperature through a 1 hour period

Figure 5.46 displays the minimum cell temperatures of the solar PV panels. The figure shows that all the solar panels continue to rise as they are exposed to the solar irradiance over the period which was set one hour at noon. The front facing panels lowest panel temperature was achieved by the top panel which had a temperature of 23.65°C. as for the middle and bottom panel temperatures they achieved a minimum cell temperature of 24.89 and 25.40°C. The temperature gain by the top, middle and bottom front facing panels, was 2.55, 0.99, and 1.33 degrees. The temperature gain relation is different than that of the maximum cell temperature relation. The middle panel experienced the lowest temperature gain, unlike the maximum cell temperature relation where the temperature gradually decreased as the heat transfer traveled to the top panel. As for the backward facing panels the lowest minimum cell temperature was achieved by the top panel at 18.68°C. As for the middle and bottom panel they had a final temperature of 19.86 and 20.55°C. The bottom, middle and top panels gained 10.01, 11.68 and 12.06 degrees. The top panel experienced the largest temperature gain as the heat transfer rate is dependent on the temperature differential. Furthermore, the working fluid also in this case helps the top facing panels to gain some of the thermal energy gained by the working fluid from the front facing bottom and middle panel. This conclusion can be made as the ammonias boiling temperature (21.5°C) is higher than the front bottom and middle panel temperature at the beginning of the hour. The colder bottom panel temperatures cause the ammonia to re condensate back its liquid phase in the middle and top panels. Even though the temperature of the back-bottom panel is lower than the boiling temperature of the ammonia, however the heat transfer rate of the bottom panel compensates for that loss. The temperature of the bottom, middle and top panels are lower than that of the ammonias boiling temperature by 1.65, 2.25 and 3.3 degrees. It could be concluded that the front panels provide thermal energy and increase the temperature increase rate of the backward facing panels. One should note that the front panels and back panels experience a coupled heat transfer relationship through the heat transfer fluid and the aluminum heat exchanger.

Figure 5.47 displays the temperature difference within each of the panels over a period of 1 hour. The temperature difference within all the panels increases until time step 0.10h, after that the temperature difference within the panels starts to decrease. The panels are slowly reaching a uniform surface panel temperature. However, because the changing

conditions with the solar irradiance, the back panels warming up from the heat transfer from the front facing panels and the boiling of the working fluid its not possible to reach a fully isothermal state for each panel. The highest temperature difference was found to be experienced by the front facing bottom panel. The panel experienced a peak of 4.84 degrees difference within the panel. The lowest temperature difference experience was by the bottom back panel at a temperature difference of 2.45 degrees. However, as the operation of the module continues the panels temperature difference keep decreasing the heat transfer rate starts to stagnate. At the end of the hour the temperature differences experienced by the front facing bottom, middle and top panel are 2.94, 2.65 and 2.66 degrees. As for the backward facing panels the bottom, middle and top panel experienced a surface temperature difference of 2.60, 2.50 and 2.46 degrees. The surface temperature difference was much lower than that of the front panels.

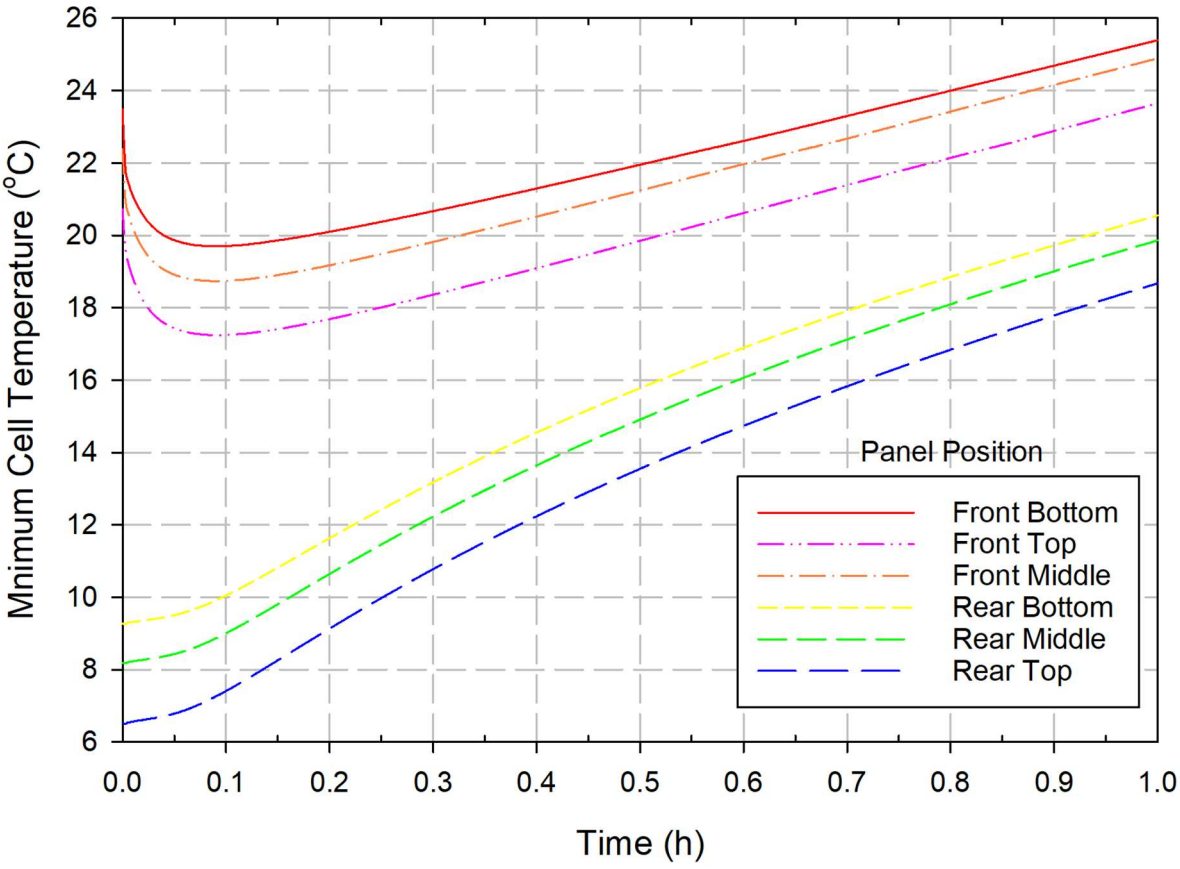

Figure 5.55: Minimum panel surface temperature through a 1 hour period

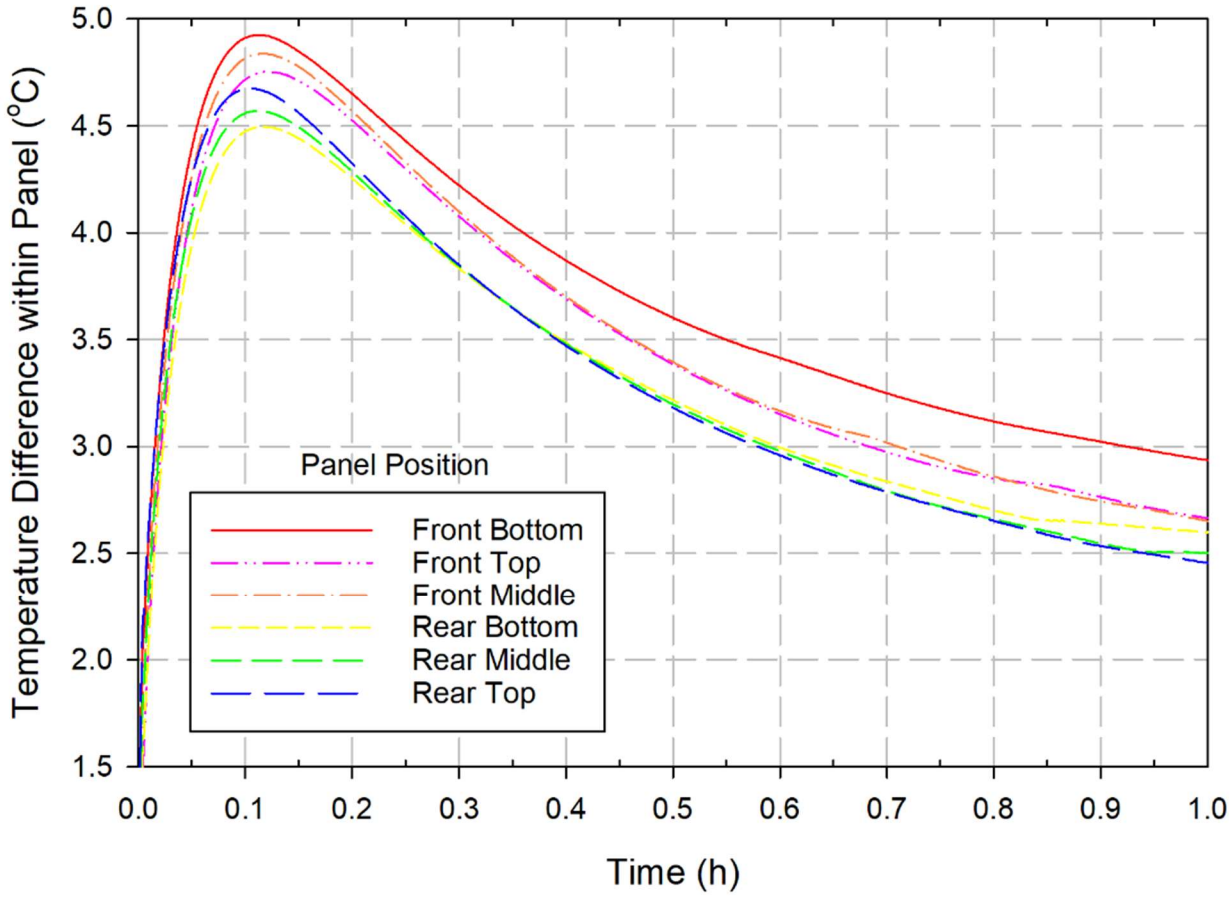

Figure 5.56: Panel surface temperature difference through a 1 hour period

Figure 5.56 displays the heat generation rate of the bottom front and back panels along with heat rate gained by the working fluid. The heat generation experienced by the front facing panel, does not vary significantly over the hour. The maximum, heat generation rate was found to be 354.34W at the time step of 0.08h. The heat generation rate decreases as the simulation continues towards the hour and reaches a steady state heat rate of 328.25W. As for the backwards facing bottom panel the maximum heat generation rate experienced by was 90.44W at a time step of 0.0025h. However, in the case of the backward facing panel the heat generation decreases drastically to a steady state heat generation rate of 25.39W. The bottom pipe experiences a maximum and minimum net heat gain of 47.47W and 13.16W towards the end of the simulation.

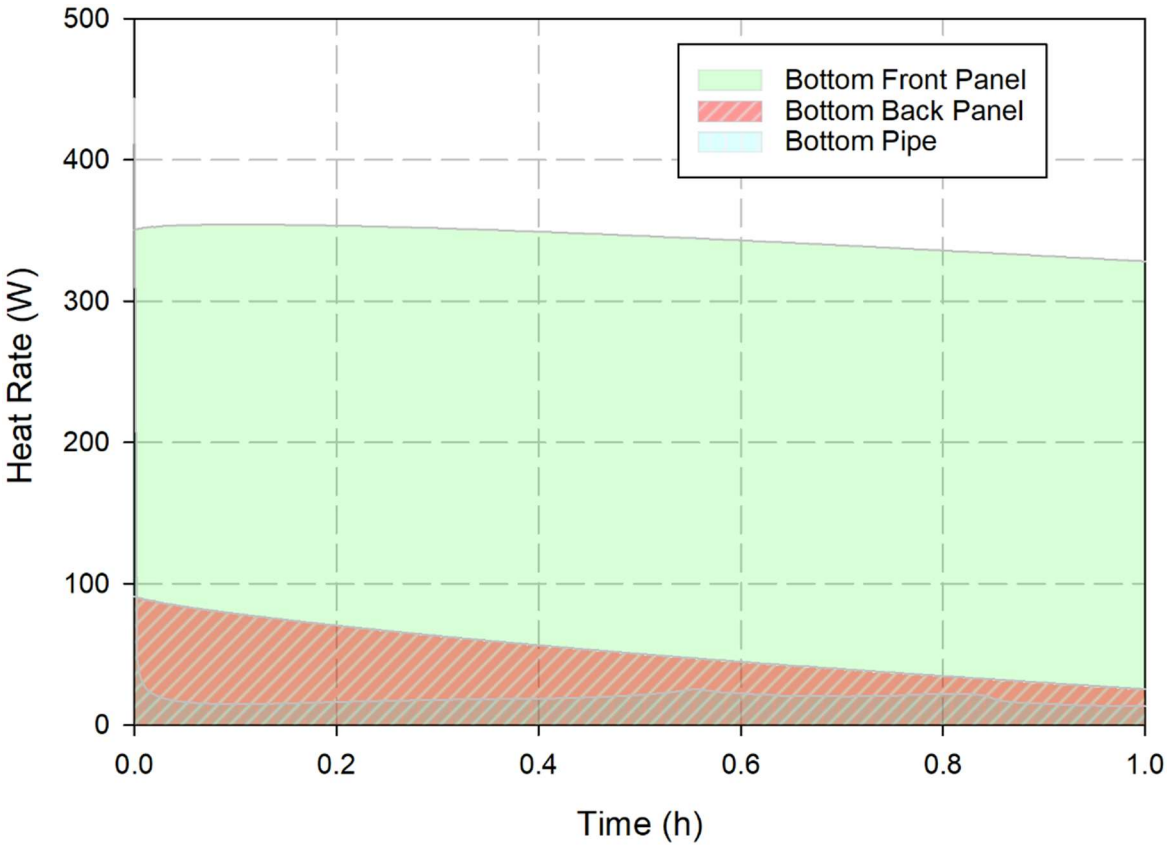

Figure 5.57: Bottom front and back panel heat generation rate and working fluid net heat gain through a 1 hour period

Figure 5.57 shows the heat generation rate of the middle front and back panels along with heat rate gained by the working fluid. The heat generation experienced by the front facing panel, does not vary significantly over the hour. The maximum, heat generation rate was found to be 360.20W at the time step of 0.075h. The heat generation rate decreases as the simulation continues towards the hour and reaches a steady state heat rate of 332.67W. As for the backwards facing bottom panel the maximum heat generation rate experienced by was 95.55W at a time step of 0.0025h. However, in the case of the backward facing panel the heat generation decreases drastically to a steady state heat generation rate of 39.53W. The middle pipe experiences a maximum and minimum net heat gain of 9.94W and 8.19W towards the end of the simulation. The final heat gain rate is like that of the bottom section of the pipe.

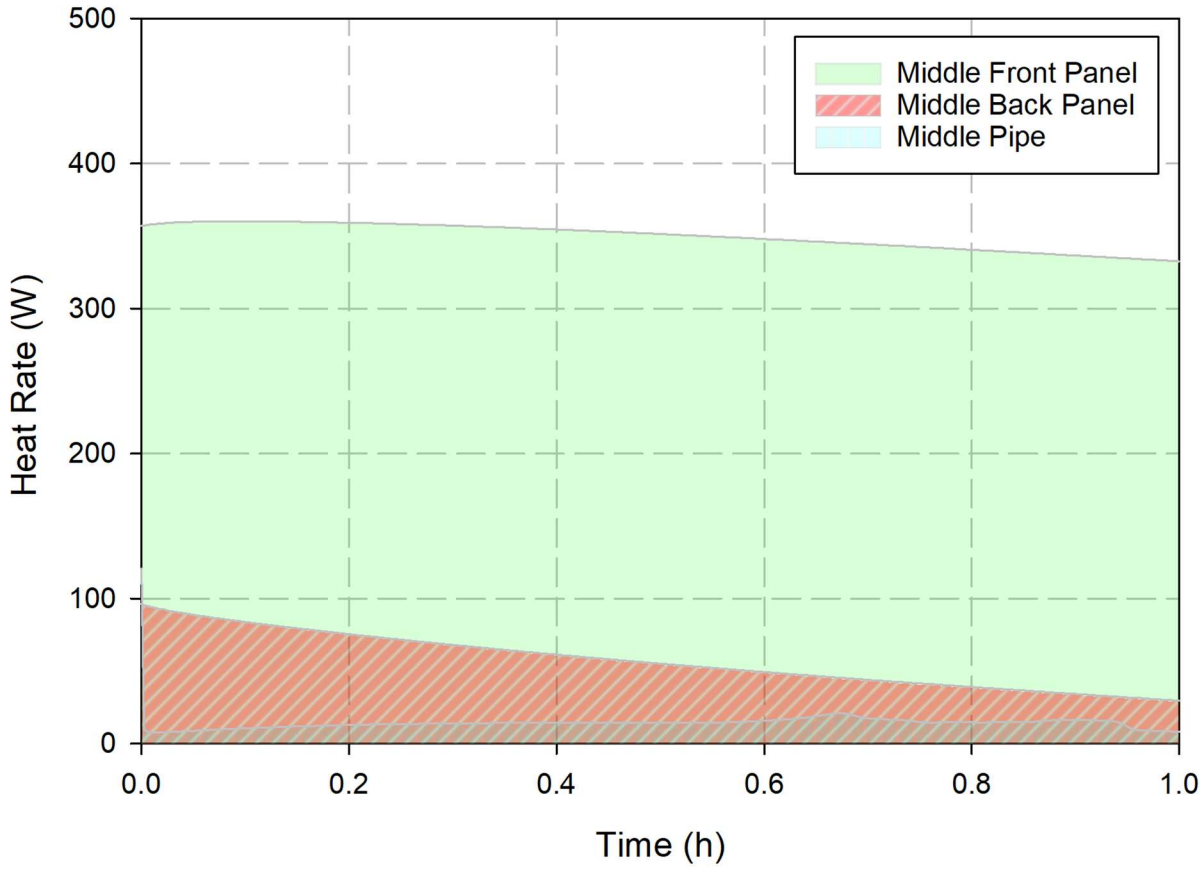

Figure 5.58: Middle front and back panel heat generation rate and working fluid net heat gain through a 1-hour period

Figure 5.58 displays the heat generation rate of the top front and back panels along with heat rate gained by the working fluid. The heat generation experienced by the front facing panel, does not vary significantly over the hour. The maximum, heat generation rate was found to be 369.02W at the time step of 0.015h. The heat generation rate decreases as the simulation continues towards the hour and reaches a steady state heat rate of 340.0W. As for the backwards facing bottom panel the maximum heat generation rate experienced by was 103.15W at a time step of 0.005h. However, in the case of the backward facing panel the heat generation decreases drastically to a steady state heat generation rate of 36.30W. The bottom pipe experiences a maximum and minimum net heat gain of -46.87 where its loosing heat. However, after that brief period a net heat gain occurs at a rate of 14.72W, respectively.

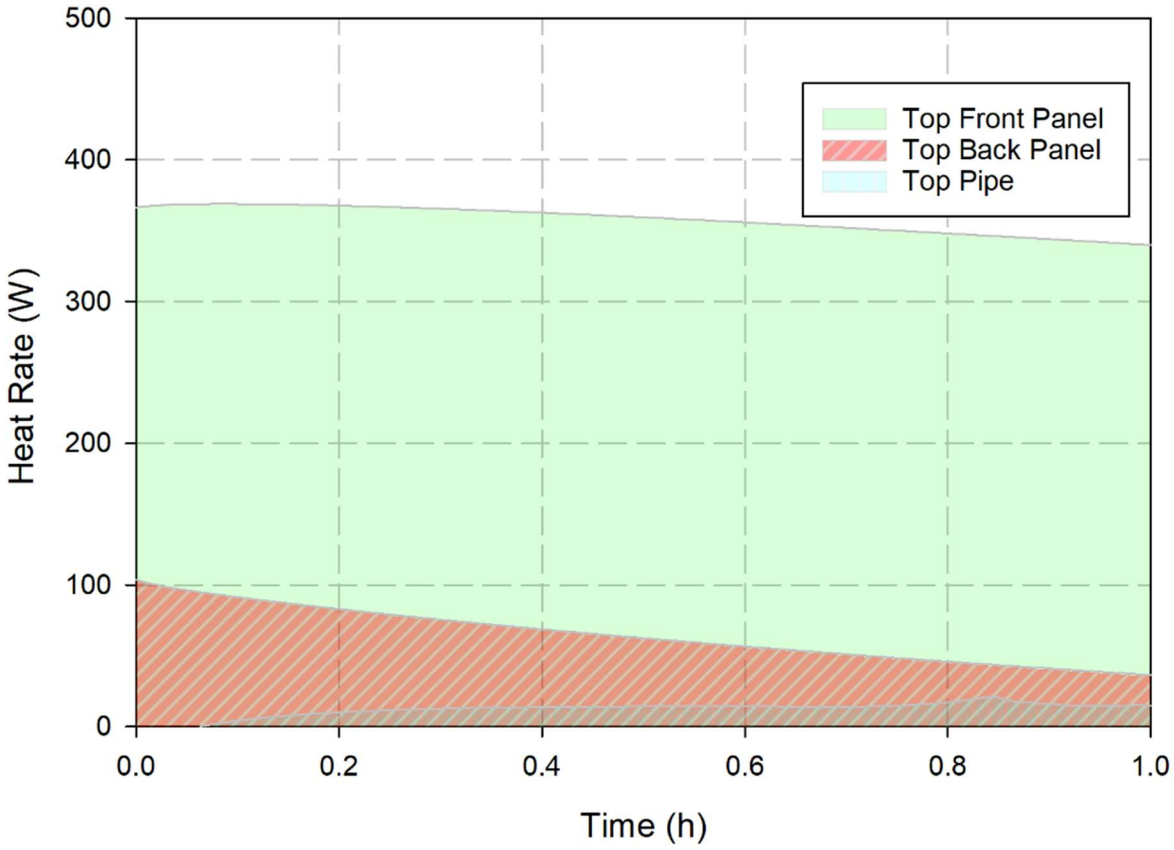

Figure 5.59: Top front and back panel heat generation rate and working fluid net heat gain through a 1 hour period

5.4.1.9 Results for an integrated heat exchanger with the bifacial PV module

In this case study a north-facing bifacial module is being tested for its viability to be combined with a thermal power plant (Ammonia Rankine Cycle). The conditions are based on the average winter (January) temperature and maximum solar irradiance of Ontario, Canada. The average maximum solar irradiance and average temperature in January were taken at 620 W/m^2 and -5^{o}C. The working fluid (Ammonia) is set at a pressure of to boil 9.25 bar, that has a corresponding boiling temperature of 21.5^{o}C. The superheated ammonia can then be used as the working fluid in a Rankine cycle. The simulated cycle was designed to perform similarly to an ocean thermal energy conversion plant, but for locations where the temperatures are cold. The results from the simulation will be discussed thoroughly in this section.

In Figure 5.59 a and b display the results for a bifacial panel with an aluminum heat exchanger with a working fluid channel diameter of 5 cm. The working fluid is flowing at a mass flow rate of 0.001 kg/s, the results are displayed for the peak solar irradiance period based on the previous sections results from the January case study for the north facing bifacial module. The front panel receives 620 W/m^2, while the back panels only receive 30% of the solar irradiance of the front panel. The maximum surface temperature for the bottom front panel reaches a steady state temperature of 27.76ºC while the coldest temperature was in the center of the panel as the working fluid is actively boiling at a temperature of 21.5ºC which led to a temperature of 24.82ºC. The middle front panel achieved a similar steady state temperature to the bottom front panel where the maximum steady state temperature achieved was 27.53ºC. The minimum panel temperature was found to be 24.38ºC. As for the top panel it achieved the lowest temperature of all the panels where the maximum and minimum surface temperature were simulated to be 26.37ºC and 23.28ºC. The temperature of the panels gradually drops as the ammonia vaporizes at the entry of the first panel and the thermal conductivity of the vaporized ammonia decreases as it passes through the other panels. Furthermore, this causes a cooling effect from the ambient conditions that cause a temperature decrease at each level of panels. As for the back-facing panels, they experienced significantly lower temperature distributions than the front facing panels. This is highly due to the lower amount of solar irradiance experienced by the backward facing panels, which is only 30% of that experienced by the front facing panels. The bottom back panel achieved the highest temperature distribution of any of the other back panels. The bottom panel experienced a maximum and minimum temperature of 22.39ºC and 19.86ºC. The middle panel experienced a maximum and minimum temperature of 22.33ºC and 19.26ºC. As for the top panel maximum and minimum temperature of 21.20ºC and 18.21ºC. It could be clearly seen that center of the modules is experiences that largest heat transfer rate due to the heat transfers cooling effect.

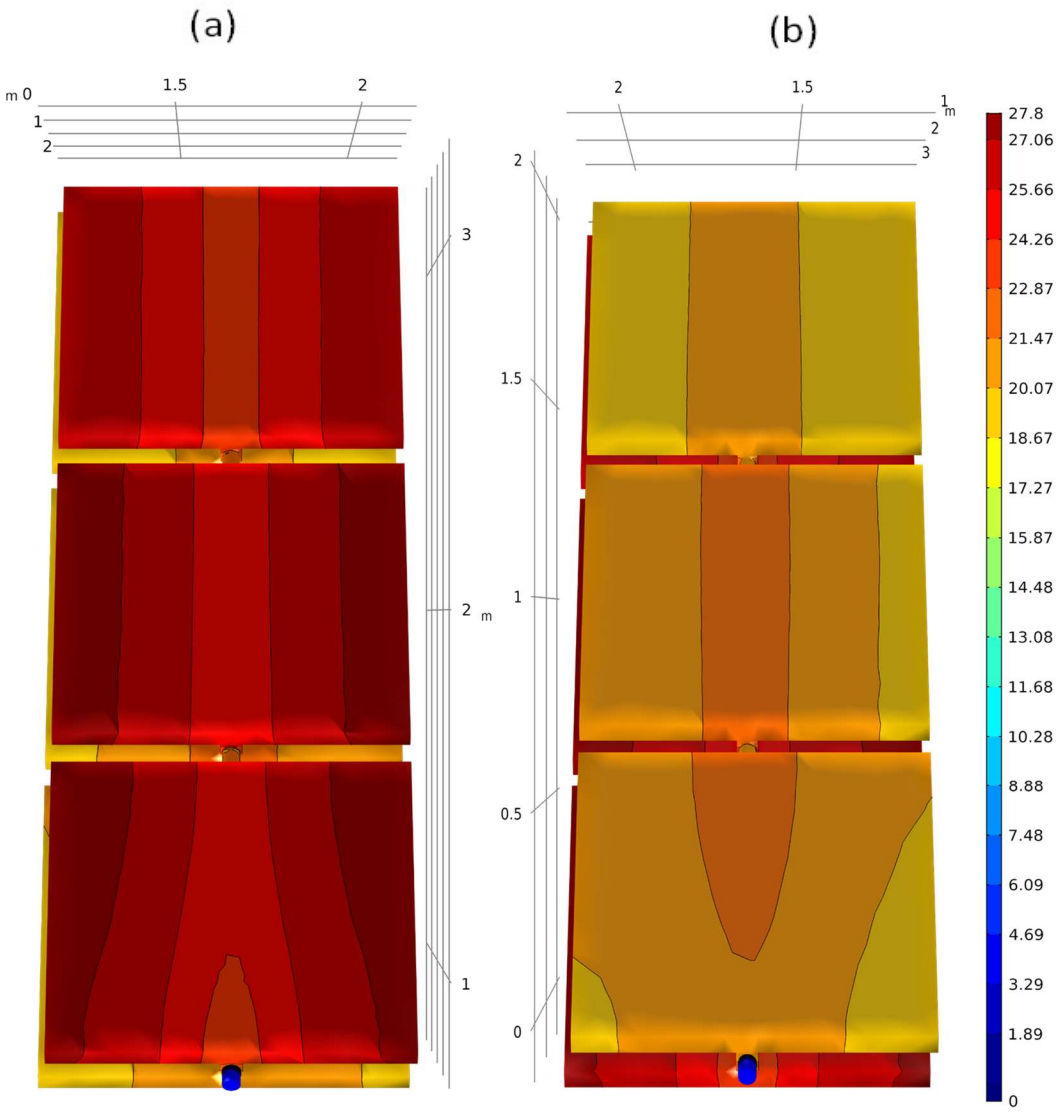

Figure 5.60: Panel surface temperature distribution at a time step of 1h. (a) Front facing (b) backward facing

Figure 5.60 displays the vapor fraction results of the bifacial module at peak solar irradiance during the noon time like the case of the temperature distribution graph. It could be seen that the ammonia vaporizes in the bottom section of the module and continues to be in gaseous stage up until it reaches the back-top panel. The colder backward facing panels in the middle and top of the module, causes the ammonia to condensate back to its liquid state. The ammonia's boiling temperature is 21.85ºC at a pressure of 9.25 bar, which is the pressure used in this simulation. However, when observing the front facing panel vapor fraction it could be seen that the ammonia a is still in its vapor state throughout the

module. In this case another stage of heating is needed to fully boil the ammonia, for it to be directly used in a thermal power plant.

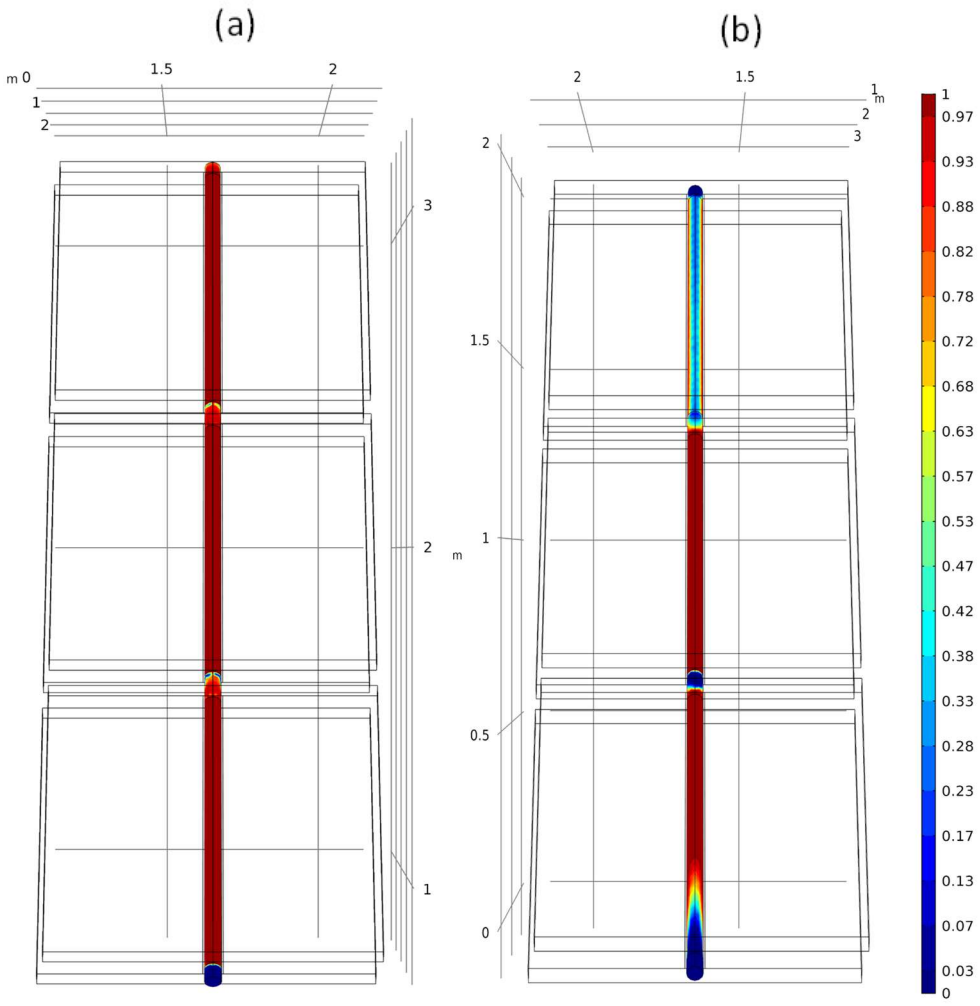

Figure 5.61: Vapor fraction distribution within the heat exchanger channel at a time step of 1h. (a) Front facing (b) backward facing

Figure 5.61 displays the maximum cell temperatures of the solar PV panels. The figure shows that all continue the solar panels continue to rise as they are exposed to the solar irradiance over the period which was set one hour at noon. The maximum cell temperature was achieved by the bottom front panel at 27.76°C. As for the middle and top panel they had a final temperature of 27.53°C and 26.37°C. The top, middle and bottom panels at the beginning of that hour were at the following temperatures 20.73, 22.39 and 23.49°C. The bottom, middle and top panels gained 4.27, 5.14 and 5.64 degrees. The top panel experienced largest temperature gain as the heat transfer rate is dependent on the temperature differential. Furthermore, the working fluid also in this case helps the top

facing panels to gain some the thermal energy gained by the working fluid from the bottom and middle panel. This conclusion can be made as the ammonias boiling temperature (21.5°C) is lower than the front bottom and middle panel temperature at the beginning of the hour. As for the backward facing panels the results is similar in terms of the bottom panel achieving the highest cell temperature. The bottom, middle, and top backward facing panels started at a cell temperature of 9.27,8.81, 6.51°C. The corresponding final maximum cell temperatures for the bottom, middle and top panels were found to be 22.39, 22.34 and 21.19°C. The colder bottom panel temperatures cause the ammonia to condensate back to its liquid phase in the top panels. The temperature of the top panel is lower than that of the ammonias boiling temperature by 0.32 degrees. The temperature gain by the backward facing panels are much higher than the front facing panels. The reason being the top panels transfer some of their thermal energy to the bottom panels. This can be noticed in figure 5.61 as it shows the front panels experience a brief decline in temperatures up to the time period of 0.2h.

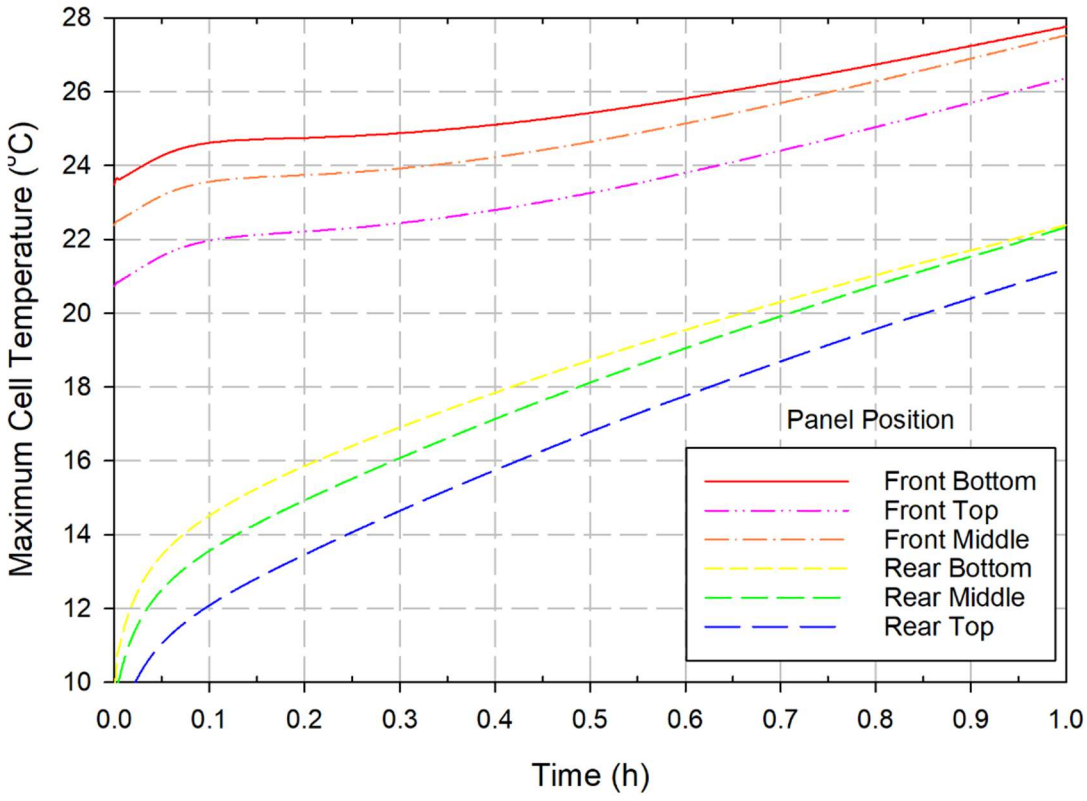

Figure 5.62: Maximum panel surface temperature through a 1 hour period

Figure 5.62 displays the minimum cell temperatures of the solar PV panels. The figure shows that all the solar panels continue to rise as they are exposed to the solar irradiance over the period which was set one hour at noon. The front facing panels lowest panel temperature was achieved by the top panel which had a temperature of 23.28^{o}C. as for the middle and bottom panel temperatures they achieved a minimum cell temperature of 23.38 and 24.82^{o}C. The temperature gain by the top, middle and bottom front facing panels, was 2.55, 0.99, and 1.33 degrees. The temperature gain relation is different than that of the maximum cell temperature relation. The middle panel experienced the lowest temperature gain, unlike the maximum cell temperature relation where the temperature gradually decreased as the heat transfer traveled to the top panel. As for the backward facing panels the lowest minimum cell temperature was achieved by the top panel at 18.21^{o}C. As for the middle and bottom panel they had a final temperature of 19.26 and 19.86^{o}C. The bottom, middle and top panels gained 10.01, 11.68 and 12.06 degrees. The top panel experienced the largest temperature gain as the heat transfer rate is dependent on the temperature differential. Furthermore, the working fluid also in this case helps the top facing panels to gain some of the thermal energy gained by the working fluid from the front facing bottom and middle panel. This conclusion can be made as the ammonias boiling temperature (21.5^{o}C) is higher than the front bottom and middle panel temperature at the beginning of the hour. The colder bottom panel temperatures cause the ammonia to condensate back its liquid phase in the top panel. Even though the temperature of the back-bottom panel is lower than the boiling temperature of the ammonia, however the heat transfer rate of the bottom and middle panels compensates for that loss. The temperature of the bottom, middle and top panels are lower than that of the ammonias boiling temperature by 1.65, 2.25 and 3.3 degrees. It could be concluded that the front panels provide thermal energy and increase the temperature increase rate of the backward facing panels. One should note that the front panels and back panels experience a coupled heat transfer relationship through the heat transfer fluid and the aluminum heat exchanger.

Figure 5.62 displays the temperature difference within each of the panels over a period of 1 hour. The temperature difference within all the panels increases until time step 0.10h, after that the temperature difference within the panels starts to decrease. The panels are slowly reaching a uniform surface panel temperature. However, because the changing

conditions with the solar irradiance, the back panels warming up from the heat transfer from the front facing panels and the boiling of the working fluid its not possible to reach a fully isothermal state for each panel. The highest temperature difference was found to be experienced by the front facing bottom panel. The panel experienced a peak of 4.49 degrees difference within the panel. The lowest temperature difference experience was by the bottom back panel at a temperature difference of 2.53 degrees. However, as the operation of the module continues the panels temperature difference keep decreasing the heat transfer rate starts to stagnate. At the end of the hour the temperature differences experienced by the front facing bottom, middle and top panel are 3.09, 3.15 and 2.94 degrees. As for the backward facing panels the bottom, middle and top panel experienced a surface temperature difference of 2.53, 3.07 and 2.99 degrees. The surface temperature difference lower on average than that of the front panels.

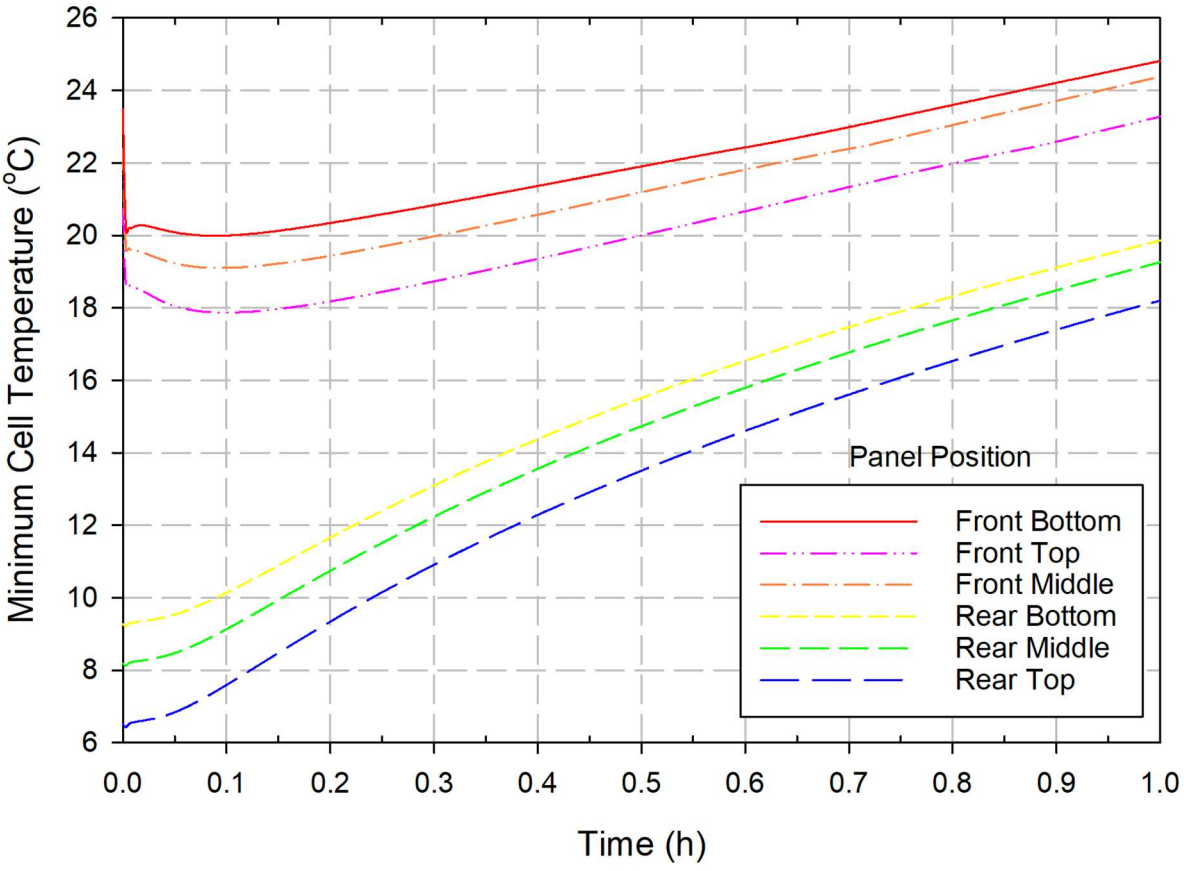

Figure 5.63: Minimum panel surface temperature through a 1 hour period

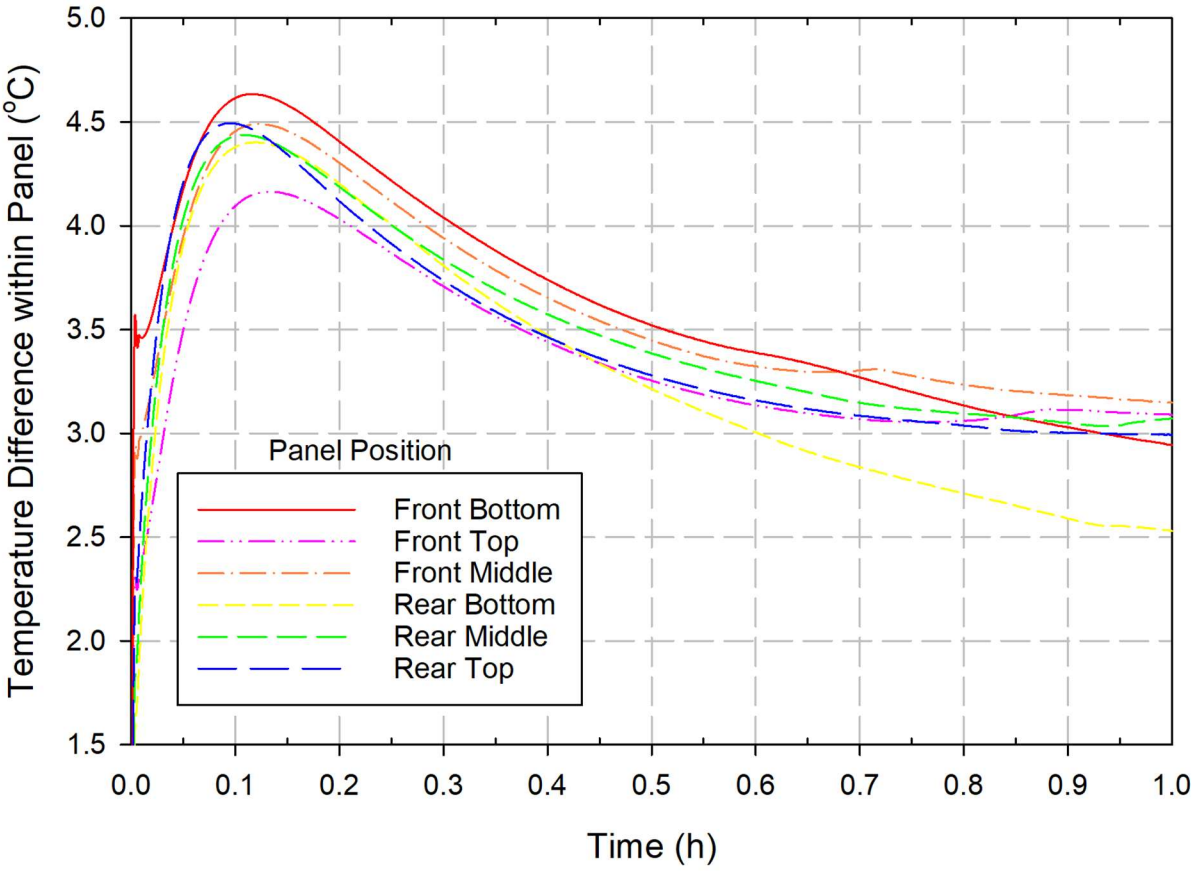

Figure 5.64: Panel surface temperature difference through a 1 hour period

Figure 5.65 displays the heat generation rate of the bottom front and back panels along with heat rate gained by the working fluid. The heat generation experienced by the front facing panel, does not vary significantly over the hour. The maximum, heat generation rate was found to be 369.02W at the time step of 0.0825h. The heat generation rate decreases as the simulation continues towards the hour and reaches a steady state heat rate of 339.68W. As for the backwards facing bottom panel the maximum heat generation rate experienced by was 105.77W at a time step of 0.0025h. However, in the case of the backward facing panel the heat generation decreases drastically to a steady state heat generation rate of 35.95W. The bottom pipe experiences a maximum and minimum net heat gain of 80.60W and 23.54W towards the end of the simulation.

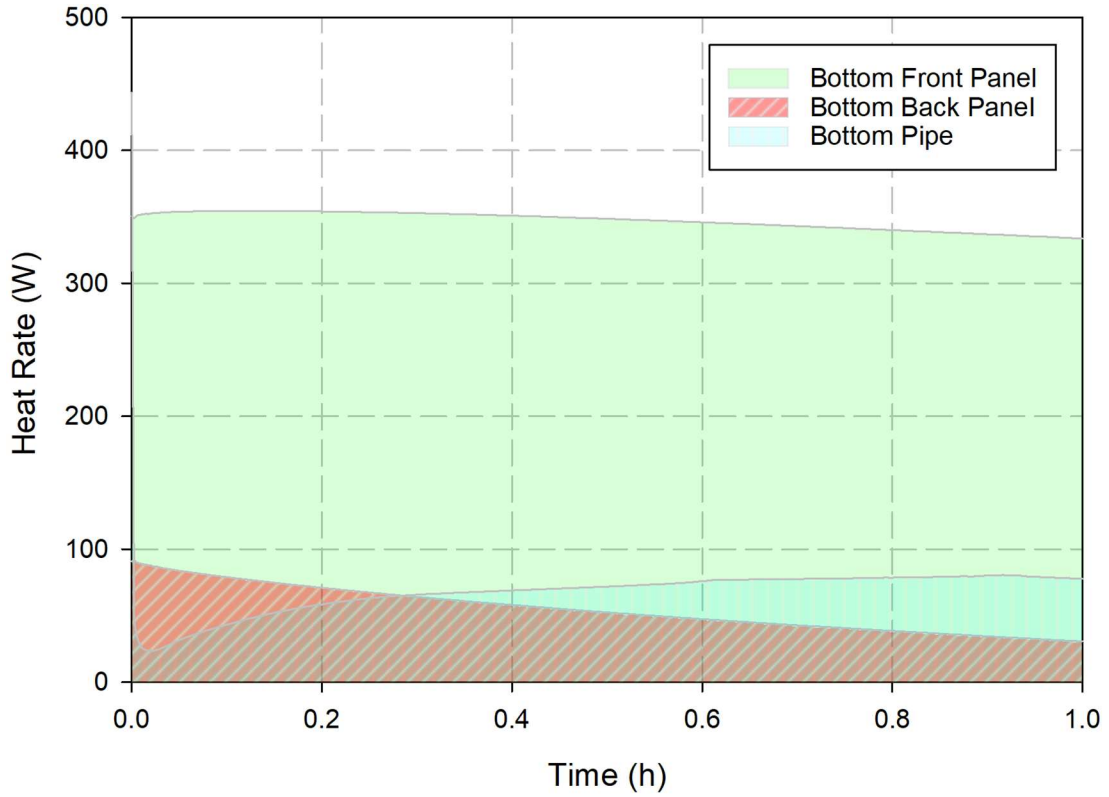

Figure 5.65: Bottom front and back panel heat generation rate and working fluid net heat gain through a 1 hour period

Figure 5.67 displays the heat generation rate of the middle front and back panels along with heat rate gained by the working fluid. The heat generation experienced by the front facing panel, does not vary significantly over the hour. The maximum, heat generation rate was found to be 360.37W at the time step of 0.09h. The heat generation rate decreases as the simulation continues towards the hour and reaches a steady state heat rate of 360.20W. As for the backwards facing middle panel the maximum heat generation rate experienced by was 97.52W at a time step of 0.0025h. However, in the case of the backward facing panel the heat generation decreases drastically to a steady state heat generation rate of 29.67W. The bottom pipe experiences a maximum and minimum net heat gain of 23.56W and 11.91W towards the end of the simulation. The final heat gain rate is similar to that of the bottom section of the pipe.

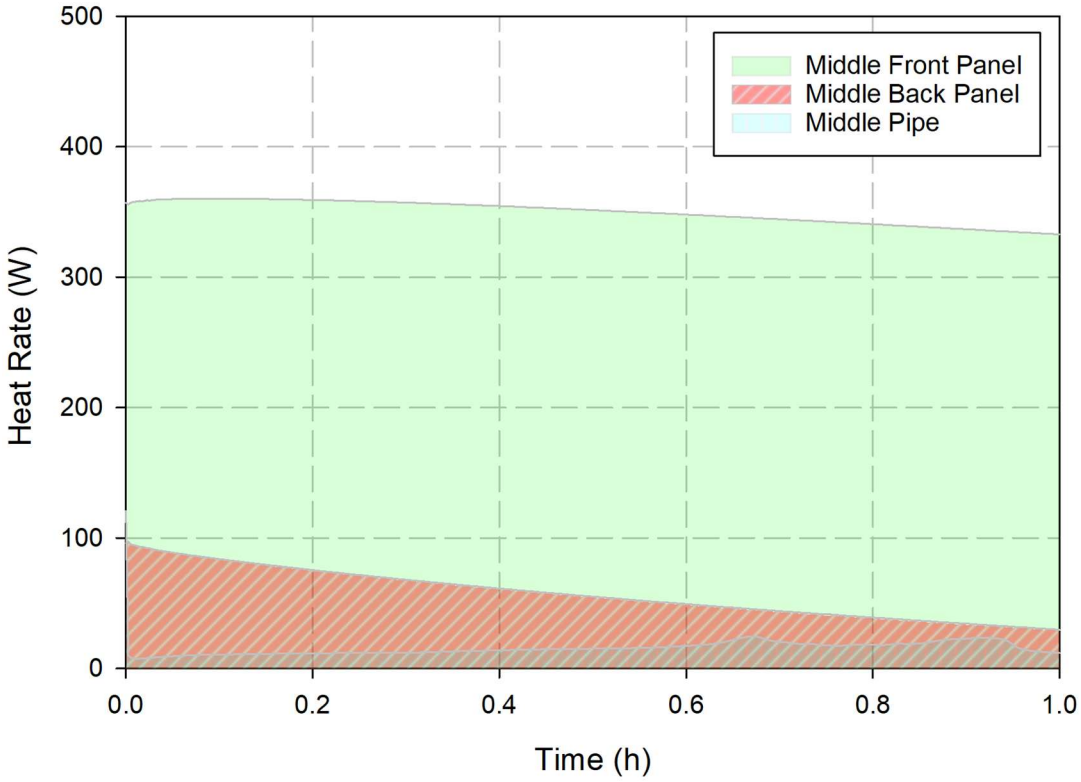

Figure 5.66: Middle front and back panel heat generation rate and working fluid net heat gain through a 1 hour period

Figure 5.68 displays the heat generation rate of the top front and back panels along with heat rate gained by the working fluid. The heat generation experienced by the front facing panel, does not vary significantly over the hour. The maximum, heat generation rate was found to be 369.02W at the time step of 0.085h. The heat generation rate decreases as the simulation continues towards the hour and reaches a steady state heat rate of 339.68W. As for the backwards facing bottom panel the maximum heat generation rate experienced by was 105.77W at a time step of 0.0025h. However, in the case of the backward facing panel the heat generation decreases drastically to a steady state heat generation rate of 35.95W. The bottom pipe experiences a maximum and minimum net heat gain of 23.56and -46.02W towards the end of the simulation. It should be noted that at the beginning of the simulation the working fluid was losing thermal energy to the top backwards facing panel, causing it to have a net loss in thermal energy.

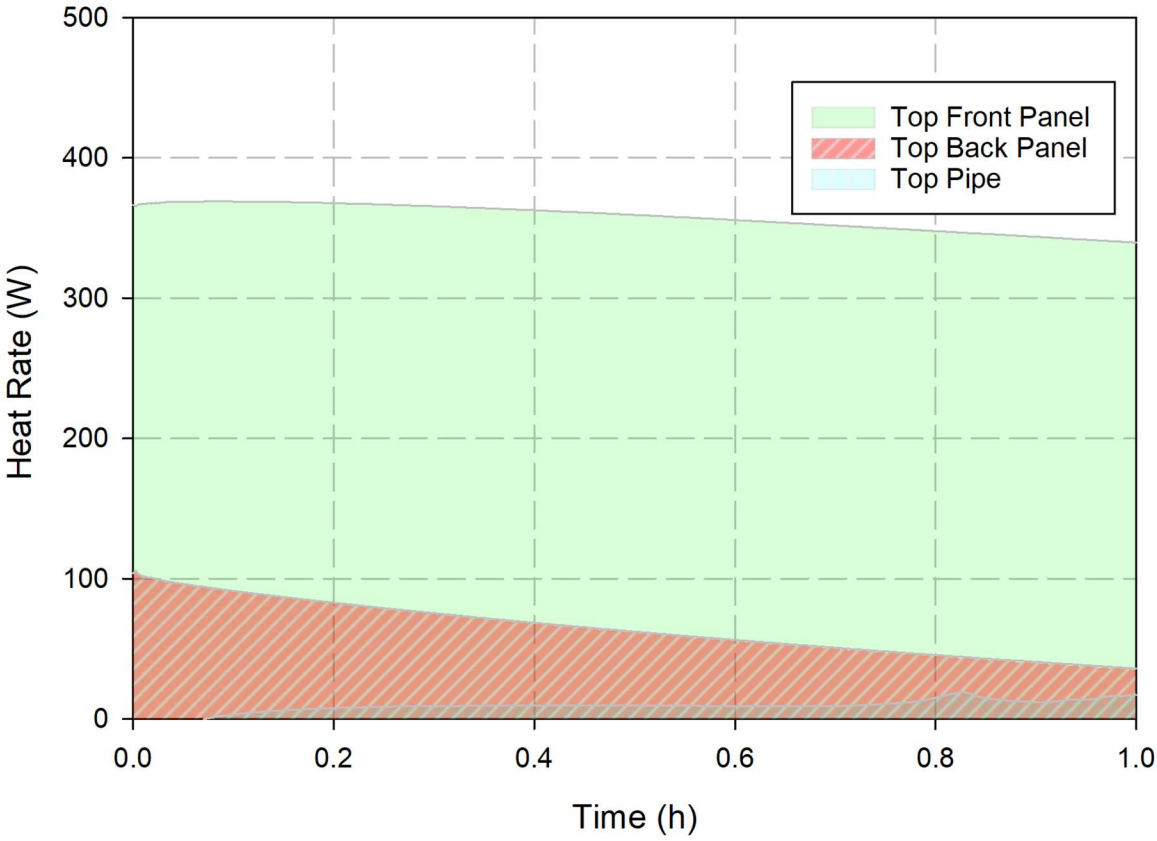

Figure 5.67: Top front and back panel heat generation rate and working fluid net heat gain through a 1 hour period

5.5 Simplified Greenization Factor Results

Another comparison between the four systems is done based on the greenization factor, which present the factor of how much CO_2 emissions are reduced based on a reference system. Note that the greenization factor (GF) calculated in this comparison is based on the operating CO_2 emitted during the operation only not considering the maintenance, manufacturing, installation and transportation. The factors not considered in the greenization analysis in this section can be the subject of further analysis of future work through life cycle assessment.

$$GF = \frac{\dot{m}_{CO_2,ref} - \dot{m}_{CO_2,Sy\ i}}{\dot{m}_{CO_2,ref}} \quad (5.1)$$

5.6 Cost Analysis

In this section the cost of the various system and production costs will be discussed. Furthermore, the savings associated with the use of cold thermal reservoirs will be assessed.

5.6.1 Cost Analysis of System 1 (OTEC integrated with ammonia)

System 1 integrates an OTEC power plant with an ammonia production system. The plant operates under two scenarios. Case 1 considers that 50% of the net power produced is provided to an electrolyzer that provides hydrogen to the ammonia synthesis system. Case two considers only power being produced. The major subsystems of the plant will be discussed in detail to give an effective cost analysis. The subsystem included in the cost analysis are as follows:

- The Proton Exchange Membrane electrolyzer for hydrogen production. The hydrogen is produced at a pressure of 1 bar and operates at current industry standards.
- The CASU is the system which is responsible for providing the N_2 to the ammonia synthesis system. The CASU produces N_2 with purity more than 95%.
- The ammonia reactors considered in this cost analysis are glass lined steal and non-agitated. The reasoned behind the glass lining is to prevent corrosion from the ammonia. The operating conditions for the Ammonia reactors were set to a pressure of 1 bar.
- Single stage Closed OTEC ammonia-based system for power production. Uses a baseline of cycle that can produce the required baseload. The cycle utilizes a single stage ammonia-based Rankine cycle.
- The condenser water discharge is used for cooling output that could be used for district cooling purposes

The OTEC plant offers an expensive base plant price relative to solar and wind at 4,000 $/kWh. However, there are unexploited benefits to using OTEC as a power source such as the cooling load available from the sea water discharge. To accommodate for this in the cost analysis, an Aspen simulation was made to estimate the power needed to reduce the temperature of the discharge water to a useable temperature of -24 ºC and heat up to 6 ºC for the use for direct use for water chillers. Conventional air chilled refrigeration cycles

consume energy at a rate of 1.2 kW/ton of cooling. System 2 integrates the discharge condenser water with the evaporator from a conventional vapor compression cycle to allow for lower exit compressor pressure. As the discharge water has a large flow rate that can be up to 25 degrees lower than that of the ambient temperature. The system at the optimum point discharges the condenser water at a temperature of 11.38°C. that temperature as mentioned has to be lower to use directly in a water chiller. The energy consumption associated with lower the cooling load to -24°C to 6°C is 0.54 kW/ton of cooling. As for figure 5.44.5.45 and 5.46 they display the refrigeration costs per ton of cooling, compressor, and reactor cost. Tables 5.6 and 5.7 display the actual costs of the proposed system at peak power production of 13MW, where 50% of the power is used to produce ammonia.

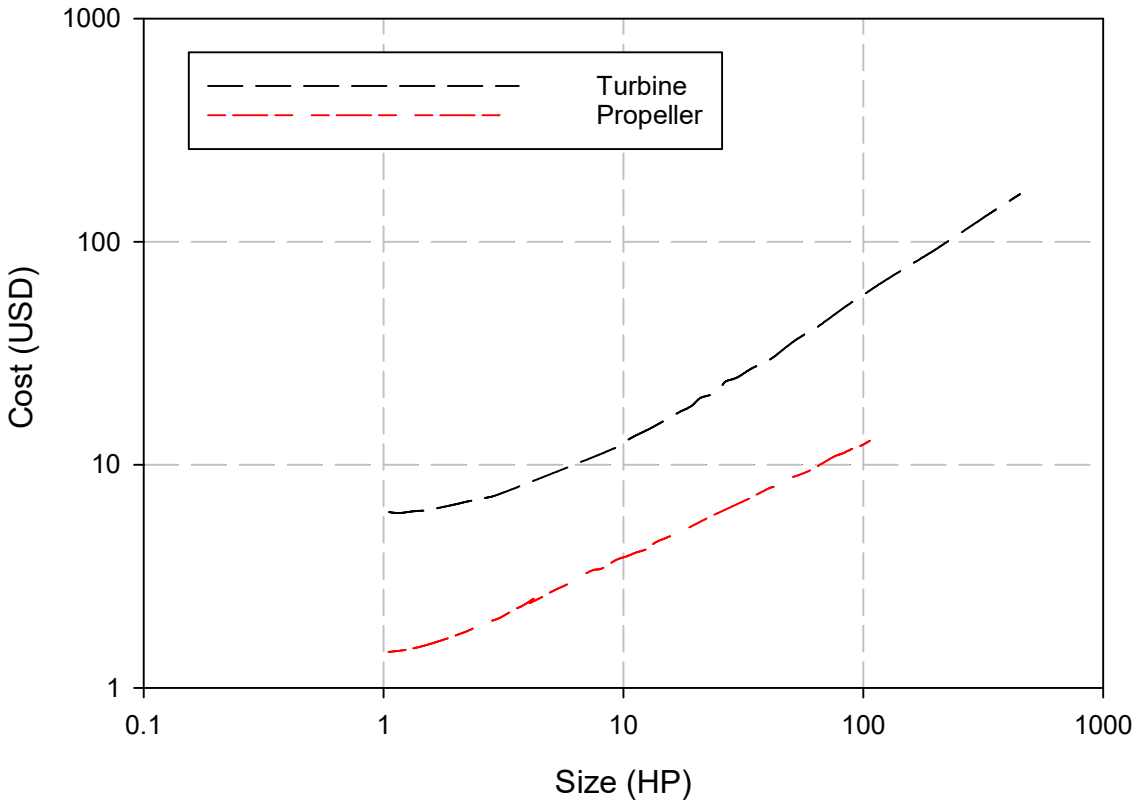

Figure 5.68: Turbine and propeller cost with power production potential [106]

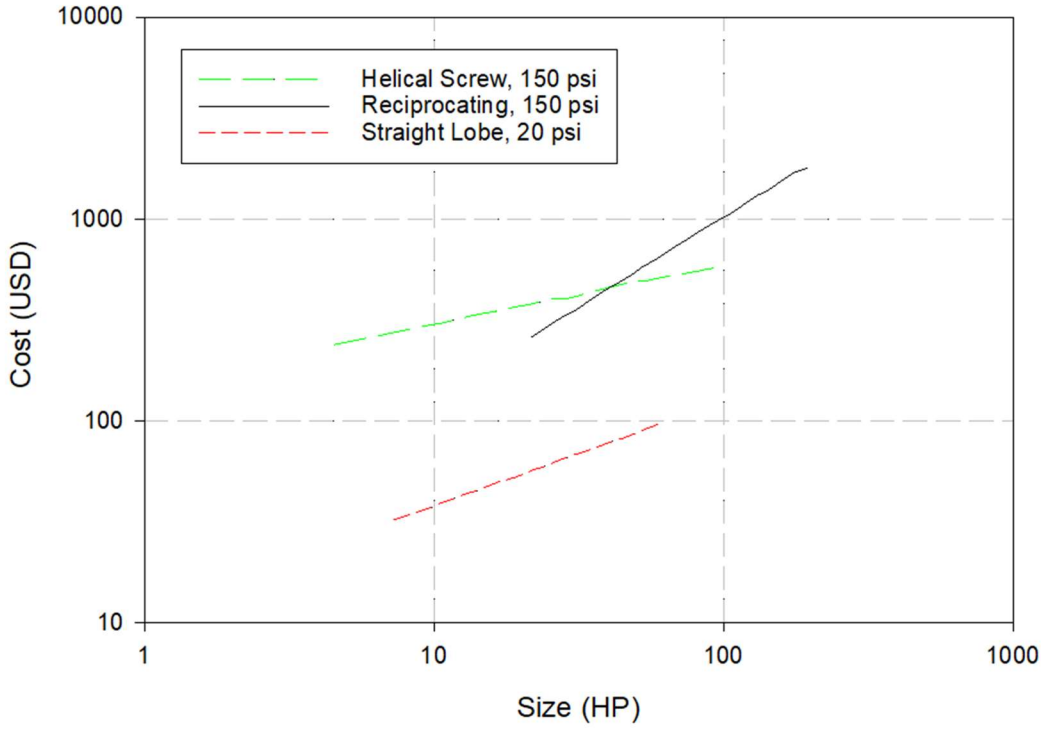

Figure 5.69: Compressor cost with power consumption potential [106]

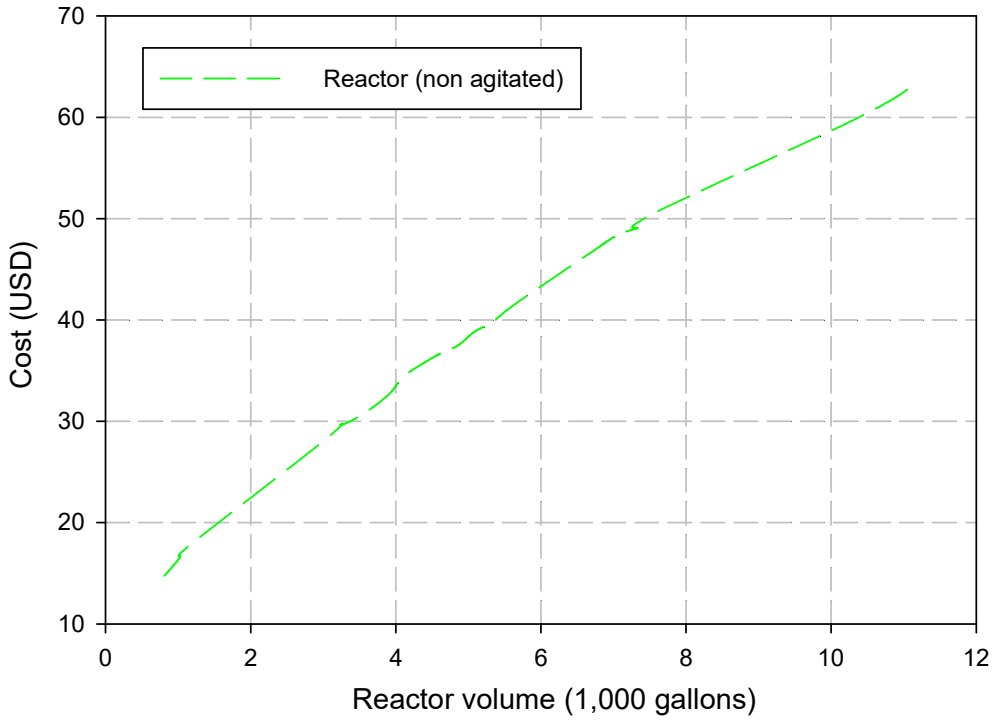

Figure 5.70: Reactor cost with power consumption potential [106]

Table 5.6: Base cost of subsystems and power production plant

Base cost of the OTEC ($/kWh)	Normalized Cost of OTEC ($/kWh)	PEM electrolyser cost ($/kW)	Ammonia reactor cost ($/gallon)	Compressor ($/hp)	Ability for liquification of Ammonia
4,000	4,666	1,300	7.3/9.1	385	Yes

Table 5.7: Final plant cost

OTEC cost (mUSD$)	PEM electrolyser cost (mUSD$)	Ammonia reactor cost (USD$)	PSA cost (kUSD$)	Cooling saving costs (USD$/ton)	Ammonia Production Cost ($/kg)	Total Cost (mUSD$)
52.9	8.6	114,900	100	0.04	0.54	61.7

5.6.2 Cost Analysis of System 2 (wind and solar integrated with ammonia)

System 2 integrates two 1.5 MW wind turbines and 7 MW solar panels power plant with an ammonia production system. The plant operates under two scenarios. Case 1 considers that 50% of the net power produced is provided to an electrolyzer that provides hydrogen to the ammonia synthesis system. Case two considers only power being produced. The major subsystems of the plant will be discussed in detail to give an effective cost analysis. The subsystem included in the cost analysis are as follows:

- The Proton Exchange Membrane electrolyzer for hydrogen production. The hydrogen is produced at a pressure of 1 bar and operates at current industry standards.
- The CASU is the system which is responsible for providing the N_2 to the ammonia synthesis system. The CASU produces N_2 with purity more than 95%.
- The ammonia reactors considered in this cost analysis are glass lined steal and non-agitated. The reasoned behind the glass lining is to prevent corrosion from the ammonia. The operating conditions for the Ammonia reactors were set to a pressure of 1 bar.
- The system consists of two GE 1.5xle wind turbines, which are popular model currently and in use in some wind power generation facilities in Ontario. The total wind power potential is 3 MW, as each of the GE 1.5xle produces a maximum of 1.5MW at wind speeds of 11m/s [88,89].

- The system also integrates solar PV panels. The model chosen for the PV cells was a thin film first solar 6420 cell. At peak production they produce 7MW of electricity.

Solar and wind offer a cheaper base electricity production cost than that of the OTEC cycle. The cost of wind and solar power based production 0.04-0.06$/kWh (wind) and 0.10$/kWh (solar)[22]. Of course, one should account for the capital cost needed for a normalized power production cost, where solar, wind and natural gas come at a cost of 2,000-3,700$/kW(commercial-residential),1200-1700$/kW, and 1,000$/kW[24]. Wind and solar energy offer a more efficient conversion efficiency; however, they do not offer continuous power production, over the day. Table 16 displays the costs associated with the subsystems associated with system 2. Tables 5.8 and 5.9 displays the actual costs of the proposed system at peak power production of 10MW, where 60% of the power is used to produce ammonia.

Table 5.8: Base cost of subsystems and power production plant

Base cost of the wind ($/kW)	Base cost of the solar ($/kW)	PEM electrolyser cost ($/kW)	Ammonia reactor cost ($/gallon)	Compressor ($/hp)	Ability for liquification of Ammonia
1,300	2,000	1,300	7.3-9.1	385	No

Table 5.9: Final plant cost

Total cost of power production (mUSD$)	PEM electrolyser cost (mUSD$)	Ammonia reactor cost (USD$)	PSA cost (kUSD $)	Cooling saving costs (USD$/ton)	Ammonia Production Cost ($/kg)
7.9	6.5	114,900	100	0.04	0.32

5.6.3 Cost Analysis of System 3 (OTEC integrated with methanol)

System 3 integrates an OTEC power plant with a methanol production plant. The plant operates under two scenarios. Case 1 considers that 100% of the net power produced is provided to an ECEM reactor that provides hydrogen and carbon dioxide to the methanol synthesis system. Case two considers only power being produced. The major subsystems of the plant will be discussed in detail to give an effective cost analysis. The subsystem included in the cost analysis are as follows:

- The main source of the continuous renewable energy is the constant temperature of the ocean at a certain depth, which is done through the use of the OTEC system for the goal of methanol production. While the other main subsystems that are integrated to deliver the utilized ocean energy to produce power and methanol are as follows:
- Electrolytic Cation Exchange Membrane for carbon dioxide and hydrogen production. The ECEM reactor recovers the carbon dioxide from the ocean water, as it electrolyzes the water to produce hydrogen.
- Multistage hydrogen and carbon dioxide compression system consists of a three-stage hydrogen compression system coupled with intercoolers for optimized performance. The intercoolers use the water discharged from the systems condenser which reduces the overall power requirements of the compression system.
- The carbon dioxide-based methanol synthesis system produces methanol from the extracted carbon dioxide from the deep ocean water that is highly concentrated with bicarbonates. The main reaction occurs in the presence of Cu/ZnO2/Al2O3 catalysts in the large-scale production of methanol
- A double stage closed OTEC ammonia-based system for power production, which is designed to produce the required baseload of 16MW, at the lowest temperature differentials in the water.
- The evaporator and the condenser use the same warm and cold-water lines of the OTEC cycle. A separate heat exchanger is used to provide cooling duties for various applications, such as district cooling.
- The condenser water discharge is used for cooling output that could be used for district cooling purposes.

The OTEC plant offers an expensive base plant price relative to solar and wind at 4,000 $/kWh. However, there are unexploited benefits to using OTEC as a power source such as the cooling load available from the sea water discharge. To accommodate for this in the cost analysis, an Aspen simulation was made to estimate the power needed to reduce the temperature of the discharge water to a useable temperature of -12 ºC and heat up to 6 ºC for the use for direct use for water chillers. Conventional air chilled refrigeration

cycles consume energy at a rate of 1.2 kW/ton of cooling. System 3 like system 1 integrates the discharge condenser water with the evaporator from a conventional vapor compression cycle to allow for lower exit compressor pressure. As the discharge water has a large flow rate that can be up to 25 degrees lower than that of the ambient temperature. The system at the optimum point discharges the condenser water at a temperature of 13.0^{o}C. that temperature as mentioned must be lower to use directly in a water chiller. The energy consumption associated with lower the cooling load to -24^{o}C to 6^{o}C is 0.59 kW/ton of cooling. Table 16 displays the costs associated with the subsystems associated with system 3. Table 5.10 and 5.11 displays the actual costs of the proposed system at peak power production of 13MW, where 50% of the power is used to produce ammonia.

Table 5.10: Base cost of subsystems and power production plant

Base cost of the OTEC ($/kWh)	Normalized Cost of OTEC ($/kWh)	PEM electrolyser cost ($/kW)	Methanol reactor cost ($/gallon)	Compressor ($/hp)	Offers cooling load
4,000	5323	1,300	46.25	385	Yes

Table 5.11: Final plant cost

OTEC cost (mUSD$)	PEM electrolyser cost (mUSD$)	Methanol reactor cost (kUSD$)	Cooling saving costs (USD$/ton)	Methanol Production Cost ($/kg)
66.8	2.17	377.5	0.01	0.36

5.6.4 Cost Analysis of System 4 (bifacial PV solar integrated with methanol)

System 4 integrates a novel concentrating bifacial PV panel with organic Rankine cycle. The main components of the system are follows:

- The main source of renewable energy is solar. It integrates concentrating bifacial modules with a heat exchanger.
- Electrolytic Cation Exchange Membrane for carbon dioxide and hydrogen production. The ECEM reactor recovers the carbon dioxide from the ocean water, as it electrolyzes the water to produce hydrogen.

- Multistage hydrogen and carbon dioxide compression system consists of a three-stage hydrogen compression system coupled with intercoolers for optimized performance. The intercoolers use the water discharged from the systems condenser which reduces the overall power requirements of the compression system.
- The carbon dioxide-based methanol synthesis system produces methanol from the extracted carbon dioxide from the deep ocean water that is highly concentrated with bicarbonates. The main reaction occurs in the presence of Cu/ZnO2/Al2O3 catalysts in the large-scale production of methanol
- A single stage ammonia-based Rankine cycle system for power production, which
- The evaporator in the system is the heat exchanger placed between two PV panel.
- The condenser water discharge is used for cooling/heating output that could be used for district cooling purposes.

Table 5.12: Base cost of subsystems and power production plant

Base cost of the ORC ($/kWh)	Solar PV ($/kWh)	PEM electrolyser cost ($/kW)	Methanol reactor cost ($/gallon)	Compressor ($/hp)	Offers cooling/heating load
2,565	5323	1,300	46.25	385	Yes

The final comparison of the systems and their cost of fuel production can be seen in table 5.13. However, one should note there are cost savings associated with running an OTEC plant due to the available cooling load. In this analysis, they were included as cost savings and were not included in the final price of the fuel.

Table 5.13: Base cost of subsystems and power production plant

System Number	Base cost of renewables ($/kW)	Energy Efficiency (%)	Liquification or cooling capability	Normalized fuel production cost ($/kg)
1	4.000	1.9	Yes	0.54
2	1,790	30.1	-	0.32
3	4,000	2.1	Yes	0.36
4	2,256	24	Yes	0.31

Chapter 6: Conclusions and Recommendations

This chapter presents conclusions of the work, research, and results of this thesis. The future recommendations are also included in this, which provide what could be done based on the inferred results of the thesis. Note that the recommendations also introduce ideas for further systems that can be proposed and further analysis ideas that are out of the scope of this thesis and its objectives.

6.1 Conclusions

In this thesis, a novel Ocean Thermal Energy Conversion (OTEC) based tri-generation system that produces ammonia, cooling, and power is developed and analyzed. An OTEC plant operates on the naturally existing temperature difference occurring in the various depths of the ocean. The OTEC plant used in this study is operated using a single-stage ammonia Rankine cycle. The discharge seawater from the condenser in the organic Rankine cycle is used to provide district cooling and liquefaction of ammonia.

Two different operation cases of the analyzed system are considered, where for the first case 50% of what potentially can be converted to power is used to produce ammonia produced for off-peak hours, the second case is for complete power production,

- In case 1 50% of the power produced was transferred to produce ammonia. The highest energy and exergy efficiency was found to be 1.37% and 56.17%, respectively.
- As for the case 2, the maximum energy and exergy efficiency of the OTEC plant is found to be 1.83% and 78.02% respectively.
- The corresponding maximum power production was 6,612 kW and 13,224 kW for cases 1 and 2.
- The maximum hydrogen production rate was found to be 94.35 kg/h and 534.7 kg/h at peak efficiency values.
- The cooling duty at the peak energy and exergy efficiency was found to be 64.4 MW, where the condenser temperature is 11.38ºC.
- The production cost of ammonia was found to be 0.54$/kg

For system 2, the proposed system was conceptually developed, modeled, simulated, and analyzed. The proposed bi-generation system consists of wind turbines, PV units, electrolyzer, and an ammonia synthesis system. The main inputs of the system are nitrogen,

water, solar irradiance, and wind. Freshwater was used as the feedstock for the electrolyzers for hydrogen production. The produced hydrogen was then used in the multistage ammonia synthesis system.

- At maximum power output from the solar field the maximum exergy and energy efficiency of the overall system was found to be 18.8% and 19.1%, respectively.
- The corresponding overall exergy destruction at peak power and ammonia production was found to be 21.1 GW.
- The cost of production of ammonia was found to be 0.32$/kg.

System 3 shows a novel ocean thermal energy conversion (OTEC) system that is proposed to produce methanol, cooling and power. The system was developed and analyzed energetically and exegetically. In this proposed trigeneration system, a two-stage Rankine cycle that operates on the inherent temperature difference along the depth of the ocean is used for power production and integrated with an electrolytic cation exchange membrane (ECEM) reactor for carbon dioxide and hydrogen production. The performance of the proposed system is assessed under various operating conditions.

- The system utilised the deep ocean water, unlike any other system in the literature for its rich carbon dioxide content.
- The maximum cooling rate was found to be 69.0 GW, at a temperature of 13ºC.
- The maximum methanol production rate was found to be 1.36 kg/s at a power input of 51.5 GW.
- Three different cases were simulated: Case 1: ECEM reactor operates at its current efficiency with fuel production and district cooling being the only products, Case 2: ECEM reactor operates at proton exchange membrane (PEM) efficiency, and Case 3: Only power was produced with no fuel.
- The maximum overall energy efficiency of the cycle was found to be 8.0, 8.6, and 7.3% for Cases 1, 2, and 3, respectively.
- The fuel production cost of methanol was found to be 0.36$/kg

System 4 proposes the novel use of bifacial photovoltaic solar panel modules for offshore power and thermal energy production. The proposed system was modeled and simulated on the COMSOL Multiphysics software under various water conditions, along with different module positioning. Furthermore, the performance of the proposed system is

simulated under various operating parameters, including the location of the sun throughout a single day is considered as well as intensity of the solar radiation.

- It was found that the north/south facing bifacial solar panels experienced a maximum of 55% of solar irradiance exposure compared to the single face panel when operating on the water surface.
- As for the east/west facing modules, it was found that a maximum 31% extra solar irradiance exposure was experienced compared to the single face panel when operating on the water surface.
- The wavy water simulation yielded similar results; the maximum increase in energy production was 49% and 33% for the north/south and east/west facing module.
- It should be noted that the east-facing modules yielded a larger energy production rate than the north-facing module.
- The east-facing modules experienced a 24% increase in overall in power production than the north-facing modules.
- The minimum and maximum energy efficiency gains were calculated as 2.8% and 11.9%.

6.2 Recommendations

In this section, a set of recommendations are provided for further study considerations that can be built on the work and results presented in this thesis. The work in this thesis mainly includes the Development and Assessment of Renewable Ammonia and Methanol Production Systems. In order to further investigate the proposed systems and expand on the introduced field of renewable fuel production systems and the recommendations can be listed as follows:

- An experimental study of the integration of a bifacial solar panel with the proposed thermal management system is recommended to investigate the performance of the system experimentally.
- The thermal management system should be tested experimentally for use in an OTEC cycle or even Lake environment.

- Performing exergoeconomic analysis on all of the proposed systems, along with the savings associated with the novel integration of the subsystems.
- Build a lab-scale version of the ammonia and methanol production systems for experimental testing.
- A life cycle analysis of the proposed systems should be evaluated to have a full understanding of the effects of the systems on the long-term, including their refurbishment and decommissioning.

As presented in the comparison sections of the results and discussion chapter, the proposed systems were able to achieve a better performance than renewable energy-based carbon neutral and carbon-free fuels. The proposed systems are promising options for the growing hydrogen economy. It is recommended that the industry focuses on investigating the viability of renewable energy-based hybrid systems for fuel and electrical production.

References

[1] Schlapbach L, Züttel A. Hydrogen-storage materials for mobile applications. Nature 2001;414:353–8. https://doi.org/10.1038/35104634.

[2] Dresselhaus, M., Crabtree, G., Buchanan M. Basic Energy Needs for the Hydrogen Economy 2003. http://www.sc.doe.gov/bes/hydrogen.pdf. (accessed May 18, 2019).

[3] Germany Turns to Hydrogen in Quest for Clean Energy Economy - Bloomberg n.d. https://www.bloomberg.com/news/articles/2019-08-02/germany-turns-to-hydrogen-in-quest-for-clean-energy-economy (accessed April 19, 2020).

[4] Neill SP, Hashemi MR. Fundamentals of ocean renewable energy : generating electricity from the sea. 1st ed. Elsevier; n.d.

[5] Bharathan D. Staging Rankine Cycles Using Ammonia for OTEC Power Production. 2009. https://doi.org/osti.gov/bridge (accessed 2018-11-11).

[6] Ocean Thermal Energy Conversion: An Overview. n.d. https://doi.org/https://www.nrel.gov/docs/legosti/old/3024.pdf, date accessed (2018-11-02).

[7] Hasan A, Dincer I. Development of an integrated wind and PV system for ammonia and power production for a sustainable community. J Clean Prod 2019;231:1515–25. https://doi.org/10.1016/j.jclepro.2019.05.110.

[8] Hasan A, Dincer I. A New Integrated Ocean Thermal Energy Conversion-Based Trigeneration System for Sustainable Communities. J Energy Resour Technol 2020;142. https://doi.org/10.1115/1.4045469.

[9] Yuan H, Zhou P, Mei N. Performance analysis of a solar-assisted OTEC cycle for power generation and fishery cold storage refrigeration. Appl Therm Eng 2015;90:809–19. https://doi.org/10.1016/j.applthermaleng.2015.07.072.

[10] Yilmaz F, Ozturk M, Selbas R. Thermodynamic performance assessment of ocean thermal energy conversion based hydrogen production and liquefaction process. Int J Hydrogen Energy 2018;43:10626–36. https://doi.org/10.1016/j.ijhydene.2018.02.021.

[11] Park S, Chun W, Kim N. Simulated production of electric power and desalination using Solar-OTEC hybrid system. Int J Energy Res 2017;41:637–49. https://doi.org/10.1002/er.3641.

[12] Park SS, Kim W joong, Kim YH, Hwang JD, Kim NJ. Regenerative OTEC systems using condenser effluents discharged from three nuclear power plants in South Korea. Int J Energy Res 2015;39:397–405. https://doi.org/10.1002/er.3251.

[13] Arias FJ. Ocean thermal energy conversion by deliberate seawater salinization. Int J Energy Res 2018;42:499–507. https://doi.org/10.1002/er.3831.

[14] Yoon JI, Seol SH, Son CH, Jung SH, Kim YB, Lee HS, et al. Analysis of the high-

efficiency EP-OTEC cycle using R152a. Renew Energy 2017;105:366–73. https://doi.org/10.1016/j.renene.2016.12.019.

[15] Yoon JI, Son CH, Baek SM, Ye BH, Kim HJ, Lee HS. Performance characteristics of a high-efficiency R717 OTEC power cycle. Appl Therm Eng 2014;72:304–8. https://doi.org/10.1016/j.applthermaleng.2014.05.103.

[16] Yeh R-H, Su T-Z, Yang M-S. Maximum output of an OTEC power plant. Ocean Eng 2005;32:685–700. https://doi.org/10.1016/J.OCEANENG.2004.08.011.

[17] Wind-to-Hydrogen Project | Hydrogen and Fuel Cells | NREL n.d. https://www.nrel.gov/hydrogen/wind-to-hydrogen.html (accessed October 23, 2019).

[18] ARPA-E | Wind Energy to Ammonia Synthesis n.d. https://arpa-e.energy.gov/?q=slick-sheet-project/wind-energy-ammonia-synthesis (accessed October 23, 2019).

[19] Ahmadi P, Dincer I, Rosen MA. Performance Assessment of a Novel Solar and Ocean Thermal Energy Conversion Based Multigeneration System for Coastal Areas. J Sol Energy Eng 2014;137:011013. https://doi.org/10.1115/1.4028241.

[20] Uehara H, Miyara A, Ikegami Y, Nakaoka T. Performance analysis of an OTEC plant and a desalination plant using an integrated hybrid cycle. J Sol Energy Eng Trans ASME 1996;118:115–22. https://doi.org/10.1115/1.2847976.

[21] Sadayuki Jitsuhara,Haruo Uehara HK. The Present Status and Features of OTEC and Recent Aspects of Thermal Energy Conversion Technology. n.d. https://doi.org/http://www.nmri.go.jp/main/cooperation/ujnr/24ujnr_paper_jpn/Kobayashi.pdf (accessed 2018-11-06).

[22] Renewable Energy Will Be Consistently Cheaper Than Fossil Fuels By 2020, Report Claims n.d. https://www.forbes.com/sites/dominicdudley/2018/01/13/renewable-energy-cost-effective-fossil-fuels-2020/#4975619a4ff2 (accessed December 13, 2019).

[23] Renewable energy will be cheaper than fossil fuels by 2020 - Business Insider n.d. https://www.businessinsider.com/renewable-energy-will-be-cheaper-than-fossil-fuels-by-2020-2018-1 (accessed December 13, 2019).

[24] Barriers to Renewable Energy Technologies | Union of Concerned Scientists n.d. https://www.ucsusa.org/resources/barriers-renewable-energy-technologies (accessed December 13, 2019).

[25] Srinivasan N, Sridhar M, Agrawal M. Study on the Cost Effective Ocean Thermal Energy Conversion Power Plant. Proc. Offshore Technol. Conf., Society of Petroleum Engineers; 2010. https://doi.org/10.2523/20340-MS.

[26] OCEAN THERMAL EXTRACTABLE ENERGY VISUALIZATION Final Technical Report Prepared by Lockheed Martin Mission Systems & Sensors (MS2). 2012. https://doi.org/http://maps.nrel.gov/mhk_atlas.

[27] Ocean Thermal Energy Conversion - Makai Ocean Engineering n.d. https://www.makai.com/ocean-thermal-energy-conversion/ (accessed December 12, 2019).

[28] Willauer HD, DiMascio F, Hardy DR, Williams FW. Feasibility of CO 2 Extraction from Seawater and Simultaneous Hydrogen Gas Generation Using a Novel and Robust Electrolytic Cation Exchange Module Based on Continuous Electrodeionization Technology. Ind Eng Chem Res 2014;53:12192–200. https://doi.org/10.1021/ie502128x.

[29] Willauer HD, DiMascio F, Hardy DR, Williams FW. Development of an Electrolytic Cation Exchange Module for the Simultaneous Extraction of Carbon Dioxide and Hydrogen Gas from Natural Seawater. Energy and Fuels 2017;31:1723–30. https://doi.org/10.1021/acs.energyfuels.6b02586.

[30] CO2 Dissolved in Ocean Water n.d. https://www.soest.hawaii.edu/oceanography/faculty/zeebe_files/Publications/ZeebeWolfEnclp07.pdf (accessed January 12, 2020).

[31] Gruber N. The Marine Nitrogen Cycle: Overview and Challenges n.d. https://doi.org/10.1016/B978-0-12-372522-6.00001-3.

[32] Al-Zareer M, Dincer I, Rosen MA. Transient Energy and Exergy Analyses of a Multistage Hydrogen Compression and Storage System. Chem Eng Technol 2018;41:1594-n/1603. https://doi.org/10.1002/ceat.201700341.

[33] Klerke A, Christensen CH, Nørskov JK, Vegge T. Ammonia for hydrogen storage: Challenges and opportunities. J Mater Chem 2008;18:2304–10. https://doi.org/10.1039/b720020j.

[34] Zamfirescu C, Dincer I. Ammonia as a green fuel and hydrogen source for vehicular applications. Fuel Process Technol 2009;90:729–37. https://doi.org/10.1016/j.fuproc.2009.02.004.

[35] Alternative Fuels Data Center: Fuel Properties Comparison n.d. https://afdc.energy.gov/fuels/properties (accessed May 16, 2019).

[36] Molar Enthalpy of Formation of Various Substances - (Updated 1/18/09) n.d. https://www.ohio.edu/mechanical/thermo/property_tables/combustion/Enth_Formation.html (accessed May 16, 2019).

[37] 1910.111 - Storage and handling of anhydrous ammonia. | Occupational Safety and Health Administration n.d. https://www.osha.gov/laws-regs/regulations/standardnumber/1910/1910.111 (accessed May 16, 2019).

[38] ASHRAE Handbook Online n.d. https://www.ashrae.org/technical-resources/ashrae-handbook/ashrae-handbook-online (accessed May 16, 2019).

[39] Christensen CH, Sørensen RZ, Johannessen T, Quaade UJ, Honkala K, Elmøe TD, et al. Metal ammine complexes for hydrogen storage. J Mater Chem 2005;15:4106. https://doi.org/10.1039/b511589b.

[40] Stitou D, Goetz V, Spinner B. A new analytical model for solid-gas thermochemical reactors based on thermophysical properties of the reactive medium. Chem Eng Process Process Intensif 1997;36:29–43. https://doi.org/10.1016/S0255-2701(96)04173-6.

[41] Choudhary TV, Sivadinarayana C, Goodman DW. Catalytic ammonia decomposition: COx-free hydrogen production for fuel cell applications. Catal Letters 2001;72:197–201. https://doi.org/10.1023/A:1009023825549.

[42] Giddey S, Badwal SPS, Kulkarni A. Review of electrochemical ammonia production technologies and materials. Int J Hydrogen Energy 2013;38:14576–94. https://doi.org/10.1016/J.IJHYDENE.2013.09.054.

[43] Cinti G, Frattini D, Jannelli E, Desideri U, Bidini G. Coupling Solid Oxide Electrolyser (SOE) and ammonia production plant. Appl Energy 2017;192:466–76. https://doi.org/10.1016/J.APENERGY.2016.09.026.

[44] Sánchez A, Martín M. Optimal renewable production of ammonia from water and air. J Clean Prod 2018;178:325–42. https://doi.org/10.1016/J.JCLEPRO.2017.12.279.

[45] Al-Zareer M, Dincer I, Rosen MA. Transient analysis and evaluation of a novel pressurized multistage ammonia production system for hydrogen storage purposes. J Clean Prod 2018;196:390–9. https://doi.org/10.1016/J.JCLEPRO.2018.06.022.

[46] Bicer Y, Dincer I. Development of a multigeneration system with underground coal gasification integrated to bitumen extraction applications for oil sands. Energy Convers Manag 2015;106:235–48. https://doi.org/10.1016/J.ENCONMAN.2015.09.020.

[47] Untitled Document n.d. https://www.ucl.ac.uk/~ucbcdab/urea/amtox.htm (accessed April 13, 2020).

[48] Safety and Health Topics | Ammonia Refrigeration | Occupational Safety and Health Administration n.d. https://www.osha.gov/SLTC/ammoniarefrigeration/ (accessed April 13, 2020).

[49] Rihko-Struckmann LK, Peschel A, Hanke-Rauschenbach R, Sundmacher K. Assessment of Methanol Synthesis Utilizing Exhaust CO_2 for Chemical Storage of Electrical Energy. Ind Eng Chem Res 2010;49:11073–8. https://doi.org/10.1021/ie100508w.

[50] Hasan A, Dincer I. Comparative assessment of various gasification fuels with waste tires for hydrogen production. Int J Hydrogen Energy 2019. https://doi.org/10.1016/j.ijhydene.2018.11.150.

[51] Byrne J, Kurdgelashvili L. Handbook of Photovoltaic Science and Engineering. Wiley; 2010. https://doi.org/10.1002/9780470974704.

[52] Bentaher H, Kaich H, Ayadi N, Ben Hmouda M, Maalej A, Lemmer U. A simple tracking system to monitor solar PV panels. Energy Convers Manag 2014;78:872–5. https://doi.org/10.1016/j.enconman.2013.09.042.

[53] Home Solar Panels, Commercial & Utility-Scale Solar Solutions | SunPower n.d. https://us.sunpower.com/solar-panels-technology/a-series-solar-panels (accessed November 11, 2019).

[54] Peng Z, Herfatmanesh MR, Liu Y. Cooled solar PV panels for output energy efficiency optimisation. Energy Convers Manag 2017;150:949–55. https://doi.org/10.1016/j.enconman.2017.07.007.

[55] Abdallah S. The effect of using sun tracking systems on the voltage-current characteristics and power generation of flat plate photovoltaics. Energy Convers Manag 2004;45:1671–9. https://doi.org/10.1016/j.enconman.2003.10.006.

[56] Clifford MJ, Eastwood D. Design of a novel passive solar tracker. Sol Energy 2004;77:269–80. https://doi.org/10.1016/J.SOLENER.2004.06.009.

[57] Koussa M, Cheknane A, Hadji S, Haddadi M, Noureddine S. Measured and modelled improvement in solar energy yield from flat plate photovoltaic systems utilizing different tracking systems and under a range of environmental conditions. Appl Energy 2011;88:1756–71. https://doi.org/10.1016/J.APENERGY.2010.12.002.

[58] Teo HG, Lee PS, Hawlader MNA. An active cooling system for photovoltaic modules. Appl Energy 2012;90:309–15. https://doi.org/10.1016/J.APENERGY.2011.01.017.

[59] Popovici CG, Hudişteanu SV, Mateescu TD, Cherecheş N-C. Efficiency Improvement of Photovoltaic Panels by Using Air Cooled Heat Sinks. Energy Procedia 2016;85:425–32. https://doi.org/10.1016/J.EGYPRO.2015.12.223.

[60] Du B, Hu E, Kolhe M. Performance analysis of water cooled concentrated photovoltaic (CPV) system. Renew Sustain Energy Rev 2012;16:6732–6. https://doi.org/10.1016/J.RSER.2012.09.007.

[61] Zhu L, Raman AP, Fan S. Radiative cooling of solar absorbers using a visibly transparent photonic crystal thermal blackbody. Proc Natl Acad Sci U S A 2015;112:12282–7. https://doi.org/10.1073/pnas.1509453112.

[62] Nižetić S, Čoko D, Yadav A, Grubišić-Čabo F. Water spray cooling technique applied on a photovoltaic panel: The performance response. Energy Convers Manag 2016;108:287–96. https://doi.org/10.1016/J.ENCONMAN.2015.10.079.

[63] Bahaidarah HMS. Experimental performance evaluation and modeling of jet impingement cooling for thermal management of photovoltaics. Sol Energy 2016;135:605–17. https://doi.org/10.1016/J.SOLENER.2016.06.015.

[64] Jouhara H, Milko J, Danielewicz J, Sayegh MA, Szulgowska-Zgrzywa M, Ramos JB, et al. The performance of a novel flat heat pipe based thermal and PV/T (photovoltaic and thermal systems) solar collector that can be used as an energy-active building envelope material. Energy 2016;108:148–54. https://doi.org/10.1016/J.ENERGY.2015.07.063.

[65] JIN Z, HAO X, MIN S, XU J, YUAN H. Efficient Photocatalytic Hydrogen

Evolution over Platinum and Boron Co-doped TiO2 Photoatalysts. Mater Sci 2014;20:392–5. https://doi.org/10.5755/j01.ms.20.4.6412.

[66] He Y, Xiao L, Li L. Theoretical and experimental study on the application of diffuse-reflection concentrators in PV/T solar system. Int J Energy Res 2016;40:963–70. https://doi.org/10.1002/er.3491.

[67] Luque EG, Antonanzas-Torres F, Escobar R. Effect of soiling in bifacial PV modules and cleaning schedule optimization. Energy Convers Manag 2018;174:615–25. https://doi.org/10.1016/j.enconman.2018.08.065.

[68] Liang TS, Pravettoni M, Deline C, Stein JS, Kopecek R, Singh JP, et al. A review of crystalline silicon bifacial photovoltaic performance characterisation and simulation. Energy Environ Sci 2019;12:116–48. https://doi.org/10.1039/c8ee02184h.

[69] Nussbaumer H, Klenk M, Morf M, Keller N. Energy yield prediction of a bifacial PV system with a miniaturized test array. Sol Energy 2019:316–25. https://doi.org/10.1016/j.solener.2018.12.042.

[70] Khan MR, Hanna A, Sun X, Alam MA. Vertical bifacial solar farms: Physics, design, and global optimization. Appl Energy 2017;206:240–8. https://doi.org/10.1016/j.apenergy.2017.08.042.

[71] Taylor T. Advantages of Long-Life Roofing for Bifacial Solar Panels - GAF Blog. GAF Blog 2019. http://blog.gaf.com/advantages-of-long-life-roofing-for-bifacial-solar-panels/ (accessed April 20, 2019).

[72] Hübner A, Aberle AG, Hezel R. Novel cost-effective bifacial silicon solar cells with 19.4% front and 18.1% rear efficiency. Appl Phys Lett 1997;70:1008–10. https://doi.org/10.1063/1.118466.

[73] Taguchi M, Yano A, Tohoda S, Matsuyama K, Nakamura Y, Nishiwaki T, et al. 24.7% Record Efficiency HIT Solar Cell on Thin Silicon Wafer. IEEE J Photovoltaics 2014;4:96–9. https://doi.org/10.1109/JPHOTOV.2013.2282737.

[74] Helm P, Taylor N. 31st European Photovoltaic Solar Energy Conference and Exhibition 1817. vol. 1. 1817.

[75] Jia G, Gawlik A, Plentz J, Andrä G. Bifacial multicrystalline silicon thin film solar cells. Sol Energy Mater Sol Cells 2017;167:102–8. https://doi.org/10.1016/J.SOLMAT.2017.04.004.

[76] Rai AK, Kaushika ND, Singh B, Agarwal N. Simulation model of ANN based maximum power point tracking controller for solar PV system. Sol Energy Mater Sol Cells 2011;95:773–8. https://doi.org/10.1016/j.solmat.2010.10.022.

[77] Wang Y, Huo J, Zhou L, Huang Q. Comparative study of high concentrating photovoltaics integrated with phase-change liquid film cooling system. Int J Energy Res 2019;43:2108–22. https://doi.org/10.1002/er.4414.

[78] Reddy SR, Ebadian MA, Lin CX. A review of PV-T systems: Thermal

management and efficiency with single phase cooling. Int J Heat Mass Transf 2015;91:861–71. https://doi.org/10.1016/j.ijheatmasstransfer.2015.07.134.

[79] Chauhan A, Tyagi V V., Anand S. Futuristic approach for thermal management in solar PV/thermal systems with possible applications. Energy Convers Manag 2018;163:314–54. https://doi.org/10.1016/j.enconman.2018.02.008.

[80] Joshi AS, Dincer I, Reddy B V. Effect of colors of light on the PV/T system performance. Int J Energy Res 2012;36:572–8. https://doi.org/10.1002/er.1816.

[81] Zhu Q, Zhu C, Liu S, Shen C, Zhao W, Chen Z, et al. A model to evaluate the effect of shading objects on the energy yield gain of bifacial modules. Sol Energy 2019;179:24–9. https://doi.org/10.1016/j.solener.2018.12.006.

[82] Kye HG, Park BS, Lee JM, Song MG, Song HG, Ahrberg CD, et al. Dual-neodymium magnet-based microfluidic separation device. Sci Rep 2019;9:9502. https://doi.org/10.1038/s41598-019-45929-y.

[83] Makai's Ocean Thermal Energy Conversion (OTEC) Power Plant, Hawaii - Power Technology | Energy News and Market Analysis n.d. https://www.power-technology.com/projects/makais-ocean-thermal-energy-conversion-otec-power-plant-hawaii/ (accessed November 1, 2019).

[84] Dincer I, Hasan A. Heat Engines. Compr. Energy Syst., vol. 4–5, Elsevier; 2018, p. 125–68. https://doi.org/10.1016/B978-0-12-809597-3.00405-3.

[85] Hasan A, Dincer I. An ocean thermal energy conversion based system for district cooling, ammonia and power production. Int J Hydrogen Energy 2020. https://doi.org/10.1016/j.ijhydene.2020.03.173.

[86] Boggs BK, Botte GG. On-board hydrogen storage and production: An application of ammonia electrolysis. J Power Sources 2009;192:573–81. https://doi.org/10.1016/j.jpowsour.2009.03.018.

[87] Al-Zareer M, Dincer I, Rosen MA. Development of an integrated system for electricity and hydrogen production from coal and water utilizing a novel chemical hydrogen storage technology. Fuel Process Technol 2017;167:608–21. https://doi.org/10.1016/J.FUPROC.2017.07.011.

[88] 1 MW Onshore Wind Turbine Platform | GE Renewable Energy n.d. https://www.ge.com/renewableenergy/wind-energy/onshore-wind/1mw-platform (accessed January 10, 2020).

[89] GE Energy 1.5MW Wind Turbine n.d. https://geosci.uchicago.edu/~moyer/GEOS24705/Readings/GEA14954C15-MW-Broch.pdf (accessed January 10, 2020).

[90] First Solar Series 6^{TM} Module | USER GUIDE Rev 2.1 | First Solar Series 6 Module User Guide COPYRIGHT AND NOTICES 2019. www.firstsolar.com. (accessed January 10, 2020).

[91] First Solar Series 6^{TM} n.d. www.firstsolar.com. (accessed January 10, 2020).

[92] Ezzat MF, Dincer I. Development, analysis and assessment of a fuel cell and solar photovoltaic system powered vehicle. Energy Convers Manag 2016;129:284–92. https://doi.org/10.1016/j.enconman.2016.10.025.

[93] Boggs BK, Botte GG. On-board hydrogen storage and production: An application of ammonia electrolysis. J Power Sources 2009;192:573–81. https://doi.org/10.1016/J.JPOWSOUR.2009.03.018.

[94] Hasan A, Dincer I. Experimental evaluation of thermal management options for bags. Appl Therm Eng 2019;148. https://doi.org/10.1016/j.applthermaleng.2018.10.082.

[95] Hasan A, Dincer I. Investigation of new insulation materials for environmentally-benign food delivery bags. Green Energy Technol., Springer; 2020, p. 751–77. https://doi.org/10.1007/978-3-030-20637-6_37.

[96] Gan LK, Shek JKH, Mueller MA. Hybrid wind–photovoltaic–diesel–battery system sizing tool development using empirical approach, life-cycle cost and performance analysis: A case study in Scotland. Energy Convers Manag 2015;106:479–94. https://doi.org/10.1016/j.enconman.2015.09.029.

[97] Şahin AD, Dincer I, Rosen MA. Thermodynamic analysis of wind energy. Int J Energy Res 2006;30:553–66. https://doi.org/10.1002/er.1163.

[98] (PDF) CFD wake modeling using a porous disc n.d. https://www.researchgate.net/publication/237755001/download (accessed September 7, 2018).

[99] Aerodynamic Performance n.d. https://www3.nd.edu/~tcorke/w.WindTurbineCourse/Aerodynamics_Presentation.pdf (accessed September 8, 2018).

[100] Pope K, Dincer I, Naterer GF. Energy and exergy efficiency comparison of horizontal and vertical axis wind turbines. Renew Energy 2010;35:2102–13. https://doi.org/10.1016/J.RENENE.2010.02.013.

[101] Published Research Papers | Nutonian, Inc. n.d. https://www.nutonian.com/research/reference/ (accessed January 10, 2020).

[102] Schmidt M, Lipson H. Distilling free-form natural laws from experimental data. Science (80-) 2009;324:81–5. https://doi.org/10.1126/science.1165893.

[103] Rollefson R, Havens R. Index of Refraction of Methane in the Infra-Red and the Dipole Moment of the CH Bond. Phys Rev 1940;57:710–7. https://doi.org/10.1103/PhysRev.57.710.

[104] Silicon (Si) - University of Reading n.d. https://www.reading.ac.uk/ir-infraredmaterials-si.aspx (accessed April 11, 2019).

[105] Sinama F, Martins M, Journoud A, Marc O, Lucas F. Thermodynamic analysis and optimization of a 10MW OTEC Rankine cycle in Reunion Island with the equivalent Gibbs system method and generic optimization program GenOpt. Appl

Ocean Res 2015;53:54–66. https://doi.org/10.1016/j.apor.2015.07.006.

[106] "Process Equipment Cost References", *Matche.com*, 2020. [Online]. Available: https://www.matche.com/equipcost/References.html. [Accessed: 19- Mar- 2020]